Characterising Exoplanets in Reflected Light: A pathway towards Earth-like worlds

Sophia Romana Vaughan

St. John's College

University of Oxford

A thesis presented for the degree of

Doctor of Philosophy

Trinity 2024

I dedicate this to my Mum, Dad, Brother and Sister.

Thank you for all the love and support you have given me over the years.

To Martin, thank you for always standing by me.

And to Jamie Smith, Romana Hobler, Roman Hobler, Missie and Angela Vaughan,

who all saw me start my PhD but not finish it.

You will always have a place in my heart.

Ex astris, scientia. [From the stars, knowledge]

— Starfleet Academy Motto, Star Trek

Declaration

The work of this thesis is comprised both of work that I completed independently and in collaboration at the University of Oxford, between October 2020 and August 2024.

I carried out this work under the supervision of Professor Jayne Birkby. This research was entirely funded by the European Research Council (ERC).

I declare that no part of this thesis has been accepted or is currently being submitted for any degree, diploma or certificate or other qualification at the University of Oxford or elsewhere.

I clarify the contributions at the beginning of each chapter.

Acknowledgements

Space may be vast and seemingly empty but our world is not. A great number of people have shaped my life and brought me to where I am today.

In chronological order:

Firstly, without the support and nurturing of my Mum and Dad, I would not be where I am today. You knew I loved the stars from an early age and you encouraged it. You fought for me when others did not believe in me and you never let the fact I am a woman dissuade me from doing what I love. I would also like to extend my deepest gratitude to my brother and sister for putting up with my weirdness and never judging me (for my career choice at least). I love you all.

Next, I cannot begin to express my thanks to Martin, who has stood by me for the last seven (almost eight!) years. You are my rock and your endless support has kept me going through both my undergraduate and graduate degrees. I love you.

I'd also like to extend my gratitude to my undergraduate tutors, especially Tony Weidberg and Georg Viehhauser. Even though my undergraduate degree got off to a bit of a rocky start you never stopped believing in me, even when I did not believe in myself. You have given, and continue to give me, so much help and advice. Thank you for everything.

The completion of my dissertation would not have been possible without the support of my supervisor, Jayne Birkby. You have been an excellent guide through the field of exoplanet atmospheres. I am grateful that you were willing to let me explore the areas I am most interested in, even if what I am reaching for is a task for the future. While I may not be able to fulfil my dream of exploring strange new worlds aboard a luxurious starship, you let me do so from the ground. Thank you for helping me get closer to my dream than I ever thought I could.

I would also like to thank the other members of Jayne's research group; Lennart, Luke, Mitch, Chloe, Eleanor, Ben and Colette. Thank you for all the invaluable support you have given me throughout my PhD, for answering my questions and for asking me questions. Additionally, I'd like to acknowledge the assistance of paper cat for being the #1 supporter of my publications.

I'd like to extend my gratitude to my other supervisor, Raymond Pierrehumbert as well as others from the Atmospheric Physics Department, especially Jake, Alex and Joost. You have given me a greater understanding of the other side of exoplanet atmospheres which I hope will serve me well in the future. A special thanks goes to Annabella, for all the coffees, lunches, chats and science.

I also had the great pleasure of working with the HARMONI team especially Niranjan Thatte, Alexis Carlotti and Mathis Houllé. Thank you for all your assistance in helping me understand HARMONI, I hope to use the instrument someday once it comes online.

I would also like to thank my SpLD tutors Jane Aimes and Alexandra Brown for all the help and support they have given me to tackle my dyslexia. I never thought I could write something as long as this! To my viva committee members, Prof Chris Lintott and Dr Sasha Hinkley, thank you for your time and expertise in reviewing my thesis.

Finally, I would like to thank all cats for their welfare support. In particular, I would like to thank Missie, my family's cat, I miss you dearly.

Abstract

The study of the reflected light of exoplanets and the insights it provides on their atmospheres is a poorly developed but crucial avenue of research in exoplanet characterisation. It will be key in characterising nearby potentially Earth-like worlds due to their low temperatures and low transit probability. The upcoming Extremely Large Telescopes will offer the first opportunities to characterise nearby, potentially Earth-like worlds but will require high spectral resolution to make robust detections. However, the reflected light of an exoplanet has never been detected at high spectral resolution, therefore this thesis lays the ground work for proving this technique.

High-resolution reflection spectra have been sought for several hot Jupiters, however robust measurements have not been made due to their low reflectivity. To prove the High-Resolution Cross-Correlation Spectroscopy (HRCCS) technique for extracting high-resolution spectra in reflected light, I first present an ongoing a study of the highly reflective planet LTT-9779 b using the world's largest optical telescope i.e. ESPRESSO@VLT in 4UT mode. I have not made a robust detection of the planet's reflected light yet, which suggests the presence of a high cloud deck, however, there is a tentative but promising signal in the post-eclipse data.

A similar high-spectral resolution technique, known as molecule mapping, could leverage the spatial resolution of the Extremely Large Telescope (ELT) to study some of the first potentially Earth-like planets in reflected light. To anticipate the capabilities of the instrument HARMONI@ELT. I simulated realistic observations of Proxima b, the nearest potentially Earth-like exoplanet. It is suitable for characterisation with HARMONI, however, the instrument's focal plane mask will obscure the planet's entire orbit. If the focal plane mask were to be shrunk or offset then I show that biosignature detection on Proxima b could be possible with around 40 hours of observation.

Looking further into the future, missions like the Habitable Worlds Observatory will enable the characterisation of potentially dozens of potentially Earth-like worlds and might even detect liquid water. However, the detection of liquid water requires the planet to be observed at small separations from its star. In this thesis, I show how the size of the unobservable region behind the coronagraph strongly impacts the number of systems where scattering phenomena that can be used to detect liquid water, such as rainbows and ocean glint, can be observed. Thus giving an initial indication of the viability of observing such phenomena.

Characterisation through reflected light is a promising and exciting research area and the coming decades are expected to see significant advancements in this field. This thesis lays out a roadmap to the characterization of habitable worlds using reflected light and where this research might take us in the next few decades.

Table of Contents

List of Figures

List of Tables

List of Abbreviations

ADC . . . . . Atmospheric Dispersion Corrector

ADI . . . . . Angular Differential Imaging

ANDES . . . . . ArmazoNes high Dispersion Echelle Spectrograph

AO . . . . . Adaptive Optics

ATMO . . . . . Name not acronym: a one-dimensional (1D) radiative/convective equilibrium code

CHEOPS . . . . . CHaracterising ExOPlanet Satellite

CORALIE . . . . Name not acronym: an echelle spectrograph

DI . . . . . Direct Imaging

ELT . . . . . The Extremely Large Telescope

ELTs . . . . . Telescopes with primary mirrors larger than $30\,\mathrm{m}$ in diameter

ESPRESSO . . . Echelle SPectrograph for Rocky Exoplanets and Stable Spectroscopic Observations

FPM . . . . . Focal Plane Mask

GMagAO-X + IFS Name not acronym: an Integral Field Spectrograph for the Giant Magellan Telescope

GMT . . . . . The Giant Magellan Telescope

GMTIFS . . . . . Giant Magellan Telescope Integral-Field Spectrograph

GPI . . . . . Gemini Planet Imager

HARMONI . . . . High Angular Resolution Monolithic Optical and Near-infrared Integral field spectrograph

HARPS . . . . . High Accuracy Radial velocity Planet Searcher

HCAO . . . . . High Contrast Adaptive Optics

HCI . . . . . High Contrast Imaging

HELIOS . . . . . Name not acronym: a radiative transfer code

HRCCS . . . . . High-Resolution Cross-Correlation Spectroscopy

HRS . . . . . High-Resolution Spectroscopy

HSIM . . . . . Name not acronym: pipeline for simulating observations with HARMONI

HWO . . . . . Habitable Worlds Observatory

HZ . . . . . Habitable Zone

IFS . . . . . Integral Field Spectrograph

IFU . . . . . Integral Field Unit

IR . . . . . InfraRed

IRIS . . . . . Infrared Imaging Spectrograph

IWA . . . . . Inner Working Angle

JWST . . . . . James Webb Space Telescope

LIFE . . . . . Large Interferometer For Exoplanets

LTT . . . . . Designation for Luyten catalogue stars

MCMC . . . . . Markov chain Monte Carlo

METIS . . . . . Mid-infrared ELT Imager and Spectrograph

MICHI . . . . . Mid-IR Camera, High-disperser & IFU spectrograph

NASA . . . . . National Aeronautics and Space Administration

NIRISS/SOSS . Near Infrared Imager and Slitless Spectrograph/Single Object Slitless Spectroscopy

OSIRIS . . . . . OH-Suppressing Infrared Imaging Spectrograph

OWA . . . . . Outer Working Angle

PCA . . . . . Principal Component Analysis

PCS . . . . . Planetary Camera and Spectrograph

PHOENIX . . . . Name not acronym: a computer model of the photosphere of a star

PI . . . . . Principal Investigator

PICASO . . . . . Planetary Intensity Code for Atmospheric Scattering Observations

PSF . . . . . Point Spread Function

RDI . . . . . Reference Differential Imaging

RISTRETTO . . Name not acronym: a visible high-resolution spectrograph fed by an extreme adaptive optics system

SDI . . . . . Spectral Differential Imaging

S/N . . . . . Signal-to-Noise

SPHERE . . . . . Spectro-Polarimetric High-contrast Exoplanet REsearch

SVD . . . . . Single Value Decomposition

SYSREM . . . . . SYStematic REMoval

TESS . . . . . Transiting Exoplanet Survey Satellite

TRAPPIST . . . . TRAnsiting Planets and PlanetesImals Small Telescope-South

TMT . . . . . The Thrity Meter Telescope

UT . . . . . Unit Telescope

VLT . . . . . Very Large Telescope

WFC3 . . . . . Wide Field Camera 3

WINERED . . . . Warm INfrared Echelle spectrograph to Realize Extreme Dispersion and sensitivity

XUV . . . . . eXtreme UltraViolet

1 | Introduction

1.1 Summary

The exploration of exoplanets is preceding apace with the characterisation of Earth-like exoplanets on the horizon. Recent years have witnessed remarkable progress in our understanding of exoplanet atmospheres. This progress has been brought about by advances in our ability extract the *transmission* and *emission* spectra of exoplanets from the glare of their host stars. However, when we think of the Earth, we do not picture it in terms of the light it thermally emits or the transparency of its atmosphere. Instead, we think of a gleaming blue marble illuminated gently by the light of our sun (see Figure 1.1). We see our world in *reflected light*. This thesis explores the potential of reflected light spectroscopy and discusses the avenue it presents towards the characterisation of Earth-like exoplanets.

1.2 What is an exoplanet?

An exoplanet is a planet that orbits a star other than the Sun[1]. The first exoplanet orbiting a Sun-like star was discovered in 1995 (Mayor et al. 1995) and is unlike anything in our solar system. Using the radial velocity wobble of the star, the planet's mass was measured to be larger than half the mass of Jupiter and its orbital period to be roughly 100 hours (Mayor et al. 1995). It was the first of many 'hot Jupiters' discovered. Since then over five thousand exoplanets have been identified (Akeson et al. 2013) and they show a diversity in mass, radius and orbital period far beyond what we see in our solar system.

[1] Since both planets and exoplanets are realistically the same type of object, in this work I will often use the word planet when describing exoplanets. This is a common substitution in exoplanet research.

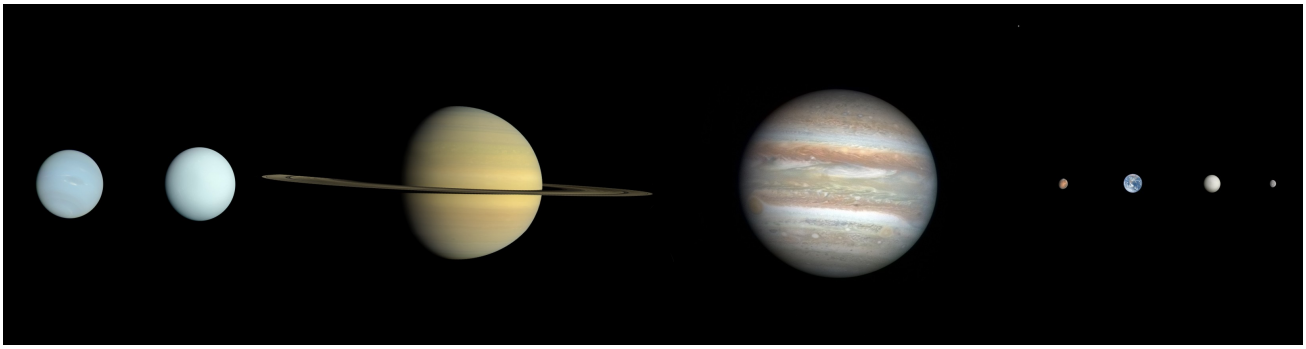

Figure 1.1: A true colour image of the solar system planets. Sizes are to scale but distances are not. We see the planets in reflected light.
Image credit: CactiStaccingCrane - Own work, CC BY-SA 4.0, https://commons.wikimedia.org/w/index.php?curid=117065900, cropped to remove the sun.

Figure 1.2 shows the mass – measured or inferred from mass-radius relationships – and orbital period of all confirmed exoplanets in the NASA Exoplanet Archive (Akeson et al. 2013) as of August 2024. The symbols indicate the method used to discover each world with transit as squares, radial velocities as triangles, direct imaging as stars and gravitational microlensing as crosses. The 68 exoplanets detected using other techniques are shown as circles.

Together, these techniques are able to constrain – to varying degrees – the mass, radius and orbit of the planet which allows us to estimate the bulk composition (e.g. gas or rock). However, the climate of an exoplanet is determined by more than just these parameters. This is exemplified well by the planets of our own solar system. Uranus and Neptune have similar mass, radii and equilibrium temperatures but different atmospheric conditions which leads to their slightly different shades of blue (Irwin et al. 2022).

At the time of writing this thesis, sending interstellar probes to exoplanets is prohibitively expensive and would take too long. Therefore, the study of their atmospheres is currently limited to the light we can detect from these planets and their stars. The good news is that the atmospheres of exoplanets affect their spectra providing us a window into the conditions on these alien worlds.

1.3 What is a reflection spectrum?

There are three types of exoplanet spectra. The first, the *transmission spectrum*, is the light that filters through an exoplanet's atmosphere as it passes in front of its star. Next, the *emission spectrum*, is the outgoing thermal radiation of the exoplanet's day-side when it faces the Earth. This thesis focuses on the final type: the *reflection spectrum*.

As the star's light passes through the atmosphere of the exoplanet, it scatters[2]. The reflected light we measure is the scattered light that escapes the atmosphere without being absorbed. Therefore, the reflection spectrum of an exoplanet is the spectrum of the star, imprinted with features from the exoplanet's atmosphere and surface as it is scattered light into the direction of the observer.

The way an exoplanet modifies the reflected stellar spectrum can be described by:

$$F_p(\lambda, v_{dop}, v_{rot}) = F_s(\lambda, v_{dop}, v_{rot}) \times \left(\frac{R_p}{a}\right)^2 \times g(\alpha, \lambda) \times A_g(\lambda). \tag{1.1}$$

Here F_p is the reflection spectrum of the planet and F_s is the spectrum of the star – which is being reflected. These are both functions of wavelength, λ. F_s is the flux of the star received at Earth, so

[2]Light can also scatter off the surface if it reaches it.

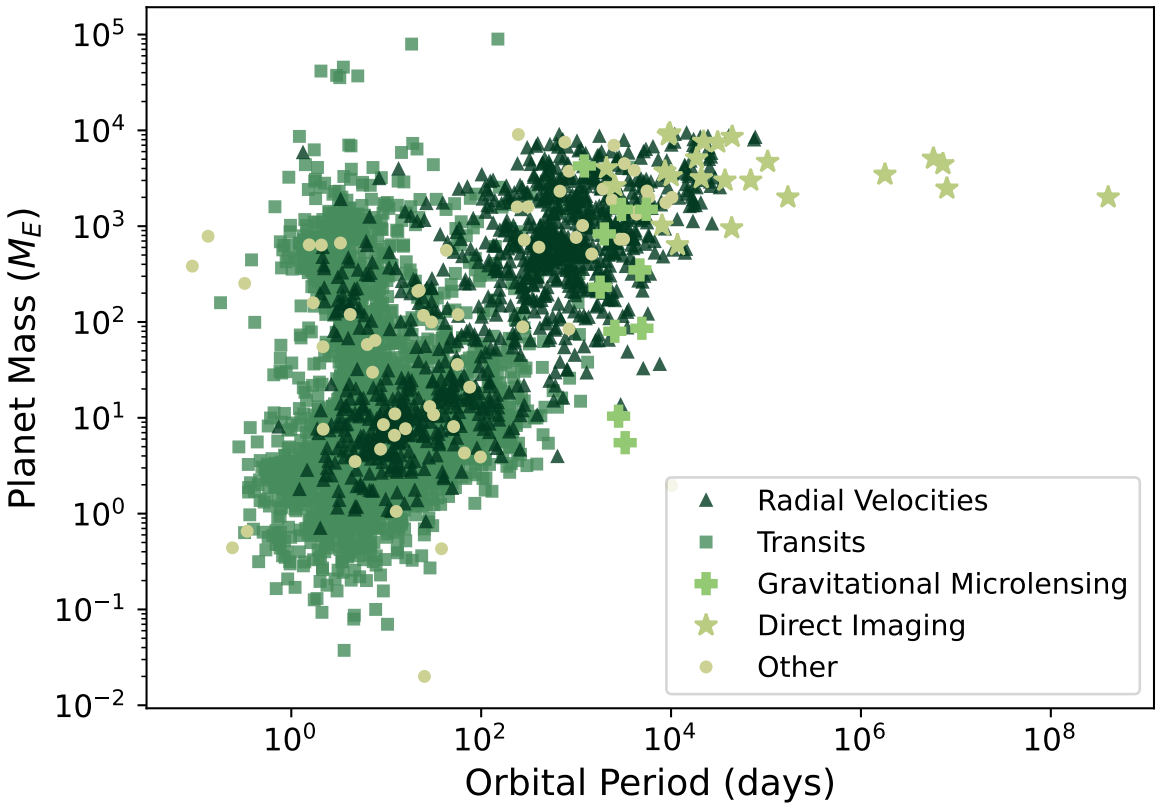

Figure 1.2: There is great diversity in the known exoplanet population. This plot shows the masses and orbital periods of all confirmed exoplanets as of 9th August 2024, with the different coloured symbols indicating the technique used to discover them. For the masses, this plot uses the best planet mass estimate available in the NASA Exoplanet Archive. This depends on the information available but in order of preference, it is: the true mass, the minimum mass divided but the sine of the inclination or the minimum mass is used.

Planet	Albedo	
Venus (V band)	0.689	Mallama et al. (2017)
Earth (V band)	0.434	Mallama et al. (2017)
Mars (V band)	0.170	Mallama et al. (2017)
Jupiter (V band)	0.538	Mallama et al. (2017)
Hot Jupiter (typical) (Kepler)	< 0.25	Esteves et al. (2015)

Table 1.1: The geometric albedos of some of the solar system planets and the typical value for a hot Jupiter.

$(R_p/a)^2$, where R_p is the radius of the planet and a the semi-major axis of its orbit, converts this into planet flux received at Earth assuming the planet is a Lambertian disk[3] at zero phase angle, α, (see Figure 1.3). The phase function, $g(\alpha)$, describes the angular dependence of the reflection due to the changing phase angle. This can be affected by the surface and atmospheric properties of the planet and can be wavelength dependent (see for example Section 1.4.3). $A_g(\lambda)$ is the geometric albedo – the ratio of the observed flux at zero phase angle seen from the light source to that of a Lambertian disk with the same cross-section (some typical values are given in Table 1.1). This is a product of the properties of the atmosphere and planetary surface. Both the phase function and geometric albedo can be time dependant although this is typically neglected as the changes are assumed to be small. For example, Earth's albedo only changes by approximately 0.01 over the course of a year (Goode et al. 2021).

F_s is not the same as the spectrum of the star which we observe from Earth. Consider an observer standing on the surface of the exoplanet and looking up at the star. If the orbit is circular and there are no other planets in the system, the planet is always the same distance from the star. This means the star appears to have zero radial velocity and so the reflected stellar spectrum is in the rest frame of the exoplanet. Therefore, for an observer on Earth, the reflected stellar spectrum is Doppler shifted to the planet's velocity, v_{dop}, in the Earth's rest frame which is a combination of the planet's orbital motion, the motion of the star system through the galaxy (systemic velocity) and the motion of the Earth (barycentric velocity). For our exoplanet bound observer, the star also appears to be rotating, not just because of the intrinsic rotation of the star but also because the exoplanet is orbiting around it. Rodler et al. (2010) and Spring et al. (2022) show that the combined intrinsic rotation and orbital motion lead to a perceived rotational velocity, v_{rot}, given by Equation 1.2. In this equation R_p, R_s are the radii of the planet and star respectively, $P_{rot,p}$, $P_{rot,s}$ are rotation periods of the planet and star, and P_{orb} is the orbital period of the planet. The reflected spectrum of the star is rotationally broadened to this rotational velocity.

[3] A Lambertian disk is a diffusely reflecting disk which has the same cross-section as the planet.

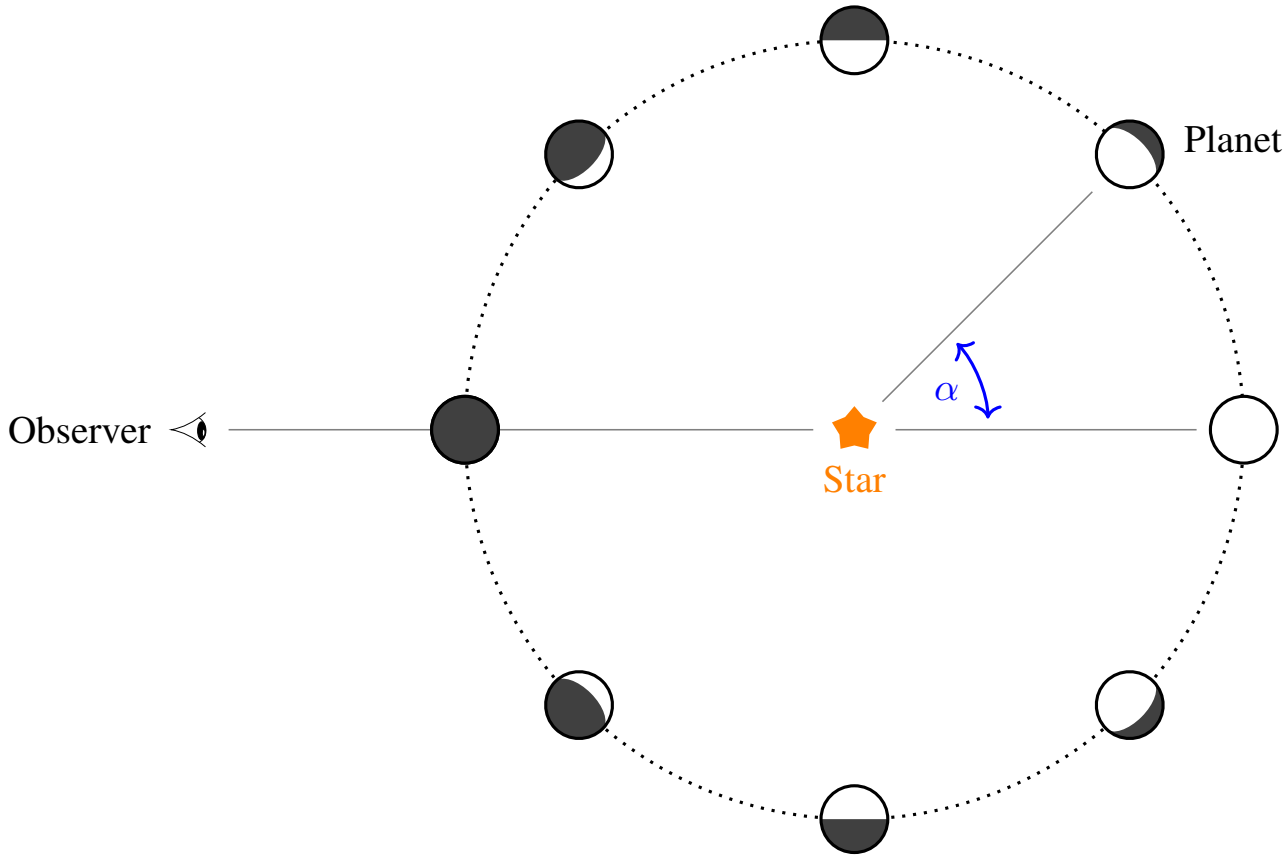

Figure 1.3: The phase angle, α, is the star-planet-observer angle. That is, it is the angle between the direction of the incident star light and the direction from which the planet is observed. Since the observer is a great distance away, this angle is equivalent to the one shown in this diagram: the angle between the planet-star and secondary eclipse point.

$$v_{rot} = \sqrt{\left(2\pi \sin(i) \frac{R_p}{P_{rot,p}}\right)^2 + \left(2\pi R_s \left(\frac{1}{P_{rot,s}} + \frac{1}{P_{orb}}\right)\right)^2} \tag{1.2}$$

1.4 What can we learn from reflection spectra?

By using the reflection spectrum of an exoplanet to measure its phase function and/or geometric albedo, it is possible to obtain information on its atmosphere and surface. The following section discusses key properties of an exoplanet that can be explored if the albedo and/or phase function of the planet is measured.

1.4.1 Energy Budget

Planetary climate, and therefore the conditions on an exoplanet, are determined by the flow of incoming solar energy through the atmosphere. This flow of energy into the planet and back out again is known as the energy budget or energy balance. For Earth-like planets, understanding the energy budget is key to assessing their potential habitability.

For example, Earth and Venus are similar in size ($R_\oplus = 6371\,\mathrm{km}$; $R_\varnothing = 6052\,\mathrm{km}$) and mass ($M_\oplus = 5.97\times10^{24}\mathrm{kg}$; $M_\varnothing = 4.87\times10^{24}\mathrm{kg}$) as well as absorbing similar amounts of energy from the sun ($I_\oplus \approx 240\,\mathrm{W\,m^{-2}}$; $I_\varnothing \approx 160\,\mathrm{W\,m^{-2}}$), however they are very different worlds. This is due to the difference in the way the incoming solar energy flows through each atmosphere (see e.g. Read et al. 2016). Venus has a thick layer of clouds and hazes that reflect approximately 70% of the incoming radiation back to space, whereas the Earth only reflects around 30% – some of which is reflected directly from the surface. Despite the fact that Earth's atmosphere and surface absorb more incoming radiation, the Earth is cooler. This is because Venus' CO_2 dominated atmosphere is much more optically thick than Earth's atmosphere at the infrared wavelengths at which the absorbed sunlight is re-emitted. The longwave radiation is therefore trapped by Venus' atmosphere, known as the greenhouse effect, which heats up the planet significantly more than Earth. This is shown schematically in Figure 1.4 using 'Trenberth' diagrams. The magnitude of the greenhouse effect can be seen in the emission to and from the ground. For Earth, these are a little bit larger than the total incoming energy due the greenhouse effect in Earth's atmosphere. However for Venus, the same numbers are much larger highlighting how much more radiation is trapped by Venus' greenhouse gas effect and therefore why this planet is much warmer.

From this example, it is clear that the energy budget of exoplanets has complex dependence on the properties of their atmospheres, like the albedo, which can be measured from the reflection spectrum. The albedo determines the wavelength-dependent energy absorption by the planet and its atmosphere which is exemplified by the works of Zsom et al. (2012) and Shields et al. (2019). These works respectively showed that the energy budget of the Earth is sensitive to changes in the albedo, and that different wavelength-dependent albedos are needed to reproduce Earth-like conditions on exoplanets orbiting stars of different spectral types.

1.4.2 Clouds and Hazes

Clouds and hazes are both types of aerosols – small particles suspended in an atmosphere. A cloud contains aerosols formed from the condensation of atmospheric gases to either liquid or solid particles,

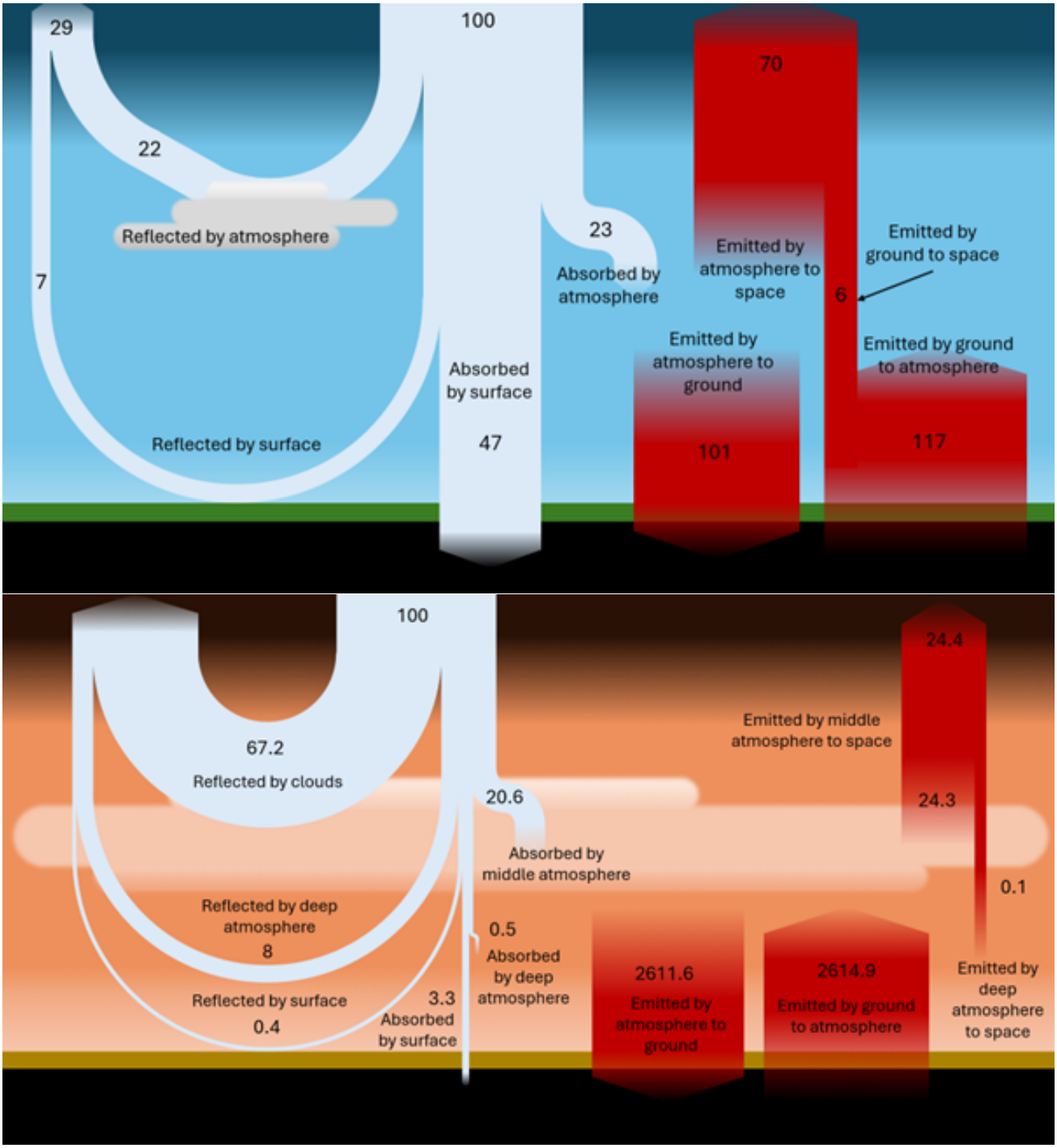

Figure 1.4: 'Trenberth' diagrams of the energy budgets of Earth (top) and Venus (bottom) based on those in Read et al. (2016). The white lines show the path of the incoming shortwave radiation and the red lines show the flow of emitted radiation through the atmosphere. The box widths are not to scale for visibility however the ratios are indicated by the numbers. Note these diagrams are simplified so the numbers do not sum to 100%. These diagrams show that while Earth's atmosphere absorbs more incoming radiation than Venus, it has a smaller greenhouse effect which leads to Earth being cooler than Venus.

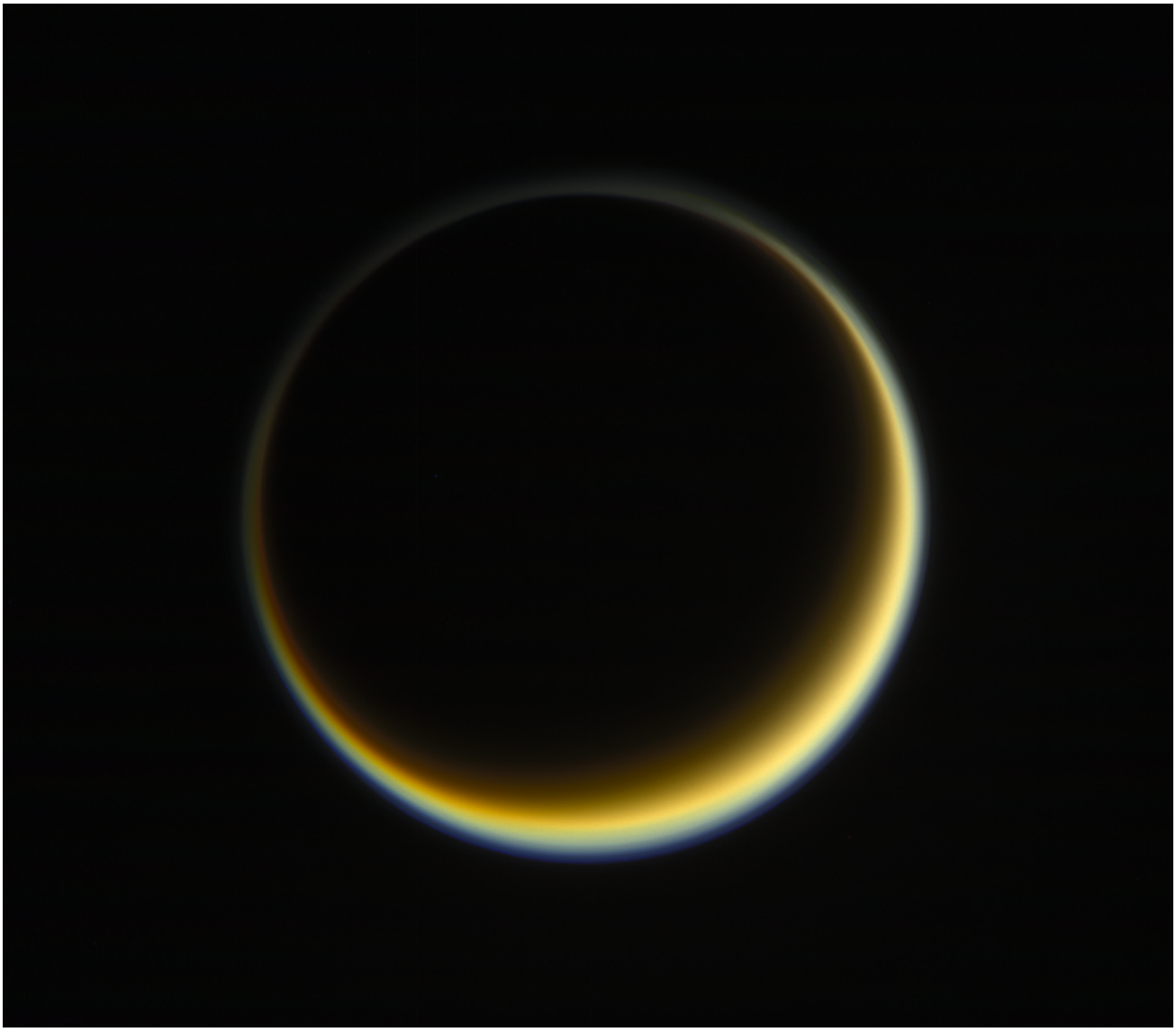

Figure 1.5: Photo of Titan taken by the Cassini spacecraft's narrow-angle camera highlighting the hazes. Image credit: NASA/JPL-Caltech/Space Science Institute, PIA21625

whereas a haze contains aerosols formed of involatile solids produced as a result of atmospheric chemistry. In the Solar system, clouds and hazes are commonly seen on those bodies that have atmospheres, from the blazing orange belts of Jupiter to the hazy yellow atmosphere of Titan (see Figure 1.5) and the overcast grey skies of Oxford. It therefore makes sense to assume that at least some of the exoplanets we observe also have clouds and/or hazes. These are not the only types of aerosols but the primary types we consider when studying exoplanets.

Clouds and hazes affect the planetary energy budget (Zsom et al. 2012) and therefore exert strong feedback on planetary atmospheres. For example, they change the range of instellations where an Earth-like planet could have liquid water on its surface (Yang et al. 2013; Windsor et al. 2024) which is needed for life as we know it. They also affect the thermal evolution of the planet and therefore its inferred history (Kurosaki et al. 2017; Poser et al. 2024) and the runaway greenhouse transition and

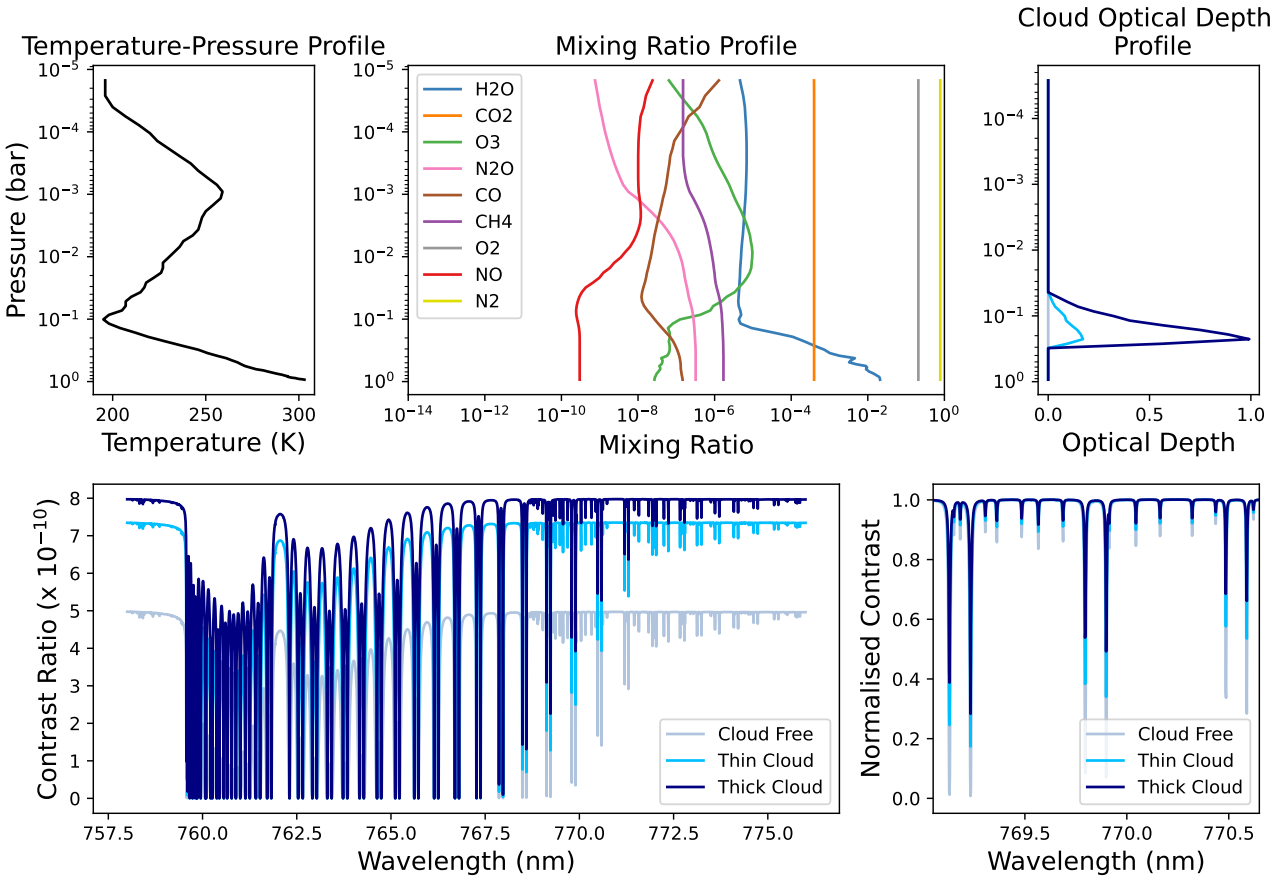

Figure 1.6: A simulated reflection spectrum at a resolution of $R = 500,000$ of the Earth centered on the oxygen A band, generated using PICASO (Batalha et al. 2019), along with the parameters used to model it. The variation in the spectrum induced by clouds is shown. **Top left panel:** The temperature-pressure profile used to model the Earth's atmosphere (Planetary Spectrum Generator; Villanueva et al. 2018). **Top centre panel:** A model of the mixing ratio profile of the molecules in the Earth's atmosphere (Planetary Spectrum Generator; Villanueva et al. 2018). **Top right panel:** The opacity of the cloud deck as a function of pressure. **Bottom left panel:** the total amount of reflected flux changes significantly when clouds are included. **Bottom right panel:** the continuum normalised spectra zoomed in on a few of the spectral lines. Clouds alter the depth of these lines.

therefore habitability of a given exoplanet (Turbet et al. 2020, 2021; Chaverot et al. 2023). Clouds and hazes can be measured via the reflection spectrum of the planet since they both alter the overall albedo and, at high spectral resolution, the spectral lines of atmospheric species (see Figure 1.6).

1.4.3 Liquid water

Liquid water and the water cycle is essential to Earth-like life and therefore key to our current definitions of planetary habitability. The habitable zone around a star is defined as the range of orbital separations at which an exoplanet could be at the right temperature to have liquid water on its surface. However, as discussed in Sections 1.4.1 and 1.4.2 the climate of an exoplanet is a complex system and an exoplanet at the right orbital separation may not have the right conditions to have liquid water on

its surface.

The bulk of current exoplanet characterisation focuses on measuring the atmosphere. However, it is possible – if the atmosphere is optically thin or there is no atmosphere – to measure the surface properties of an exoplanet (e.g. Hu et al. 2012; Li et al. 2022).

One way to detect liquid water on the surface of an exoplanet is to detect and measure certain scattering phenomena that are a result of the way it reflects and scatters light. These phenomena affect the amount of light reflected – both in total intensity and in linearly polarised light – as a function of planetary phase angle (see Figure 1.3 for definition of phase angle). Figure 1.7 shows the phase curve – a measure of the phase function – of a cloudy Earth-like planet with a wavy ocean surface. The variation in the amount of reflected light as a function of phase angle and also wavelength is clearly visible and the features due to different scattering phenomena have been highlighted.

For detecting liquid water, two key phenomena are of interest: rainbows/cloudbows and ocean glint. The former is caused by light scattering through liquid droplets in the atmosphere. Upon entering the droplet, the light is diffracted due to the change in refractive index. It is then reflected off the back of the droplet which polarises the light due to the difference in the efficiency of the reflection as a function of polarisation. As the light exits the droplet, it is diffracted again adding to the dispersion. The peak phase angle and wavelength dependence of the rainbow feature is dependent on the composition of the droplets (different refractive indexes) and their size (different path lengths lead to different amounts of dispersion) (Stam 2008; Karalidi et al. 2011; Trees et al. 2019). Consequently, rainbows could help distinguish between an exo-Earth and an exo-Venus (West et al. 2022; Mahapatra et al. 2023).

Glint is the specular reflection of light off a smooth surface – in this case an ocean. As seen in Figure 1.7, the glint feature is more prominent at redder wavelengths as this is where – on an Earth-like planet – atmospheric attenuation is smallest (Robinson et al. 2010; Zugger et al. 2011). The phase angle of the maximum seen in polarised light varies slightly with wavelength and also with the composition of the ocean (e.g. water, methane etc) and the atmosphere. The width of the feature is dependent on the wave height (Williams et al. 2008; Trees et al. 2019, 2022). It is harder to constrain the type of ocean from measurements of the glint feature due to its weaker dependence on this but also because forward scattering of light by cloud particles could be confused with glint (Robinson et al. 2010). This can be resolved by observing the rainbow feature which can better constrain the composition of the liquid pooling on the planet's surface.

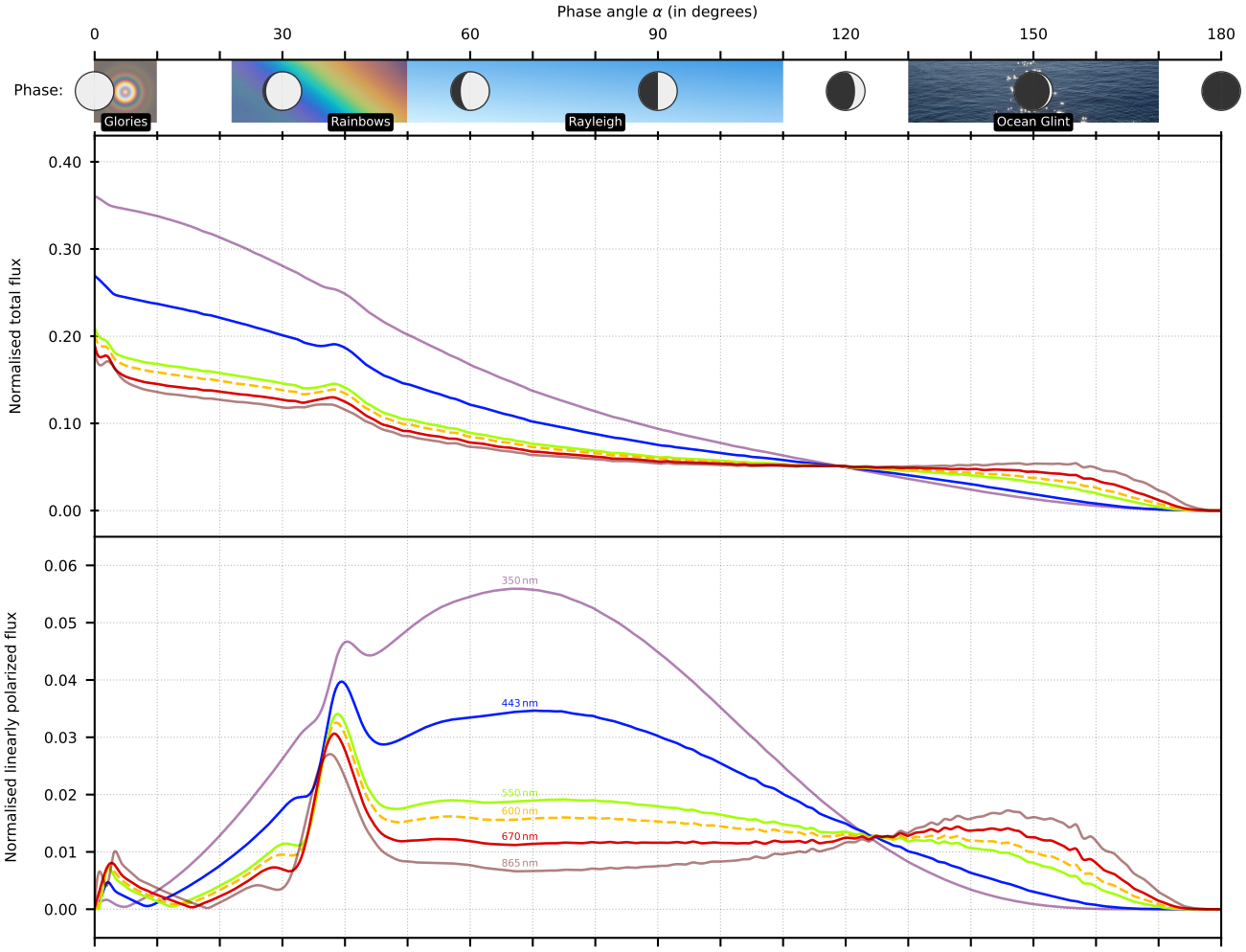

Figure 1.7: An example of the phase curve of an Earth-like planet. The top scale indicates the planetary phase of the exoplanet with accompanying graphics for demonstration as well as images of the different scattering phenomena of interest at the phases at which they occur. The top panel shows the normalised total flux of the exoplanet as a function of planetary phase for a range of optical wavelengths – indicated by the colour of the line. The bottom plot shows the normalised linearly polarised flux of the exoplanet, again as a function of planetary phase and wavelength. The normalisation is such that the total flux equals the planet's geometric albedo at zero phase angle. The bottom scale highlights the phase range where the scattering phenomena of glories, rainbows, Rayleigh scattering, and ocean glint contribute significantly to the phase curve – there is however some overlap between the phenomena not shown here. Adapted from Vaughan et al. (2023).

1.4.4 Atmospheric Biomarkers

Atmospheric biomarkers are atmospheric gases that indicate the presence of life on an exoplanet. This is in contrast to the other properties I have discussed so far which only indicate if a planet could host life, as opposed to whether it actually does host life. Finding life beyond the Earth will be one of the greatest discoveries of our time and is sure to inspire future work for generations to come.

Life on Earth interacts with a large number of atmospheric species some of which accumulate in Earth's atmosphere becoming biomarkers (Seager et al. 2012). However, the detection of life using biomarkers is not as simple as detecting a single biomarker species (e.g. Meadows 2017; Catling et al. 2018; Fujii et al. 2018; Meadows et al. 2018). Exoplanets are an extremely diverse set of objects with different instellations, compositions and geologies, all of which alter the chemical and photochemical processes occurring in the atmosphere (Grenfell 2017; Kaltenegger 2017). This leads to pathways by which biosigature gases can be present in a planet's atmosphere without the need for life: creating false positive scenarios (Seager et al. 2015; Schwieterman et al. 2018; Walker et al. 2018; Schwieterman et al. 2024).

For example, oxygen has long been proposed as a biosignature (Owen 1980; Sagan et al. 1993) as without the oxygenic photosynthesis of life, the oxygen in our atmosphere would be removed in a geologically short amount of time (e.g. Lécuyer et al. 1999; Catling 2014). However, more recent studies have shown that the action of life is not the only mechanism to build up oxygen in an atmosphere. It could instead result from, regardless of host star type, an exoplanet with a low non-condensible gas inventory and therefore water in the stratosphere (it is not cold trapped in the troposphere like on Earth) which is photolysed into oxygen (Wordsworth et al. 2014). Additionally, for planets that orbit M dwarfs, significant O_2 build up can also be the result of massive ocean loss where a large amount of water is photolysised to oxygen (Luger et al. 2015; Tian 2015) or due to various photochemical processes, driven by the increased UV radiation, such as CO_2 photolysis in a N_2 and H_2O atmosphere or in a dry atmosphere (Domagal-Goldman et al. 2014; Tian et al. 2014; Gao et al. 2015; Harman et al. 2015).

For oxygen, the false positive scenarios can be identified using other atmospheric species. Table 1.2 summaries the detectability of O_2, O_3, O_4, CO[4], CO_2, CH_4 and H_2O in these scenarios highlighting how a more complete atmospheric characterisation can be used to distinguish them. Figure 1.8 shows the locations of the key spectral features for the molecules in Table 1.2 except O_4. This is formed from O_2 collisional pairs which could be detected by measuring the relative depths of the oxygen A band and

[4]This is an anti-biosignature as it is toxic to Earth-like life.

Scenario	O_2	O_3	O_4	CO[4]	CO_2	CH_4	H_2O
Earth							
Exoplanet with a low non-condensible gas inventory							
Massive ocean loss on an M-dwarf planet							
CO_2 photolysis on a N_2 and H_2O rich M-dwarf planet							
CO_2 photolysis on a dry M-dwarf planet							

Table 1.2: It is not just the action of life that can create atmospheres that have detectable O_2 signatures, however the atmospheres resulting from different mechanisms contain different amounts of other molecules compared to the Earth. This table summarises the molecules that can be detected (green) verse those that cannot (red) for each of these atmospheric scenarios (Meadows 2017). This highlights how these scenarios can be distinguished via a comprehensive characterisation of the planet. Molecules highlighted orange cannot be used to distinguish the scenarios. For a given planet, some molecules may be harder to detect than others so careful thought should go into determining an appropriate observing strategy.

IR band at $1.27\,\mu m$ as its broad spectral feature changes the depths of these bands differently (Leung et al. 2020). Additionally, Figure 1.9 shows which parts of the spectrum are dominated by reflection and which are dominated by emission highlighting the need for both spectra.

Oxygen is not the only biomarker with false positives. Other biomarkers such as O_3, CH_4 or N_2O alongside H_2O (Leger et al. 1993; Sagan et al. 1993; Kaltenegger et al. 2007; Rauer et al. 2011) also have false positives, such as solar flare induced photochemistry creating N_2O (Airapetian et al. 2016; Chen et al. 2020) or volcanic production of CH_4 (Liggins et al. 2022, 2023), that require a more detailed characterisation to identify.

A further complication in the search for life beyond Earth is that a non-detection of atmospheric biomarkers does not mean a planet is lifeless: a false negative. For example, there has been life on Earth for much of its history, however, there has not always been a large amount of oxygen in our atmosphere (e.g. Stüeken et al. 2024). In addition to this, due to the different instellations, compositions and geology of exoplanets, the action of life may not always result in the same abundances of gases that we see on Earth today (e.g. Segura et al. 2005).

Another consideration is that extraterrestrial life may simply be very different to us resulting in different biosignatures (e.g. Davila et al. 2014). If the major components of the atmosphere are measured, as well as the composition of the surface, it is possible to look for chemical disequilibrium which may indicate the presence of life without assuming that life is Earth-like (e.g. Sagan et al. 1993; Krissansen-Totton et al. 2016; Kaltenegger 2017; Krissansen-Totton et al. 2018a)

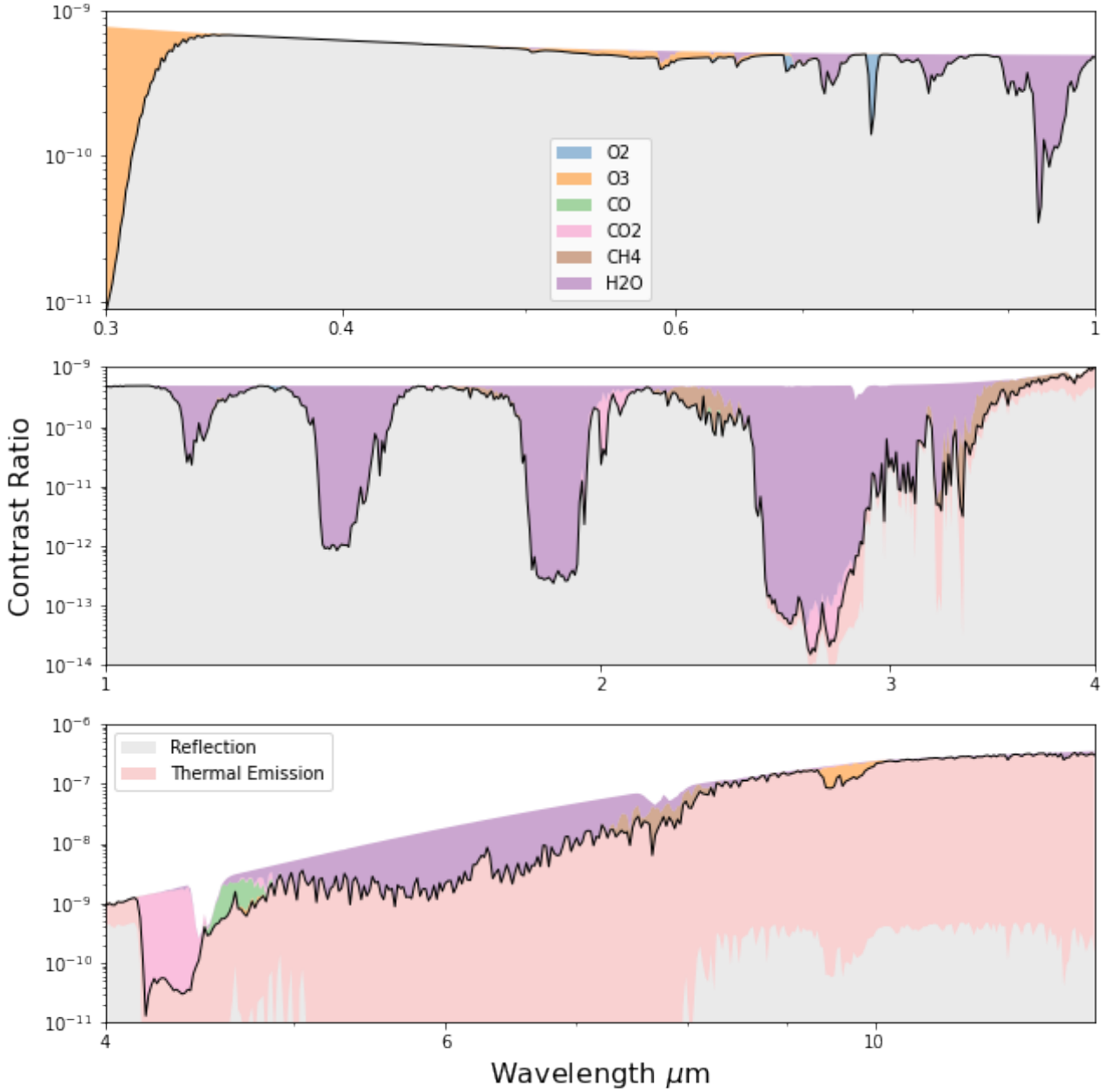

Figure 1.8: A simulated spectrum of the Earth at a resolution of $R = 300$ (black line). Above this line, the contributions of key biomarker species are highlighted – indicated in the legend on the top panel. Below the black line, the contributions to this spectrum from reflected light and thermal emission are indicated (note the log scale) – legend on the bottom panel. Thermal emission begins to dominate over reflection at wavelengths longer than $3\,\mu\mathrm{m}$, therefore, there are many biomarker species present in the reflection spectrum. This spectrum was computed using PICASO (Batalha et al. 2019) for a hypothetical planet similar to Earth.

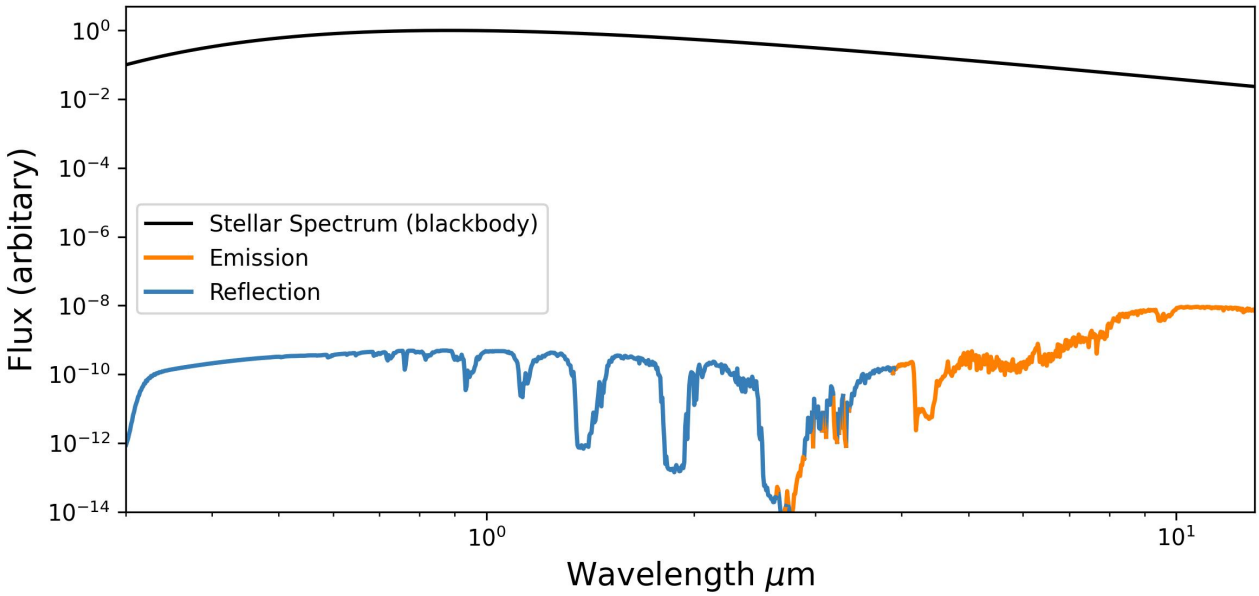

Figure 1.9: The same spectrum as Figure 1.8 but now shown along side the blackbody spectrum of the star. The spectrum has been coloured blue where the reflected flux is greater than the emission and orange where the opposite is true. There is an intermediate region around $3\,\mu\mathrm{m}$ where the reflected and emitted fluxes are of similar magnitude. The reflection part of the spectrum has worse contrast (the planet is much fainter than the star than it is in emission) however, this part of the spectrum offers access to key biomarkers such as oxygen. A comprehensive characterisation would use both emission and reflection spectra.

1.5 Observational history

1.5.1 Thermal emission and transmission

Transmission and emission spectroscopy of exoplanets have long observational histories which have been reviewed in detail in Seager et al. (2010) and more recently in Madhusudhan (2019).

Transmission spectra have been used to measure the chemical composition of planetary atmospheres by measuring the absorption features of numerous species at both high (e.g. Snellen et al. 2010; Hoeijmakers et al. 2015; Brogi et al. 2016; Giacobbe et al. 2021; Maguire et al. 2024; Nortmann et al. 2024) and low spectral resolution (e.g. Charbonneau et al. 2002; Pont et al. 2008, 2013; Sing et al. 2016; Chen et al. 2021; Gressier et al. 2023). Emission spectra have also been used to measure the chemical composition but also the temperature structure, using the emission or absorption features of numerous chemical species, at both high (e.g Rodler et al. 2012; Birkby et al. 2013; Schwarz et al. 2015; Birkby et al. 2017; Ramkumar et al. 2023; Finnerty et al. 2024; Guo et al. 2024) and low spectral resolution (e.g. Madhusudhan et al. 2009; Stevenson et al. 2010; Swain et al. 2013; Line et al. 2016; Evans et al. 2017; Dragomir et al. 2020; Taylor et al. 2023a).

In transmission, the sensitivity to cloud opacity comes from, for example, the muting or flattening of spectral features (e.g. Pont et al. 2008; Bean et al. 2010; Berta et al. 2012; Pont et al. 2013; Kreidberg et al. 2014; Sing et al. 2016) or from measuring the difference between the transit spectrum during ingress (probing the morning part of the atmosphere) and egress (probing the evening) (Kempton et al. 2017)[5]. Emission spectra are also sensitive to clouds by for example, mapping the thermal phase curve (Hu et al. 2015; Parmentier et al. 2016; Irwin et al. 2020) as the peak of this curve in orbital phase is sensitive to the presence of clouds. Hot Jupiters have strong equatorial jets that push the hottest part of the planet towards the evening side of the planet. Without clouds, the peak in flux therefore occurs just before the secondary eclipse. However, if the light being detected is dominated by the reflection from clouds on the morning side of the planet, and not thermal emission as would be expected, the peak will occur just after secondary eclipse.

It is possible to use low to medium resolution transmission or emission spectra to infer the species responsible for the clouds or haze (e.g. Sing et al. 2016; Gao et al. 2020; Blain et al. 2021; Lothringer et al. 2022; Grant et al. 2023; Radica et al. 2023; Taylor et al. 2023b; Dyrek et al. 2024). However care is required when making these inferences as demonstrated by Taylor et al. (2023a). In this work, the authors showed that some spitzer observations of WASP-43 b indicated the presence of clouds at $> 3\sigma$ while others showed no evidence of them. This implies that the data was not of sufficient quality to detect clouds even though they were confidently detected in some observations. Additionally, Holmberg et al. (2024) highlighted that the wavelength range covered by the observations strongly impacts their sensitivity to clouds and Radica et al. (2024) demonstrated the inferred cloud properties can be degenerate with other atmospheric properties such as metallisity.

Some of the uncertainty can be mitigated at high spectral resolution where the depths of individual spectral lines can be used to infer the presence of clouds and constrain their properties with reduced degeneracy (Inglis et al. 2024; Landman et al. 2024). In emission and transmission spectra, weak or non-detections of expected molecular species have been used to suggest the presence of clouds and in some cases weakly constrain their properties (e.g. Charbonneau et al. 2002; Allart et al. 2020; Cabot et al. 2024; Inglis et al. 2024; Nortmann et al. 2024).

1.5.2 Reflection

Thus far measurements of the reflection of exoplanets have been largely limited to secondary eclipse measurements of close-in giant planets. This technique takes a measurement of the flux of the unre-

[5]This works if clouds are only expected to be present on the morning side of the planet resulting in a difference between the two spectra.

solved planet and star just before secondary eclipse and subtracts the flux measured during the eclipse. The remainder is the flux from the planet which, when measured in the optical, is usually dominated by the reflected light[6]. This reflected light flux can then be converted into a measurement of the planet's albedo.

Most of the planets measured so far have had low optical albedos (e.g. Cowan et al. 2011; Heng et al. 2013; Angerhausen et al. 2015; Esteves et al. 2015; Shporer et al. 2015; Mallonn et al. 2019; Blažek et al. 2022, and references therin). However, a few exoplanets have been measured to have high optical albedo (Angerhausen et al. 2015; Blažek et al. 2022; Deline et al. 2022; Hoyer et al. 2023; Jacobs et al. 2023; Kempton et al. 2023; Krenn et al. 2023; Pagano et al. 2023) which is indicative of clouds and hazes (e.g. Pagano et al. 2023).

For the hot Jupiters, this variation in albedo can broadly be explained by transitions between cloudy and cloud-free states as a function of the equilibrium temperature of the planet (Parmentier et al. 2016). As equilibrium temperature decreases, species that form cloud decks at higher temperatures rain out and become cold trapped in the lower atmosphere where they cannot be observed. They can then be replaced by a cloud deck from a different species if the planet's temperature-pressure profile crosses its condensation curve or there maybe a regime where there are no clouds. Different cloud species have different albedos so the albedo of hot Jupiters can be highly variable depending on the clouds present. Additionally, hot Jupiters have equatorial jets which move the hottest point of the planet eastward. This means the west side of the planet is cooler and clouds preferentially form there. This adds an additional element of variability to the albedo depending on which side of the exoplanet is observed.

Attempts have been made to expand the study of reflection spectra at high-spectral resolution however, these have yet to result in a robust detection of an exoplanet's spectrum (Charbonneau et al. 1999; Collier-Cameron et al. 1999, 2002, 2004; Rodler et al. 2013; Martins et al. 2015; Hoeijmakers et al. 2018a; Scandariato et al. 2021; Spring et al. 2022). Martins et al. (2015) claimed a detection of the reflected light of 51 Pegasi b, but Scandariato et al. (2021) and Spring et al. (2022) later showed this to be an unfortunate false positive.

This failure has largely been due to the low albedos of the planets targeted by these studies. One of the planets most amenable to high resolution characterisation in reflected light, LTT-9779 b, is known to have a high optical albedo (≈ 0.8; Hoyer et al. 2023). This planet is a rare hot Neptune that would have been expected to have undergone rapid photo-evaporation (e.g. Lopez 2017), which should have stripped it of its atmosphere within 100 Myrs (Owen et al. 2016)[7]. However, it still retains an

[6]This is not true for some of the hottest exoplanets.

[7]By comparing the stellar spectrum to evolution models, the star's age has been determined to be approximately 2 Gyr

atmosphere to this day (Crossfield et al. 2020; Dragomir et al. 2020). In Section 3, I present my work analysing the high resolution reflection spectra of this planet. This analysis is still in progress but the aim is to measure the cloud properties and energy budget in attempt to reveal why this atmosphere still exists.

1.6 Future prospects

There is a lot of valuable information to be gained on exoplanets from their reflection spectra as well as by combining the reflection spectrum with transit and/or thermal emission spectra. This Section summarises what we could hope to learn in the coming decades.

1.6.1 Energy budgets

The energy budget of an exoplanet is the flow of energy through its atmosphere which determines its climate. The incoming solar energy is either reflected (leaving as shortwave radiation) or absorbed and then remitted by the planet (leaving as longwave thermal radiation). Assuming negligible energy input from the internal heat of the planet, energy conservation means that if either the net shortwave or longwave radiation is measured, then the other can be calculated. However, this is not necessarily the case for cool planets and therefore both the shortwave and longwave radiation would need to be measured. This would require measurements of both the thermal emission and reflection of the planet in question.

Additionally, information can be gained by measuring the wavelength dependence of the emission and reflection. If the shortwave radiation is used to obtain the albedo function, then the properties of the surface or cloud decks can be constrained (e.g. Hu et al. 2012; Jacobs et al. 2023; Borges et al. 2024). Additionally, if this is combined with the thermal emission, a wealth of additional information can be obtained such as constraints on the greenhouse effect (e.g. Li et al. 2018; Teinturier et al. 2024).

1.6.2 Clouds and Hazes

Clouds and hazes are a key part of exoplanet atmospheres (see Section 1.4.2) and may have spatial and/or temporal variability (Parmentier et al. 2016; Kempton et al. 2017; Charnay et al. 2021). Reflection spectra are able to measure the properties of the clouds and hazes present on the planet's day-side whereas transmission spectra are sensitive to the presence of clouds on the planet's terminator. By combining these observations, the spatial distribution of the clouds could be inferred (Parmentier et al.

(Jenkins et al. 2020)

2016). These can then be compared to the cloud distributions predicted from global circulation models allowing us to quantify how well these models represent real exoplanets potentially providing us with key insights into the atmospheric conditions on planets for which we have no analogue in the solar system. In addition to learning about the distribution of the clouds combining observations can improve our knowledge of their properties (e.g. Kok et al. 2013; Pont et al. 2013; Morley et al. 2015; Edwards et al. 2020; Glidic et al. 2022).

As well as affecting the atmosphere of an exoplanet, clouds and hazes alter the spectrum of an exoplanet – typically inhibiting the study of the lower atmosphere through optical and near infrared transmission spectroscopy. This is key in the study of Earth-like planets as the presence of aerosols strongly influences their overall albedo and the strength of molecular features both of which affect our ability to characterise these worlds (Wang et al. 2018a; Singla et al. 2023) and may be key to interpreting biosignatures (Damiano et al. 2023). Transits can be used to characterise the clouds by measuring the increase in planetary radius they cause at blue wavelengths (Benneke et al. 2012; Jaiswal et al. 2023) however, reflected light may provide better constraints (Gilbert-Janizek et al. 2024). Current studies show aerosols on Earth-like and giant planets can be measured with the soon-to-be-launched Nancy Grace Roman Space Telescope, the future planned Habitable Worlds Observatory and Large Interferometer For Exoplanets (LIFE) and similar proposed missions like HabEx and LUVOIR but the achievable constraints will depend on the signal-to-noise and spectral resolution of the spectrum obtained (Marley et al. 2014; Lupu et al. 2016; Gao et al. 2017; Nayak et al. 2017; Batalha et al. 2018; Feng et al. 2018; MacDonald et al. 2018; Carrión-González et al. 2020; Damiano et al. 2020, 2021; Mukherjee et al. 2021; Hall et al. 2023; Konrad et al. 2023; Gilbert-Janizek et al. 2024).

1.6.3 Liquid water

The rainbow features have been used to determine Titan's reflection are due to hydrocarbon atmospheric haze (Zellner 1973) as well as constrain the composition and droplet size distribution of Venus's sulfuric acid clouds (Hansen et al. 1974). Additionally, we have observed the glint feature for Earth (Emde et al. 2017; Sterzik et al. 2019; Takahashi et al. 2021) and Titan (Stephan et al. 2010). However, neither of these phenomena have been detected on any exoplanets yet. Section 5 discusses the future Habitable Worlds Observatory and how it may have the capability to begin measuring these features on Earth-like planets in the habitable zones of their stars.

1.6.4 Atmospheric Biomarkers

In Section 1.4.4, I discussed the detection of atmospheric biosignatures and how the detection of multiple species is required to rule out false positives for life. This will require a combination of the reflected light, thermal emission and/or transmission spectra. By combining these spectra, detections of certain species can also be cross-checked by different techniques, increasing the confidence in the detection, as has been done for close-in giant planets (Schwarz et al. 2015; Bell et al. 2023; Ridden-Harper et al. 2023).

There have been numerous studies into the detectability of various biomarkers in transmission, emission and reflection spectra for current and future observatories. JWST is an infrared $6.5\,\mathrm{m}$ space telescope currently in operation. It has the sensitivity to potentially detect biomarker species on Earth-like exoplanets orbiting nearby M-dwarfs, such as the planets in the TRAPPIST-1 system, as these have more favorable detectablility than Sun-like stars (Charbonneau et al. 2007). Simulations of the transit spectra of TRAPPIST-1 d and e show that the spectral signatures of CO, CO_2, CH_4 and H_2O may be detectable, or have a useful upper limit put on their abundances (Krissansen-Totton et al. 2018b; Wunderlich et al. 2019; Gialluca et al. 2021; Lin et al. 2021; Mikal-Evans 2021; Meadows et al. 2023; Rotman et al. 2023). In theory it is possible to detect O_2 and O_3 with JWST as well although these require on the order of 100 transits and so are unlikely to be observed (Lustig-Yaeger et al. 2019; Lin et al. 2021; Meadows et al. 2023). In addition to this, transit observations could be affected by clouds and the detectability might be over estimated (Pidhorodetska et al. 2020; Mikal-Evans 2021; Doshi et al. 2022). Thermal emission observations with JWST of another M dwarf exoplanet, Proxima b, the nearest Earth-like exoplanet orbiting an M-dwarf, requires significant amounts of observing time for molecular detection (Kreidberg et al. 2016). An alternative suggestion to characterise this would involved coupling SPHERE@VLT to ESPRESSO@VLT which would allow O_2, CH_4 and H_2O to be detected but this has not been put into practice (Lovis et al. 2017).

With the upcoming class of $30\,\mathrm{m}+$ telescopes, the Extremely Large Telescopes or ELTs, the detection of biosignatures on a wider range of planets is possible. Detections of O_2, CO, CO_2, CH_4 and H_2O could be achieved with transit observations of nearby M-dwarfs using the ELTs (Snellen et al. 2013; Serindag et al. 2019; Currie et al. 2023a; Hardegree-Ullman et al. 2023) but O_2, CO and H_2O will require a large number of transits limiting the feasibility of this technique. On the other hand, simulations of reflected light observations indicated that detections of O_2, CO_2, CH_4 and H_2O can also be achieved and in a much more reasonable time frame than with transits (Hawker et al. 2019; Vaughan et al. 2024; Zhang et al. 2024). In Section 4, I demonstrate detailed instrumental simulations of HARMONI@ELT

and discuss the possibility of detecting biosignatures on Proxima b using this instrument.

Further into the future, direct imaging or interferometry missions will be able to characterise many more habitable exoplanets, including those around higher mass stars. The Large Interferometer For Exoplanets (LIFE), sensitive to the thermal emission of exoplanets, will be able to detect O_3, CO_2, CH_4 and H_2O as well as a few other biomarker species (Alei et al. 2022; Konrad et al. 2022; Angerhausen et al. 2023; Konrad et al. 2023; Angerhausen et al. 2024; Mettler et al. 2024) but results depend on the resolution of the instrument, signal-to-noise obtained (e.g. Konrad et al. 2022), the presence of clouds (e.g. Mettler et al. 2024) and the technical capabilities for the formation alignment.

Optical direct imaging missions such as the Habitable Worlds Observatory (HWO), which are sensitive to the reflected light, will also be able to detect O_3, CO_2, CH_4 and H_2O as well as O_2 (Feng et al. 2018; Wang et al. 2018a; Smith et al. 2020; Damiano et al. 2022, 2023; Hall et al. 2023; Latouf et al. 2023; Gilbert-Janizek et al. 2024; Latouf et al. 2024). However, the time required depends on the cloud conditions (e.g Wang et al. 2018a), the resolution of the instrument and signal-to-noise of the spectrum (e.g. Feng et al. 2018). Additionally, modelling of both reflection and emission spectra can be biased if the radius of the planet is not well constrained (Carrión-González et al. 2020)

1.6.5 Low vs high spectral resolution

Section 1.5 discusses characterisation at both low and high spectral resolution. The distinction between these is not set by a specific resolution but rather is to do with how the spectra are currently extracted. Methods that extract low resolution spectra are able to retain the continuum information while those for high resolution cannot although they contain more information in the spectral features. The choice between low and high resolution is currently one between having the continuum of the spectra or having more information on the spectral features.

Each of these has its benefits and drawbacks. For example, low spectral resolution with its continuum information, is better for measuring the broad band albedo of an exoplanet for the purpose of measuring the planet's energy budget or detecting features such as ocean glint. Whereas high resolution with its additional spectral information is better for unambiguously measuring the composition of a planet's atmosphere and determining cloud properties such as their altitude which in turn reveals more information on the energy budget.

It is of course possible to combine low and high resolution spectra and this has been shown to improve atmospheric constraints (Gandhi et al. 2024; Inglis et al. 2024; Smith et al. 2024). However, future instrumentation is currently split with the ground-based ELTs having high resolution instruments and

space-based direct imaging missions having low resolution instruments[8]. These may not be operating at the same time and other factors such as observing restrictions will mean it is not always be possible to get low and high resolution data for the same planet.

If the goal is to search for alien life on Earth-like exoplanets, I would recommend the use of high-resolution spectra as their less ambiguous detections and ability to constrain cloud properties are key in robustly determining the validity of any biomarkers detected.

1.7 Outline towards rocky worlds

The pathway towards the atmospheric characterisation of Earth-like exoplanets in reflected light begins today with the study of close-in giant planets. This work has been hampered in recent years by the low albedos of the exoplanets otherwise most amenable to characterisation with current instrumentation. However, this can now be mitigated by using broadband secondary eclipse measurements to identify the planets with high albedos for further characterisation. By studying these reflective worlds, we will learn more about how reflection affects planetary climates as well as be able to test the techniques we will be using on Earth-like planets.

Moving into the next decade with the soon-to-be-completed ELTs, the first potentially Earth-like exoplanets will be characterised in reflected light. These worlds will be orbiting M dwarfs as they are more amenable to characterisation, however, their habitability is currently uncertain. Higher stellar activity may have completely eroded their atmospheres (e.g. Khodachenko et al. 2007) so, in addition to searching for biomarkers, these studies will also be able to constrain the prevalence of atmospheres on these worlds. This has large implications for the number of habitable planets in the galaxy as M dwarfs are the most common type of star.

Even further into the future, the era of space-based direct imaging missions will open the doors to study a larger number of potentially Earth-like exoplanets around a variety of stellar types. Not only will these observations be able to characterise the atmospheres of these worlds but they may also have access to their surfaces. This will allow comprehensive characterisation of ideally a few tens of worlds and may potentially lead to the discovery of alien life.

1.7.1 What is in this Thesis

This thesis begins with a discussion on reflected light spectra in Chapter 1. This covers how planets reflect light and what studying it can reveal about their atmospheres. Chapter 2 then discusses the

[8]Due to launch weight restrictions, it is not currently possible to launch high resolution spectrographs into space.

observational techniques used in this thesis to obtain the reflection spectrum of an exoplanet. After this, Chapters 3, 4 and 5 present various projects aimed at creating a pathway towards the characterisation of Earth-like exoplanets.

Chapter 3 covers the first part of this pathway: the characterisation of close-in giant planets with current instrumentation. This chapter presents the initial work towards the characterisation of the highly reflective giant planet LTT-9779 b with recent observations. This planet likely has a high cloud deck which will mute spectral features at low resolution. Therefore this work uses high-spectral resolution techniques with the aim of making the first robust detection of the reflected light of an exoplanet at high spectral resolution.

Chapter 4 covers the next part of the pathway: the era of the Extremely Large Telescopes. This chapter shows the simulated characterisation of Proxima b (the nearest potentially Earth-like exoplanet) with HARMONNI@ELT with the aim of detecting an atmosphere and biosignatures on this world. I demonstrate the feasibility of the observing program and what we could hope to learn about this potentially Earth-like world using these observations.

Chapter 5 then covers the more distant future: towards population studies of Earth-like worlds. In this chapter I present the work of a collaboration, which I lead, formed at the Lorentz centre meeting: *Optical Exoplanet Imagers*, Leiden, 20 - 24$^{\text{th}}$ February 2023. This work highlights how the currently planned Habitable Worlds Observatory might have the capacity to discover liquid water on an Earth-like world – a key indicator of habitability.

Finally, I conclude in Chapter 6, further highlighting the pathway towards the characterisation of Earth-like planets and where I plan to take this research next.

2 | Extracting high-resolution spectra

2.1 Direct Imaging with Coronagraphy

As discussed in Chapter 1, to learn about the atmospheres of exoplanets we can measure their reflected light. Unfortunately, the light of the planet is contaminated by the light of the nearby and much brighter host star. This contamination can be reduced by spatially resolve the planet from its star: a technique called Direct Imaging or High Contrast Imaging (HCI).

The spatial resolving power of a telescope is fundamentally limited by the diffraction limit. Ground-based observations are further limited by atmospheric turbulence which deteriorates image resulting in a 'seeing limited' image instead. The deterioration in the image is caused by atmospheric turbulence distorting incoming wavefronts, however, Adaptive Optics (AO) systems are able to largely correct this. This is achieved by splitting a small amount of the incoming light off and using it to measure the shape of the wavefront. Then, in the main beam of light, the shape of a mirror is changed to cancel out the distortions. This is repeated hundreds times every second to continually compensate for the changing distortions which has resulted in near diffraction limited observations (e.g. Davies et al. 2012, and refereces therin). Space-based observations are obviously not affected by atmospheric turbulence but imperfections in their optics and other small effects will degrade their images as well (e.g. Currie et al. 2023b).

In the diffraction limit, to be seen as distinct sources, two objects on the sky must have an angular separation of at least $1.22\lambda/D$[1] where λ is the wavelength of light and D is the diameter of the primary mirror of the telescope (e.g. Zurlo 2024). Figure 2.1 shows the exoplanet-star angular separations of the known exoplanet population out to a distance of 50pc and indicates which planets are spatially resolvable for a given size of telescope. However, small widely separated planets are hard to detect with current instrumentation (Gaudi et al. 2021), so while most of this population is not spatially resolvable, it is likely that there are more undiscovered exoplanets that could be observed in this way within 50 pc and beyond.

2.1.1 The Observations

To directly observe a planet, not only must it be spatially separable from its host star but also bright enough (have a favourable contrast) that its light is detectable. Planets are orders of magnitude fainter

[1] For direct imaging it is more typically assumed $> 2\lambda/D$ as observations will not be perfectly diffraction limited (Zurlo 2024).

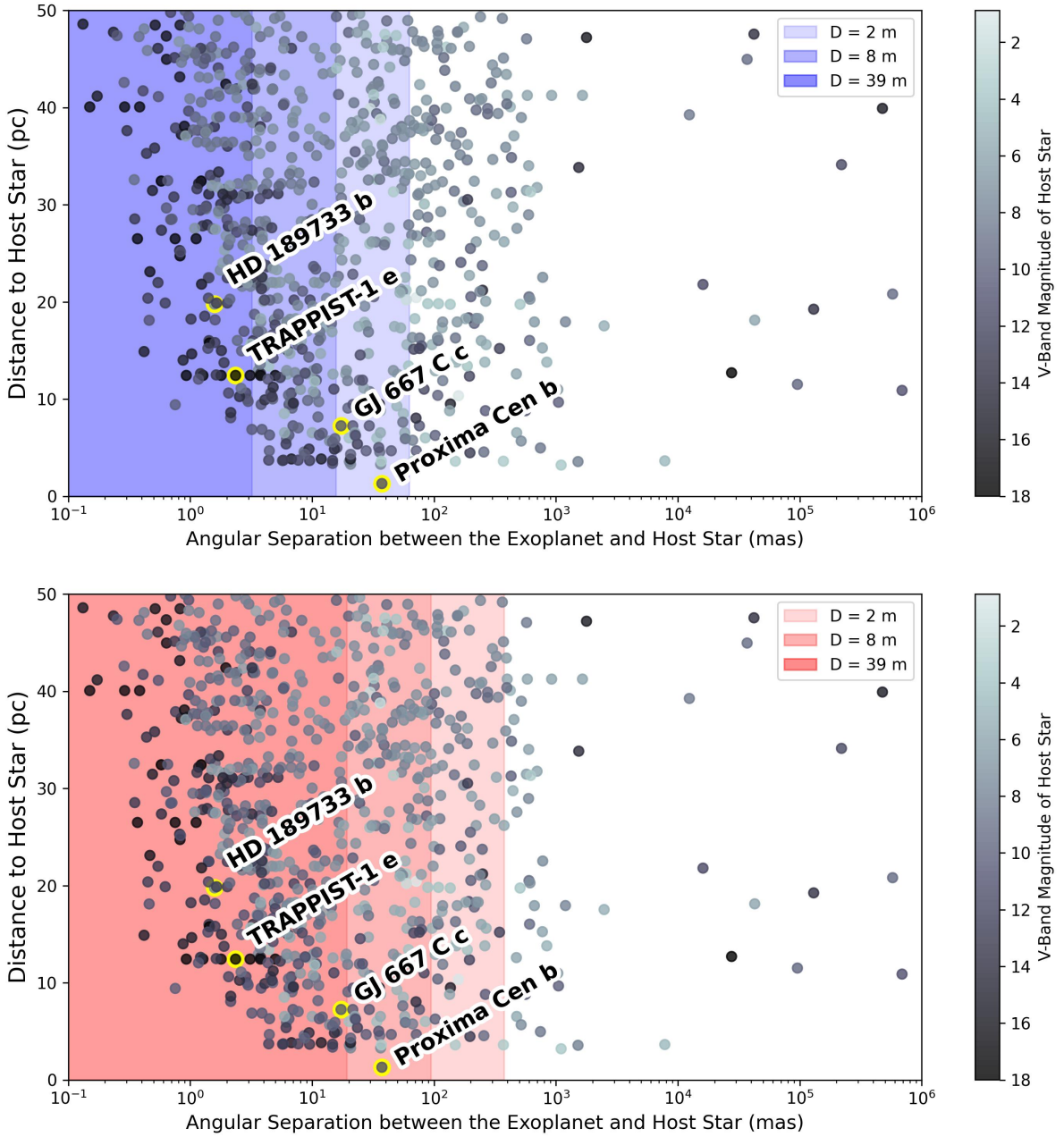

Figure 2.1: The angular separation of all known exoplanets out to a distance of 50pc. The colour scale indicates the visible magnitude of the host star. Fainter host stars will require longer integration times for planet detection. The shaded regions in the top panel highlight separations less than $1.22\lambda/D$ for three sizes of telescope assuming $\lambda = 0.5\,\mu\text{m}$. The bottom panel does the same but for $\lambda = 3\,\mu\text{m}$. 8-m class telescopes are the largest currently in operation however several 30-m class telescopes are in the planning and construction phases. The ELT will be $\simeq$ 39-m in diameter. Four planets are highlighted on these plots, three of which are candidates for Earth-like worlds: TRAPPIST-1 e, GJ 667 C c and Proxima Cen b. The final planet, HD 189733 b is an archetypal hot Jupiter. Not many exoplanets can be directly imaged today but this will change in the future.

than their host stars and will therefore will be overwhelmed by the stellar flux at small separations. To directly image these planets, the stellar light must be suppressed at the separations of interest. This can be done with corongraphy which employs occulters in the imaging optics to block the majority of the on-axis star light while only removing a fraction of the off-axis planet light. The Habitable Worlds Observatory, which is discussed in Chapter 5, will be coronagraph enabled. Alternatively, the stellar light can be suppressed with apodisers. These alter the instrumental PSF through constructive and destructive interference and can be used to suppress the star light at the separations of interest. Chapter 4 discusses HARMONI@ELT which uses an aposider to create a ring of reduced diffracted starlight.

Current state of the art instrumentation is able to reach contrasts of $10^{-5} - 10^{-6}$ for example with the Gemini Planet Imager or the Spectro-Polarimetric High-contrast Exoplanet REsearch (Nielsen et al. 2019; Vigan et al. 2021). However, direct imaging observations currently suffer from 'quasi-static speckles' of residual star light which limit the achievable contrast. These can originate from imperfect AO correction or, for space based observations, imperfections in the optics. These 'speckles' appear as point sources with a spectrum similar to that of the star and change slowly over time. In a single image, speckles are indistinguishable from a point source of the same brightness meaning they can be mistaken for planets. However, their wavelength and time dependence can be used to isolate them as discussed in Section 2.1.2.

2.1.2 Isolating the Exoplanet's spectrum

Speckles can masquerade as directly imaged planets and so they must be isolated and removed from the image as shown in Figure 2.2. This is typically done with one of the three following techniques.

Spectral Differential Imaging (SDI). This technique makes use of the fact that the position of the speckle pattern changes with wavelength whereas the planet's position remains the same. Consequently, two simultaneous images taken at different but close wavelengths can be used to remove the speckle pattern. One image is rescaled so that the speckles fall in the same place in both images. When the images are subtracted, the speckles are removed but the planet remains (Racine et al. 1999; Sparks et al. 2002). This technique can also provide information on the spectrum of the planet by comparing its brightness at the different wavelengths.

Angular Differential Imaging (ADI). This technique uses intrinsic field of view rotation during the observations to isolate the speckle pattern. Over time, the position of the planet on the detector will rotate around the star as the position angle changes. The speckle pattern however, will not rotate. A reference image of the speckles can then be created either by averaging the time series of observations

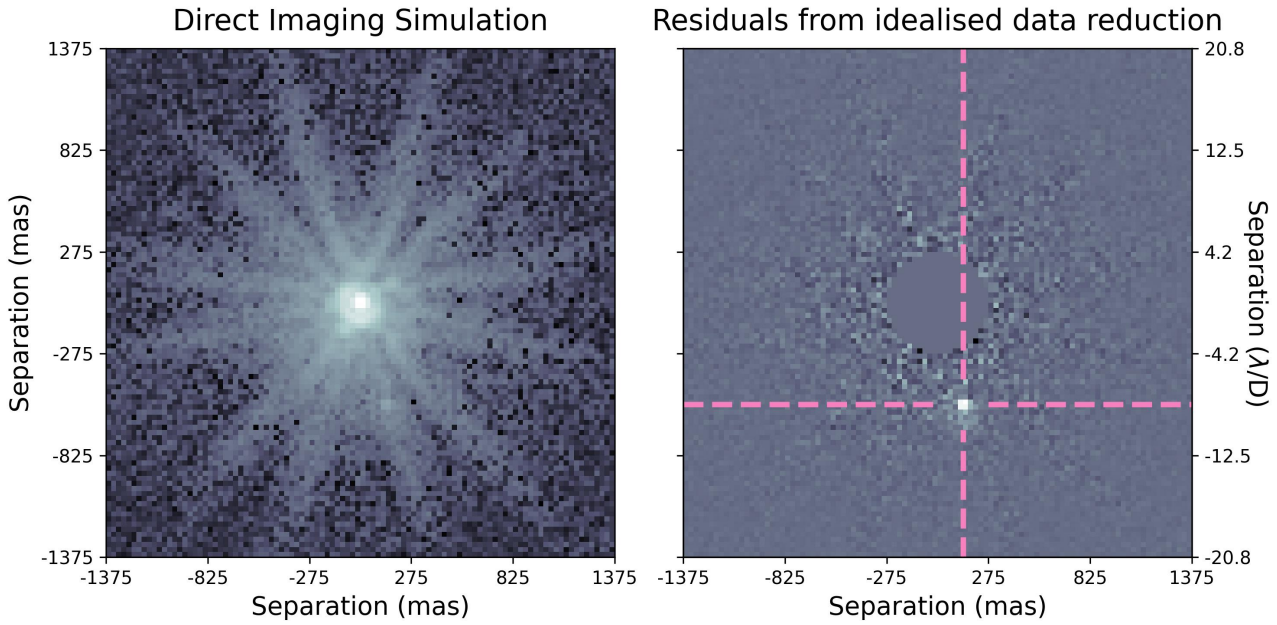

Figure 2.2: A simulated example of a direct imaging observation. In this simulation the planet is separated from the star by $570\,\mathrm{mas}$ and $1.22\lambda/D = 66.1\,\mathrm{mas}$ so it is well resolved. The left panel shows the simulated noisy observation and the right panel shows the residuals after an exact model of the PSF is removed. This model is a copy of the PSF used in the simulations and is not created using the data and the methods described in this Section. Therefore this plot does not demonstrate a realistic direct imaging detection but serves as an example of what these techniques aim to achieve. In the residual image the center of the field of view has been masked for clarity of viewing due to high residual noise. The planet is clearly visible in the residual image with its location marked by the pink dashed lines. This simulation made use of WEBBPSF to simulate the diffraction pattern (Perrin et al. 2014).

(typically a few hours long; Marois et al. 2006) or by using algorithms to predict the planet-free speckle image for each frame (e.g. Lafreniere et al. 2007; Amara et al. 2012; Soummer et al. 2012). By removing the model of the speckles, the planet can then be identified through its motion in the residual images (Marois et al. 2006).

Reference Differential Imaging (RDI). An observing sequence is taken consisting of alternating observations of the star with the planet and a similar and nearby reference star. The images of the reference star is used to create a reference image of the speckles which is then subtracted from the image of the star with the planet, ideally removing most of the contamination (Xie et al. 2022).

2.1.3 Atmospheric retrievals

Figure 2.2, shows that once the speckle pattern has been removed, the light of the exoplanet should be revealed. This can be used to obtain information on the planet's atmosphere by fitting a model spectrum to the measured spectrum.

For example, the H- and K- spectrum of HR 8799 b ($7^{+4}_{-2} M_{\mathrm{Jup}}$) has been measured with direct images

taken with the OH-Suppressing Infrared Imaging Spectrograph on KeckII (Barman et al. 2011, 2015) and Wide Field Camera 3 on Hubble (Rajan et al. 2015). The spectrum has been used to measure the effective temperature, gravity, metalicity and radius of this world as well as constrain the abundance of water and CO (Barman et al. 2011; Konopacky et al. 2013; Lee et al. 2013; Barman et al. 2015; Rajan et al. 2015). Barman et al. (2015) also claimed a detection of CH_4 however other works using both direct imaging and molecule mapping (see Section 2.3) techniques did not show CH_4 (Konopacky et al. 2013; Petit dit de la Roche et al. 2018). Lee et al. (2013) showed the measured spectrum could be fit with both cloud-free and cloudy models but that these resulted in different best fit values for atmospheric parameters such as the mean molecular weight of the atmosphere, hence the data is not sensitive to the presence of clouds but they can bias the fit.

Similarly for 51 Eri b ($\approx 2M_{\rm Jup}$) direct images with SPHERE@VLT and GPI@Gemini have measured the H-, J-, K- and Y- band spectrum which has been used to constrain the effective temperature, gravity, metalicity and radius of this world as well as measure the abundance water and CH_4 (Macintosh et al. 2015; Rajan et al. 2017; Samland et al. 2017; Whiteford et al. 2023). The presence of clouds was also inferred by Samland et al. (2017) and Rajan et al. (2017) however, Whiteford et al. (2023) showed a cloud-free model with a flexible temperature-pressure profile could also fit the data. It is clear that a great deal can be learned from directly imaging exoplanets but more work is needed to disentangle the degeneracies in the recovered atmospheric parameters.

Direct imaging observations have characterised these and a handful of other worlds (Bonnefoy et al. 2016; De Rosa et al. 2016; Chauvin et al. 2018; Stone et al. 2020; Wilcomb et al. 2020; Ward-Duong et al. 2021) largely limited to widely separated ($> 10\,\mathrm{au}$), young and self-luminous, giant companions[2] ($> 2Mj_{\rm Jup}$) as these objects have favourable angular separations and contrast ratios in the infrared. In the future, direct imaging missions such as the Habitable Worlds Observatory (HWO) (Astro2020) or the Large Interferometer for Exoplanets (LIFE)[3] (Konrad et al. 2022) will aim to measure the spectra of potentially Earth-like exoplanets in reflected light and infrared in the search for biomarkers.

2.2 High-Resolution Cross-Correlation Spectroscopy

As shown in Figure 2.1 a large number of the currently known exoplanets will not be spatially resolvable – even with the next generations of $30\,\mathrm{m}$ telescopes. However, it is possible to disentangle the planet's spectrum from the contaminating star light even if the latter is many orders of magnitude

[2]Some of these objects are low mass stars hence 'companion' instead of 'exoplanet' although the boundary between stars and planets is somewhat fuzzy.

[3]This not strictly a direct imaging mission as it will be an interferometer.

greater in brightness and the two are not spatially resolved. This technique, first demonstrated by Snellen et al. (2010), is now known as High-Resolution Cross-Correlation Spectroscopy (HRCCS).

For short period planets like hot Jupiters have angular separations of the order of $10\,\mathrm{mas}$ and are not spatial resolvable with current instrumentation. However, as a planet orbits its star, its radial velocity as seen from Earth changes and the orbital velocities of these planets can be of the order of $100\,\mathrm{km\,s^{-1}}$ whereas the star's reflex motion is only on the order of $10 - 100\,\mathrm{m\,s^{-1}}$. This means that when the spectrum of the star-planet system is observed at high-spectral resolution, the spectral lines of the exoplanet move significantly while the stellar lines remain quasi-stationary. This is shown graphically in Figure 2.3. If this spectrum is taken through Earth's own atmosphere, then there will also be telluric spectral lines. However, as the telescope is at rest relative to the Earth, these will be stationary. The exoplanet's spectrum can be isolated from the contamination by taking a time series of spectra from which quasi-stationary trends are removed.

While this technique has been very successful at characterising exoplanet thermal emission and transmission spectra, it has yet to be used successfully in reflection (Charbonneau et al. 1999; Collier-Cameron et al. 1999, 2002, 2004; Rodler et al. 2013; Martins et al. 2015; Hoeijmakers et al. 2018a; Scandariato et al. 2021; Spring et al. 2022)[4]. Chapter 3 shows my current work on using this technique to detect the high resolution reflection spectrum of LTT-9779 b. Unfortunately, I have not made a robust detection of the reflected light from this planet at the time of writing this thesis although the analysis is still ongoing.

2.2.1 The Observations

In order for this technique to work, the time-series of high resolution stellar spectra must have certain properties. First, it must have high enough spectral resolution that spectral lines are well resolved and that the net Doppler shift of the planet over the time-series is at least a few resolution elements. The latter is required so that the planet's spectrum is not significantly affected by the process used to remove the stellar contamination. This technique has been used successfully down to resolutions of approximately $R \approx 15000$ (e.g. Sluijs et al. 2023) however the planet in this work has a particularly high orbital velocity ($230\,\mathrm{km\,s^{-1}}$) and the spectral resolution must be chosen appropriately for each system being observed.

A second requirement is that the time-series, which is typically around 5 hours long, must be obtained as a continuous observing run. This is because stopping the observation and returning to it at a later

[4]Martins et al. (2015) claimed a detection of the reflected light of 51 Pegasi b, but Scandariato et al. (2021) and Spring et al. (2022) later showed this to be an unfortunate false positive.

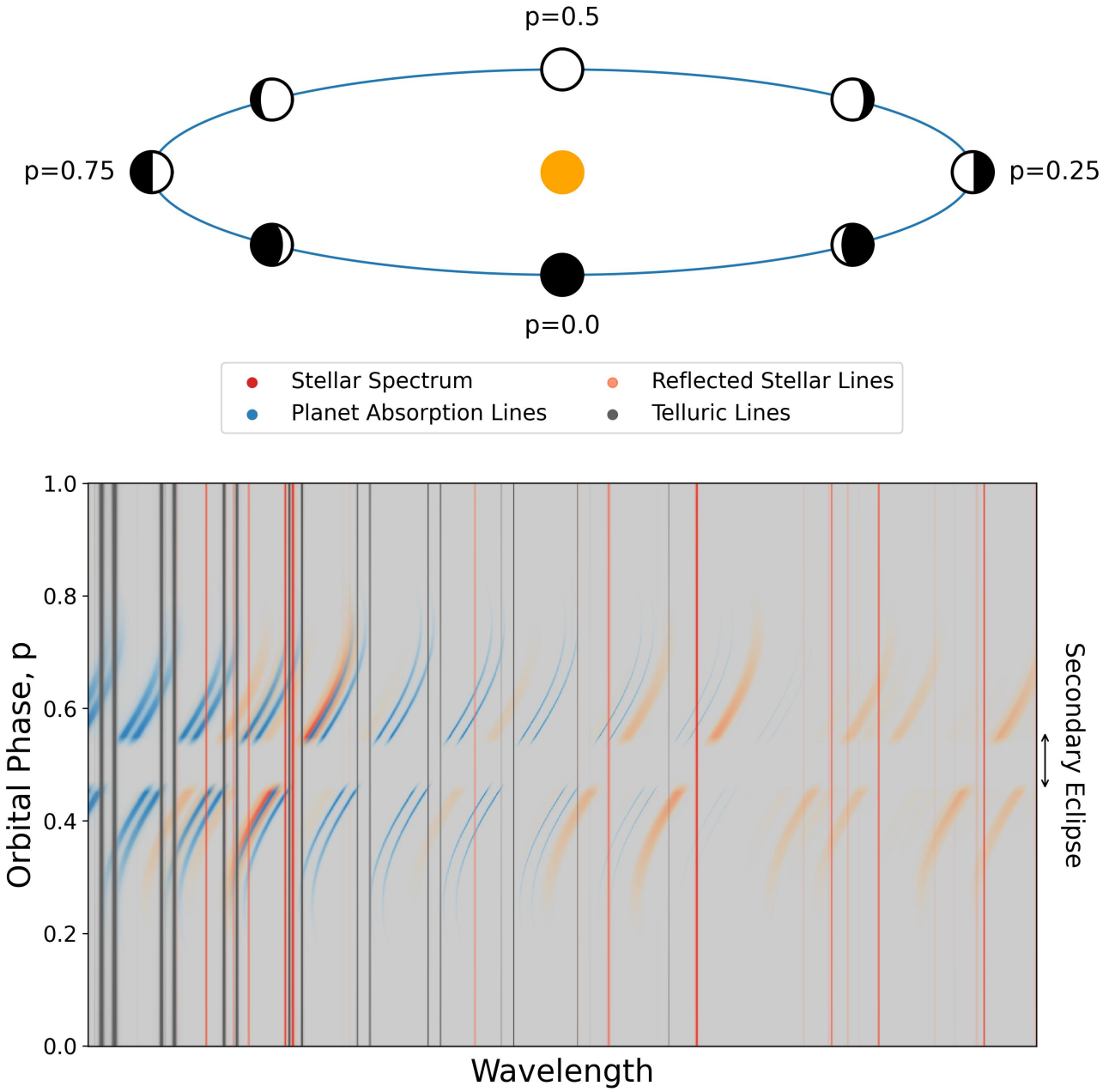

(a) The top panel shows the planet's orbit as well as how the planet's phase changes. The bottom panel shows the spectral lines of the star and planet throughout the orbit of the planet. This has been created using the simulated spectra in panel (b) where each set of spectral lines is Doppler shifted by an appropriate amount and the planet's spectral lines are modulated by the planet's phase function, including the secondary eclipse. The motion of the star's lines (red) is imperceptible whereas the motion of the planet's lines (blue and orange) is clearly visible. The planet's lines vanish at small and large orbital phases as this is when the planet's night side is facing the observer (see top panel) and so there is little reflected light. There is a small gap in the planet's lines around an orbital phase of 0.5. This is caused by the planet passing behind the star during secondary eclipse. The stellar lines reflected by the planet (orange) are rotationally broadened and so are noticeably wider than the stellar lines.

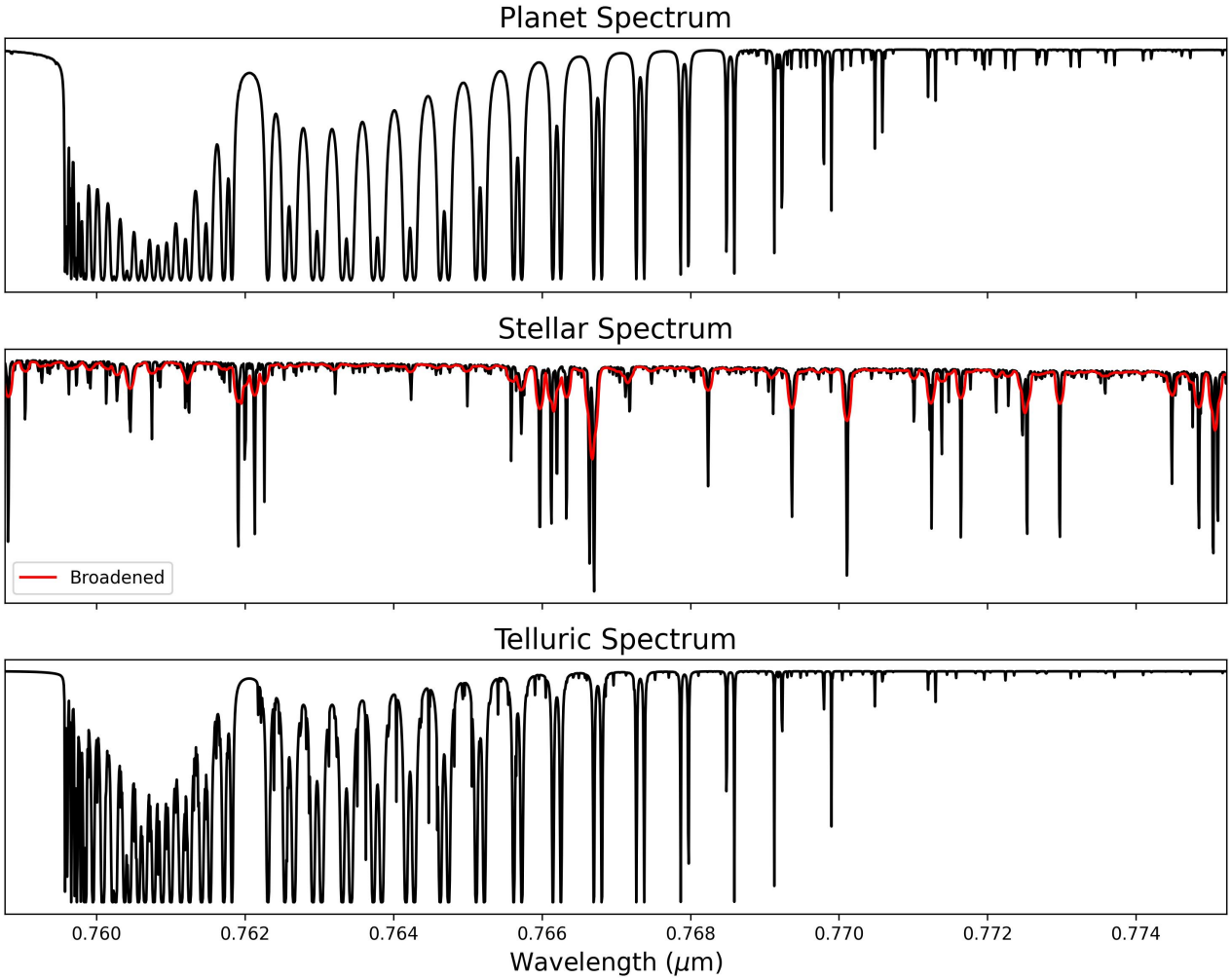

(b) The spectra used in the simulation shown in panel (a). The y-axis is removed as the units are arbitrary. **Top panel:** The planet's contrast ratio is a model of the Earth's reflection spectrum generated using PICASO (Batalha et al. 2019). The rotatioally broadened stellar spectrum is multiplied by this to produce the planet's spectrum. **Middle panel:** The stellar spectrum is a PHOENIX model (Husser et al. 2013) with an effective temperature $5400\,\mathrm{K}$, logg$=4.5$ and solar metalicity. Also shown in red is rotational broadened version of this spectrum. **Bottom panel:** The telluric spectrum is a model generated with telfit (Gullikson et al. 2014) assuming the mean conditions at Paranal for airmasses ranging from 1.9 to 1.3 and back again.

Figure 2.3: Panel (a) shows schematic demonstrating how the spectral lines of a star-planet system change throughout the orbit of the planet. Panel (b) shows the model spectra used in this schematic.

time introduces unknown systematics. Different observing runs can still be combined after the cleaning steps but they must be cleaned separately. This means that, for example, the requirement that the Doppler shift of the planet exceeds a few resolution elements must be true over the course of the observing run which is a stricter constraint, especially when limited by the day-night cycle of the Earth.

For ground based observations, the Earth's thermal background imposes the requirement that the observed wavelengths are $< 5\,\mu\mathrm{m}$. This is because, at longer wavelengths, the Earth's thermal background will dominate the observed spectra which introduces too much noise and systematics for the planet's spectrum to be successfully recovered. For space based observations, this restriction does not apply, however space-based spectrographs are limited in spectral resolution ($\lesssim 3000$) as the weight of high-resolution spectrographs makes them difficult to launch and so they are unsuitable for HRCCS.

The final requirement is that the spectrum of the planet in the time-series is bright enough that it could be detected with these observations. This is typically estimated using the following equation (modified from Birkby 2018):

$$S/N_p = C \times S/N_s \times \sqrt{N_{lines}} \times \sqrt{N_{obs}} \tag{2.1}$$

where S/N_p is the signal-to-noise of the recovered exoplanet's signal, C is the ratio of the planet's brightness to that of the star (contrast) and S/N_s is the average signal-to-noise of the stellar spectrum. There is also N_{lines} which is the number of spectral lines in the observed exoplanet's spectrum and N_{obs} is the number of observations in the time-series. However, this typically overestimates the signal-to-noise of the planet as it assumes the planet's spectrum is only contaminated with residual photon noise. This is typically not the case as the data reduction will not perfectly remove the contaminating spectra. So while it is a good metric for quickly deciding if planet could be characterised with HRCCS, it should not be used when determining an observing plan. Instead, the observations should be simulated and treated as real data to determine robustly how well the planet's spectrum could be detected.

2.2.2 Isolating the Exoplanet's spectrum

Assuming the time series has the properties discussed in Section 2.2.1, the planet's spectrum can be largely isolated from the contaminating stellar and telluric spectra by techniques that remove quasi-stationary trends. First, the time-series of spectra are typically wavelength calibrated and corrected for bad pixels. After this though, there is a great diversity in the literature in the techniques used to remove the contaminating spectra. The following describe the most common of these techniques

however it should be stressed that these are not in sequential order since the literature is diverse in the implementation and order of the steps used.

Choosing a rest frame for the time-series. Throughout the time-series, the velocity of the star with respect to the Earth will change slightly. Therefore, the removal of quasi-stationary trends can be conducted in either the telluric rest frame or the stellar rest frame. The processing techniques used to remove quasi-stationary trends are more efficient the more stationary the trend is so if the telluric rest frame is used, the telluric lines will be removed more completely and if the stellar frame is used, the stellar spectral lines will be more completely removed. Therefore the frame used will depend on which affects the data more, the tellurics or the stellar spectral lines. Typically, the telluric frame is used for infrared observations (e.g. Snellen et al. 2010; Birkby et al. 2013; Kok et al. 2013; Schwarz et al. 2015; Birkby et al. 2017; Ridden-Harper et al. 2023) as these contain significant telluric contamination. However, for most stellar spectral types, optical data is more contaminated by the stellar lines so typically the stellar frame is used (e.g. Gibson et al. 2019, 2020; Azevedo Silva et al. 2022; Spring et al. 2022; Prinoth et al. 2023; Maguire et al. 2024; Yang et al. 2024). Additionally, for reflected light spectra, the planet's spectrum also contains a copy of the stellar lines as this is the spectrum it is reflecting and so it is of greater importance that the contamination from the stellar spectrum must be well removed.

Continuum normalising the observations. Due to atmospheric and instrumental effects, the flux of the star reaching the detector is not constant in time. In order for some processing methods to effectively remove quasi-stationary trends, the continuum flux of each observation needs be the same. Therefore one of the first steps employed is often to normalise the continuum of the spectra (e.g. Snellen et al. 2010; Brogi et al. 2012; Schwarz et al. 2015; Guilluy et al. 2019; Scandariato et al. 2021; Azevedo Silva et al. 2022; Spring et al. 2022; Ramkumar et al. 2023; Sluijs et al. 2023; Gandhi et al. 2024; Guo et al. 2024; Nortmann et al. 2024). Throughout the literature there are a number of ways this normalisation is achieved. For example, Snellen et al. (2010) fit a second order polynomial multiplied by the mean spectrum to each observation, whereas Guilluy et al. (2019) used the median of the 300 brightest pixels in each spectrum.

Removing a representative spectrum from the time-series. As an initial step, many works remove a representative spectrum – either a mean or median – from the time series (e.g. Rodler et al. 2012; Brogi et al. 2016; Hoeijmakers et al. 2018a; Guilluy et al. 2019; Azevedo Silva et al. 2022; Spring et al. 2022; Finnerty et al. 2023; Gandhi et al. 2023; Ramkumar et al. 2023; Yan et al. 2023; Finnerty et al. 2024; Yang et al. 2024). This spectrum can either be subtracted or divided from the data but is typically subtracted for emission and reflection spectra. This is because emission and reflection

spectra add light to the stellar spectrum whereas transit spectra multiply the stellar spectrum by their transmission. For transmission spectra, the in-transit spectra are often excluded when computing the representative spectrum so that the planet's spectrum does not affect it (e.g. Azevedo Silva et al. 2022). For emission and reflection spectra, if the planet goes into secondary eclipse, these observations can be used to create a model that does not contain the planet's spectrum instead.

Removing polynomial trends. Continuum normalised spectra often show residual trends even after the mean is removed. For example, changing airmass changes the line depths of the tellurics as a function of time. This causes the mean spectrum to under and over-remove of these lines. This residual trend can be corrected by fitting a polynomial to each wavelength in the spectral time series (e.g. Snellen et al. 2010; Brogi et al. 2012; Schwarz et al. 2015; Guilluy et al. 2019; Azevedo Silva et al. 2022; Prinoth et al. 2023). These trends can also be a function of wavelength, such as changes in the blaze function of the detector. This can be corrected for by fitting a polynomial to the spectrum of each observation (e.g. Snellen et al. 2010; Gibson et al. 2019, 2020; Spring et al. 2022; Prinoth et al. 2023; Ridden-Harper et al. 2023). These polynomials are typically low order to avoid removing or distorting the planet's spectrum.

Non-parametrically removing trends with algorithms. There are two algorithms that are commonly used to non-parametrically remove trends, the first of these is Principal Component Analysis (PCA) or Single Value Decomposition (SVD) (e.g. Kalman 1996). This decomposes the spectral time-series into a set of orthogonal basis vectors (singular vectors) and their associated weights (variances). The singular vectors can be thought of as a set the spectra that make up the time series where each spectra cannot be described as a combination of the others. The variances determine how much each of these spectra contributes to the time series. If the singular vectors with the highest variance are removed, this eliminates most major quasi-stationary trends without any assumption on the functional form of these trends. The second is the SYSREM algorithm (Tamuz et al. 2005). This works in a similar way to PCA/SVD but it is iterative and it additionally takes into account the unequal errors on each data point in the spectrum, typically meaning that high signal-to-noise data has a higher weighting when computing the singular components. Both of these algorithms are commonly used in HRCCS analyses (PCA/SVD; e.g. Kok et al. 2013; Brogi et al. 2016; Hoeijmakers et al. 2018a; Giacobbe et al. 2021; Finnerty et al. 2023; Gandhi et al. 2023; Sluijs et al. 2023; Finnerty et al. 2024; Smith et al. 2024) (SYSREM; e.g. Birkby et al. 2013, 2017; Gibson et al. 2019, 2020; Spring et al. 2022; Ramkumar et al. 2023; Ridden-Harper et al. 2023; Yan et al. 2023; Gandhi et al. 2024; Guo et al. 2024; Maguire et al. 2024; Nortmann et al. 2024). However, both have to be halted at some stage to prevent them from removing the planet's signal. There is an ongoing discussion as to how and where this should be done

[Spring et al., in prep].

Removing tellurics through model fitting. It is possible to model the tellurics by using a line-by-line radiative transfer model of the Earth's atmosphere, such as Molecfit (Smette et al. 2015). Some works use these models to fit the telluric lines in their spectra and therefore correct for their effects (Gandhi et al. 2023; Prinoth et al. 2023; Seidel et al. 2023; Yang et al. 2024; Young et al. 2024). However, the telluric spectrum is difficult to model and residuals may still remain after such a fit. This can subsequently be corrected with PCA/SVD or SYSREM.

Removing low order continuum variations. Some works use a high-pass filter to remove a slowly varying continuum from each observation (e.g. Brogi et al. 2012; Birkby et al. 2017; Hoeijmakers et al. 2018a; Sluijs et al. 2023; Yang et al. 2024). This residual may be the result of atmospheric or instrumental effects and affects the extraction of the exoplanet's spectrum. If this step is used then the cross-correlation model (see Section 2.2.3) must be continuum subtracted the same way in order to fit the data.

Masking contaminating spectral lines. If regions containing the contaminating spectral lines are removed from the analysis, their effects can be negated. However, careful consideration is needed when choosing how much of the line to mask and which lines to mask to minimise the number of the planet's spectral lines that are lost in the process. Most works only mask strong or saturated spectral lines (e.g. Birkby et al. 2017; Azevedo Silva et al. 2022; Spring et al. 2022; Gandhi et al. 2023; Yan et al. 2023; Gandhi et al. 2024; Guo et al. 2024) as these will not contain any significant planetary signal, as it will all be absorbed, but can strongly affect the analysis due to their non-linear behaviour.

To demonstrate how these techniques are used to clean the data, I created some simplified example data. For the stellar spectrum, I used a PHOENIX model (Husser et al. 2013) with an effective temperature $5400\,\mathrm{K}$, logg$= 4.5$ and solar metalicity. For the planet's spectrum, I generated a model contrast ratio with PICASO assuming a hydrogen/helium dominated atmosphere with trace amounts of water, MgH and CO however, the CO abundance is too low to produce detectable spectral lines at the simulated wavelengths. This contrast ratio is multiplied by a $25\,\mathrm{km\,s^{-1}}$ rotationally broadened copy of the stellar spectrum. These spectra are then doppler shifted to appropriate velocities for a hot Jupiter system. Seeing variation is included and then photon noise is added assuming a mean signal-to-noise of 100. The tellurics are not included in this simulation as well as many other effects and thus it is highly idealised. For the data reduction, the data is first continuum normalised to remove the seeing variation and then the mean spectrum is subtracted. Due to the idealised nature of the simulation, the data is well cleaned after these two steps and no further cleaning is required.

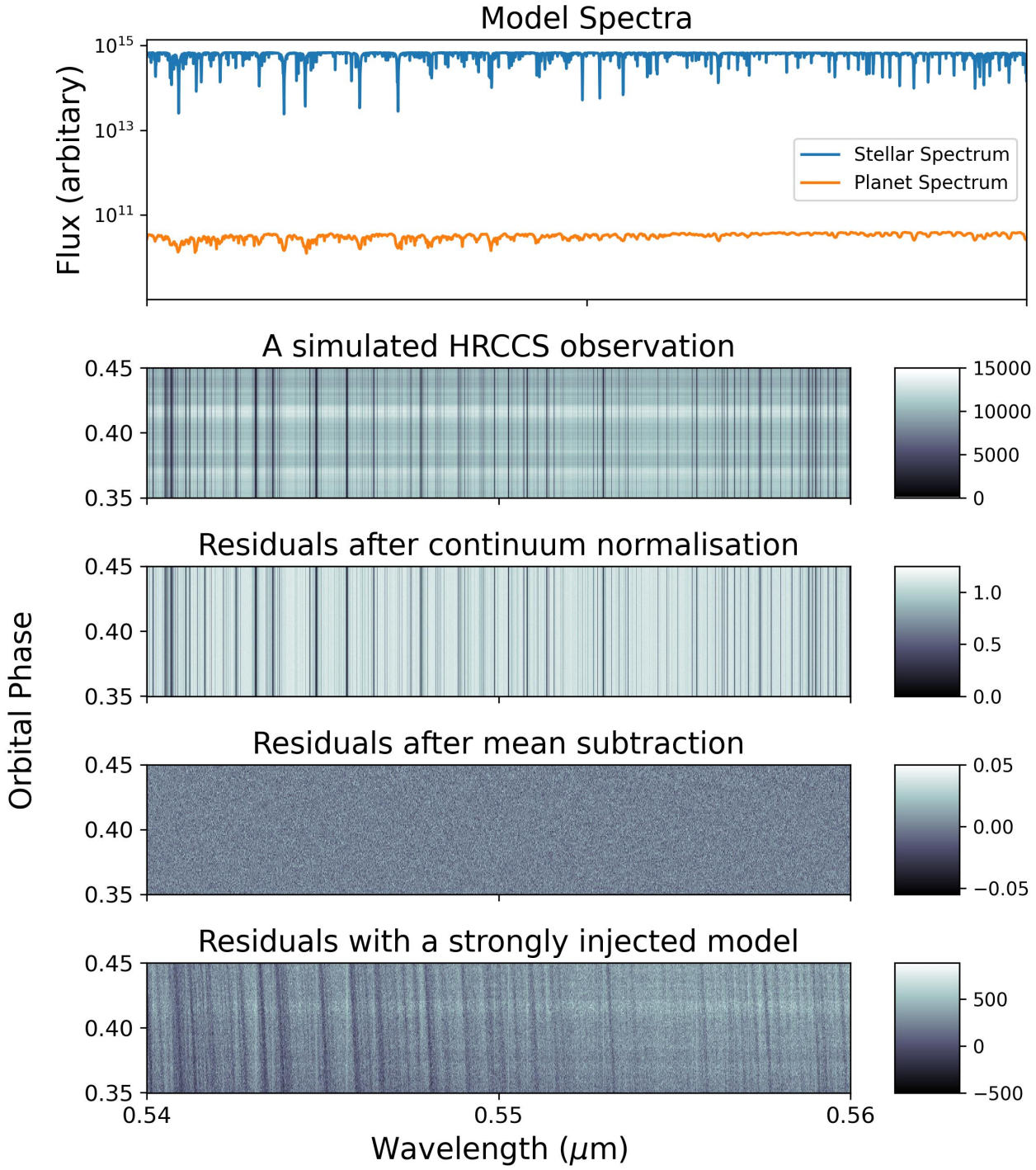

Figure 2.4: A simulated HRCCS time series observation and data reduction. **Top panel:** The spectra used in the simulation. **Second panel:** The simulated time series observation. **Middle panel:** The data after it has been contiuum normalised. **Fourth panel:** The residuals after the mean of all spectra are subtracted. The data are well cleaned by these two steps due to its idealised nature. However, the residual photon noise from the stellar spectrum still dominates the residuals in the middle panel so the planet's lines cannot be seen directly. **Bottom panel:** The residuals after an idealised data reduction if the planet was orders of magnitude brighter. In this panel, the planet's lines are visible from within the original noise.

2.2.3 Extracting the Exoplanet's Spectrum

Once the quasi-stationary trends have been removed, what should be left is the planet's spectrum and residual photon noise. Figure 2.4 shows an example of a simulated time series before and after the data reduction. The photon noise is often much larger than the lines of the planet's spectrum meaning additional steps are required to fit the planet's spectrum. This can be achieved by combining the planet's spectral lines to boost the signal strength by e.g. cross-correlating the residual spectra with a model of the planet's spectrum in order to reveal its presence in the data. The cross-correlation[5] is defined as:

$$C(v) = w\frac{\sum_\lambda (m_\lambda(v) - \bar{m}(v))(r_\lambda - \bar{r})}{\sqrt{\sum_\lambda (m_\lambda(v) - \bar{m}(v))^2 \sum_\lambda (r_\lambda - \bar{r})^2}} \tag{2.2}$$

where $C(v)$ is the cross-correlation coefficient. It is a function of the Doppler shift, v of the model spectrum, m and is weighted by the variance of the model and the data. In this equation, r is the residual spectrum from one observation in the time series and w is a weighting factor that determines how the cross-correlation coefficients from each observation in the time-series are combined. For example, low signal-to-noise observations could be down weighted. $\bar{m}(v)$ and $\bar{r}$ are the mean over wavelength of the Doppler shifted model and residuals, respectively. The sum λ is over all the wavelengths bins in the spectrum.

The cross-correlation coefficient, $C(v)$, is a measure of the similarity (correlation) between the Doppler-shifted model and the data, where a large absolute value indicates greater similarity with positive meaning the two are correlated and negative meaning they are anti-correlated. When the cross-correlation model used is a good match to the planet's spectrum in the data, it will result in a higher cross-correlation coefficient than if the wrong spectrum was used. The magnitude of the increase is related to the brightness of the planet's spectrum compared to the photon noise. If the planet is bright enough, then the change in the cross-correlation coefficient when the right model is used will be significant. This can be used to characterise the planet by determining which model spectra produce high cross-correlation coefficients and therefore match the planet's spectrum well. For reflected light spectra, it's worth noting that, since the exoplanet's spectrum contains the stellar spectral lines too, the cross-correlation method can also add up the signal of any residual stellar spectrum that's left in the data. This means good removal of the stellar spectrum is paramount.

Figure 2.5 shows several examples of a 'trail plot' where the residuals of each spectrum in a time series

[5] Specifically this is the Pearson correlation coefficient so it will have a value between -1 and 1.

have been cross-correlated with a model of the planet's spectrum for a range of Doppler shifts shown on the x-axis. Each trail plot shows the cross-correlation coefficients for a model spectrum containing a different single molecule. The trail plot for H_2O shows an increase in the cross-correlation coefficients following the expected velocity of the planet – its trail. This means that H_2O is present in the planet's atmosphere. This method has been used to detect molecules in the atmospheres of exoplanets with favourable contrast ratios ($\mathcal{O}(10^{-3} - 10^{-4})$) (e.g. Snellen et al. 2010; Brogi et al. 2016; Giacobbe et al. 2021; Nortmann et al. 2024).

The other two trail plots show no obvious signal from the planet. To identify faint trails, the cross-correlation coefficients of all the observations can be summed along the trail (e.g. Snellen et al. 2010; Brogi et al. 2012; Rodler et al. 2012; Kok et al. 2013; Brogi et al. 2016; Birkby et al. 2017; Nugroho et al. 2017; Guilluy et al. 2019; Giacobbe et al. 2021; Azevedo Silva et al. 2022; Jiang et al. 2023; Prinoth et al. 2023; Ridden-Harper et al. 2023; Seidel et al. 2023; Maguire et al. 2024; Yang et al. 2024). This is typically done for a range of values for the projected orbital velocity (gradient of the trail) and the systematic offset (position of trail along the x-axis). This produces a 'Kp-Vsys' plot where each row (Kp) in this plot is the sum of all the cross-correlation function for the time series for a given orbit of the planet. The Kp-Vsys plots for the trails shown in Figure 2.5 are shown in Figure 2.6. The plot for H_2O shows a clear peak in the cross-correlation coefficients at the right parameters for the trail. However, there is also a peak in the same place in the plot for MgH meaning that it is also present in the atmosphere of the planet – it's just that its trail was too faint to see in the trail plot.

There is still no detection of CO in this simulation for which injection tests can be used to put an upper limit on its abundance in the atmosphere (e.g. Schwarz et al. 2015; Hoeijmakers et al. 2018a; Guilluy et al. 2019; Spring et al. 2022; Rasmussen et al. 2023; Cabot et al. 2024; Yang et al. 2024). However, as can be seen in the Kp-Vsys plot for CO, while there is no signal, there are peaks and troughs in the cross-correlation coefficients which are caused by random noise. Therefore, there needs to be a metric for determining at what point a peak becomes a detection. There is an ongoing discussion in the field as to the best way to do this. Typically the Kp-Vsys plot is converted into signal-to-noise by dividing each row by its standard deviation – sometimes excluding the region around where the planet is expected in Vsys-space. Using this metric it is still possible to get spurious peaks at a signal-to-noise of S/N≈ 4 (e.g. Cabot et al. 2019; Cheverall et al. 2023) hence in this thesis, I adopt a signal-to-noise of S/N$= 5$ as the threshold for a detection. It should be noted that detection thresholds for HRCCS are typically fairly arbitrary rules of thumb and the S/N itself does not represent a statistical confidence. Determining the statistical significance of HRCCS detections is still an ongoing discussion and what constitutes a robust detection is still being debated.

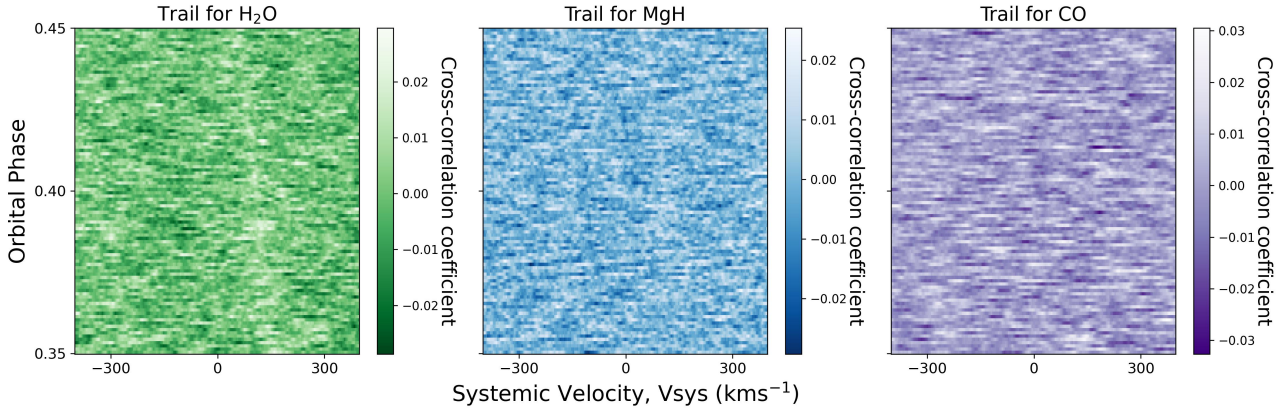

Figure 2.5: An example of a HRCCS trail plot. The x-axis is the Doppler shift of the model spectrum and each row on the y-axis is one observation, now labelled by the orbital phase of the planet. The colours represent the cross-correlation coefficients with lighter colours representing higher numbers. When a cross-correlation model containing only the spectral lines of water is used (left) a faint increase in the cross-correlation coefficients around $150\,\mathrm{km\,s^{-1}}$ can be seen. When models for MgH (middle) and CO (right) are used, the cross-correlation coefficients show no obvious increases.

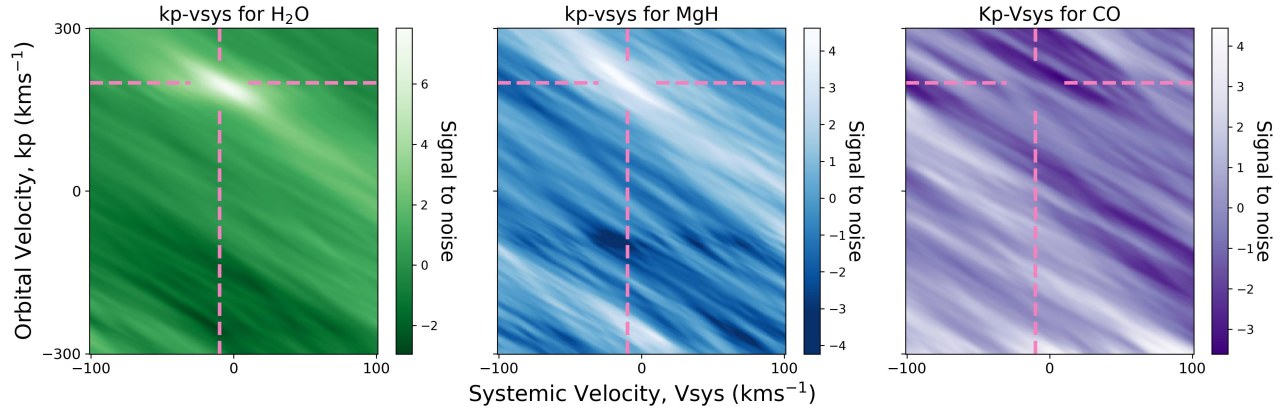

Figure 2.6: An example of a HRCCS Kp-Vsys plot. The x-axis is the velocity of the star system with respect to the Earth and the y-axis is the radial velocity semi-amplitude of the planet. The colours represent the summed cross-correlation coefficients from the trail plots, converted to signal-to-noise, with lighter colours representing higher numbers. The signal-to-noise is calculating by dividing each row by its standard deviation excluding the region where the planet's signal is expected. The Kp-Vsys plot created from the H_2O trail plot (left) shows a strong localised increase in the cross-correlation coefficients at the right orbital parameters of the planet, indicated by the pink lines. The diagonal shape of the detection is an effect of the limited orbital phase range in these observations (0.35 to 0.45). The Kp-Vsys plot created from the MgH trail plot (middle) shows a localised increase in the signal-to-noise at the right orbital parameters of the planet although it is below the detection threshold of S/N$=5$. This molecule is present in the simulated data so in this case this signal is coming from a weak trail that was too faint to see in Figure 2.5. However, if this were real data this would not be sufficient evidence for a detection. There is not a clear increase in the right place on the CO Kp-Vsys plot (right) meaning that either this molecule is not present or it is not abundant enough to detect with these data.

2.2.4 Atmospheric retrievals

The cross-correlation analysis can reveal the presence of molecules in the atmosphere of exoplanets as well as infer other atmospheric properties such as the temperature profile and dynamics (Snellen et al. 2010; Brogi et al. 2012; Kok et al. 2013; Brogi et al. 2016; Birkby et al. 2017; Nugroho et al. 2017; Guilluy et al. 2019; Giacobbe et al. 2021; Azevedo Silva et al. 2022; Jiang et al. 2023; Prinoth et al. 2023; Ridden-Harper et al. 2023; Seidel et al. 2023; Maguire et al. 2024; Nortmann et al. 2024; Yang et al. 2024). To constrain the molecular abundances of these molecules and other atmospheric parameters such as temperature, an atmospheric retrieval with the likelihood method is run (Brogi et al. 2019; Gibson et al. 2020). In an atmospheric retrieval, the cross-correlation coefficients are converted into a likelihood which is a measure of the probability that the data would have the that form if the model were true. The higher the probability, the more likely the model represents the data. The likelihood has the advantage that it can be easily combined with inferences made with other techniques such as low resolution spectroscopy (e.g. Gandhi et al. 2024; Smith et al. 2024) and that it can be used in a Markov Chain Monte Carlo (MCMC) fit which can robustly constrain the atmospheric parameters (e.g. Brogi et al. 2019; Gibson et al. 2020; Giacobbe et al. 2021; Finnerty et al. 2023; Gandhi et al. 2023; Ramkumar et al. 2023; Ridden-Harper et al. 2023; Yan et al. 2023; Blain et al. 2024; Finnerty et al. 2024; Guo et al. 2024; Nortmann et al. 2024). Figure 2.7 shows the output of an MCMC fit to the reduced simulated data shown in Figure 2.4. The MCMC is started from an initial guess for each of the parameters and allowed to run for a few thousand iterations. The values of the parameters start to fluctuate around a constant value after a few hundred iterations indicating the MCMC has converged. These few hundred iterations are then discarded. The MCMC shows that H_2O and MgH are constrained and CO has an upper limit as expected from the Kp-Vsys plots.

2.3 Molecule mapping

Direct Imaging is able to reduce the stellar contamination of the exoplanet's light by spatially resolving it while HRCCS is able to extract the faint exoplanet's spectrum from within the glare of the orders of magnitude brighter stellar spectrum. The combination of these two techniques – aka Molecule Mapping or HRCCS+HCI (Hoeijmakers et al. 2015; Snellen et al. 2015) – can be used to characterise faint, spatially-resolvable exoplanets that remain buried in the stellar contamination.

This technique requires a high resolution spectrum to be taken for each 'pixel' in an image of the exoplanet-star system. These 'spectral pixels' are often referred to as *spaxels* and can be arranged in a number of ways but typically in a 2d grid or a 1d slit. While HRCCS uses the changing velocity

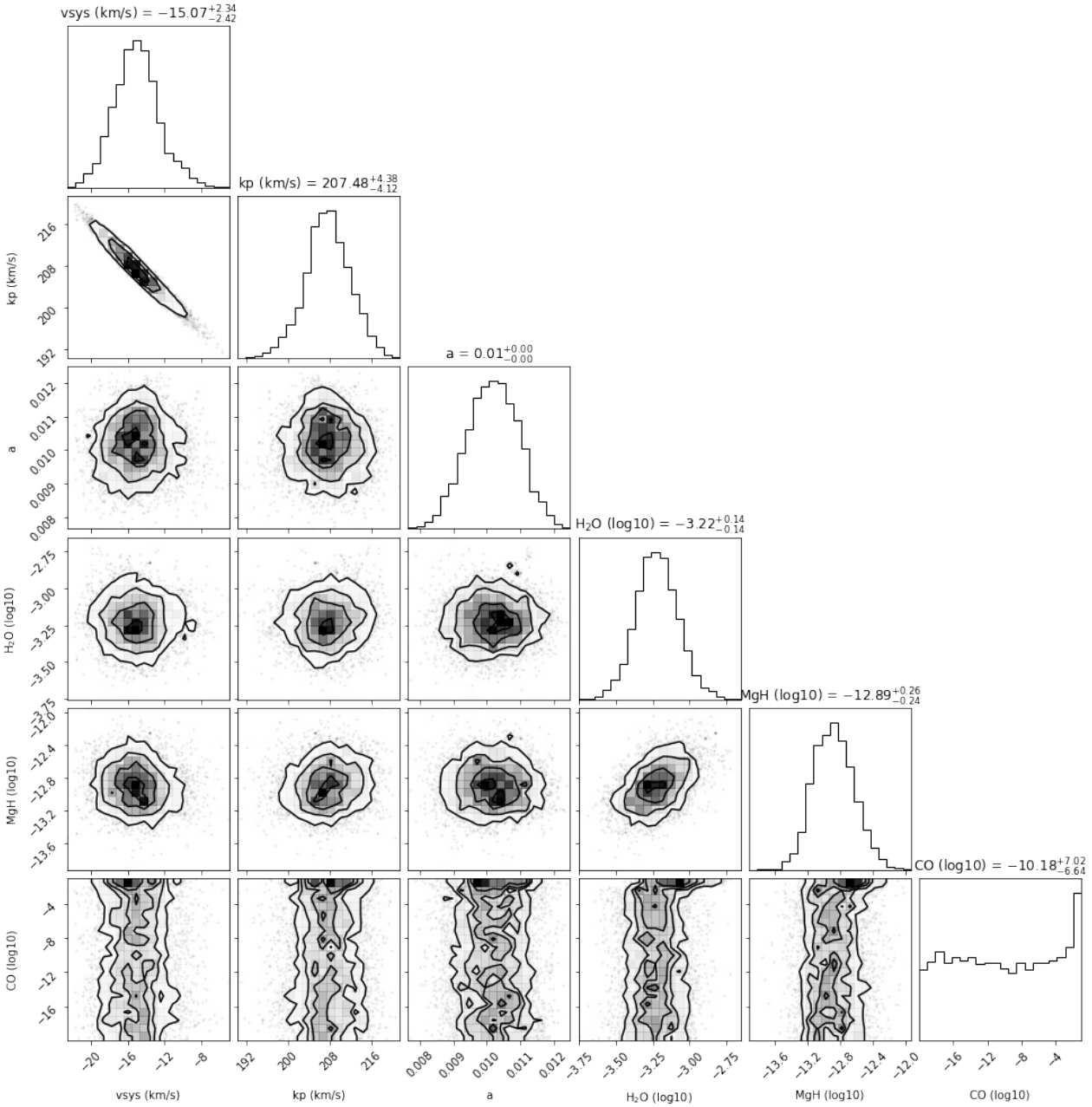

Figure 2.7: An example of the an MCMC fit to the residuals of the simulated data. Using PICASO to create the model spectra, the abundances of H_2O, MgH and CO have been fit to the residuals along with the systemic velocity, vsys, projected orbital velocity, kp and a scaling parameter, a (see Gibson et al. 2020) which uniformly scales the model spectrum in order to account for unmodeled effects. The histograms show the posterior distributions of each parameter. A peaked distribution indicates that parameter has been constrained. The rest of the panels show the joint posterior distributions of each pair of parameters. A circular residual indicates that the parameters are uncorrelated with each other. Kp and Vsys show an elongated joint posterior distribution as these two parameters are correlated which was also seen in the elongated shape of the detection in the Kp-Vsys plots. A random or uniform residual, for example those in the bottom row, indicate that one or both of the parameters is not well constrained. As H_2O and MgH were detected in the cross-correlation analysis, it makes sense that the MCMC fit was able to constrain their abundances. Since CO was not detected, its abundance is not well constrained.

of the planet's spectrum to isolate it, molecule mapping uses the spatial separation of the planet and star and localisation of the planet's spectrum in the image to isolate it. Since most of the spaxels will be dominated by the stellar and telluric spectra, these can be used as a reference to remove the contamination from the exoplanet's spectrum.

2.3.1 The Observations

This technique requires a spectrum to be taken for each spaxel in an image which requires an instrument such as an Integral Field Unit (IFU) or Long-Slit Spectrograph. The star-planet system must be resolved in this image so that they appear on different spaxels – placing an upper limit on their size and a lower limit on the primary mirror size.

As with HRCCS, the spectral lines must be resolved which puts a lower limit on the spectral resolution. However, unlike with HRCCS, the planet's Doppler shift need not change significantly. It is still recommended that the stellar and planet's spectral lines be separated in wavelength from each other – which places limits on the velocity of the planet. Additionally, there must be some spaxels where the stellar spectrum dominates significantly over the planet's spectrum. However, given the extreme contrast ratio between exoplanets and their host stars, this is usually the case.

Finally, the spectrum of the planet must be bright enough that it could be detected with these observations. That is, the stellar suppression via HCI+HRCCS at the planet's location is sufficient that its spectrum could be characterised within a reasonable amount of integration time. This is can be estimated using the following equation (modified from Snellen et al. 2015) assuming the planet's lines are not overlapped by the stellar lines or the tellurics and that the photon noise is the dominant noise source on the planet's spectrum:

$$S/N_p = C \times \sqrt{K} \times S/N_s \times \sqrt{N_{lines}} \times \sqrt{N_{obs}} \tag{2.3}$$

where S/N_p is the signal-to-noise of the recovered exoplanet's signal. As before, C is the ratio of the planet's brightness to that of the star (contrast), however there is now a factor K which is the factor by which the star's flux is reduced at the planet's location compared to its peak[6]. S/N_s is the average signal-to-noise of the stellar spectrum on the spaxel of its peak flux. Again, N_{lines} is the number of spectral lines in the observed exoplanet's spectrum and N_{obs} is the number of observations. As with the equivalent for HRCCS observations, this metric typically overestimates the signal-to-noise as it assumes photon noise is the dominant noise source and that there is no interference from the stellar or

[6]That is if the star is 10 times brighter than the planet, then $K = 10$

telluric lines. For molecule mapping observations, photon noise may not be the dominant noise source on the exoplanet's spaxel due to, for example, thermal background (Parker et al. 2024) or read noise (Vaughan et al. 2024). To robustly estimate the signal-to-noise, detailed instrumental simulations are needed such as those presented in Vaughan et al. (2024) (see Chapter 4).

2.3.2 Isolating the Exoplanet's spectrum

If observations have the properties discussed in Section 2.3.1, it is again possible to isolate the planet's spectrum from the contaminating stellar and telluric spectra. This is done by using the spaxels that do not contain the planet's spectrum to create a model of the contamination which can be scaled and removed from all spaxels. First observations typically undergo standard calibrations such as bad detector pixel correction and the spectra are extracted from the image on the detector. After this there is some variation in the techniques used to remove the contamination. The following summarises the main steps however, it should be stressed that these are not in sequential order since the literature is diverse in the implementation and order of the steps used.

Removing tellurics through model fitting. The tellurics are modeled using a line-by-line radiative transfer model and are fit to a reference spectrum. This spectrum is usually obtained by averaging the spectra near the peak of the star's flux. The model is then divided out from the data since the telluric transmission has a multiplicative affect on the spectra (Bryan et al. 2017; Petit dit de la Roche et al. 2018; Inglis et al. 2024; Kiefer et al. 2024).

Removing a representative spectrum from the image. This step is often employed to remove the majority of the contaminating stellar spectrum and the tellurics if they have not already been removed (Snellen et al. 2014; Schwarz et al. 2016; Hoeijmakers et al. 2018b; Petit dit de la Roche et al. 2018; Wang et al. 2018b; Haffert et al. 2019; Cugno et al. 2021; Petrus et al. 2021; Kiefer et al. 2024; Landman et al. 2024; Parker et al. 2024). A representative spectrum is created by computing the mean or median spectrum in some region of the image e.g. the peak of the star's flux. Next the continuum flux in each spaxel is estimated – often using a high pass filter – and the combined continuum and representative spectrum is subtracted from the image. Some works also scale the resolution of the reference spectrum or include wavelength offsets to better remove it from all the spaxels in the image (Snellen et al. 2014; Schwarz et al. 2016; Landman et al. 2024; Parker et al. 2024).

Removing a representative background spectrum. While the stellar spectrum will vary in flux strength across the spaxels, the sky background will be broadly the same given the small field of view. This background can be estimated by creating a representative spectrum of spaxels far away from

the planet and star's positions. This representative spectrum can then be subtracted to remove the background spectrum (e.g. Kiefer et al. 2024).

Non-parametrically removing trends with algorithms. As with HRCCS, there may be residual trends in the data that are not currently modeled. These can be removed with algorithms such as PCA or SYSREM which can identify common components in the spectra of all spaxels without any apriori information on their functional form (Hoeijmakers et al. 2018b; Wang et al. 2018b; Haffert et al. 2019; Cugno et al. 2021; Landman et al. 2024; Parker et al. 2024). A related technique called spectral unmixing builds up a model of the data from a set of spectra with the largest differences to each other (Rameau et al. 2021). If the planet's spectrum is bright enough, one or more of the spectra should be representative of it – isolating it from the rest of the data.

Derotation to align the planet's signal. Depending on the instrumental set up, it is possible that the position of the planet on the detector will change over time due to the rotation of the sky in the field of view (pupil tracking). If this is the case, the images will need to be derotated so that the planet's spectrum is localised in one place (Hoeijmakers et al. 2018b). Pupil tracking mode is used as the speckles in the PSF will remain stationary in the image while the planet will move. This aids in the removal of the speckles and the isolation of the planet. The disadvantage is that, for planets with unknown positions, this rotation could move it behind the central obscuration (see Chapter 4).

2.3.3 Extracting the Exoplanet's Spectrum

After the contamination has been removed, what is ideally left over is the planet's spectrum, present in one of the spaxels[7], and photon noise. Figure 2.8 shows an example of a simulated observation before and after the data reduction. This was created by taking a PHOENIX spectrum (Husser et al. 2013) with an effective temperature $5400\,\mathrm{K}$, logg$= 4.5$ and solar metalicity which was multiplied by an Airy function with a spatial sampling of $1.22/5 \times \lambda/D$. The planet's model, which is for a planet with a hydrogen/helium dominated atmosphere with water, multiplied by an Airy function was then added to the spaxels with its peak separated from the star. Photon noise was added assuming the peak of the stellar psf has a signal-to-noise of 200. To simulate reduced data, a perfect model of the injected spectrum without noise was subtracted from the data to serve as an example of what the data reduction techniques aim to achieve.

Depending on the brightness of the planet, its spectrum may not be clearly distinguished from the residual photon noise and therefore cannot be fit directly. As with HRCCS, a cross-correlation with a

[7] In the case of HARMONI@ELT in Chapter 4 the spectrum will actually be present in a few spaxels as they over sample the spatial resolution.

model of the planet's spectrum can combine its signal and reveal its presence within the residuals. The cross-correlation is defined as before (see Section 2.2.3):

$$C(v) = w\frac{\sum_\lambda (m_\lambda(v) - \bar{m}(v))(r_\lambda - \bar{r})}{\sqrt{\sum_\lambda (m_\lambda(v) - \bar{m}(v))^2 \sum_\lambda (r_\lambda - \bar{r})^2}} \tag{2.4}$$

however, $C(v)$ is now the cross-correlation coefficient for a given spaxel where r is the residual spectrum from that spaxel. The weighting factor w applies equally to all spaxels in a given observation. It can be used to change how different observations are combined by weighting them differently e.g. by down weighting observations with low signal-to-noise.

Figure 2.8 also shows an example detection with molecule mapping by cross-correlation with the same model of the planet's spectrum that was used in the simulation. The signal-to-noise is calculated by dividing each spaxel by the standard deviation in the cross-correlation coefficients as a function of velocity, excluding the velocities where the planet's signal is expected. The localised increase in the signal-to-noise at the right velocity at spatial location indicates the presence of the planet. This example assumes that the planet does not move significantly between observations such that its position and velocity do not change.

While this is a reasonable assumption for widely separated planets, for shorter period planets the velocity and spatial location of the planet may change between observations and may not be known apriori. If this is the case then an algorithm such as K-Stacker which searches through different Keplerian orbits to maximise the signal (Nowak et al. 2018; Le Coroller et al. 2020) can be used to detect it. However, this can only be used for nearby star systems and may be subject to false positives. Alternatively, as discussed later in Section 4, observations could be chosen to target one of the quadrature points to guarantee the planet has the same position and velocity. This avoids the need to fit for the orbit but requires the observations to be taken within relatively small time windows.

2.3.4 Atmospheric retrievals

As with HRCCS, cross-correlation can determine which molecules are present in detectable levels in the exoplanet atmosphere as well as infer other parameters such as the rotation rate of the planet and its orbital velocity (Snellen et al. 2014; Schwarz et al. 2016; Hoeijmakers et al. 2018b; Petit dit de la Roche et al. 2018; Wang et al. 2018b; Haffert et al. 2019; Cugno et al. 2021; Petrus et al. 2021; Kiefer et al. 2024; Landman et al. 2024; Parker et al. 2024). However, just with cross-correlations, it is not possible to robustly measure molecular abundances or combine the results with other techniques. This requires an atmospheric retrieval with the likelihood method (Ruffio et al. 2019) where the cross-correlation

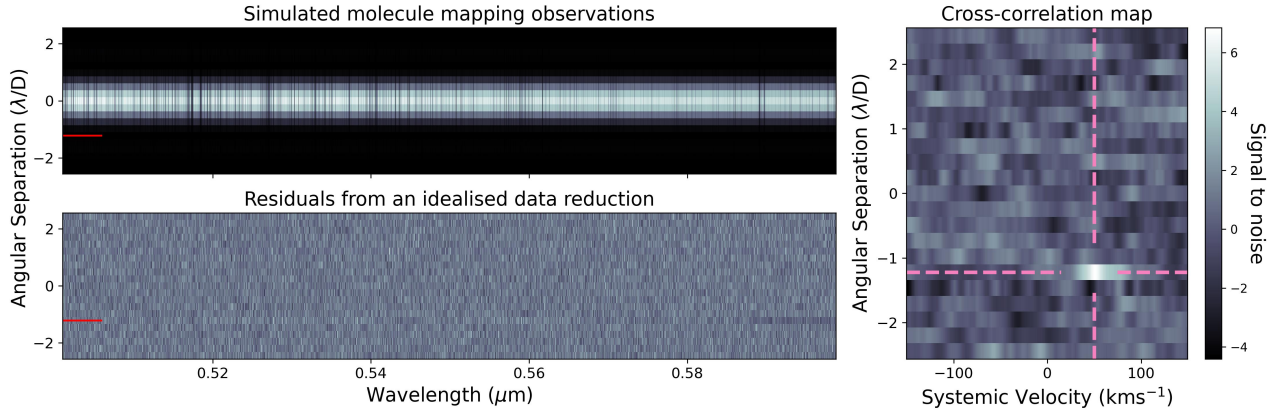

Figure 2.8: A demonstration of the Molecule Mapping technique. The top left panel shows simulated observations with a slit spectrograph meaning that the y-axis represents the spaxels measured along their angular separation while the x-axis represents wavelength. The bottom left plot shows the residuals of the simulated data after an idealised data reduction. The residuals have been normalised by their standard deviation but the planet's spectrum (located in the spaxel marked with a red line) is still not clearly visible. The right panel shows the cross-correlation map with the spaxel position on the y-axis and the Doppler shift of the model on the x-axis. A localised increase (lighter colours) in the cross-correlation coefficients is seen at the position and Doppler shift of the planet.

becomes part of the likelihood function.

In the likelihood method, the data are reduced using steps similar to those described here in Section 2.3.2, however, the contamination is not removed. Rather the amplitudes of representative spectra – e.g. the stellar and/or telluric spectra, and PCA components – on the spaxel(s) containing the planet's spectrum become part of an MCMC fit along with a forward model of the planet's spectrum. This avoids over subtraction of the planet's spectrum and allows some sensitivity to the continuum of the planet's spectrum which is otherwise lost in the normalisation process (Ruffio et al. 2021). This MCMC fit also constrains the atmospheric parameters such as the effective temperature, surface gravity, metalicity and rotation rate (Wilcomb et al. 2020; Ruffio et al. 2021; Agrawal et al. 2023; Landman et al. 2024).

3 | Mirror in the desert: Characterising the reflection of LTT-9779 b with the world's largest optical telescope

3.1 Overview

This chapter shows my current work towards the characterisation of the highly-reflective exoplanet LTT-9779 b with High-Resolution Cross-Correlation Spectroscopy (HRCCS). This analysis uses data obtained from my observing program (112.25T7) on ESPRESSO@VLT in 4UT mode, which combines all four of the VLT's unit telescopes into the worlds largest optical telescope. This work is not finalised, however the results from the initial cross-correlation analysis which aimed to identify which species are detectable in the planet's spectrum are shown. While not the main goal of this work, I also show a re-measurement of the orbit of the planet using these and archival observations which improves upon previous measurements.

To analyse these data, the planet's atmosphere had to be modelled in order for model spectra to be generated. For the planet's model, I use the temperature-pressure profile measured for the planet using JWST kindly provided to me by Micheal Radica and Jake Taylor. I also use atmospheric profiles generated using HELIOS (Malik et al. 2017) and kindly provided to me by Chloe Fisher. To generate the model spectra, I use PICASO (Batalha et al. 2019) at high spectral resolution with opacities provided to me by Natasha Batalha.

3.2 Motivation

LTT-9779 b is a rare example of an intermediate-mass ($M \approx 29 M_{\oplus}$), ultra-short period (P ≈ 0.79d) planet (Jenkins et al. 2020, see Table 3.1). It resides in the Neptune desert (see Figure 3.1) where it is expected to have undergone rapid photo-evaporation (e.g. Lopez 2017). Ordinarily, this should have stripped it of its atmosphere and pushed it out of the desert within 100Myrs (Owen et al. 2016). However, measurements of the current XUV flux of LTT-9779 indicate that this star may have instead had relatively low XUV emission throughout its life, insufficient to completely evaporate the atmosphere of LTT-9779 b (Fernandez Fernandez et al. 2023). Additionally, observations with the Transiting Exoplanet Survey Satellite (TESS), Spitzer and the CHaracterising ExOPlanet Satellite (CHEOPS) show this planet has an unusually high albedo ($A_B = 0.72^{+0.12}_{-0.12}$; Crossfield et al. (2020)[1]; $A_g = 0.80^{+0.10}_{-0.17}$;

[1] A_B is the Bond albedo which is the fraction of the power of the incident radiation on an astronomical body that is scattered back out into space.

Hoyer et al. (2023)[2]). This could be due to the presence of clouds which would cool the planet via their high albedo and may further protect this world from atmospheric loss (Parmentier et al. 2016).

So far atmospheric characterisation of this world has been limited to photometric or low spectral resolution ($R < 1000$) observations. Spitzer observations reveal CO absorption and favour a non-inverted temperature pressure profile (Dragomir et al. 2020), unusual since planets as hot as LTT-9779 b typically have temperature inversions (Baxter et al. 2020). Transit observations with Hubble's Wide Field Camera 3 have limiting constraining power but showed evidence for H_2O, CO_2, and FeH absorption (Edwards et al. 2023a,b). Additionally, a non-detection of the $1.083\,\mu\mathrm{m}$ helium line with both Hubble and WINERED/Magellan II indicates there is presently no significant atmospheric loss (Edwards et al. 2023a; Vissapragada et al. 2024). Finally, transit JWST NIRISS/SOSS observations show muted transmission features but retrievals were unable to distinguish between very sub-solar (< 0.1x solar) metallicity, super-solar metallicity and low-pressure (Pcloud ≤ 1 mbar) clouds, and an extremely high (> 500x solar) metallicity since the spectra for these different scenarios are indistinguishable at low resolution given the signal-to-noise of the measured spectrum (Radica et al. 2024).

At high spectral resolution, spectral features can be strongly affected by clouds and are sensitive to their properties. To exemplify this, I create a number of simple planet spectra using the method described in Section 3.6 with varying cloud deck height. These are shown in Figure 3.2 and demonstrate that the width and depth of the spectra lines is strongly affected. To put this theory into practice, high-spectral resolution observations of LTT-9779 b were obtained (see Section 3.3).

This planet is amenable to HRCCS characterisation (see Section 2.2) so I observed it with the high resolution optical spectrograph: the Echelle SPectrograph for Rocky Exoplanets and Stable Spectroscopic Observations (ESPRESSO; Pepe et al. 2021) on the Very Large Telescope (VLT) at Paranal Observatory, Chile.

3.3 Observations

I observed LTT-9779 for four half nights, each covering a secondary eclipse of LTT-9779 b, using ESPRESSO@VLT. These observations were taken in 4UT mode which combines the light from all four unit telescopes, seen in Figure 3.3, resulting in an effective primary mirror diameter of $16.4\,\mathrm{m}$. In 4UT mode, ESPRESSO covers a continuous wavelength range from $380\,\mathrm{nm}$ to $788\,\mathrm{nm}$ at a spectral resolution of $R = 70,000$.

[2] A_g is the geometric albedo which is the ratio of the brightness seen from the light source compared to that of an Lambertian disk with the same cross-section.

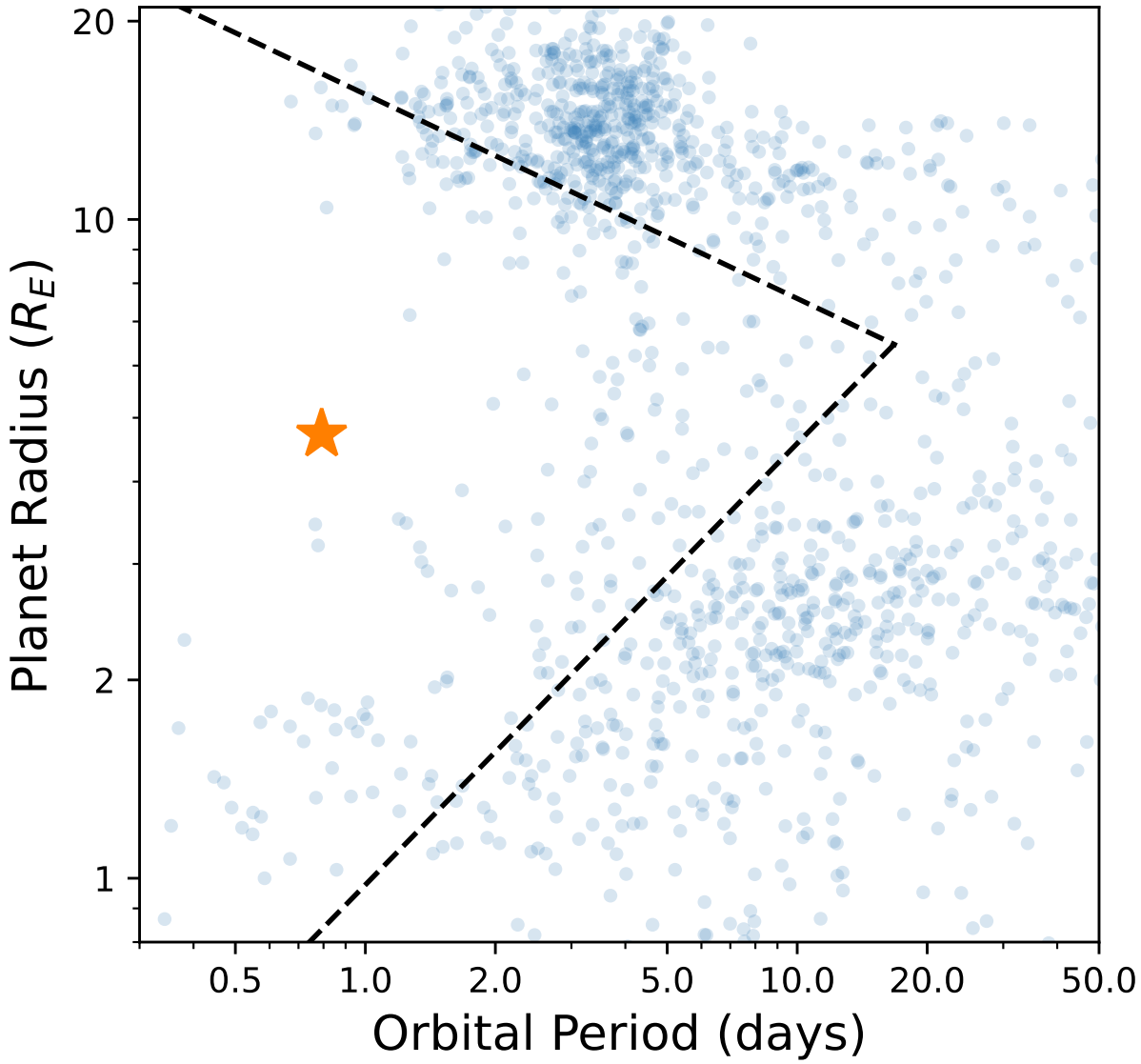

Figure 3.1: The Neptune desert is predicted to be caused by photoevaporation stripping the atmospheres of lower mass planets if they orbit too close to their host stars. This leaves two distinct populations of exoplanets on short orbital periods, those that were massive enough to retain their atmospheres and those that have been eroded to their rocky cores. These distinct populations can be seen in the above plot of the orbital periods and planetary radii of planets in the NASA Exoplanet Archive (Akeson et al. 2013). LTT-9779 b, indicated by the star, and is one of a few planets that resides between these populations. The dashed lines indicate the borders of the Neptune dessert as described by Mazeh et al. (2016).

Table 3.1: A summary of the parameters of the LTT-9779 system.

LTT-9779	Jenkins et al. (2020)	Edwards et al. (2023a)	this work
Mass ($M_\odot$)	$0.770^{+0.290}_{-0.210}$	$1.02^{+0.02}_{-0.03}$	-
Radius ($R_\odot$)	$0.949^{+0.006}_{-0.006}$	$0.949^{+0.006}_{-0.006}$	-
Temperature (K)	5443^{+14}_{-13}	5480^{+42}_{-42}	-
Stellar Type	G7V	-	-
Age (Gyr)	$1.9^{+1.7}_{-1.2}$	$2.0^{+1.3}_{-0.9}$	-
LTT-9779 b			
Mass ($M_\oplus$)	$29.32^{+0.78}_{-0.81}$	$29.32^{+0.78}_{-0.81}$	-
Radius ($R_\oplus$)	$4.72^{+0.23}_{-0.23}$	$4.72^{+0.23}_{-0.23}$	-
Effective Temperature (K)	1978^{+19}_{-19}	1978^{+19}_{-19}	-
Semi-major axis (au)	$0.01679^{+0.00014}_{-0.00012}$	-	
Period (d)	$0.7920520^{+0.0000093}_{-0.0000093}$	$0.79206410^{+0.00000014}_{-0.00000014}$	$0.792064276^{+0.000000115}_{-0.000000119}$
Transit Midpoint (d)	$2458354.21430^{+0.00025}_{-0.00025}$	$2459043.310602^{+0.000090}_{-0.000090}$	$2459043.310666^{+0.000114}_{-0.000113}$
Argument of Periastron (degree)	-	-	218^{+14}_{-18}
Eccentricity	0	< 0.058	$0.00992^{+0.00230}_{-0.00212}$
Inclination (degrees)	$76.39^{+0.43}_{-0.43}$	$76.39^{+0.43}_{-0.43}$	$75.12^{+0.07}_{-0.06}$

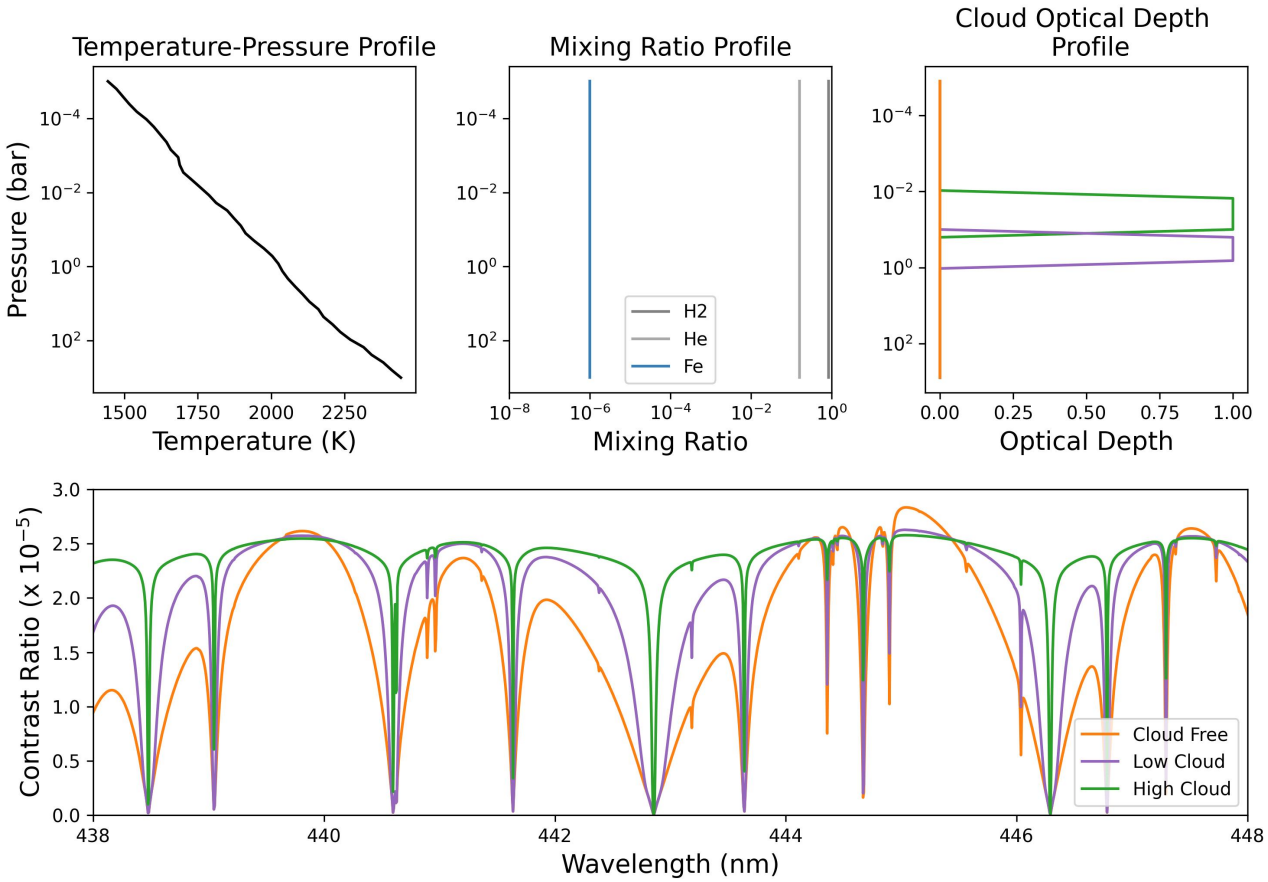

Figure 3.2: Several example spectra generated as in Section 3.6 demonstrating the effect of clouds on a high resolution spectrum. The top panels show the atmospheric conditions assumed in these model spectra, which are shown in the bottom panel. The spectral lines present in this section of the spectrum are those produced by Iron. The cloud depth height causes a marked difference in the spectral line widths and depths.

Figure 3.3: The Very Large Telescope in Chile with me in the foreground for scale. The four unit telescopes are contained within the four large domes. There are additional telescopes to this on site one of which can be seen in the background of this image. Image credit: Jayne Birkby, 10th October 2023.

Table 3.2: A summary of the LTT-9779 eclipse observations. The average S/N of order 47 is quoted as this contains the peak of LTT-9779's blackbody spectrum.

Date	Integration time (s)	Number of frames (pre-eclipse/post-eclipe)	S/N of order 47
10-10-2023	300	64 (28/26)	171
14-10-2023	200	89 (32/44)	170
21-10-2023	200	43 (43/0)	153
17-11-2023	200	76 (43/19)	153

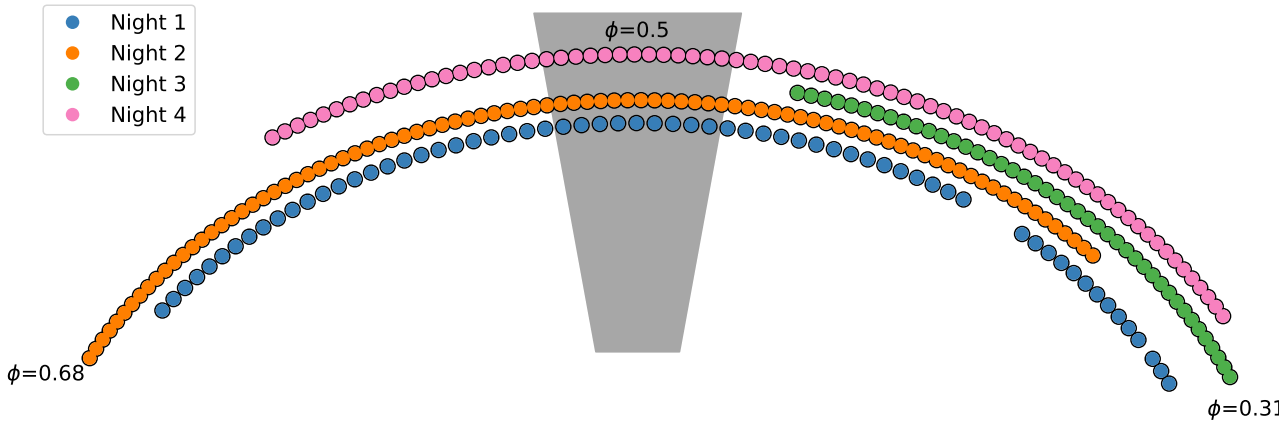

Figure 3.4: The phases of LTT-9779 b, assuming the ephemeris from Edwards et al. (2023a), covered by these observations. Each coloured circle represents an observation taken and the shaded area indicates the secondary eclipse of the planet. In this figure, time runs from right to left.

I used an integration time of 300 s during the first night of observations as poorer seeing conditions meant there was little risk of saturation. For subsequent nights, I used an integration time of 200 s to ensure saturation was not reached. The third night of observation had to be halted due to precipitation at the VLT site and was not restarted. A summary of the observations is given in Table 3.2, and Figure 3.4 shows the phases of LTT-9779 b during these observations. I extracted the calibrated spectra from the raw data using the standard ESPRESSO pipeline (Pepe et al. 2021).

3.4 Refitting the orbit

A planet's ephemeris, which determines its orbit, loses precision over time primarily due to uncertainty in the orbital period. There are three ephemerides for this planet, Jenkins et al. (2020) used TESS sector 2 and NGTS light curves along with HARPS and CORALIE radial velocity measurements to calculate the initial ephemeris for this planet. More recently, Edwards et al. (2023a) used TESS sector 2, 29 and 69 along with Spitzer and HST light curves as well as the same HARPS and CORALIE radial velocity measurements to update the ephemeris whereas Kokori et al. (2023) just used the TESS light curves

as part of a large survey to update the ephemerides of 450 planets. Figure 3.5 shows the predicted secondary eclipse times for each ephemeris assuming a circular orbit as well as the uncertainty in the secondary eclipse midpoint for each night of the ESPRESSO observations.

The Jenkins et al. (2020) ephemeris has large uncertainties when propagated through to the days of the ESPRESSO observations and it would not be possible to do a HRCCS analysis with this ephemeris. The Edwards et al. (2023a) and Kokori et al. (2023) ephemerides have one sigma errors corresponding to $\simeq 30\,\mathrm{s}$ when propagated to the days of the observations and their predictions of the midpoint are within $\simeq 30\,\mathrm{s}$ of each other. Assuming a circular orbit for this planet, $30\,\mathrm{s}$ corresponds to a difference in the planet's velocity of $\simeq 0.7\,\mathrm{km\,s^{-1}}$ at secondary eclipse or roughly one sixth of a resolution element for ESPRESSO 4UT spectra. This may cause small offsets in the detection in a 'Kp-Vsys' map but should be sufficiently accurate to not hinder the analysis.

A larger problem is the eccentricity which has not been constrained by any of the previous works. Even small eccentricities $\simeq 0.01$ could result in changes on the order of kilometers per second in the planet's velocity when compared to a circular orbit. This could significantly affect the alignment of the signal in the 'Kp-Vsys' map and reduce the overall detection significance possibly to a point where the detection is no longer significant.

ESPRESSO was originally designed to precisely measure the radial velocities of stars over long baselines in order to detect small changes in the stellar radial velocity induced by planets. As such, one of the standard outputs of the ESPRESSO pipeline is the measured radial velocity of the star for each observation. The radial velocities for this data set are shown in Figure 3.6 where there is a clear trend in each observation. This is the radial velocity wobble of LTT-9779 induced by LTT-9779 b. The previous radial velocity and light curve observations are not sensitive to small eccentricities however the radial velocity data from the ESPRESSO observations could be, due to its fine temporal sampling.

To determine if the eccentricity can be measured with this radial velocity data, I refit the planet's orbit. It is not possible to robustly constrain the orbit with just the ESPRESSO eclipse data as the radial velocities are limited to phases near secondary eclipse and a more complete sampling of the orbit is needed to avoid degeneracies. To create a more complete radial velocity curve, I extracted the radial velocities from three nights of ESPRESSO transit observations (PI: Ramirez Reyes, Program ID:108.22FQ) using the same method as for my data. I also included the tabulated radial velocities from HARPS presented in Jenkins et al. (2020) but not the CORALIE values as these have much larger errors. Additionally, I extracted the short cadence ($<$ 2mins) TESS light curves for this star using the `lightkurve` python package (Lightkurve Collaboration et al. 2018).

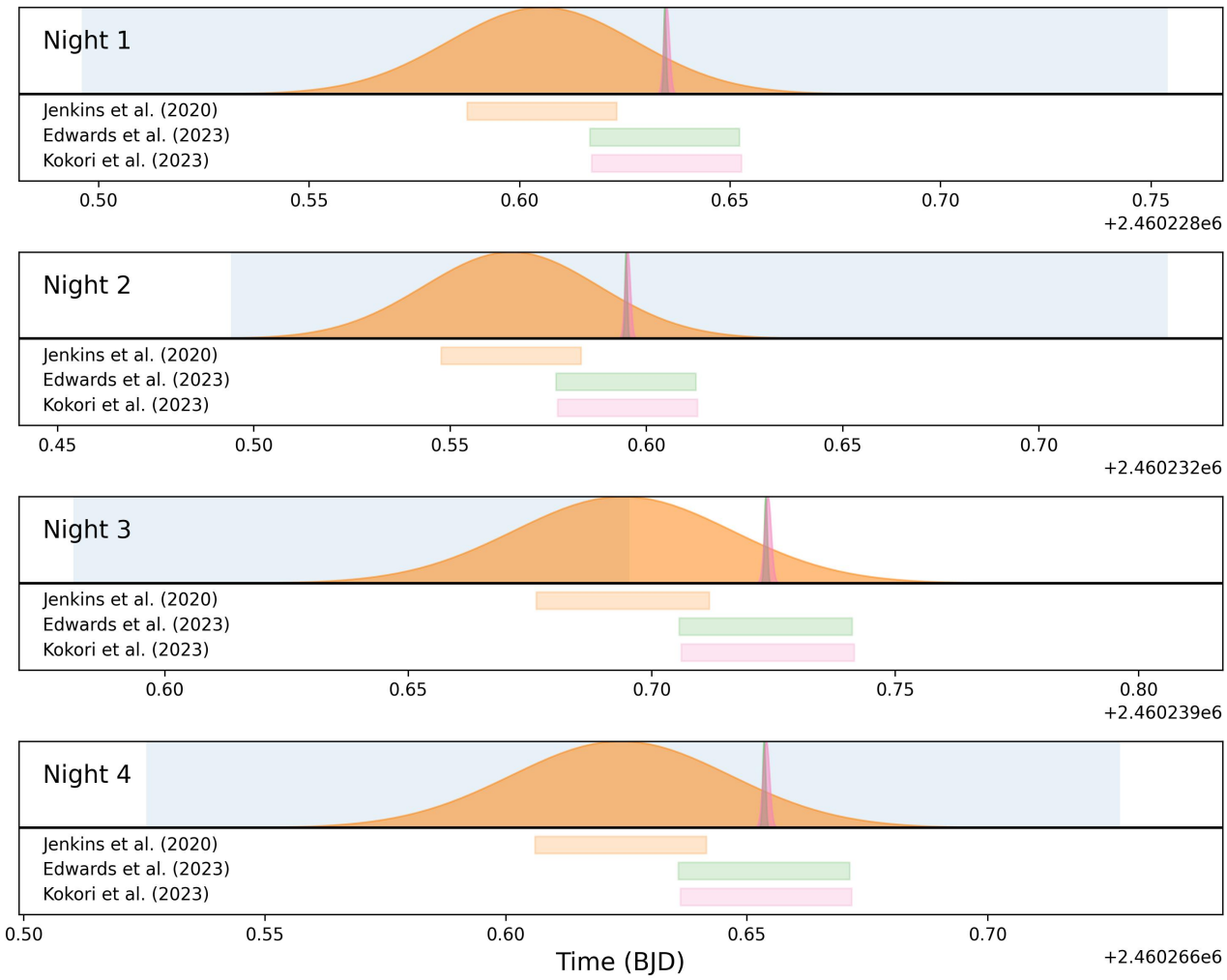

Figure 3.5: The predictions of the three ephemerides for LTT-9779 b for the nights of the ESPRESSO observations listed in Table 3.2. The top part of each panel shows the observations as the blue shaded region. The shaded Gaussian's show the predicted midpoint of the secondary eclipse and its propagated error for each of the ephemerides. The shaded regions on the bottom part of each panel shows where the secondary eclipse is predicted to be for each ephemeris. The Jenkins et al. (2020) ephemeris has large uncertainties and predicts a different secondary eclipse time to the other two ephemerides however the two newer ephemerides are in agreement and are have small enough errors that they could be used in the HRCCS analysis.

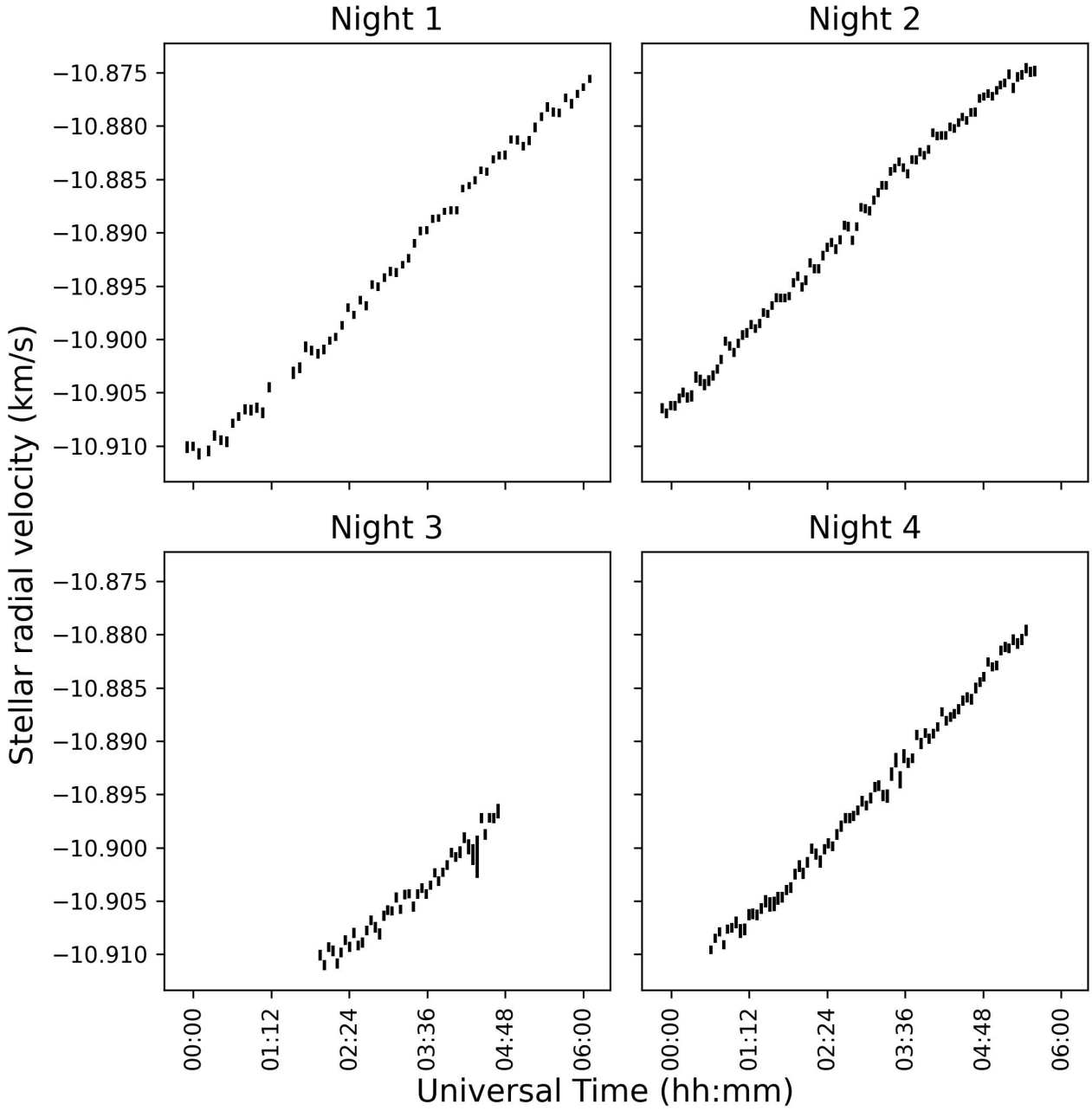

Figure 3.6: The radial velocity of LTT-9779 as measured by the ESPRESSO pipeline for the observations listed in Table 3.2. There is a clear trend in each night's data. This is the reflex motion of LTT-9779 induced by LTT-9779 b and it can be used to measure the latter's orbit.

Both the stellar radial velocities and light curve were modeled with the `exoplanet` python package (Foreman-Mackey et al. 2021) and fit to the data with the `pymc3` package (Salvatier et al. 2016). The parameters and priors of the fit are summarised in Table 3.3. For the orbital period, transit midpoint, semi-amplitude and inclination, I chose to fit a deviation from the value of Edwards et al. (2023a) as the difference is expected to be small. While ESPRESSO is an exceptionally stable spectrograph, the velocity measured may drift over time. Therefore, an additional constant offset in velocity is fitted to each night of ESPRESSO observations in addition to an offset for the HARPS data. The light curve also included additional parameters for the limb darkening parameters of the star and the depth of the transit.

The posterior distributions of the orbital parameters are listed in Table 3.3 and shown in Figure 3.7. Figure 3.8 shows the phase folded radial velocities and light curve against the best fit model for the orbit. Figure 3.7 shows that the orbital parameters of LTT-9779 b are well constrained with the exception of the position angle of the ascending node. This parameter represents a rotation on-sky of the system to which neither transits nor radial velocities are sensitive, therefore the lack of constraint is expected. The orbital parameters are consistent with the literature (Jenkins et al. 2020; Edwards et al. 2023a; Kokori et al. 2023) although now with reduced errors due to the additional data. These data have also allowed me to constrain the eccentricity to a small but non-zero value along with the associated argument of periastron. While small, this eccentricity causes a $\pm 2\,\mathrm{km\,s^{-1}}$ change in the velocity of the planet compared to a circular orbit which is comparable to the spectral resolution of ESPRESSO ($4\,\mathrm{km\,s^{-1}}$ in 4UT mode). Therefore, I included it and the updated orbital parameters in the analysis.

Interestingly the ESPRESSO velocity offsets change more than would be expected over time which may indicate the presence of a long period companion to LTT-9779. This could explain the eccentricity of LTT-9779 b's orbit, however further investigation is required to confirm this hypothesis. If there is an additional companion in the system, its contribution to the radial velocity could bias the orbital fit for LTT-9779 b. However, since the eclipse observations were all taken within a month of each other and radial velocity offsets increase throughout this time, it is likely the orbital period is significantly longer than that of LTT-9779 b and so this bias should be small.

3.5 Cleaning the data before cross-correlation

The 1D spectra extracted from the raw 4UT data using the ESPRESSO pipeline must be cleaned to remove the contaminating stellar spectrum and tellurics using some of the techniques described in Section 2.2.2. For this data set, I used the following process, exemplified in Figure 3.9, for each night

Orbital Parameters	Prior	Posterior
Orbital period (days)	$0.79206410 + U(-7, 7) \times 10^{-7}$	$0.79206410 + 1.76^{+1.15}_{-1.19} \times 10^{-7}$
Transit midpoint (JD)	$2459043.310602 + U(-35, 35)/86400$	$2459043.310602 + 5.50^{+9.88}_{-9.72}/86400$
Semi-amplitude of the star's velocity ($\mathrm{m\,s^{-1}}$)	$19.65 + U(-2, 2)$	$19.65 + 0.454^{+0.093}_{-0.091}$
Eccentricity	$U(0, 0.06)$	$0.00992^{+0.00230}_{-0.00212}$
Argument of Periastron (degree)	$U(0, 360)$	218^{+14}_{-18}
Position Angle of the Ascending Node (degree)	$U(0, 360)$	179^{+123}_{-121}
Inclination (degree)	$76.39 + U(-2, 2)$	$76.39 + -1.27^{+0.07}_{-0.06}$
Other Parameters	Value	
ESPRESSO eclipse observations (112.25T7)		
Velocity offset Night 1 ($\mathrm{km\,s^{-1}}$)	$-10.9 + 0.001 \times U(-50, 50)$	$-10.9 + 0.001 \times 7.24^{+0.09}_{-0.09}$
Velocity offset Night 2 ($\mathrm{km\,s^{-1}}$)	$-10.9 + 0.001 \times U(-50, 50)$	$-10.9 + 0.001 \times 7.24^{+0.09}_{-0.09}$
Velocity offset Night 3 ($\mathrm{km\,s^{-1}}$)	$-10.9 + 0.001 \times U(-50, 50)$	$-10.9 + 0.001 \times 7.60^{+0.10}_{-0.10}$
Velocity offset Night 4 ($\mathrm{km\,s^{-1}}$)	$-10.9 + 0.001 \times U(-50, 50)$	$-10.9 + 0.001 \times 8.28^{+0.10}_{-0.10}$
ESPRESSO transit observations (108.22FQ)		
Velocity offset Night 1 ($\mathrm{km\,s^{-1}}$)	$-10.9 + 0.001 \times U(-50, 50)$	$-10.9 + 0.001 \times -4.81^{+0.19}_{-0.19}$
Velocity offset Night 2 ($\mathrm{km\,s^{-1}}$)	$-10.9 + 0.001 \times U(-50, 50)$	$-10.9 + 0.001 \times -5.39^{+0.14}_{-0.13}$
Velocity offset Night 3 ($\mathrm{km\,s^{-1}}$)	$-10.9 + 0.001 \times U(-50, 50)$	$-10.9 + 0.001 \times -4.46^{+0.15}_{-0.15}$
HARPS observations (Jenkins et al. 2020)		
Velocity offset ($\mathrm{m\,s^{-1}}$)	$U(-50, 50)$	$^{+}_{-}$
TESS light curves		
Light curve continuum	$U(0.9999, 1.0001)$	$1.000036^{+0.000003}_{-0.000003}$
Limb darkening	$U_1(0, 2); U_2(-1, 1)$	$0.442^{+0.388}_{-0.308}; 0.107^{+0.339}_{-0.393}$
Square root of the transit depth	$U(0.01, 0.1)$	$0.0452^{+0.0018}_{-0.0016}$

Table 3.3: The input parameters, priors and the posteriors of the fit to the TESS light curves and the combined radial velocity data from ESPRESSO 1UT transit (PI: Ramirez Reyes, Program ID:108.22FQ) and 4UT eclipse (Program ID: 112.25T7, Table 3.2) observations as well as HARPS data (Jenkins et al. 2020). The priors for the orbital period, transit midpoint, semi-amplitude and inclination were chosen to be roughly five times the width of the one sigma errors from Edwards et al. (2023a) and the upper limit of the eccentricity was also set by the work of Edwards et al. (2023a). All other parameters are given wide uninformative priors. The ESPRESSO velocity offsets are measured relative to $-10.9\,\mathrm{km\,s^{-1}}$ which is the approximate mean of the ESPRESSO radial velocities.

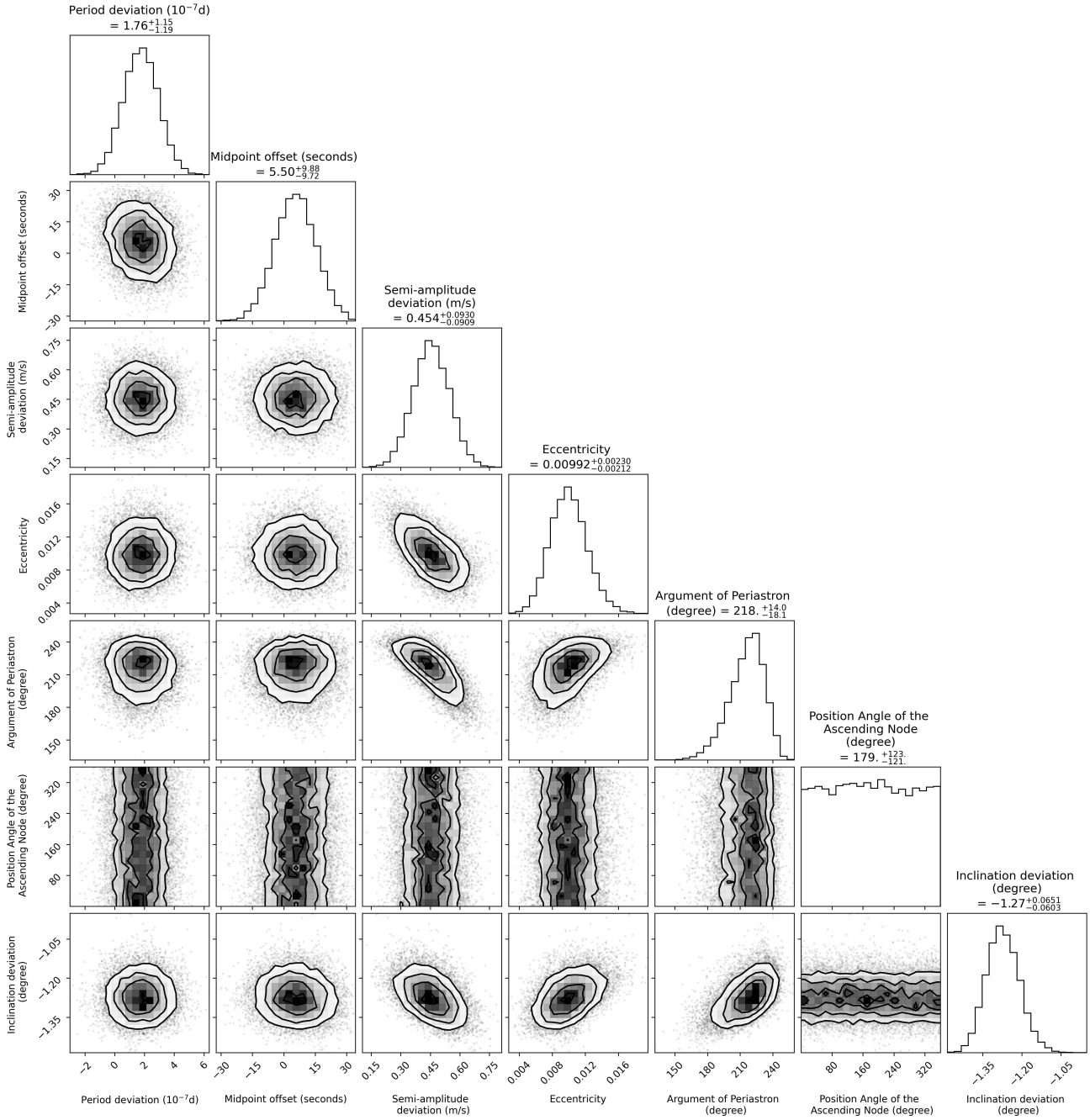

Figure 3.7: The posterior distribution of only the orbital parameters from the fit to the combined ESPRESSO and HARPS radial velocity and TESS light curve data. The histograms show the posterior distribution of each fit parameter and the contour plots show the joint distributions between parameters. Most of the orbital parameters of LTT-9779 b are now well constrained and show little correlation. The exception is the position angle of the ascending node to which this data is not sensitive. The eccentricity is constrained to a small but non-zero value along with the associated argument of periastron allowing the orbit to be modeled with greater accuracy.

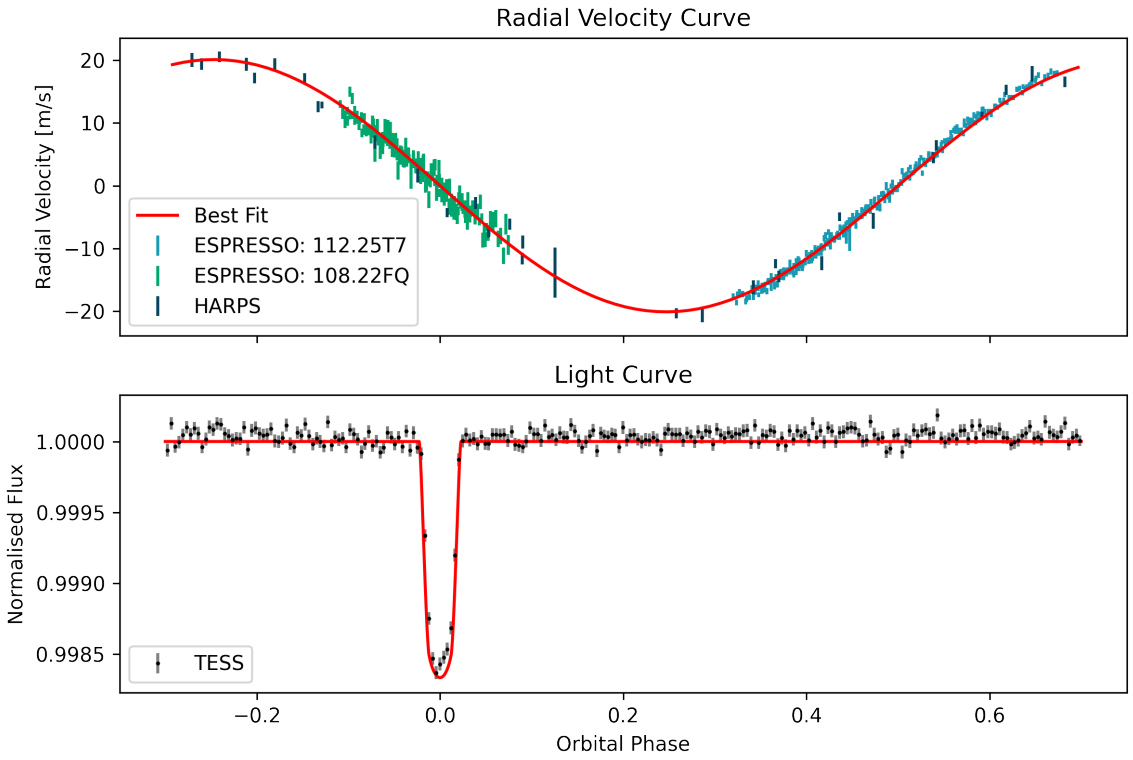

Figure 3.8: **Top panel:** The phase folded radial velocity curve of the combined ESPRESSO and HARPS radial velocities along with the best fit radial velocity curve due to LTT-9779 b's orbital motion. **Bottom panel:** The phase folded and binned TESS light curve with the best fit transit model. The secondary eclipse is too shallow to be visible in these data.

of observations:

1. **Continuum/blaze correction:** Each spectrum was divided by a fourth order polynomial that was fit to the continuum of that spectrum. This removes variations in the throughput as well as corrects for the blaze function of the instrument.

2. **Outlier correction:** Outliers were detected using the blob detection algorithm and interpolated over using nearest good pixels in the dispersion direction (e.g. Kong et al. 2013; Sluijs et al. 2023). I set a strict boundary for outliers at 2.5σ away from the mean after five iterations which flags roughly 1% of pixels ensuring any bad pixels are removed.

3. **Shift to stellar rest frame:** Each spectrum is shifted into the stellar rest frame using the radial velocities computed by the ESPRESSO pipeline. This is accomplished by interpolating each spectrum to a common wavelength grid, taken from the first observation, with a cubic spline. The stellar rest frame was chosen as this optical data is largely dominated by the stellar spectral lines.

4. **Remove the median spectrum:** For Nights 1, 2 and 4, the median spectrum of the observations taken during the planet's secondary eclipse is subtracted from all spectra taken that night. This is not possible for Night 3 as there are no observations during the eclipse (see Figure 1.3) so instead all the median of all observations is subtracted from all spectra taken that night. For all nights, this removes most of the contaminating stellar spectrum.

5. **SYSREM:** To remove any residual contamination, the SYSREM algorithm is iterated ten times on each night of data. The number of iterations used in the analysis is selected on a per night and per order basis at the point at which the change in the standard deviation of the residuals plateaus with increasing numbers of SYSREM iterations as in Spring et al. (in prep). As shown in Figure 3.9, this is chosen as the point at which the change in the standard deviation of the data between SYSREM iterations is within two standard deviations of the changes between iterations five to ten which is a variation of the method in Spring et al. (in prep).

Figure 3.9 shows the results of some of these steps on a section of the spectra from Night 1, Order 75. The data appears relatively clean after step 4 however there are still clear residuals from some of the spectral lines. These are well removed after the first few SYSREM iterations. According the metric for choosing SYSREM iterations, the optimal number for this night and order is four. After this, some bad pixels and columns remain so there are some refinements to be made to this reduction.

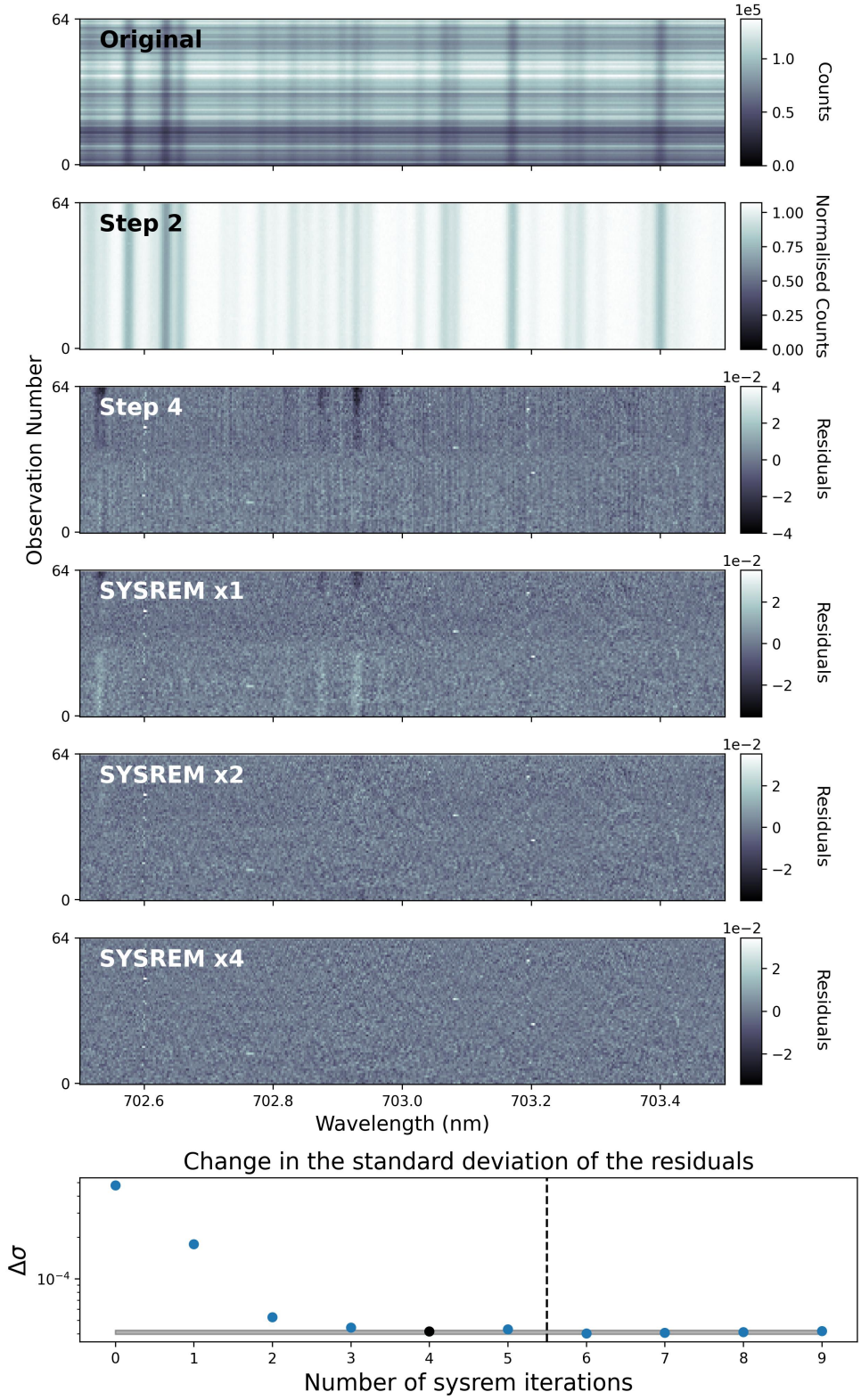

Figure 3.9: An example of how the data reduction removes the contaminating spectra from these data using the steps described in Section 3.5. The top six panels show a section of the data from Night 1, order 75 as it is cleaned. The bottom panel shows how the standard deviation of the residuals change with the number of system iterations used. The mean and standard deviation of the points to the right of the vertical line are measured and the number of SYSREM iterations chosen is the first point to lie within two sigma of this mean (highlighted by the shaded region). For Night 1, order 75 this corresponds to 4 SYSREM iterations. After 4 SYSREM iterations there still appears to be some bad pixels and columns so there are some refinements to be made to this reduction.

3.6 Creating a cross-correlation template

One way to determine if spectral lines from a given molecule are present in a planet's spectrum is to cross-correlate with a model spectrum that only contains the spectral lines from that species. If a detection of the planet is made with such a model, then those spectral lines are in the spectrum[3] and that species is present in the atmosphere. To create a reflection spectrum containing only the spectral lines from a target molecule (plus those of hydrogen and helium) using PICASO (Batalha et al. 2019), I assume the planet's atmosphere is hydrogen-helium dominated with a trace amount of the target molecule with an isotropic distribution in the atmosphere. For the planet's temperature-pressure profile, I use the measured values from Radica et al. (2024). Figure 3.10 shows some examples of the simple spectra generated using this technique along with the atmospheric profiles used to create them. These spectra are generated at a resolution of $R = 70,000$ to match that of the data.

In this initial analysis, I do not include the effect of clouds in the spectrum so the planet's reflection is entirely from Rayleigh scattering. Scattering by clouds primarily affects the continuum of the spectrum as well as the width and depth of the spectral lines but it does not change their positions. Therefore a cloud-free model spectrum will still match with the planet's spectrum if the spectral lines of that species are present, even if the planet is cloudy. The match will not be as good as if the right model was used, however it should be sufficient for an initial test to see if the spectral lines of a given species are present.

During the data reduction, the continuum of the planet's spectrum is removed and so the same must be done with the cross-correlation model. Normally, the high resolution model spectrum would be smoothed using the same process that was performed on the data. However, these simple spectra can have strong band head features that do not smooth well using these techniques which creates artifacts in the cross-correlation. Instead, the high resolution spectrum is divided by a lower resolution ($R = 1,000$) copy of the spectrum. This continuum corrected model is used as the cross-correlation model. This method may over correct the band head features in the spectrum, reducting the depths of the spectral lines in that region as well as alter the line wings of broad spectral lines. A future part of this analysis will investigate whether a lower resolution spectrum or different continuum correction method is better for this analysis.

[3]The spectral lines of molecules are like unique fingerprints, the spectral lines from one species will not match another.

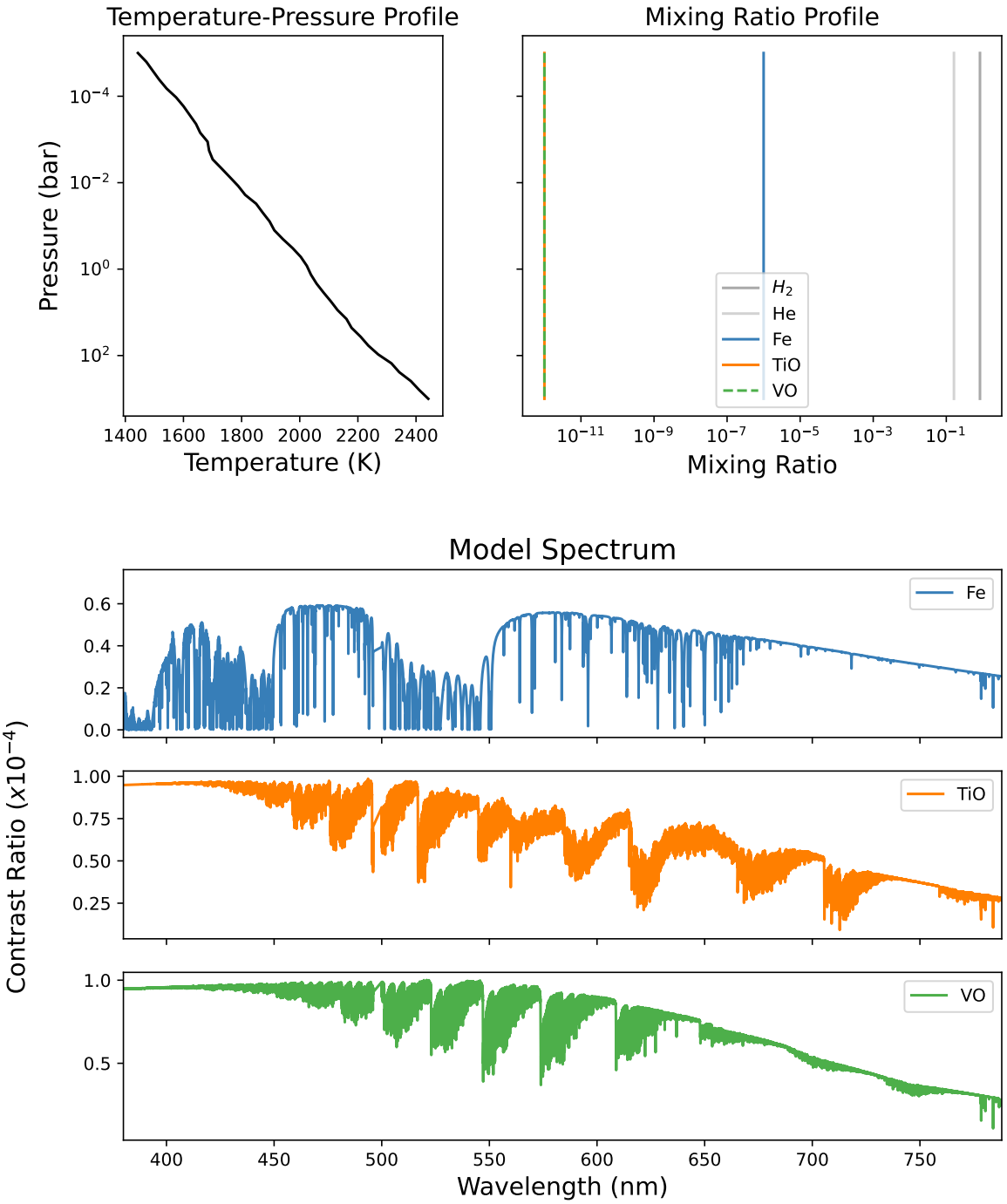

Figure 3.10: Some examples of the template spectra used in this work. The top panels show the atmospheric conditions and the bottom the spectra generated using PICASO at a resolution of $R = 70,000$.

3.7 Initial cross-correlation analysis

The first step towards characterising this planet is determining which molecules are present and detectable in its atmosphere. To do this, I cross-correlate the cleaned data with simple model spectra generated as described in Section 3.6.

To determine which molecules are most likely to be detectable and therefore which to start with, I computed the high resolution spectrum of the planet (R = 70,000) assuming the temperature-pressure profile from JWST data and mixing ratios for chemical equilibrium at solar metalicity (see Figure 3.11). For simplicity, the planet is assumed to be cloud free as this spectrum is only meant to provide an indication of which molecules to search for and not be a perfect model of the planet's spectrum. The chemical equilibrium mixing ratios are generated with HELIOS (Malik et al. 2017) and the associated temperature-pressure profile is also shown. It is worth noting that the temperature profile for the equilibrium chemistry model is different to the one that was measured. HELIOS is a one dimensional, plane-parallel model meaning the associated temperature-pressure profile is the integrated temperature-pressure profile over the planet's day-side. However, the measured temperature-pressure profile is for the day-night terminator. The difference between these indicates that, as expected, this planet is three dimensional object which is more complicated than a one-dimensional, cloud-free, equilibrium chemistry model.

The spectrum of the planet is compared to a similarly generated spectrum with the species of interest removed from the atmosphere. Figure 3.11 shows the difference between these model spectra. The species that produces the largest difference (by an order of magnitude) and has many spectral lines is Fe. Therefore, I chose to start my analysis with this species.

This Chapter is limited to the analysis of Fe only as the analysis of other molecules is still pending. Fe has broad spectral lines (see Figure 3.2) which makes it a good tracer of cloud properties.

Figure 3.12 shows the trail plots (see Section 2.2.3) created by cross-correlating the cleaned data with the Fe model shown in Figure 3.10. The cross-correlation is evaluated in $4\,\mathrm{km\,s^{-1}}$ steps to match the instrument resolution. The trails are in the planet's rest frame and thus any signal will appear as a vertical line. The auto-correlation function of the model is shown for reference and is noticeably broader than the instrument resolution. There is no clear trail in the plots for the individual nights or if all the data is binned into phase bins of 0.01.

As there is no clear signal of the planet in the trail plots, the next step is to make a 'Kp-Vsys' map (see Section 2.2.3) which will sum the planet's signal over all observations. Each row (Kp) in these

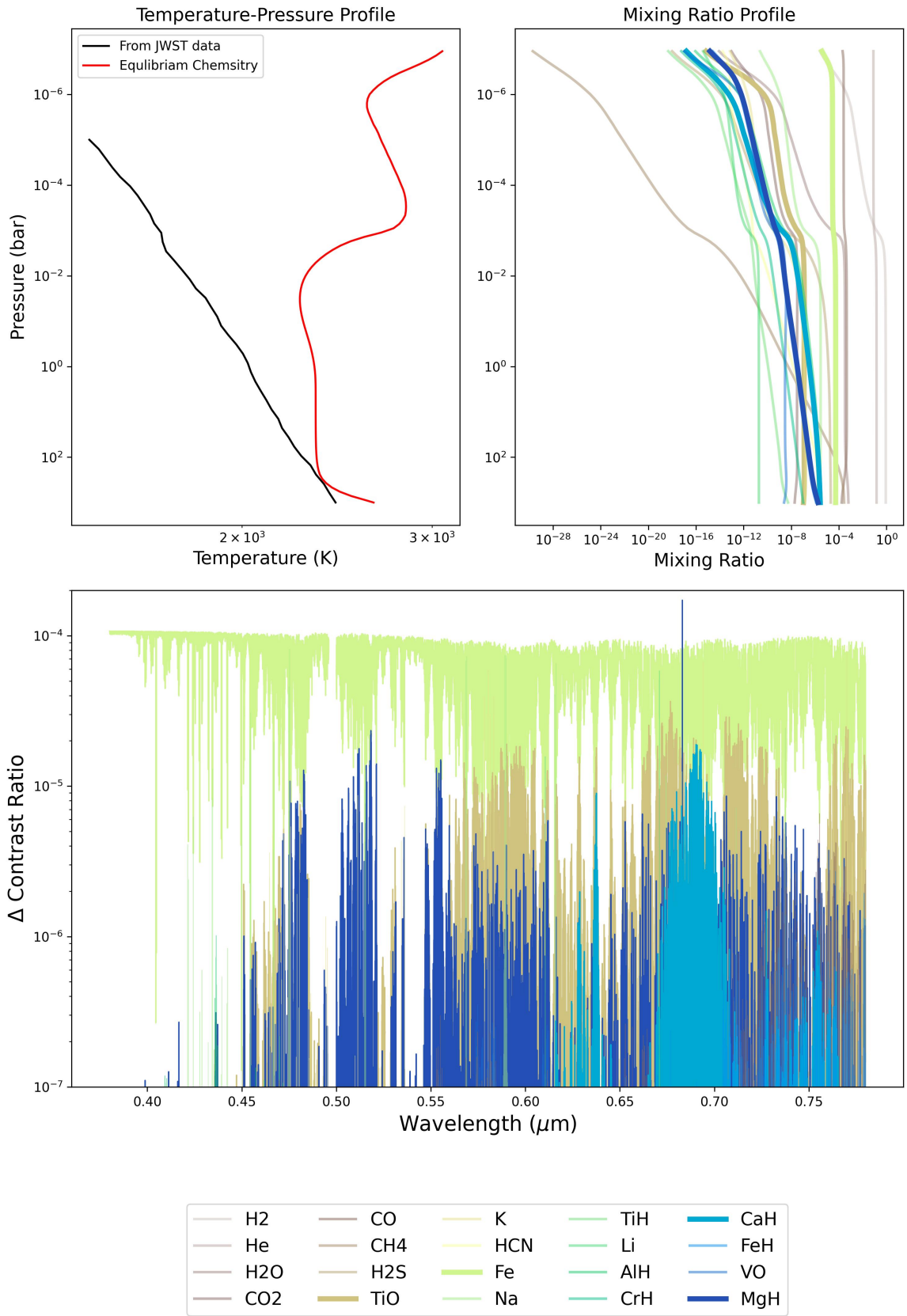

Figure 3.11: **Top panels:** The temperature-pressure profile and chemical abundances of LTT-9779 b assuming a solar metalicity atmosphere in chemical equilibrium. **Bottom panels:** The difference in contrast ratio in the ESPRESSO wavelength range between a model that contains all the molecular species and one with the species of interest removed (note the log scale). The larger the difference, the greater impact that species has on the spectrum. The highlighted molecules are those that have the greatest impact on the spectrum of which Fe has at least an order of magnitude larger impact than all the others.

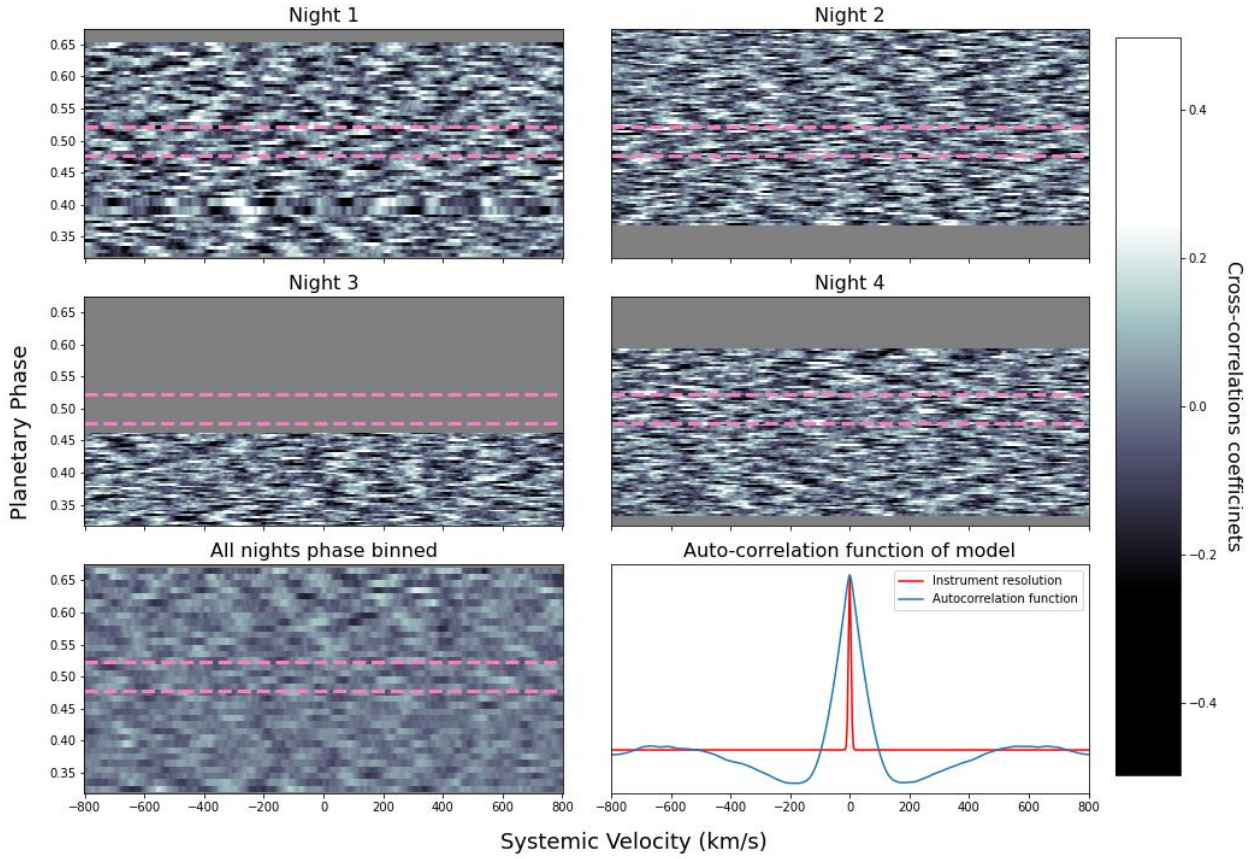

Figure 3.12: The four top panels show the trail plots in the planet's rest frame using the Fe model in Figure 3.10 as a template. The secondary eclipse is marked by the pink dashed lines. There is no obvious trail from the planet present. The bottom left panel shows all the data binned into phase bins of 0.01 where the eclipse is again highlighted. There is no clear trail in this plot either. The bottom right panel shows the auto-correlation function of the cross-correlation model. It is noticeably broader than the instrumental resolution.

maps is the sum of the cross-correlation function for each observation for a given orbit of the planet. The signal-to-noise of these maps are calculated by dividing each row (Kp) by the standard deviation of that row excluding the region $\pm 70\,\mathrm{km\,s}$ in systemic velocity. Such a wide region is chosen due to the broad auto-correlation function of the model. Since the clouds could be concentrated on the evening limb of the planet (e.g. Parmentier et al. 2016) making that side more reflective, I split the pre- and post-eclipse data to see if there is a notable difference. Figures 3.13 and 3.14 show the pre- and post-eclipse 'Kp-Vsys' plots for each night of data and for all nights combined.

There is no detection of Fe in the pre-eclipse data shown in the Kp-Vsys maps for phases less than 0.4957 in Figure 3.13. There are a number of reasons why this could be the case. Firstly, there could be no signal because there is no Fe (or it is obscured by clouds) on the morning side of the planet. Alternatively, there could be low signal which is undetectable amongst the noise because either the pre-eclipse data is noisier, the morning part of the planet is less reflective, or the cross-correlation model is not a good enough match and the weakened signal is being overwhelmed by noise. Further investigation is needed to determine what this non-detection means.

For the post-eclipse data, phases greater than 0.5043, there is a peak in the cross-correlation coefficients in the Kp-Vsys maps for Fe at the expected location of the planet's signal when all nights are combined as shown in Figure 3.14. However, the signal-to-noise of this peak is 3.31 which is lower than my S/N = 5 threshold for a robust detection (see Section 2.2). However, unlike in the pre-eclipse data, there appear to be very weak peaks at the planet's location in each of the nights individually. This could indicate that this signal is real but not strong enough to be robustly detected with the current analysis. To improve this, more observations could be obtained but unfortunately, my request for more observations was rejected in round P114. Instead, I am going to improve the analysis via employing a better data reduction or a better matching cross-correlation model as discussed in Section 3.8.

The planet's reflection will be greatest near secondary eclipse as that is when more of its day-side faces the Earth. Therefore, the observations closer to secondary eclipse will contribute more to the detection. Figures 3.15 and 3.16 show the pre- and post-eclipse 'Kp-Vsys' plots for each night of data limited to phases within 0.09 from the secondary eclipse. This region in phase was chosen so that each of the maps covers the same phase range. The pre-eclipse maps (phases 0.41–0.4957) are shown in Figure 3.15 but still show no signal of Fe. However, the signal in the post-eclipse map (phases 0.5043–0.59), which is shown in Figure 3.16, has become marginally stronger as would be expected if this Fe signal was real. Unfortunately, the signal-to-noise of all the post-eclipse data combined is 3.75 which is lower that the S/N = 5 threshold for a robust detection.

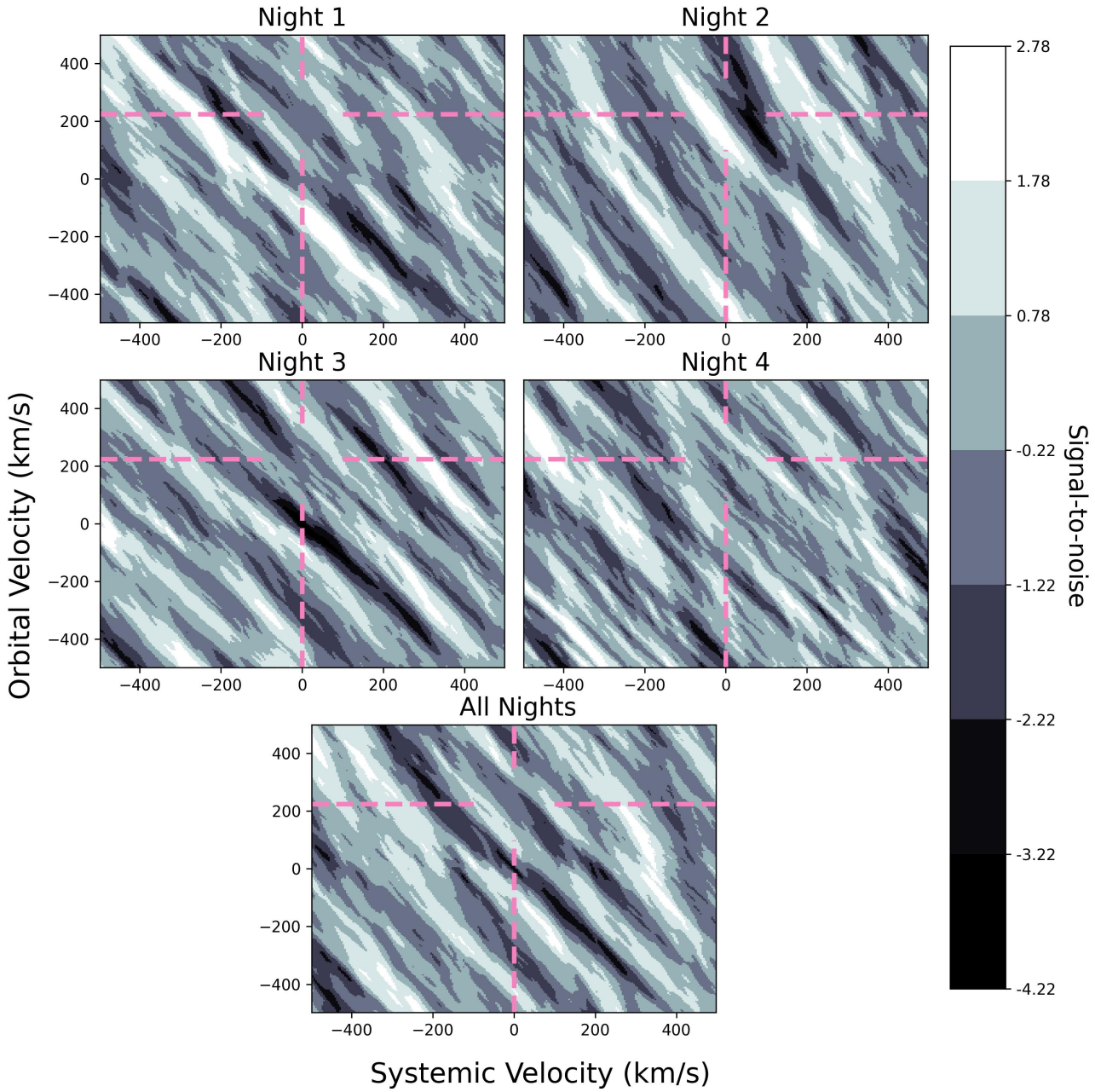

Figure 3.13: The 'Kp-Vsys' maps, for phase less than 0.4957 with the Fe model in Figure 3.10 as the cross-correlation model, for each night individually and for all nights combined. There pink dashed lines indicate the expected location of the planet. Night 2, which had the best observing conditions, shows a peak in the right location but with an S/N = 2.78 which is well below the S/N = 5 threshold for a robust detection. There are no peaks at in the other nights of data and overall there is no detection of the planet in the pre-eclipse data.

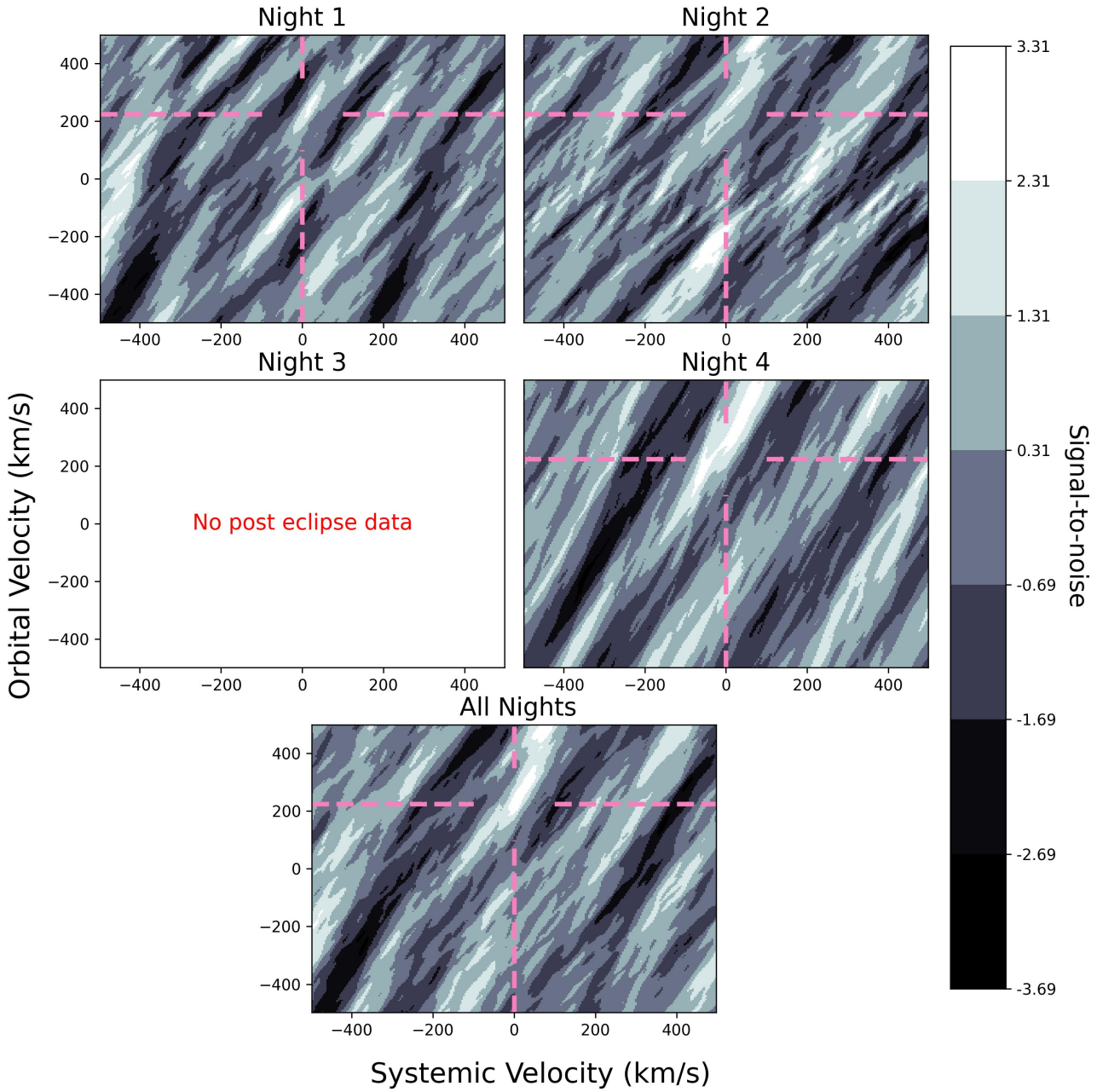

Figure 3.14: The 'Kp-Vsys' maps, for phase larger than 0.5043 with the Fe model in Figure 3.10 as the cross-correlation model, for each night individually and for all nights combined. There pink dashed lines indicate the expected location of the planet. There is no robust detection of the planet in these data however, there are peaks at the planet's location in each of the nights. All nights combined result is a S/N=3.31 peak which is lower than the S/N=5 threshold for a robust detection. It is possible that this is the planet but further investigation is required.

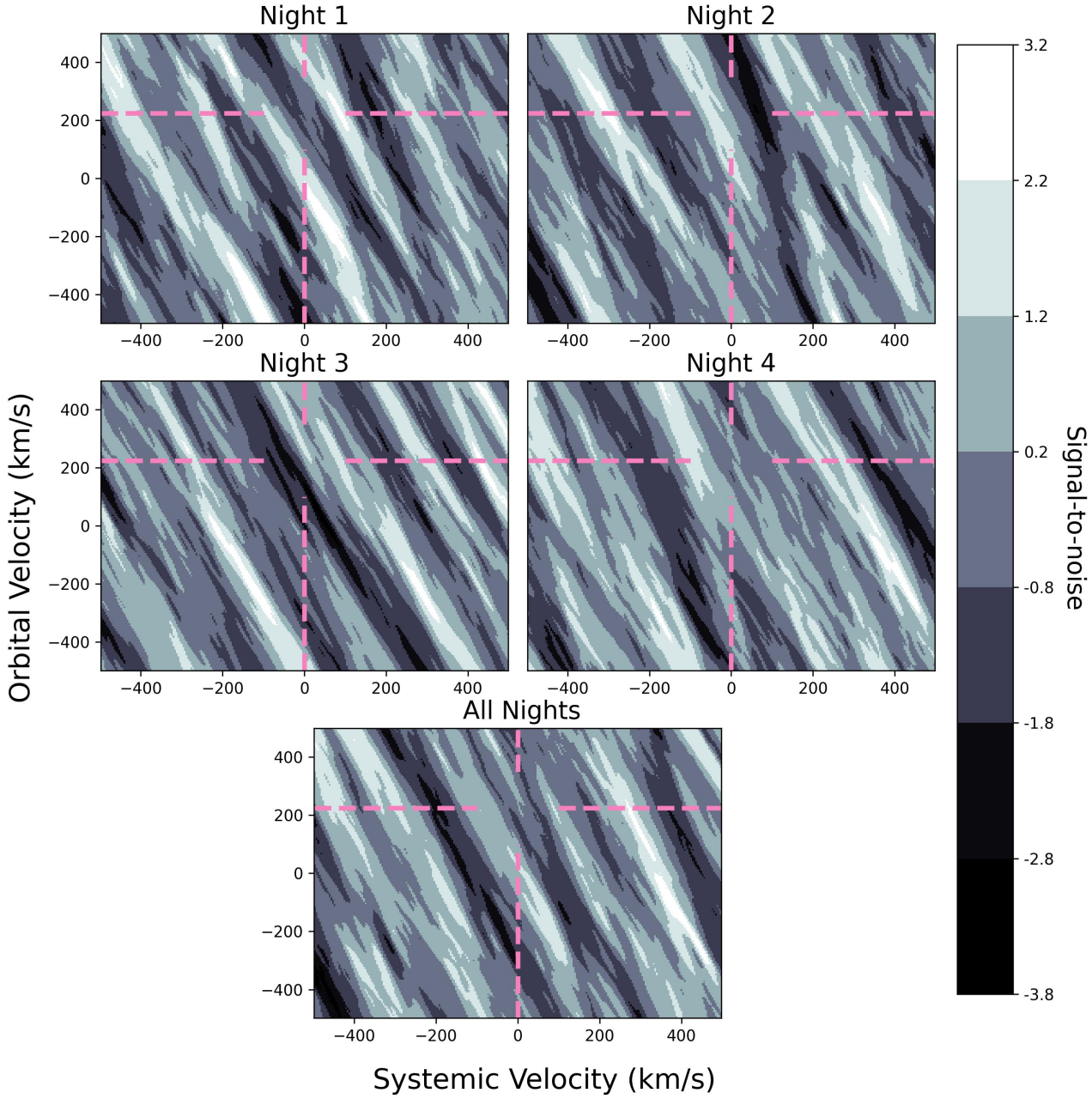

Figure 3.15: The 'Kp-Vsys' maps, for phase 0.41–0.4957 with the Fe model in Figure 3.10 as the cross-correlation model, for each night individually and for all nights combined. The pink dashed lines indicate the expected location of the planet. The signal-to-noise throughout the maps varies from +3.2 to -3.8 and there is no evidence of any planetary signal highlighting the need for an S/N = 5 detection threshold.

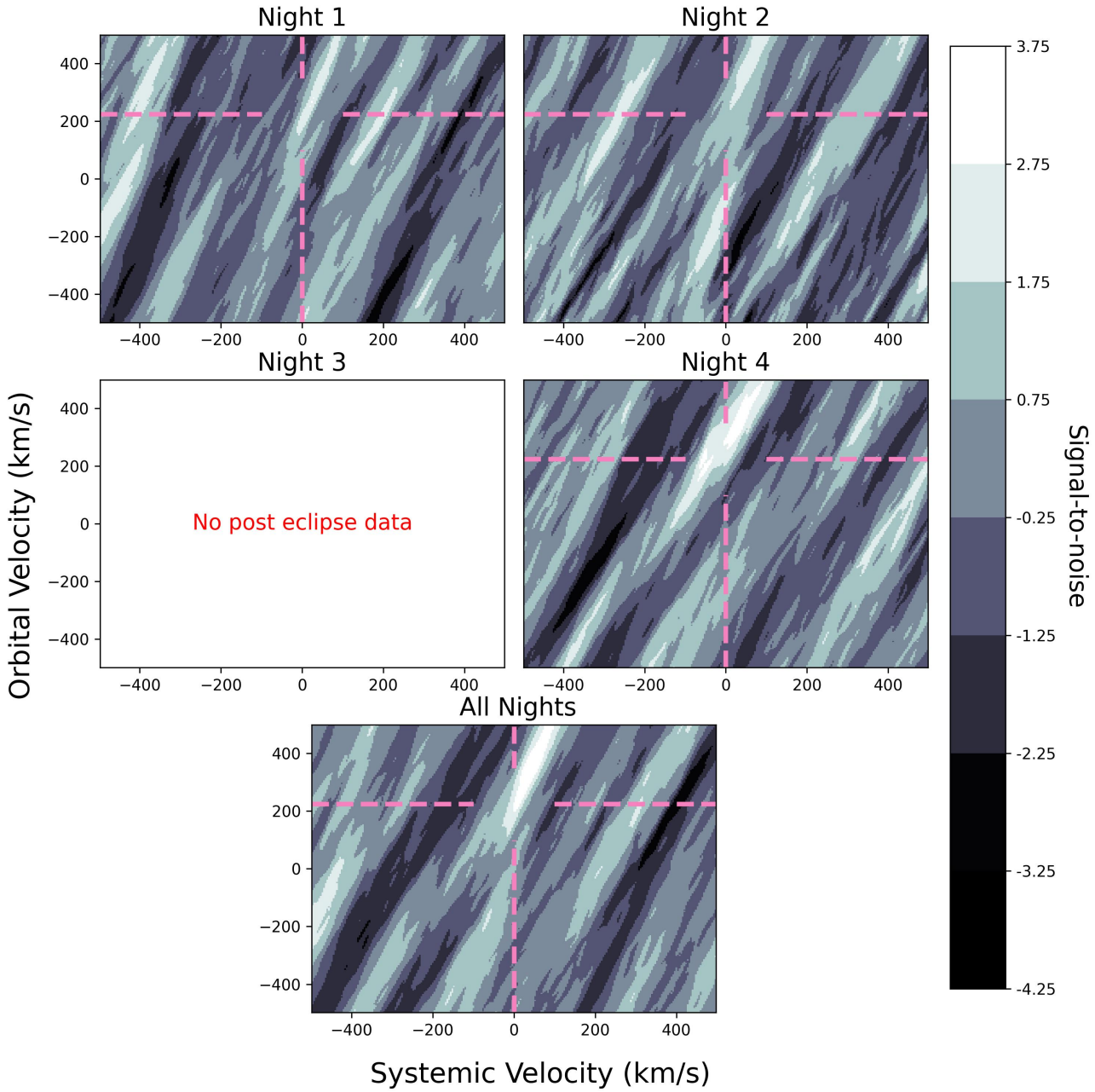

Figure 3.16: The 'Kp-Vsys' maps, for phase 0.5043–0.59 with the Fe model in Figure 3.10 as the cross-correlation model, for each night individually and for all nights combined. The pink dashed lines indicate the expected location of the planet. There is no robust detection of the planet in these data however, there are peaks at the planet's location in each of the nights. All nights combined result result in a slightly higher S/N=3.75 peak however this is still lower than the S/N=5 threshold for a robust detection. It is possible that this is the planet but further investigation is required.

3.8 Summary and future work

LTT-9779 b is an highly reflective exoplanet and an ideal target to test the High-Resolution Cross-Correlation Spectroscopy technique on reflected light. It is also a rare inhabitant of the Neptune desert and its clouds, which I aim to study with HRCCS, may be the key to illuminating its survival in the desert.

I have four half nights of ESPRESSO@VLT 4UT mode data to which I am applying the HRCCS technique to in order to extract information on this unusual atmosphere. To do so, however, I had to refit the planet's orbit which I have identified as being slightly eccentric.

Having tried a simple cross-correlation template for Fe, the species likely to cause the largest spectral feature, I have thus far been unable to obtain a robust detection of the planet's spectrum. This could be astrophysical for example, due to a high cloud deck obscuring the Fe spectral lines or low reflection reducing the signal strength or it could be related to the analysis, for example, the cross-correlation template is a poor match to the Fe lines in the planet's spectrum or the bad pixels and columns left by the data reduction are introducing excess noise into the cross-correlation.

To improve the analysis, I intend to review the data reduction to increase the efficiency of the bad pixel correction. This could by done by, for example, running the bad pixel detection algorithm on the cleaned data where the bad pixels more obviously stand out. To identify a better matching cross-correlation model, I have started running a likelihood analysis on the post-eclipse data which contains some evidence of a signal. In this analysis, I am fitting a model spectrum with variable Fe mixing ratio and a grey cloud deck of varying height and scattering parameters. This is computationally expensive and unfortunately I have no results yet however, if successful a better matching model may result in a stronger detection in the Kp-Vsys maps and hopefully result in a robust S/N > 5 detection. I am also planning to search for additional molecules which may also increase the significance of the signal by increasing the number of spectral lines in the model, however the number of detectable molecules is likely limited.

In the event of a non-detection, I will run injection tests to determine what range of atmospheric conditions can be ruled out by these observations. This is likely to put useful constraints on the height of the cloud deck.

4 | Behind the mask: Can HARMONI@ELT characterise the atmosphere of the nearest exoplanet, Proxima b?

4.1 Overview

This chapter demonstrates the feasibility of characterising the potentially Earth-like exoplanet Proxima b with the High Angular Resolution Monolithic Optical and Near-infrared Integral field spectrograph (HARMONI) on the ELT. This involved creating an instrumental simulation of HARMONI's High Contrast Adaptive Optics mode. I was responsible for creating this simulator with the HARMONI instrument team providing point spread function of HARMONI's High Contrast Adaptive Optics mode and other instrumental data such as throughput values and detector noise parameters. They also provided their expertise on the design of HARMONI with special thanks to Niranjan Thatte, Fraser Clarke, Alexis Carlotti and Elizabeth George who helped me understand how this complex instrument worked. The subsequent analysis of the observations was done by myself with the model spectra of Proxima b obtained from Lin et al. (2019) who also provided support in their use. The comparison with the work of Houllé et al. (2021) was aided by the authors of that work who kindly provided some of their data. The work in this chapter is published in Vaughan et al. (2024).

4.2 Motivation

For a long time exoplanet science has strived to answer the question 'Are we alone in the Universe?', a question we are just starting to answer. As discussed in Section 1.4.4, one way to identify the presence of life on a planet is to look for certain combinations of atmospheric biomarkers – such as the combination of oxygen (O_2), carbon dioxide (CO_2), water (H_2O) and methane (CH_4) – in the spectrum of an exoplanet.

With current instrumentation and the upcoming ELTs, measuring the spectrum of a temperate rocky exoplanet in the habitable zone of a Sun-like star is difficult. For transit observations, small planet-star radius ratios and low transit probabilities pose great challenges (see Table 4.1). Additionally, for emission and reflection observations, problems are encountered due to the small planet-star contrast ratios and very close spatial separations.

Therefore, there has been a greater focus on characterising exoplanets orbiting M-dwarfs. These stars have smaller radii and lower luminosity and thus more favourable ratios, plus higher transit probabili-

	Transit probability	Planet-star radius ratio
G-dwarf	0.3%	0.009
M-dwarf	1.2%	0.03

Table 4.1: The approximate transit probability and planet-star radius ratio for an Earth radius planet with an Earth-like instellation orbiting different stellar types.

ties giving greater observability (Charbonneau et al. 2007, see Table 4.1). This comes with the added bonus that M-dwarfs are the most common type of star in the galaxy (e.g Henry et al. 1997; Kirkpatrick 2001; Henry et al. 2018; Reylé et al. 2021; Reyle et al. 2023) and have a higher occurrence rate of rocky planets than FGK stars (e.g. Mulders et al. 2015; Sabotta et al. 2021; Ment et al. 2023) meaning there are more potentially habitable exoplanets to observe around these stars. The disadvantage is that the habitability of temperate, rocky exoplanets orbiting M-dwarfs is currently uncertain (e.g. factors relating to atmospheric loss due to stellar activity, tidal locking and photosynthetic viability: Khodachenko et al. 2007; Kiang et al. 2007; Showman et al. 2013; Kreidberg et al. 2019; Claudi et al. 2020). Of particular concern is whether these planets can retain an atmosphere with the increased stellar activity of M-dwarfs compared to G-dwarfs. However, the only way to know for sure if a planet has an atmosphere or not is to measure it. This has begun with JWST observations of the terrestrial TRAPPIST-1 planets which have ruled out large H/He atmospheres and favour bare rock models (Greene et al. 2023; Ih et al. 2023; Zieba et al. 2023). TRAPPIST-1 is a particularly active M-dwarf (Reiners et al. 2010) and so studies of more quiescent M-dwarf stars are needed to truly understand if these stars can host terrestrial planets with atmospheres.

Proxima b is a potentially temperate rocky exoplanet that orbits in the habitable zone of the bright and less active M-dwarf Proxima Centauri (Anglada-Escudé et al. 2016; Jenkins et al. 2019; Damasso et al. 2020; Faria et al. 2022). It is a promising target for atmospheric characterisation with the ELTs. However, since this planet does not transit (Gilbert et al. 2021, and references therein) it will have to be characterised via its thermal emission or reflection spectra. As discussed in Section 1.4, high spectral resolution measurements of the reflection spectrum of an exoplanet can be used to characterise atmospheric biomarkers as well as other atmospheric properties. This could yield valuable information on the environment of this world and inform our theories on the habitability of M-dwarf exoplanets. Using HRCCS (see Section 2.2) to measure the high resolution reflection spectrum of Proxima b will be extremely challenging, if not impossible, due to an unfavorable contrast ratio and low orbital velocity. However, since Proxima b is spatially resolvable with the $30\,\mathrm{m}+$ class of telescopes, the molecule mapping technique (see Section 2.3) is feasible.

Molecule mapping requires a spectrum to be taken of each spatial pixel (spaxel) in the field of view and

will therefore need an instrument such as an Integral Field Spectrograph (IFS). These will also need to be Adaptive Optics (AO) enabled in order to reach the contrast limits needed to observe Proxima b given its close spatial separation ($37\,\mathrm{mas}$) from its host star. There are many AO-enabled Integral Field Spectrographs (IFSs) among the next generation of instruments for the ELTs. These include HARMONI, METIS, ANDES and PCS on the ELT, GMTIFS and GMagAO-X + IFS on the Giant Magellan Telescope (GMT) and IRIS and MICHI on the Thirty Meter Telescope (TMT) to name a few (Sharp et al. 2016; Wright et al. 2016; Packham et al. 2018; Brandl et al. 2021; Kasper et al. 2021; Marconi et al. 2021; Thatte et al. 2021; Males et al. 2022). The wavelength ranges covered by these instruments separately cover the thermal emission and reflection of Proxima b. So by combining observations from multiple instruments, the thermal emission and reflection of Proxima b could be measured, leading to the possibility of characterising the planet's energy budget which is key to understanding its environment (see Section 1.4.1). Additionally, they can be used to identify and characterise four biomarker species: CO_2, H_2O, CH_4 and O_2. RISTRETTO, a new IFS planned for the Very Large Telescope (VLT), aims at detecting the O_2 A-band, 0.759–$0.771\,\mu\mathrm{m}$, on Proxima b (Chazelas et al. 2020; Blind et al. 2022) prior to the operation of the ELTs. The work presented here aims to determine the feasibility of characterising the reflection of Proxima b with HARMONI@ELT.

4.3 A short description of HARMONI@ELT

HARMONI is an IFS that will be one of the first instruments mounted on the ELT (Tecza et al. 2009; Thatte 2010; Thatte et al. 2014, 2016; Thatte et al. 2020, 2021, 2022). In the wavelength domain it has a non-simultaneous wavelength coverage between $0.47 - 2.45\,\mu\mathrm{m}$ with a choice of three spectral resolutions. In the image plane, there is a choice of four spatial pixel scales and several AO modes as well as a high contrast module which uses and apodiser and coronagraph to modify the point spread function (HCAO mode; Carlotti et al. 2018; Houllé et al. 2021).

To observe Proxima b, the HCAO mode is required in order to achieve the high-contrast requirements. The rest of this Chapter focuses only on the use of this mode. The HCAO mode provides coverage of the H and K bands between $1.45 - 2.45\,\mu\mathrm{m}$ at a range of resolutions and can be configured with one of two available apodizers (named SP1 and SP2) and one of three partially transmissive focal plane masks (FPMs). An apodiser is an optical device placed in the pupil plane to modify the pupil function of the instrument which is related to the PSF via a Fourier transform. They are typically designed to smooth out sharp edges in the pupil function which reduces speckle noise and improves stellar suppression. In the case of HARMONI's HCAO mode, the apodisers are designed in such a way as to modify the point spread function (PSF) of the instrument to improve starlight suppression in an annulus around

Parameter	Value	ref
Spaxel Scale	3.88 mas	1, 2
Spectral Resolving Power	17385	1, 2
Wavelength range	1.538 – 1.678µm (H-High)	1, 2
AO mode	HCAO - SP1 apodizer	3
FPM for SP1 apodizer (H band)	ellipse: 50 mas x 58 mas	-

Table 4.2: The observing mode of HARMONI used in the simulations.
1 Thatte et al. (2021); 2 using information from HSIM v310 Zieleniewski et al. (2015); 3 Houllé et al. (2021)

the star. The core of the stellar PSF is masked by the FPMs which are partially transmissive filters that block 99.99% of the light in the centre of the field of view and therefore allow longer integration times to be used for bright stars, like Proxima (H band magnitude = 4.8; Cutri et al. 2003). The slightly wavelength-dependent refractive index of Earth's atmosphere changes the position of objects in the image as a function of wavelength. This is largely corrected by the use of an atmospheric dispersion corrector (ADC); however the dispersion is an airmass-dependent effect and HARMONI's ADC is only optimised for a single airmass. This means there will be residual dispersion. To compensate for this, each FPM is elongated in one direction to better match the shape of the PSF core. To keep the dispersion at a fixed angle in the image, the instrument rotator is set to track the parallactic angle, otherwise known as pupil tracking.

In this work, I simulate observations with HARMONI's HCAO mode using the "H-high grating" (1.538 – 1.678 µm, $R = 17,385$) with a spatial sampling of 3.88 mas, which over samples the spatial resolving power (10 mas at 1.6 µm). I select the SP1 apodiser (due to it's smaller inner working angle) and the smallest FPM. The instrument mode is summarised in Table 4.2.

4.4 Simulating HARMONI@ELT observations

Comprehensive simulations of HARMONI have demonstrated that the molecule mapping technique can be used to detect the thermal emission of young, widely-separated gas giants (Houllé et al. 2021; Bidot et al. 2024). While using the same instrument and technique, this work focuses characterising old temperate rocky exoplanets in reflected light which poses its own unique set of challenges. These include the smaller angular separations between the planet and star and the greater similarity between the planet's spectrum and that of the star. instead on the reflection from old rocky exoplanets My simulations aim to be as comprehensive as these and other works (e.g. for HabEx/LUVOIR, HARMONI and MIRI@JWST respectively Wang et al. 2017; Houllé et al. 2021; Patapis et al. 2021) by including the effects of Earth's atmosphere; the optics of the ELT; and HARMONI's detector performance

as well as several noise sources as in Houllé et al. (2021). Additionally, I include the on-sky orbital motion of Proxima b as its short orbital period results in a non-negligible amount of motion over the course of an observing night.

The simulation method I use is based on that in HSIM v310[1] (Zieleniewski et al. 2015) but with modifications for multi-exposure simulations to reduce computation time and output file size and to improve the ease of accommodating different instrumental designs.

4.4.1 Modeling the orbits

HARMONI's HCAO mode is operated in pupil tracking mode which means the position angle of the image will appear to rotate over time. I include this effect in the simulations which correspond to a rotation of $\sim 150°$ in 10 hours. In addition to this, I include the orbital motion of Proxima b which, at a spatial sampling of 3.88mas, will change the planet's position by up to one spaxel every 5 hours. The image rotation caused by the pupil tracking mode can be corrected but the orbital motion of Proxima b can only be corrected if the orbital orientation is known. Section 4.5 discusses the difficulty of determining Proxima b's full 3-D orbit before HARMONI observes this system and how the molecule mapping analysis might proceed if the orbit is unknown.

I include the orbits of both the star[2] and planet in the simulation which I modelled as ellipses. Alongside the parameters measured from radial velocity studies shown in Table 4.3, I specify the orientation using three parameters (shown in Figure 4.1:

1. Inclination, i: the angle between the plane of the sky and the plane of the orbit.
2. The longitude of the ascending node, Ω: a rotation in the plane of the sky.
3. The argument of periastron, ω: a rotation in the plane of the orbit.

The longitude of the ascending node is currently unknown and the inclination is only weakly constrained by the non-detection of transits (Gilbert et al. 2021, and references therein). Proxima b's orbit is close to circular (Faria et al. 2022) so, for simplicity, I assume zero eccentricity so that the argument of periastron no longer affects the shape of the orbit. This also means I can set the phase of the orbit using the mean longitude, the orbital phase (as an angle) assuming a circular orbit at the accompanying reference time, which has been measured (Anglada-Escudé et al. 2016). In the following simulations, I choose an intermediate inclination of $45°$ and a longitude of the ascending node of $90°$. This orbit represents a good compromise between having large radial velocity shifts and spending longer at

[1] https://github.com/HARMONI-ELT/HSIM
[2] The star's motion only includes its reflex orbit due to Proxima b and is insignificant.

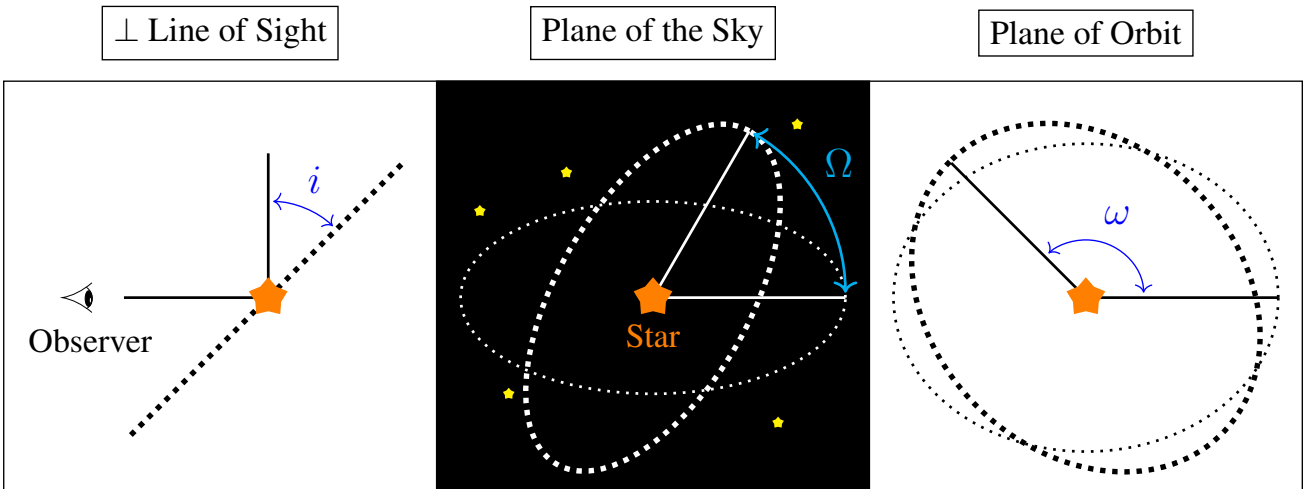

Figure 4.1: A diagram showing the three angles that specify the orientation of an orbit (dashed line). **Left panel:** The diagram shows an orbit in the plane perpendicular to the line of sight. The inclination is the angle between the plane of the sky (solid vertical line) and the plane of the orbit (dashed line). **Middle panel:** The orbit is shown in the plane of the sky which is represented by a black background with yellow stars. The longitude of the ascending node is a rotation in the plane of the sky. **Right panel:** The orbit is shown in the plane of the orbit. The argument of periastron is a rotation in the plane of the orbit.

maximum elongation.

In these simulations, I take the radial velocity of each object to be the combined sum of the velocity of the Earth (barycentric), the velocity of the star system (systemic), and the planet orbital velocity which can be computed for a given observing time.

4.4.2 Modeling the spectra of Proxima b and its host star

HARMONI will be sensitive to the reflected light of Proxima b meaning the planet's spectrum, F_p, is a Doppler shifted and rotationally broadened copy of the stellar spectrum, F_s, modulated by the planet's

Parameter	Value	ref
Systemic Velocity, V_{sys}	$-22.204\,\mathrm{km\,s^{-1}}$	1
Radial Velocity Amplitude, $K_\star$	$1.24\,\mathrm{m\,s^{-1}}$	2
Semi-major axis, a	$0.0485\,\mathrm{au}$	2, 3
Orbital Period, P	$11.186\,\mathrm{d}$	2, 3, 4, 5
Orbital Velocity, K_p	$47.2\,\mathrm{km\,s^{-1}}$	*
Eccentricity, e	0	*
Inclination, i	45°	*
Longitude of the Ascending Node, Ω	90°	*
Mean Longitude, $\mathcal{M}$	110°	3
Reference time for $\mathcal{M}$ (JD), T_λ	2451634.73146	3

Table 4.3: Parameters of Proxima b's orbit used in this work. 1 Kervella et al. (2017); 2 Faria et al. (2022); 3 Anglada-Escudé et al. (2016); 4 Jenkins et al. (2019); 5 Damasso et al. (2020); * assumed

Parameter	Value	ref
Stellar Type	M5.5 V	1
Distance	1.302 pc	2
PHOENIX Model, F_s	$T = 3000$ K; $\log(g) = 5$	3
	$[Fe/H] = 0$; $[\alpha/M] = 0$	3
Magnitude *(H)*	4.8 mag	4
Proxima b Spectral Model, $A_g(\lambda)$	1 bar oxic atmosphere	5
Average $A_g(1.538–1.678\mu m)$	0.23	5
Proxima b Radius (estimate), R_p	$1.07R_\oplus$	6
Proxima b Minimum Mass, $M\sin(i)$	$1.07M_\oplus$	7
Semi-major axis, a	0.0485 au	7, 8
$g(\alpha)$	$\frac{1+\cos(\alpha)}{2}$	*

Table 4.4: Parameters used to create the spectra of Proxima Centauri and Proxima b. 1 Bessell (1991); 2 Gaia Collaboration (2020); 3 Husser et al. (2013); 4 Cutri et al. (2003); 5 Lin et al. (2019); 6 Bixel et al. (2017); 7 Faria et al. (2022); 8 Anglada-Escudé et al. (2016); * assumed

geometric albedo, A_g, as shown in Equation 1.1. Table 4.4 lists the parameters I used to compute the spectrum of Proxima b with the exception of the rotational broadening, v_{rot}, which I calculated to be small enough that this effect is insignificant following Spring et al. (2022).

The geometric albedo model spectrum obtained from Lin et al. (2019) has been computed specifically for Proxima b, deviating from Earth's spectrum by accounting for the higher planet mass, lower instellation, and different stellar spectral type. It assumes Proxima b has an Earth-like 1 bar oxic atmosphere with an Earth-like surface albedo and Earth-like abundances for atmospheric gases except the CO_2 concentration. This is approximately 100 times larger than on Earth to keep the planet from freezing. To be consistent with Lin et al. (2019), I used a PHOENIX model (Husser et al. 2013) with the parameters listed in Table 4.4 for the stellar spectrum. The model spectra of Proxima Centauri and Proxima b are shown in Figure 4.2. The phase function $g(\alpha)$ assumes the form shown in Table 4.4 which is slightly brighter at quadrature phases than the typically assumed Lambertain scattering (e.g. Carrión-González et al. 2021; Spring et al. 2022). I used this phase function as it is simpler than the Lambertain function and the true $g(\alpha)$ is unknown at this time.

4.4.3 Choosing when to observe

The on-sky orientation and velocities of the Proxima system vary with time and can be predicted if the 3-D orbit is known. As I account for this motion in the simulations, the observing times must be picked using the same criteria as real observations. These criteria are:

1. It must be at least nautical twilight[3] or darker at Paranal.

[3]The centre of the sun is more than 6° below the horizon.

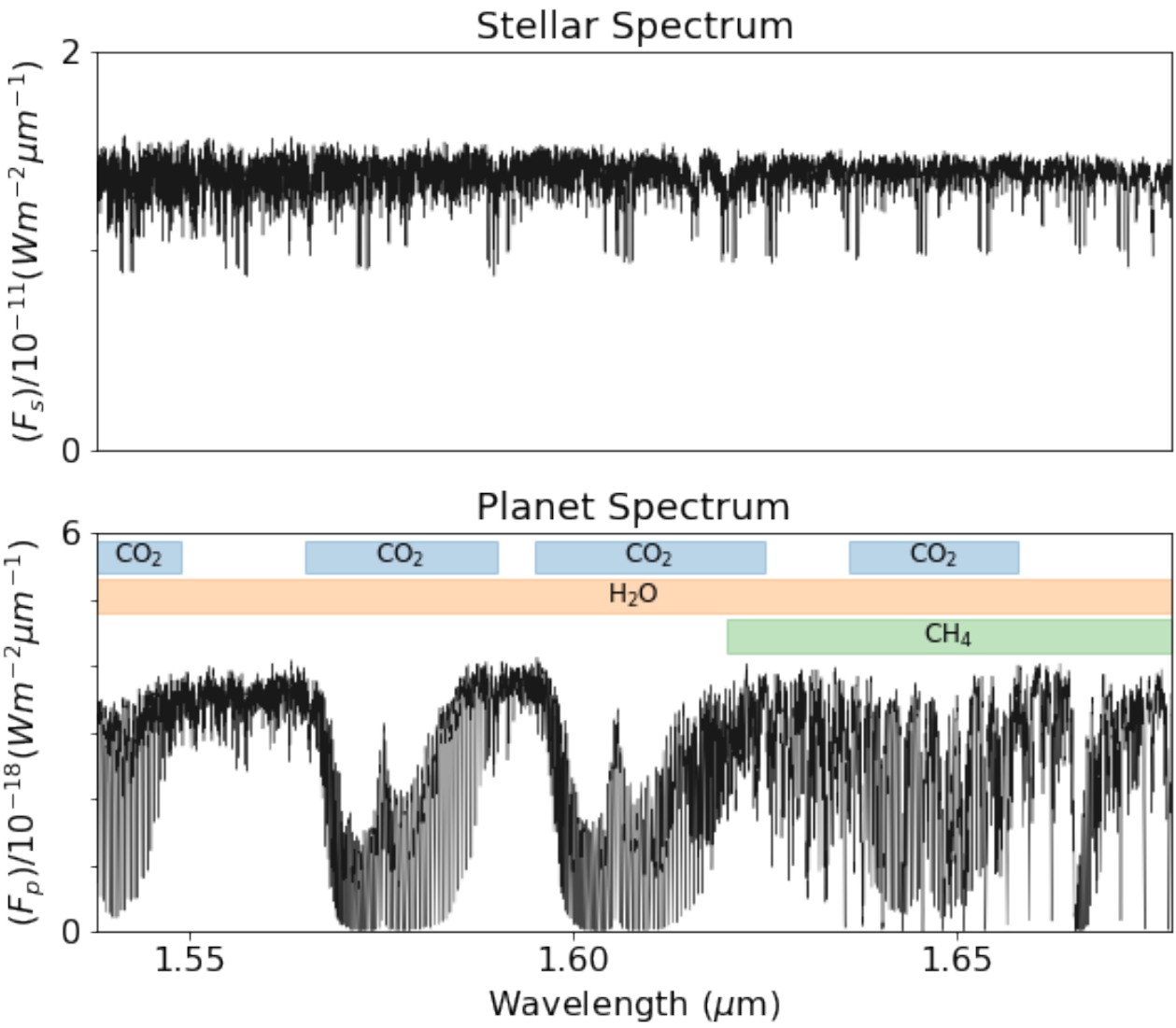

Figure 4.2: **Top:** The model PHOENIX stellar spectrum for Proxima Centauri in units of intensity at Earth. The spectral lines in this region come from a variety of ionised species. **Bottom:** the exoplanet's reflected light spectrum, as computed in Lin et al. (2019) and Equation 1.1, in units of intensity at Earth. The features caused by different molecules in the planet's atmosphere have been highlighted. Note the difference in y-axis scale.

2. Proxima Centauri must be more than $45°$ in elevation above the horizon at Paranal (airmass$<$ 1.4). This is required for the AO to function well.

3. Proxima b must not be behind the FPM at any time. This is because the throughput of the mask will reduce the reflected light signal too much for it to be detected.

4. Proxima b must have at least half of its hemisphere illuminated as this leads to a higher reflected light signal.

5. Proxima b's velocity must be at least $1\,\mathrm{km\,s^{-1}}$ different from Proxima Centauri and the Earth as this prevents the spectral lines from overlapping, which aids in isolating the planet's spectrum (see e.g. Lovis et al. 2017).

To identify suitable observing times, I check these criteria at 10-minute intervals between 1^{st} January 2030 and 1^{st} January 2032, centered around the expected first light of HARMONI. For each night, I choose the start time that minimises the airmass of the of observation. Items 3-5 require the knowledge of the Proxima b's orbit for which I use the parameters in Table 4.3. If the orbit is not known, Section 4.5.1 discusses possible strategies for determining when to observe.

On its assumed orbit, Proxima b can remain widely separated from Proxima Centauri over an entire night, however, this can be severely limited by the FPM. As the mask is elongated in one direction, the region of the sky covered by it changes over time. This can result in the mask covering the planet for part of the night. Additionally, for smaller masks, stricter restrictions may need to be placed on the airmass to prevent the detector reaching the persistence limit around the edge of the mask.

4.4.4 Modeling Earth's atmosphere

Earth's atmosphere both absorbs and emits radiation which will act as a source of contamination in these observations. These spectra (tellurics) are airmass dependent so I generate the spectra for each observation separately. I use TelFit (Gullikson et al. 2014) for the telluric transmission spectrum and SkyCalc (Noll et al. 2012; Jones et al. 2013) for the telluric emission spectrum. I could have used SkyCalc for the transmission spectrum but this contains discontinuities due to airmass interpolation which causes artefacts in the simulation. This does not affect the emission spectrum as it is computed using a different method. While both codes are able to simulate the spectra for different weather conditions, I kept these constant at the parameters shown in Table 4.5 for simplicity. These are consistent with average conditions at Paranal and therefore very similar to those at Armazones, the ELT site.

Parameter	Value	ref
Right Ascension	$14:29:42.94613$	1
Declination	$-62:40:46.16468$	1
Longitude	$-70°24'18''$	2
Latitude	$-24°37'39''$	2
Airmass	1.25–1.4	-
Seeing	$0.57''$ (fixed)	2, 3
Surface Pressure	795 hPa	2
Temperature	283 K	2
Relative Humidity	20 per cent †	2

Table 4.5: The coordinates and weather parameters used to simulate the spectra of the Earth. † This corresponds to a precipitable water vapor of approximately 1.0. 1 using information from HSIM v310 Zieleniewski et al. (2015) 2 https://www.eso.org/sci/facilities/paranal/astroclimate/site.html 3 https://www.eso.org/sci/facilities/eelt/docs/ESO-193696_2_Observatory_Top_Level_Requirements.pdf

4.4.5 Modeling HARMONI@ELT

Observing Proxima b will push HARMONI to its design limits and the detectability of Proxima b will depend on many factors. For these simulations to be as realistic as feasible, I included the following effects (see values in Table 4.6): the throughput and emissivity of the ELT; the PSF of the combined ELT and HARMONI optics; the residual atmospheric dispersion; the FPM; the throughput and emissivity of HARMONI; and several noise sources from the detector and optics.

First, for the throughput of the ELT optics, I used the pre-calculated transmission as a function of wavelength from HSIM v310. In line with HSIM, I also assumed thermal emission is that of a non-ideal emitter i.e. a greybody with an emission temperature of 273 K and an emissivity equal to one minus the transmission of the ELT.

Next, I generate a long exposure PSF (> 10 s to average highly time-variable phase aberrations c.f. Fétick et al. 2018; Fétick et al. 2019) using the Power Spectral Density (PSD) from Houllé et al. (2021) and the methods presented in Fétick et al. (2018) where the sum of the PSF at 3.88mas sampling is normalised to unity. While realistic, it is computationally intensive to compute the PSF this way. I therefore only compute the PSF for a constant seeing of $0.57''$ (occurs $\approx 30\%$ of the time at Armazones[4]) and for a single wavelength – the central value of the spectrum. I use this same realisation of the PSF for each observation. This results in a more optimistic and well-behaved PSF than would likely be achieved on sky. In section 4.7, to determine if this affects the feasibility study, I compare my simulations to those of Houllé et al. (2021), who have a more realistic treatment of the PSF.

[4] https://www.eso.org/sci/facilities/eelt/docs/ESO-193696_2_Observatory_Top_Level_Requirements.pdf

Since HARMONI's HCAO mode uses an ADC with an optimal correction angle of $32.6°$, the image will still show a residual dispersion in altitude that depends on both airmass and wavelength. I calculate the corresponding image displacement as a function of airmass and wavelength using the equations presented in Schubert et al. (2000). This displacement does not change the position of the mask but changes the image under it.

For the FPM, I either use a template provided to me by the HARMONI team for the FPM for SP1 apodizer (H band), which is an ellipse with dimensions $50\,\mathrm{mas} \times 58\,\mathrm{mas}$, or custom generated FPMs. These templates are made by calculating the fraction of the new mask covering each spaxel and multiplying by the throughput, 0.01%. The template is then applied to the image which contains the star and planet.

Next, to account for the throughput and emissivity of each of the HARMONI components, I used the same method and parameters as HSIM v310. That is, the thermal emission is calculated using the throughput and emissivity at the component level and the total throughput is the combined throughput of the all individual components.

Finally, the reflected light of Proxima b will be below the noise level and so the feasibility of recovering it will be strongly dependent on the amount and properties of the noise. Therefore I add the following sources of noise to the simulation:

1. *Poisson noise*; caused by counting statistics, it is calculated using the flux and quantum efficiency values.
2. *The crosstalk*; caused by charge leakage from neighbouring pixels.
3. *The read noise*; caused by noise in the electronics.
4. *The dark current*; caused by small currents in the detector present even when it is not exposed to light.
5. *The thermal noise*, caused by the thermal emission of several components within view of the detector but that are not along the optical path and so they were not included in the previous calculations.

In my simulations, the Poisson noise and read noise contribute similar amounts to Proxima b's spectrum. Therefore Equation 2.3 is not valid for calculating the expected signal-to-noise.

Parameter	Value	ref
ELT Transmission$_{\text{Havg}}$	0.755	1
ELT Emission$_{\text{Havg}}$	$3.8\,\text{ph}\,\text{s}^{-1}\,\text{m}^{-2}\,\mu\text{m}^{-1}\,\text{as}^{-2}$	1
Atmospheric DispersionCorrector angle	$32.6°$ (fixed)	2
Focal Plane Mask transmission	10^{-4}	2
HARMONI Transmission$_{\text{Havg}}$	0.438	1
HARMONI Emission$_{\text{Havg}}$†	$0.5\,\text{ph}\,\text{s}^{-1}\,\text{m}^{-2}\,\mu\text{m}^{-1}\,\text{as}^{-2}$	1
Total Throughput$_{\text{Havg}}$∗	0.30	–
Quantum Efficiency$_{\text{Havg}}$	0.9	1
Crosstalk	0.02 per adjacent pixel	1, 2
Read Noise	$12e^-$ per pixel	1, 2
Dark Current	$0.0053e^-s^{-1}$ per pixel	1, 2
Thermal Noise from Cryostat	$0.017e^-s^{-1}$ per pixel	1
Persistence Limit	$30000e^-$	1

Table 4.6: Instrumental parameters of HARMONI used in the simulation.
Havg indicates wavelength dependant quantities in the simulation that have been averaged over 1.538–$1.678\mu\text{m}$ for this Table. † This assumes the focal plane relay has a temperature of $-10\,°\text{C}$. In the current design, this temperature has increased to $2\,°\text{C}$ however this difference will not significantly change the noise. ∗ This excludes the focal plane mask. 1 using information from HSIM v310 Zieleniewski et al. (2015); 2 Houllé et al. (2021)

4.4.6 Effects not included in the simulation

Simulations rarely capture all of the nuances of real observations and my simulations are not the exception. The following are some additional effects that I have not included in the simulation but could impact the detectability of Proxima b.

The first effect I have not included is saturation. When a pixel on the detector is nearing the saturation limit, the relationship between the charge on that pixel and the number of photons becomes non-linear. I do not model this non-linear relationship in the simulations. However, as Proxima b's spectrum is not located on or near a pixel reaching this limit, it is not likely to significantly affected the results of this work unless there is significant saturation present in the image.

Secondly, I have not included persistence. This occurs when a pixel on the detector reaches the limit beyond which the charge on that pixel cannot be completely discharged during a detector read. The residual charge is then carried into the next observation leading to an 'after glow' and possibly affects subsequent observations. I do not account for this 'after glow', however, most of the pixels in the simulations I created for this work are kept below this limit by restricting the integration times.

Thirdly, the edge of the focal plane mask could scatter the star's light leading to increased noise in the observations. However, HARMONI's optics downstream of the FPM are oversized by a factor of approximately 15 times for the $3.88\,\text{mas}$ spatial scale to accommodate the larger spaxel scales of the

other modes. Therefore the majority of the scattered light will be successfully reimaged back to the mask edge. I have therefore neglected the additional background this might create. This effect is not expected to be significant, but the exact leakage term is not known at this time so it is possible this extra background may increase the amount of integration time required.

As discussed in Section 4.4.5, I also use the same simplified PSF for each observation which has no wavelength dependence. This results in the speckles behaving as white noise sources instead of pink noise which decreases the amount of time required for a detection.

Finally, I also assume perfect flat fielding and wavelength calibration as an optimistic case since it is hard to anticipate how good these will be once HARMONI begins operation. Despite these caveats, these are still some of the most detailed instrument simulations to date.

4.4.7 Simulating the observations

To be the most realistic, each detector integration should be simulated separately like in Houllé et al. (2021). However, since the integration time is limited to around one minute and the total integration time is likely on the order of 50 hours, this is computationally infeasible. Both the final output data volume and computational time were too large for the computing resources I could access. Instead, I simulated groups of detector integrations e.g. a single simulation of a 1 hour observation is made of a group of 60 detector integrations, which are each $60\,\mathrm{s}$ long.

For each group – referred to as 'sub-simulations' – I scaled the noise appropriately so that it is equivalent to the noise (including read noise) that would be present if each detector integration was simulated separately. Additionally, I account for time dependent changes in the motion of the planetary system and the airmass dependence in the tellurics. These simulations are therefore a reasonable approximation to simulating all the detector integrations individually. Since the sky rotation discussed in Section 4.4.1 is included in the sub-simulations but cannot be corrected for since there is only one output image, I limit the length of the sub-simulations to 1 hour in Section 4.8 and 30 minutes in Section 4.6 in order to prevent the exoplanet's signal from moving over more than 3 spaxels or approximately one spatial resolution element.

4.5 Constraining the orbit of Proxima b

In this work, I assume an orbital solution for Proxima b, as it is currently not well constrained. To constrain Proxima b's full 3-D orbit and know its location precisely at any time, the line-of-sight measurements of Proxima Centauri's motion measured with radial velocities (Anglada-Escudé et al.

2016; Jenkins et al. 2019; Damasso et al. 2020; Faria et al. 2022) could be combined with astrometric measurements of the star's on-sky motion. Gaia's astrometric precision for Proxima Centauri is approximatly 7 μas (Lindegren et al. 2021) and it is not expected to improve significantly by the end of GAIA's mission having already reached the noise floor of the instrument. Accounting for the change in true mass as the orbital inclination increases, Gaia could be sensitive to the astrometric motion of orbits with inclinations less than $\simeq 8°$. However, this is at the limits of Gaia's sensitivity and it is likely a number of measurements would be required to usefully constrain the orbit of Proxima b. Gaia's observing cadence for this system may not be sufficient for this task.

An alternative would be to measure the on-sky position of Proxima b via direct imaging or molecule mapping. JWST does not have the spatial resolution to image Proxima b and a detection via direct imaging is unlikely with current planned instrumentation for the ELT. Further into the future (2040s), the Large Interferometer for Exoplanet (LIFE) will be able to directly image this system but the Habitable Worlds Observatory (HWO) probably will not (Carrión-González et al. 2023). However, with molecule mapping, a different integral field spectrograph (e.g. METIS@ELT[5]) or long-slit spectrograph on a large telescope may provide suitable constrains. Such observations would have to be simulated to properly determine the level of constrain they could provide.

4.5.1 Using what we already have

Assuming the orbit of Proxima b is not constrained any better than it currently is, it is still possible to proceed with these HARMONI observations. From radial velocity studies, the time at which Proxima b reaches quadrature is known. During quadrature, Proxima b will be maximally separated from Proxima Centauri on-sky and there will be a sufficient Doppler shift between the two spectra[6]. At this time, approximately half of Proxima b's surface should be illuminated and thus the observing criteria from Section 4.4.3 have been met.

If observations could be scheduled for a small orbital phase range around one of the quadrature points then, to align the planet's signal, the observations will only need to be aligned to the equatorial coordinate system and Doppler shifted to remove the barycentric motion. This could allow Proxima b to be characterised without the knowledge of its full 3-D orbit.

[5]METIS has larger spaxels and lower spatial resolution as it operated at longer wavelengths so is less impacted by the change in the position the planet during a night of observations. However, it should be possible to identify the position angle of the planet at maximum elongation.

[6]As long as the orbit is not too close to face-on.

Date	Average Separation	Average Fractional Illumination
2030-04-02	68.3 mas	0.70
2030-04-03	74.5 mas	0.52
2030-04-09	74.0 mas	0.56
2030-04-10	65.5 mas	0.74
2030-04-13	65.9 mas	0.73

Table 4.7: The dates of the simulated observations along with the separations and fractional illuminations of the fiducial planet (not Proxima b) during the observation. Higher illumination fractions can only be observed at smaller star-planet separations so there is a trade off between increased flux and increased contamination.

4.6 Molecule mapping with HARMONI@ELT

Proxima b has a maximum separation from Proxima Centauri of 37.3 mas. This puts it within the inner working angle of the smallest apodiser – SP1: ~ 40 mas or $5\lambda/D$ at 1.538 µm – however, the molecule mapping technique can operate within this limit (e.g. Hoeijmakers et al. 2018b). Unfortunately, its orbit is completely covered by even the smallest of HARMONI's FPMs – 50 mas by 58 mas – which prevents HARMONI from observing Proxima b in its current design configuration.

Before determining what kind of design changes may be required to observe this planet, in this Section I will demonstrate that a planet like Proxima b can be detected with HARMONI, if it were not behind the mask. To do this, I simulated observations of a 'fiducial exoplanet', optimally located in the middle of the dark annulus, and assumed to have the same parameters as those in Tables 4.3 and 4.4, but with a semi-major axis two times that of the real Proxima b, i.e. at 0.097 au (74.6 mas). Note that while this puts the 'fiducial exoplanet' in the centre of the dark annulus created by the apodiser, it is not a physically realistic system.

I simulated observations using the instrument setting shown in Table 4.2 for the five nights in Table 4.7, chosen based on when the fiducial exoplanet is observable. For each night, I simulate six sub-simulations of 30 detector integrations of 60 s – near but not at the persistance limit. The simulation for the 2nd of April 2030, with all six sub-simulations stacked, is shown in Figure 4.3.

4.6.1 Isolating the exoplanet's spectrum

In order to detect the exoplanet's spectrum, I used the following steps to remove the contaminating stellar and telluric spectra.

Step 1: The crosstalk was removed to first order by subtracting the original spectrum of each adjacent pixel on the detector multiplied by the crosstalk (0.02).

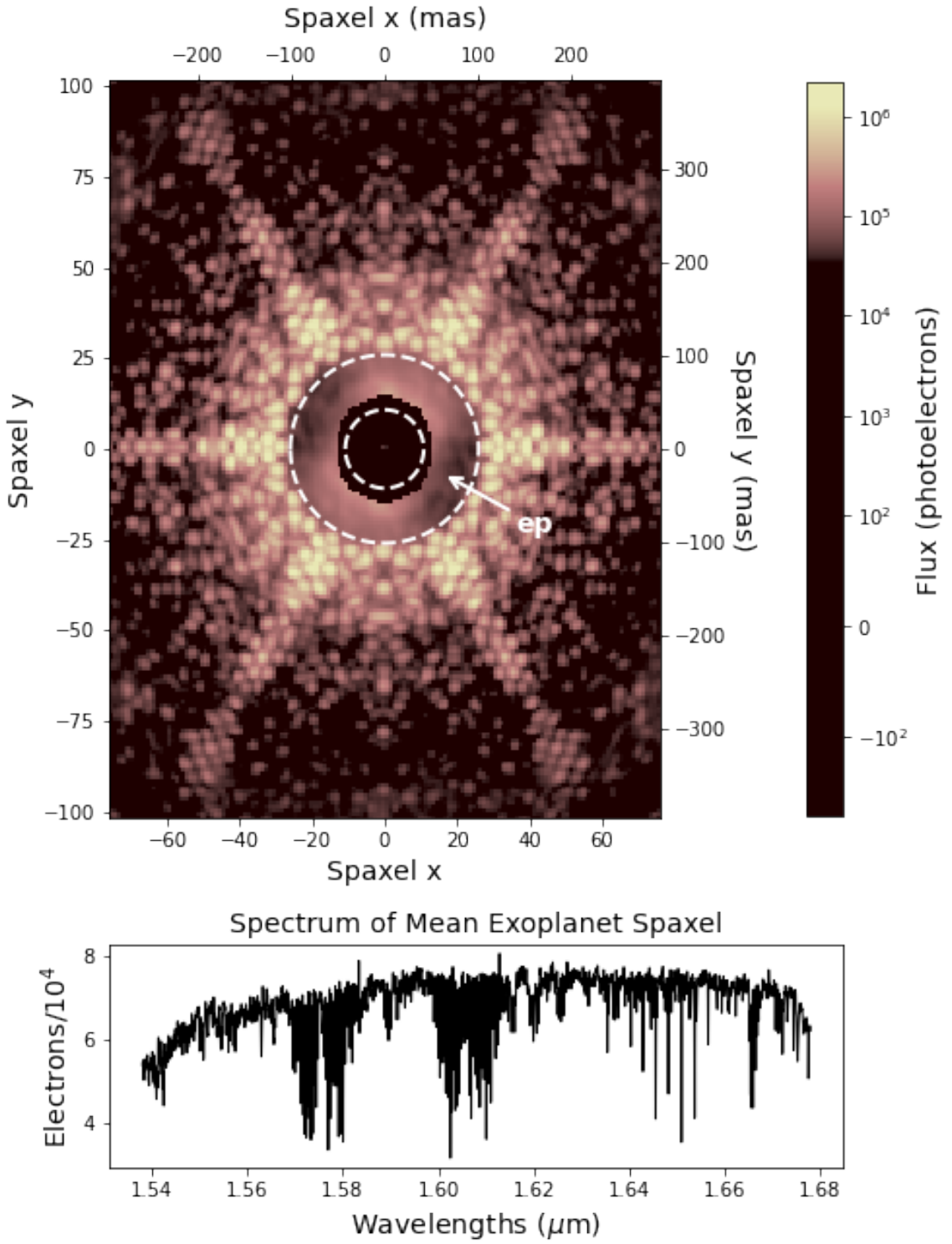

Figure 4.3: The fiducial simulation for the instrument mode shown in Table 4.2. **Top panel:** the on-sky image at a single wavelength for 3 hours of observations. The mean position of the planet is indicated by the 'ep' label but it is too faint to be seen directly. The inner and outer working angles of the apodizer are indicated by the dashed lines showing that the FPM is larger than the inner working angle. The diffuse emission inside the dark annulus is the wind-driven halo. **Bottom panel:** the spectrum of the 'ep' spaxel. It is largely dominated by tellurics and the stellar spectrum.

Step 2: The background spectrum was removed by subtracting the median spectrum of the $1,000$ spaxels with the lowest total flux excluding spaxels within the FPM.

Step 3: The stellar and telluric contamination was removed using the method in Hoeijmakers et al. (2018b) which subtracts the smoothed continuum of each spaxel, multiplied by mean spectrum of the $10,000$ spaxels with the highest flux.

The first step was required in order for subsequent steps to effectively remove the stellar contamination. I chose the parameters used in the latter two steps through trial and error and selected those that gave the best signal-to-noise out of the parameters tested. Figure 4.4 shows the simulated data before this analysis and after step 2 and step 3.

4.6.2 Extracting the exoplanet spectrum

As described in Section 2.3.3, to extract the fiducial planet's spectrum from the noise, I cross-correlate the residuals with a model of the exoplanet's spectrum. The model spectrum I use as the cross-correlation template is an exact match to the planet's spectrum in the simulated data.

For each sub-simulation, I cross-correlated with the model spectrum, Doppler shifted to a range of velocities centered on the injected velocity of the planet so that its signal is velocity-aligned. This produces a cube, with two spatial dimensions and one velocity dimension, of cross-correlation functions, hereafter a 'CCF cube'. I then de-rotated these so the expected position of the planet is in the same spatial location. Finally, I added the CCF cubes from each sub-simulation together to create the final CCF cube for the full integration time.

I converted the final CCF cube into signal-to-noise by dividing the cross-correlation coefficients of each spaxel by the standard deviation of these coefficients. I excluded the velocities expected to include the main peaks in the model's auto-correlation function – a $168\,\mathrm{km\,s^{-1}}$ window centered on the velocity of the planet. Figure 4.5 shows two slices of the final CCF cube created from the fiducial simulation with a $S/N = 7.4$ detection of the planet's spectrum at the expected position and velocity.

4.7 Comparison with Houllé et al. (2021)

As discussed in Section 4.4.5, I use a somewhat idealised PSF and simulate groups of integrations (sub-simulations) rather than simulating each detector integration separately. These simplifications are not made in Houllé et al. (2021) who simulated giant, widely separated exoplanets with HARMONI, so a comparison could highlight the effects of these assumptions. Unfortunately, a direct comparison is

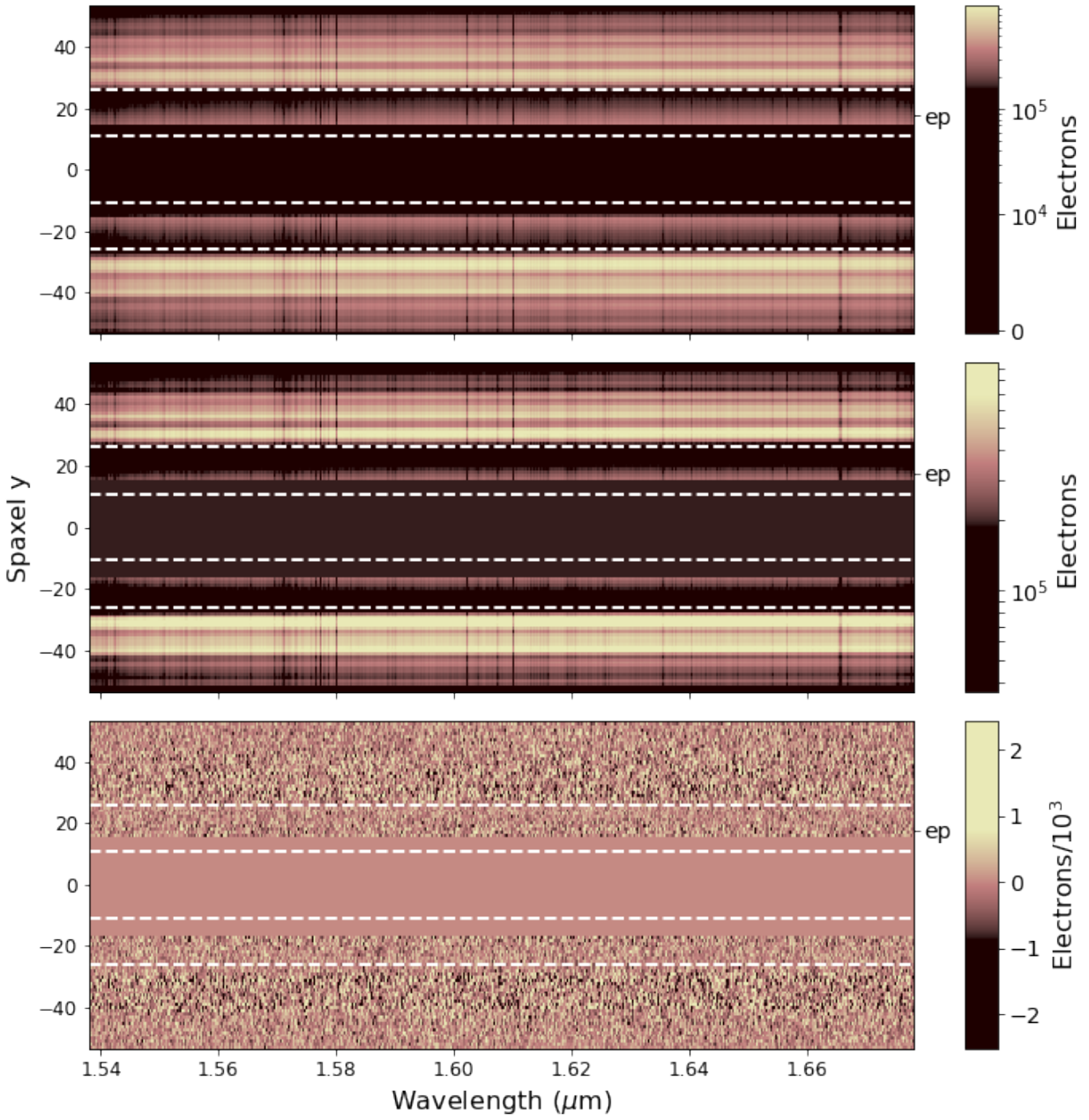

Figure 4.4: A demonstration of the data reduction as applied to the fiducial simulation. Each panel shows the stacked sub-simulations residuals for one of the simulated nights for a slice along the spaxel $x = 0$. For visual purposes, these have been de-rotated to show the residuals at the exoplanet's location – indicated by 'ep'. Additionally, the dashed lines show the locations of the inner and outer working angles of the apodizer. **Top panel:** the original flux; **middle panel:** the residual after step 2; and **bottom panel:** the residuals after step 3 which this appears to only contain residual noise with the exoplanet's spectrum still not visible. The region covered by the FPM is masked in the middle and bottom panels.

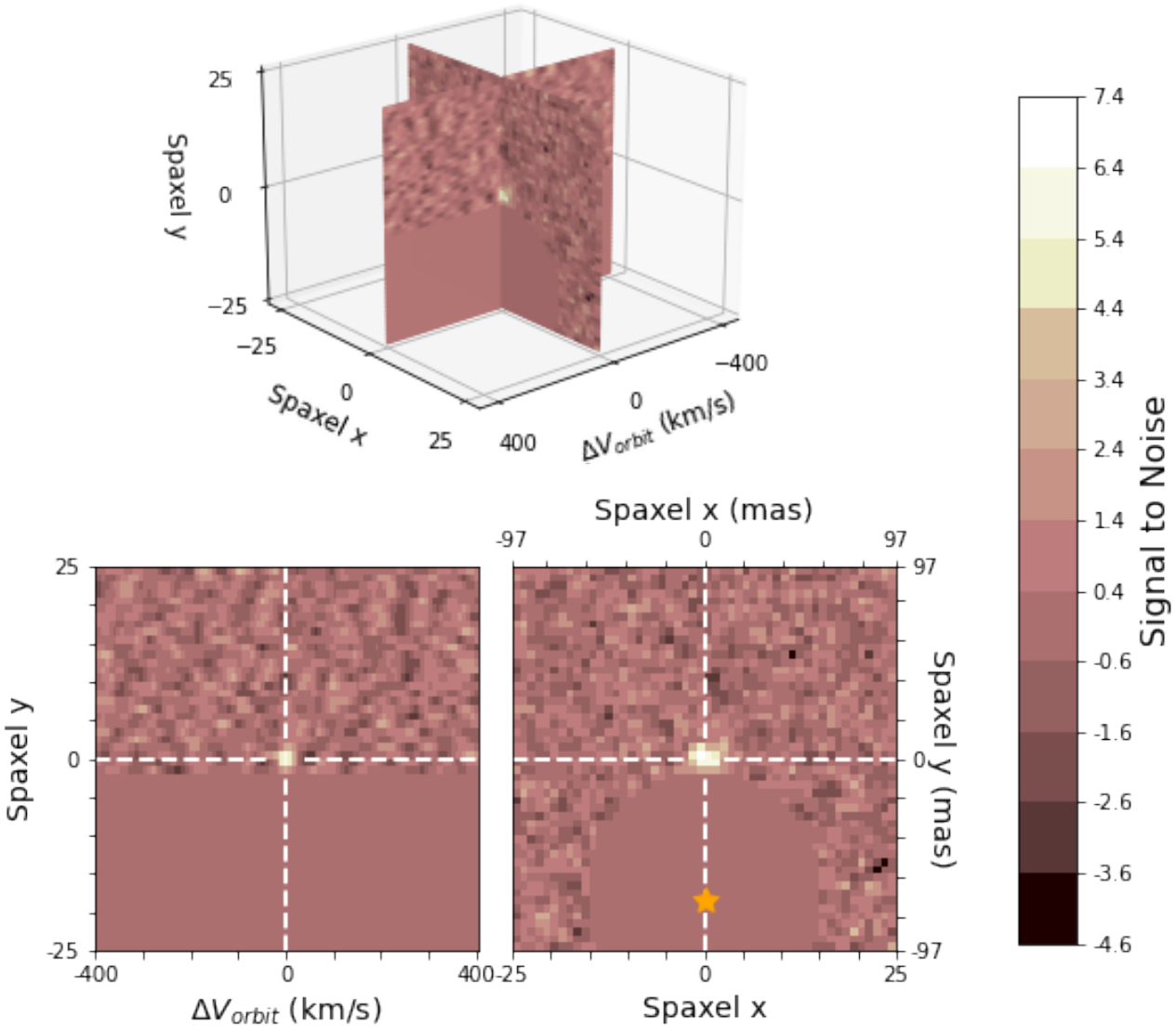

Figure 4.5: The recovered signal-to-noise of the fiducial planet spectrum. Note the region covered by the FPM is masked. **Top panel:** two slices of the CCF cube, one in the plane on the sky and one along the velocity axis. **Bottom panels:** the same two slices separated for clarity with white dashed lines indicating the expected position of the signal. Note the different x-axes. **Bottom left panel:** the signal-to-noise for the spaxels along $x = 0$ for different velocities relative to the exoplanet's velocity. **Bottom right panel:** the signal-to-noise of all the spaxels with the model Doppler shifted to the exoplanet's velocity. The yellow star symbol indicates the location of the host star. The signal is slightly spread out in the x axis due to the sky rotation in the sub-simulations.

not possible as their method for computing the signal-to-noise of the detection requires individual detector integrations to be simulated. Additionally, differences in methods used to isolate the exoplanet's spectrum could alter the efficiency with which the planet is detected. This is hard to quantify and is not investigated here but it will impact the real observations.

To perform a rudimentary comparison, I created a simulation using the same spectral models (ATMO companion model at $T_{eff} = 800\,K$, log(g)$= 4.0$; Phillips et al. 2020), Doppler shifts and airmasses as in Houllé et al. (2021). I inject the planet at the following separations: $60, 75, 100, 125, 150, 175, 200$mas. I isolate the planet's spectrum as in Section 4.6.1 and cross-correlate and compute the signal-to-noise as in Section 4.6.2. Houllé et al. (2021) provided me with an example data set and their contrast curve for comparison.

The contrast curve for a $S/N = 5$ detection with 2 hours of integration time and its equivalent from Houllé et al. (2021) for a 5σ detection are shown in Figure 4.6. The absolute values should not be compared, however the similarity in the shape and order of magnitude indicates that the simulations used in this work are valid and a reasonable approximation of previous work.

It is worth reiterating that these observations will be pushing the limits of what HARMONI could achieve and it is ultimately very hard to predict how an instrument will behave prior to its operation. Once HARMONI is in operation, observations of wider-separated and brighter planets could be used to reevaluate the feasibility of these observations. However, any changes in instrument design required to facilitate these observations would have to be committed to hardware before HARMONI's true performance is known.

4.8 Observing Proxima b with HARMONI@ELT

As shown in Section 4.6, a planet like Proxima b could be detected with HARMONI if it were not behind the focal plane mask. However, to observe the real Proxima b with HARMONI using the current design, the instrument would have to be operated in a non-standard way so that the mask does not cover the planet. Proxima Centauri would be offset from the centre of the field of view such that the mask would not cover the on-sky location of Proxima b. In principle, this offset should not affect the performance of the AO system even with Proxima Centauri as the AO guide star.

Alternatively, the real Proxima b could also be observed by HARMONI with the implementation of a relatively minor change to the instrument design – a new FPM. Unfortunately, due to space limitations, it is not possible to add additional apodizers or FPMs to HARMONI. Therefore adding a new FPM would mean replacing one of the current masks. This could be accomplished during construction or

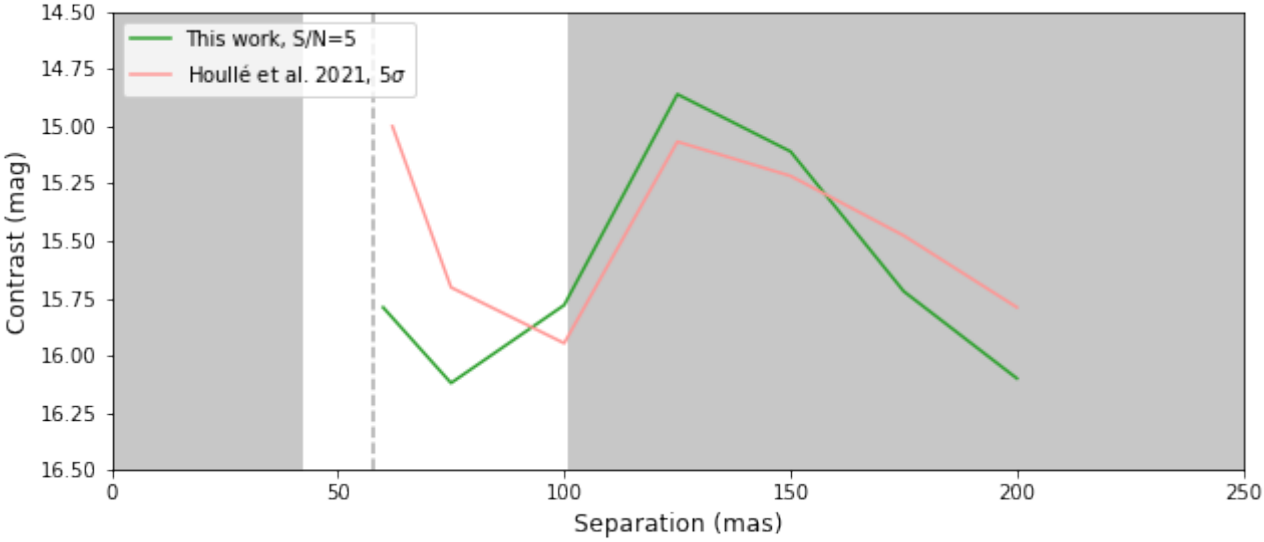

Figure 4.6: A contrast curve for an $S/N = 5$ detection of a T-type dwarf companion ($T_{eff} = 800\,K$) with 2 hours of integration time as a function of the exoplanet-star separation (green) using the simulation process and analysis described in this Chapter and its comparison 5σ detection (pink) curve from Houllé et al. (2021). The regions outside the inner and outer working angles for the apodizer are shaded and the edge of the focal plane mask at its widest point is indicated by the dashed line. Speckle noise reduces detection efficiency at around $125\,mas$. The curves cannot be directly compared as they use different signal-to-noise metrics although the order of magnitude and shapes broadly agree.

operation; however, the latter would likely only occur during a scheduled intervention approximately 5-10 years after first light as the instrument would need to be warmed up and opened for this change to be made because the FPMs sit in the cryogenically cooled part of the instrument. Such a change would require a careful assessment on the impact to other science cases. The first step would be to determine the benefit of using a new mask over offsetting the old one.

During the analysis, I treat each simulated observation separately due to the changes in relative positions and velocities of the star, planet and Earth. I isolate the planet's spectrum as in Section 4.6.1 and extract it as in Section 4.6.2 assuming a perfectly matching cross-correlation model. I assume that the orbit of Proxima b is already known at the time of the observations and has the parameters in Table 4.3. This allows the observations to be simulated only when the planet is not behind the mask and makes it straight-forward to align the planet's position for each observation. Section 4.5.1 discusses how these observing and analysis strategies could be modified if the orbit is not known.

For the offset case, I simulated 70 observations spread out over two years. Each observation has a total of one hour integration time, using a detector integration time of $60\,s$. For the new FPMs and no FPM cases, I simulated a similar set of 56 observations spread out over two years – using the same set of dates for all three cases. While the offset case uses a different set of dates, the average separation and illumination fraction of Proxima b is similar (see Table 4.8).

	Average Separation	Average Fractional Illumination
Offset mask	35.5 mas	0.63
Other cases	36.9 mas	0.56

Table 4.8: The average separation and fraction of the planet illuminated for the set of dates used in the offset mask simulation and the other cases simulated.

With a 60 s integration time, the detector is near but not at the persistence limit in the circular and elliptical cases. However, the airmass of these observations has to be restricted due to starlight leakage around the circular mask caused by atmospheric dispersion. In the no FPM simulation, the core of the PSF is over the persistence limit. This solution is not permitted by the instrument team as it will create afterimages in subsequent observations however, it serves as a good baseline to compare the performance of the other masking options.

4.8.1 How much observing time is needed to detect Proxima b?

To compute the amount of observing time that would be needed to detect Proxima b in each of the masking scenarios, I stack the CCF cubes for each simulated observation and convert them to signal-to-noise as in Section 4.6.2 with the detection being measured as the maximum at the planet's velocity in a three-by-three spaxel grid surrounding its expected position. The signal-to-noise as a function of the integration time (number of cubes stacked) is shown in Figure 4.8. There is significant variation in the recovered signal-to-noise depending on which of the cubes are stacked. The one sigma deviation of this variation is calculated by stacking randomly chosen observations together (no repeats) up to 4000 times. This is shown as the shaded region in Figure 4.8. This variation is due to i) differences in the stellar contamination depending on the on-sky location of the planet, ii) changes in the amount of Proxima b which is illuminated, and iii) the random nature of the noise.

Assuming a signal-to-noise of 5 as the detection threshold (see e.g. Cabot et al. 2019; Spring et al. 2022), a detection of Proxima b with the assumed orbital orientation will require around a minimum 20 hours of observations on HARMONI@ELT. The circular FPM and no FPM cases require the least time with between 12 to 30 hours being required. The elliptical and offset masks required longer, with 18 to 45 hours and 14 to 43 hours being required respectively. However, see Section 4.8.4 for a discussion on which mask is ultimately the best choice.

In Equation 2.3, the signal-to-noise of the detection scales with the square root of the number of observations i.e. the photon noise. However, as discussed in Section 4.4.5, this equation is not valid in this case as the planet's spectrum is not photon noise dominated in these observations. This is reinforced by the results in Figure 4.8 which do not scale with the square root of the integration time.

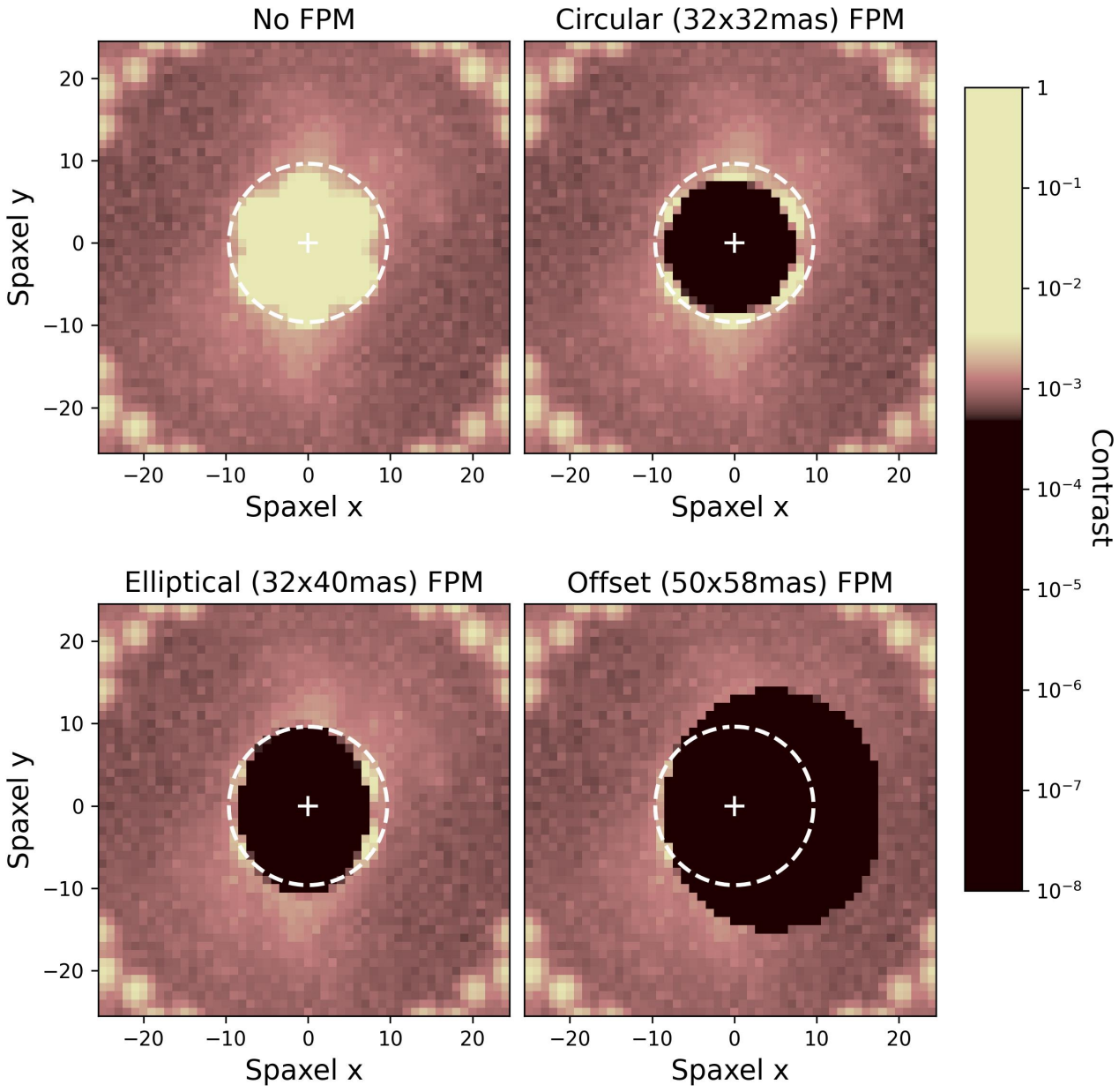

Figure 4.7: FPM's analysed in this work displayed on a map of the stellar PSF. The white cross indicates the position of the star and the white dashed line is the maximum separation of Proxima b, that is Proxima b will always lie somewhere inside this circle assuming the adopted orbital solution. Starlight leaking around the edge of the mask will scatter and may increase the stray light in the instrument. This is not modelled in the simulation.

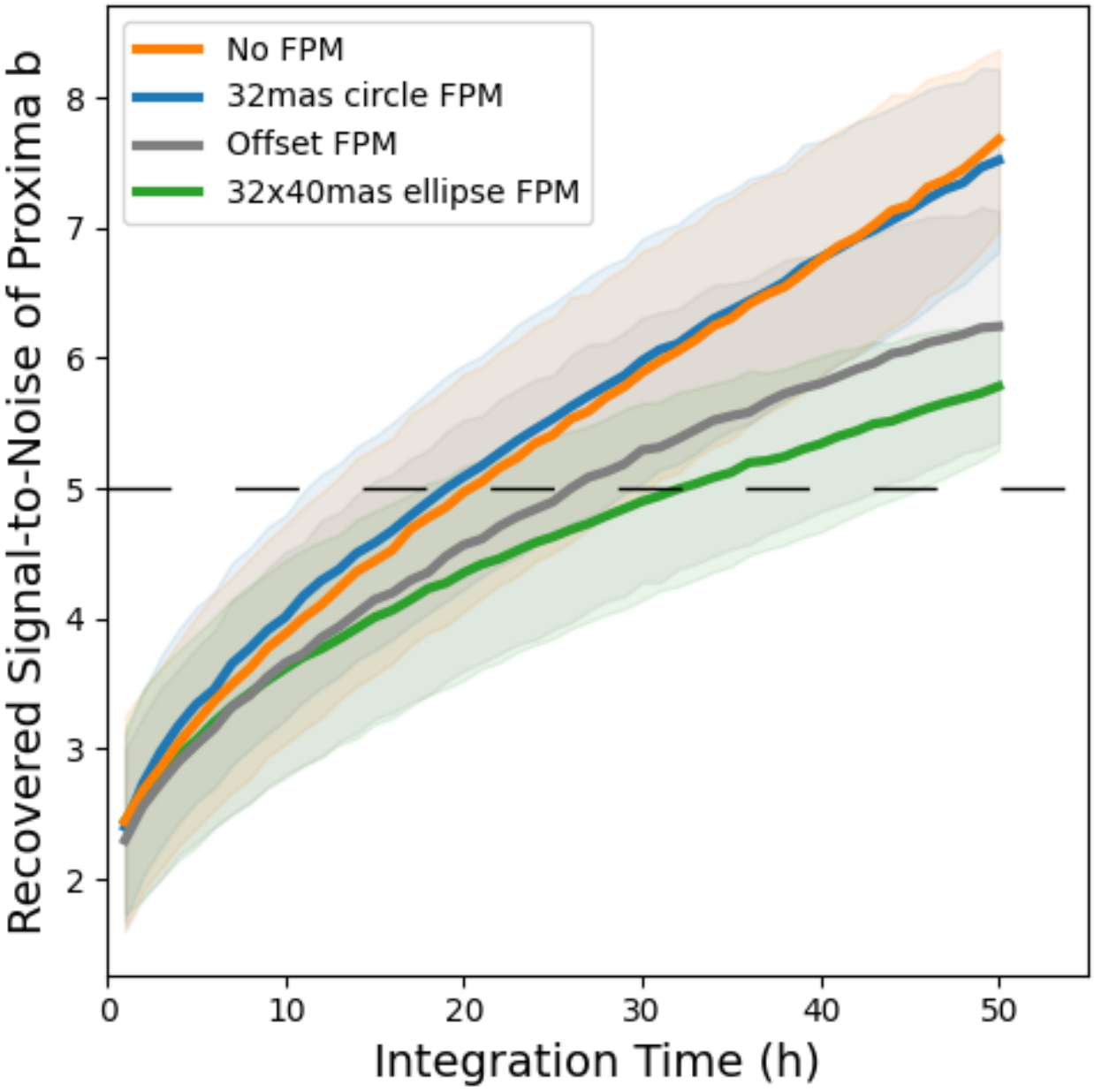

Figure 4.8: Average recovered signal-to-noise of Proxima b with the threshold signal-to-noise of 5 is indicated by the dashed line. The standard deviation in the recovered signal-to-noise is indicated by the shaded region and shows significant variation from the mean. See Section 4.8.4 for a discussion of the implications of using these options and ultimately which is the most suitable. Note the signal-to-noise does not follow $\sqrt{\text{time}}$ i.e. it does not scale with the photon noise.

4.8.2 Can the atmosphere of Proxima b be characterised with HARMONI@ELT?

As discussed in Section 4.2 the detection of key biomarker species is of great interest for Proxima b. To determine which biomarker molecules HARMONI could detect on Proxima b, I reanalyse the no FPM simulation, as it was the best performing case, with the following cross-correlation models:

1. full model spectrum (planet absorption features and stellar features) used in Section 4.8.1.
2. the stellar spectrum (no planet absorption features) shown in the top panel of Figure 4.2.
3. only the planet's absorption lines (no stellar features) which is the spectrum in the bottom panel of 4.2 divided by the spectrum in the top panel.
4. only the CO_2 lines of the planet.
5. only the CH_4 lines of the planet.

The recovered signal-to-noise as a function of time for these models is shown in Figure 4.9.

With the full model (1), the detection threshold is reached in approximately 20 hours which increases to 40 hours if the stellar lines are not included in the model (3). However, using only the stellar lines (2) does not lead to a strong detection. This is likely due to imperfections in the cleaning process which leaves behind some of the stellar contamination. This contamination correlates well with the model and prevents a robust detection. The CH_4 in the assumed spectrum from Proxima b is more detectable than the CO_2 even though CO_2 has deeper features. This is because, similar to model (2), the CO_2 model is more susceptible to residual contamination. This is because, as described in Section 4.6.1, the data reduction involves making a model of the spectral lines at high resolution and subtracting this model multiplied by a continuum model from the data. Since the telluric contamination has a multiplicative effect on the spectra, this data reduction method may not perfectly clean the telluric lines. In this analysis, this results in the signal-to-noise of the residuals growing as fast as the signal-to-noise of the planet grows which prevents the detection of the planet's signal. For the CO_2 model strong side wings in the auto-correlation function increase the amount of residual noise more than the CH_4 model preventing the detection of CO_2 but not CH_4.

4.8.3 Is the time required feasible?

Since Proxima b has limited observability, it could be that the required observing time is not obtainable over the lifetime of the ELT. To determine if this is the case, I calculated the observing time available between midday on the 1^{st} January 2030 and midday on the 1^{st} January 2031 assuming the following

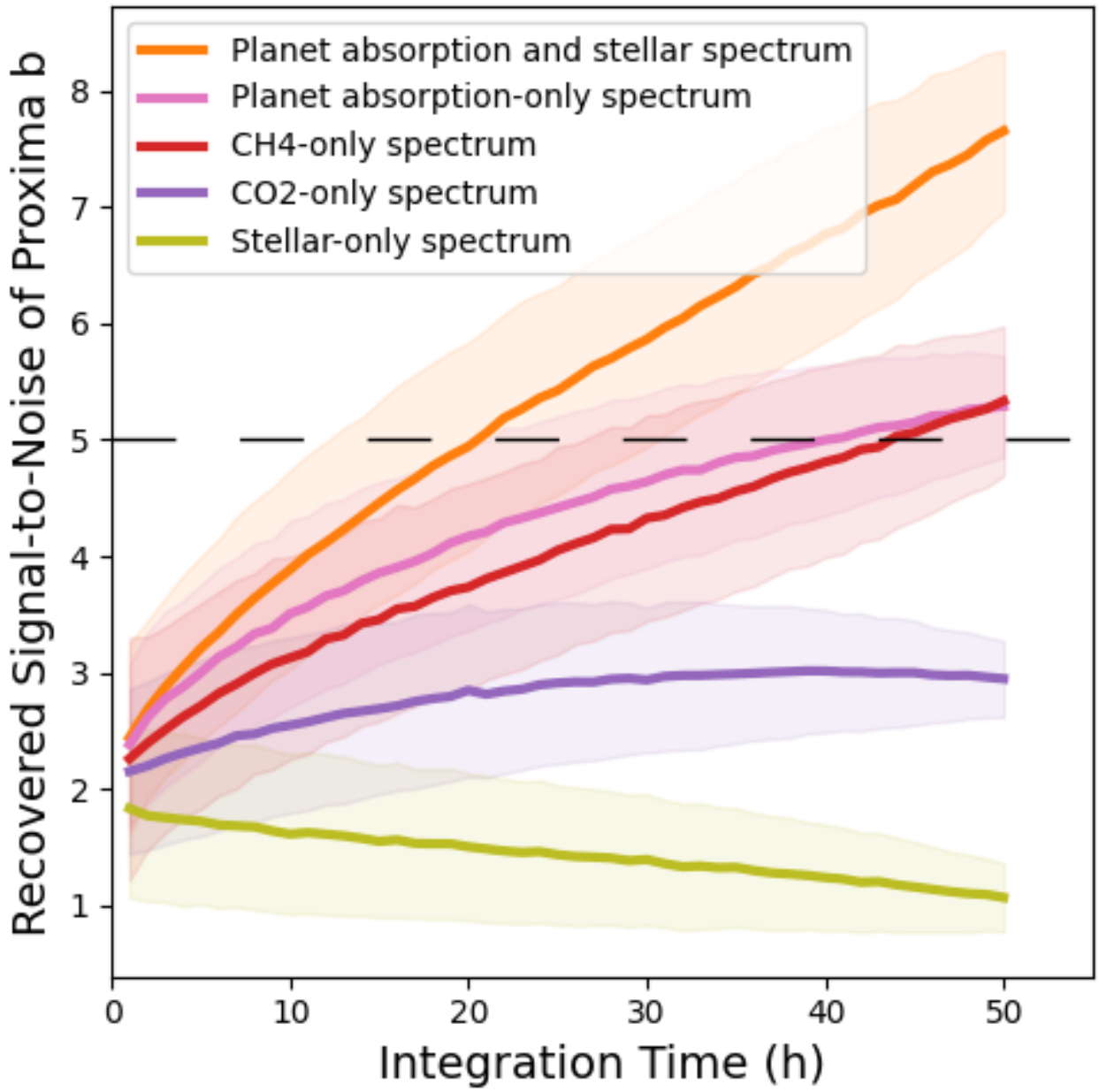

Figure 4.9: The average recovered signal-to-noise of Proxima b for the no FPM simulation as a function of integration time when cross-correlated with the stellar spectrum only model (yellow), planet absorption only model (pink), the model planet spectrum (atmospheric absorption and reflected stellar lines, orange), a model containing only the planet CH_4 lines (red) and a model containing only the planet CO_2 lines (purple). The 1σ variation in the recovered signal-to-noise is indicated by the shaded region.

observing criteria:

1. It must be nautical twilight or darker at Paranal.
2. Proxima Centauri must be more than $45°$ in elevation above the horizon at Paranal.
3. Proxima b must not be behind the FPM at any time.
4. Proxima b's velocity must be at least $1\,\mathrm{km\,s^{-1}}$ different from Proxima Centauri's and Earth's.
5. In the 'no FPM' case, Proxima b is not on a spaxel which is above the persistence limit.
6. For the circular and elliptical FPMs, there are no spaxels above the persistence limit assuming an integration time of $60\,\mathrm{s}$.

Criteria 1-5 are the same as in Section 4.4.3. I do not calculate the time available for the offset case as the range of offsets that do not significantly affect the AO is currently undetermined. For the remaining case, the time available, for a range or orbital orientations described by the inclinations and longitude of the ascending node, are shown in Figure 4.10.

Assuming all observations need a seeing better than $0.57''$, then around 30 per cent[7] of the time available can be used. With the circular mask and no mask it is possible, in most cases, to obtain 20 hours of integration time under the right conditions within ~ 1 year with the exception of near face-on orbits. For the elliptical mask it may take longer as some orbits more frequently align with the elongated direction of the mask than others. Near face-on orbits have very little time available due to the velocity criterion. However, the inclinations where this effect is significant correspond to over a factor of 10 difference between the measured minimum mass and the true mass of Proxima b, which changes the amount of reflected light and therefore time required significantly.

4.8.4 Deciding on a mask

Figure 4.8 indicates that for characterising Proxima b the best to worst masks are: no FPM, circular FPM, offset FPM and elliptical FPM. However, there are other considerations when deciding on which mask to use.

Observing with no FPM using $60\,\mathrm{s}$ integrations will cause significant persistence in the detector. Ultimately, such observations are unlikely to be approved. To avoid the persistence limit, the integration time could be reduced to $\sim 0.5\,\mathrm{s}$. These observations would incur significant observational overheads,

[7] https://www.eso.org/sci/facilities/eelt/docs/ESO-193696_2_Observatory_Top_Level_Requirements.pdf

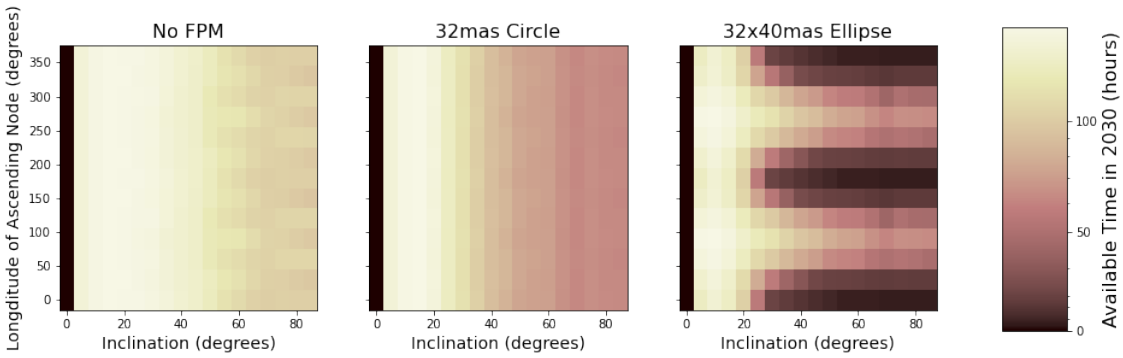

Figure 4.10: The amount of time available for which the observing conditions for Proxima b are met between 1st January 2030 and 1st January 2031 as a function of the inclination and longitude of the ascending node of Proxima b's orbit. Each plot shows the results for the different FPMs.

increasing the amount of time required. Additionally, the read noise would be increased which could hinder the characterisation of Proxima b.

The circular mask has the largest amount of light leaking around its edge and to avoid persistence with 60 s integrations, the observations are limited to low airmass. Since this will replace one of the current masks, it may affect the observability of other targets. If the apodiser were changed to make central diffraction peak more compact, then this mask could be the best option. However, these observations would need to be simulated to confirm this assessment.

While the offset mask performs well, if the orbit of Proxima b is unknown, observing with the offset mask becomes difficult as the correct offset is not known, even if observations are made at quadrature. Trial and error could be used however, this increases the amount of telescope time needed. The same is true for the elliptical FPM, however, it covers less of the orbit and so would be more efficient. Therefore, despite performing the worst, the elliptical FPM is likely the most viable option if the apodiser is not changed. I am now working with the HARMONI team to investigate changing both the apodiser and the FPM.

4.9 Summary

I have simulated observations made with the HCAO mode of HARMONI@ELT to determine the viability of using the molecule mapping technique to characterise the atmosphere of the terrestrial exoplanet Proxima b in reflected light. To observe Proxima b with this mode, the observations either have to be off-axis or an instrumental change needs to be made as the current, smallest focal plane mask fully obscures Proxima b's orbit. I use these simulations to determine if there is a significant

improvement in the detectability of Proxima b with the design change and therefore whether it would be worth considering.

I have shown that, within the caveats of the simulations, characterising Proxima b with HARMONI will require at least 20 hours and ideally at least 30 hours of integration time for a $S/N \geq 5$ detection assuming an orbital inclination of $45°$. This is not an unreasonable amount of time to request for this potentially high impact science case. The integration time required does not depend greatly on the mask used so ultimately the choice will depend on whether the orbit of Proxima b will be known at the time of the observations. If the orbit is known, then the offset mask can be used assuming the offset made is approved and the AO works stably in this configuration. If the orbit is unknown, then a new FPM would be more efficient as it could be designed to cover less of the planet's orbit. Unfortunately, the instrument's design will likely have to be committed to hardware before more information on the planet's orbit is available and careful consideration of the impact on other science cases would be required.

I have also demonstrated that the signal-to-noise of the detection is dominated by the atmospheric features in the planet's spectrum and that the stellar lines alone are unlikely to produce a detection of the reflected light. I have also shown that with molecule mapping HARMONI's H-band is particularly sensitive to the atmospheric biomarker CH_4. Importantly, I have shown the signal-to-noise of the detection does not scale with the idealised scaling, Equation 2.3, which highlights the need for such detailed simulations of future characterisation studies.

5 | Chasing rainbows and ocean glints: Could the Habitable Worlds Observatory see an exo-rainbow?

5.1 Overview

This chapter shows how the accessibility of scattering phenomena key to the detection of liquid water are affected by the inner working angle (IWA) of the Habitable Worlds Observatory (HWO). This work was presented in *Chasing rainbows and ocean glints: Inner working angle constraints for the Habitable Worlds Observatory*, Vaughan et al. (2023). This is the work of a small collaboration formed at the Lorentz centre meeting: *Optical Exoplanet Imagers*, Leiden 20 - 24th February 2023. The author list of Vaughan et al. (2023) contains the names of everyone present at the conference and the first alphabetical section lists those primarily involved in this work. I described my contribution to this collaborative work in this Section. This Chapter was authored entirely by me.

I was chosen to lead this group and as such my contribution was primarily the organisation of the analysis and writing up after the conference had ended. To that end I organised weekly telecons and supervised the writing of the paper to ensure it was a coherent piece even though different sections were written by different people – including myself. I was also responsible for seeing the paper through the publication process. To the analysis, I contributed code to the analysis to calculate the projected on-sky orbit of a planet. However, in the end we decided to go with a simpler implementation because the code was to be made public; as a result, this was not used in the final version of the work. I also led the interpretation of the results and pushed to have a discussion on contrast limits added to this work as it is an important consideration for the future of these observations. The phase curves used in this work were kindly provided by Trees et al. (2019).

5.2 Motivation

Liquid water implies the presence of a water cycle which is key to interpreting planetary habitability and atmospheric biomarkers (e.g. Meadows et al. 2018).

As discussed in Section 1.4.3, liquid water causes a number of scattering phenomena which create variations in the total flux and polarisation of an exoplanet as a function of planetary phase. For example, as shown in Figure 1.7, rainbows cause an increase in flux at gibbous phases. The planetary phase and the wavelength dependence of the rainbow feature can be used to identify the composition

and size distribution of the droplets, for example water. Additionally, ocean glint, which provides evidence of specular reflecting surfaces such as liquid water, increases the flux at crescent phases.

Therefore if the total flux or polarisation of an exoplanet could be measured at the right planetary phases, the presence of liquid water could be inferred using these scattering phenomena.

5.3 The Habitable Worlds Observatory

The Habitable Worlds Observatory is a NASA-proposed space-based telescope designed to directly detect and characterise potentially Earth-like exoplanets in the habitable zones of their host stars, in line with recommendations from the US National Academy of Sciences in their Decadal Review for a new 'Great Observatories' program (Astro2020), along with similar recommendations from ESA Voyage 2050 and the AstroNet roadmap 2022-2035. The design is still in its early stages as this telescope is not envisioned to launch until after 2040. However, it will likely be a coronagraph enabled (Astro2020), high-contrast imager with low-resolution spectroscopy at optical to near-infrared wavelengths.

The coronagraph is needed to provide the star light suppression required for high contrast imaging. Its size will be a trade off between the spatial separations it can probe and the star light suppression required.

5.3.1 Target list

There is a preliminary target list for the Habitable Worlds Observatory containing stars within 25 parsecs that have spatially resolvable habitable zones (Mamajek et al. 2024). This assumes the planet is observed at quadrature. The list has been filtered such that an Earth-like planet in the habitable zone would be brighter than 31 mag in the Cousins R_c band and have a planet-star contrast larger than 2.5×10^{-11}. This filtering limits the list to potentially detectable systems with future technology envisioned for HWO.

Overall the list contains 164 stars, the majority of which are Sun-like dwarfs along with 66 F dwarfs, 55 G dwarfs, 40 K dwarfs, and 3 M dwarfs. Proxima Centauri is not included in the list as its habitable zone is not considered resolvable (separation $> 1.22\lambda/D$) at near the infrared wavelengths HWO may cover (up to $\approx 1\,\mu\mathrm{m}$) for a $6\,\mathrm{m}$ primary mirror.

5.4 Observing exo-rainbows and glints

The range of planetary phases a planet shows depends on its orbit. In a face-on orbit, the planet is always at quadrature and only shows quarter (half illuminated) phases. On an inclined orbit, it will show a larger range of planetary phases and an edge on orbit will show the full range.

As a planet orbits its star, not only does its planetary phase change but so does its on-sky separation from its star. A planet will be half illuminated when it is at quadrature and its separation is maximum. To see other planetary phases, the planet has to be observed at smaller separations. A coronagraph is designed to cover the star and a small region around it in order to reduce the amount of star light being imaged. If the planet is within the region being blocked by the coronagraph, it cannot be observed. Therefore the coronagraph of HWO could obscure the planet at these smaller separations, as shown schematically in Figure 5.1, preventing the scattering features of interest being measured.

5.4.1 Contrast Limits

The detectability of these scattering phenomena will of course depend on the signal-to-noise at which the planet's flux can be measured which will depend on the contrast limits of HWO and the planet-star contrast. The latter is dependent on the planetary phase due to a combination of the changing illumination fraction of the observable planetary disk and non-isotropic reflection by the planet. As HWO is in the early design stage, the achievable contrast is currently unknown. Therefore this parameter is not included in the following study and instead the accessibility of different scattering phenomena[1] is evaluated instead. The results therefore represent an upper limit on the number of planets where these scattering features can be observed. However, to highlight the high-contrast requirements that will be needed to measure these features, Figure 5.2 shows an illustrative example of how the contrast of an Earth-twin varies over its orbit.

For this illustrative example, the contrast, F_p/F_s, is assumed to be given by Equation 1.1 and for all the targets in the HWO target list, the contrast is computed at quadrature for an Earth-twin. The phase function is assumed to be Lambertian (Russell 1916) that is $g(\alpha = 90°) = 1/\pi$, which is a reasonable assumption for the Earth (Pallé et al. 2003; Qiu et al. 2003). A geometric albedo A_g equal to 0.2 (Robinson et al. 2011) is also assumed and that the orbital separation is such that the planet receives the same instellation as Earth and has the same radius as the Earth. For one system, the K dwarf 40 Eridani A, I replaced the phase function with that from Trees et al. (2019) which assumes an Earth-like planet with an ocean surface, a wind-speed of $7\,\mathrm{m\,s^{-1}}$, and patchy liquid water clouds observed at

[1] Whether the coronagraph blocks the planet at the planetary phases of interest.

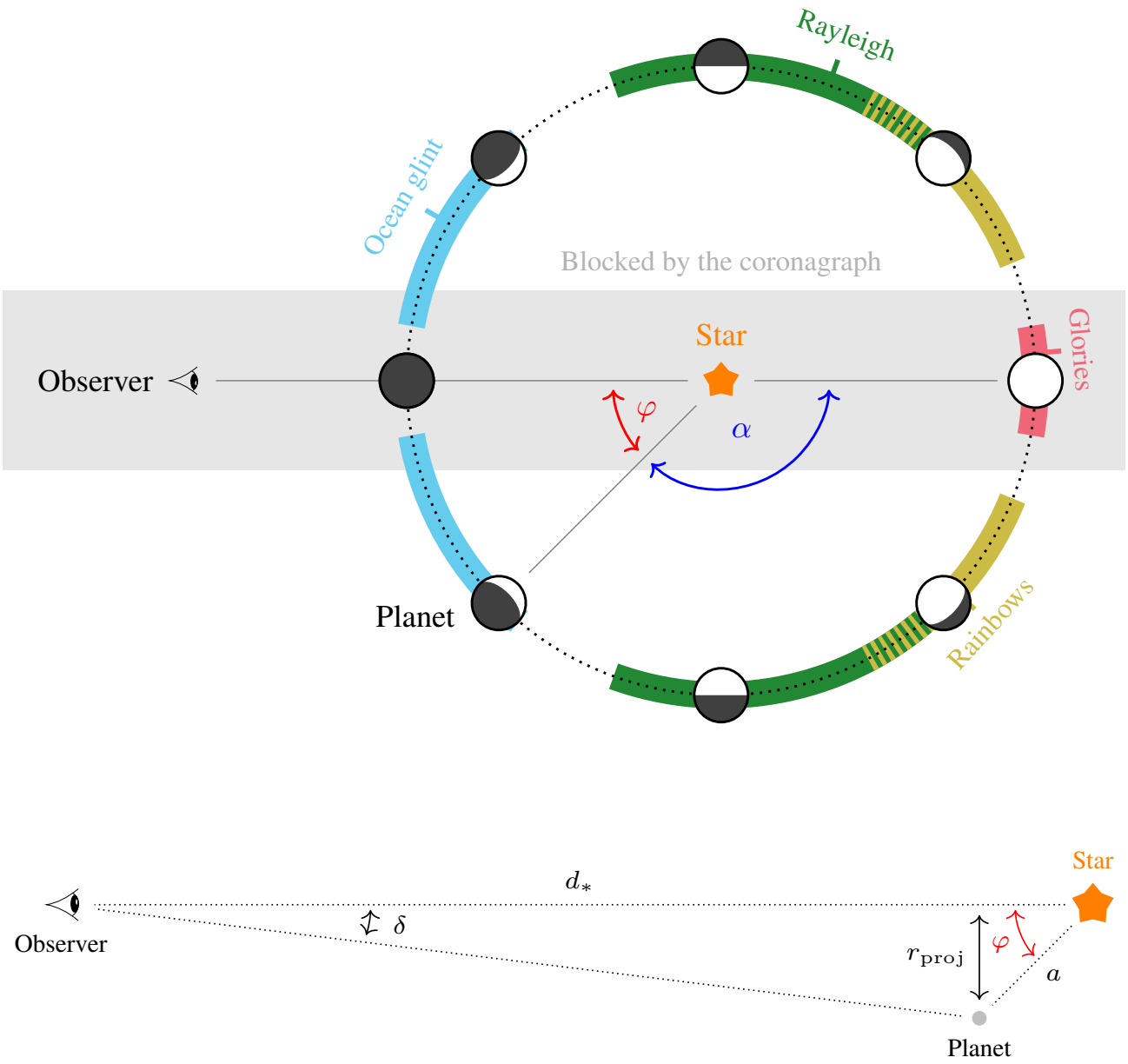

Figure 5.1: **Top panel:** A schematic showing how a coronagraph can obscure a planet at small and large planetary phases and thus prevent the characterisation of key scattering phenomena. The planetary phase angle, α, and scattering angle φ are also indicated. **Bottom panel:** A schematic showing how the angular separation of a planet from its star, δ, is related to the scattering angle φ. These are related to each other by the distance to the star, d_*, the orbital separation, a and the projected distance between the star and planet $r_{\rm proj}$. Note that $a << d_*$.

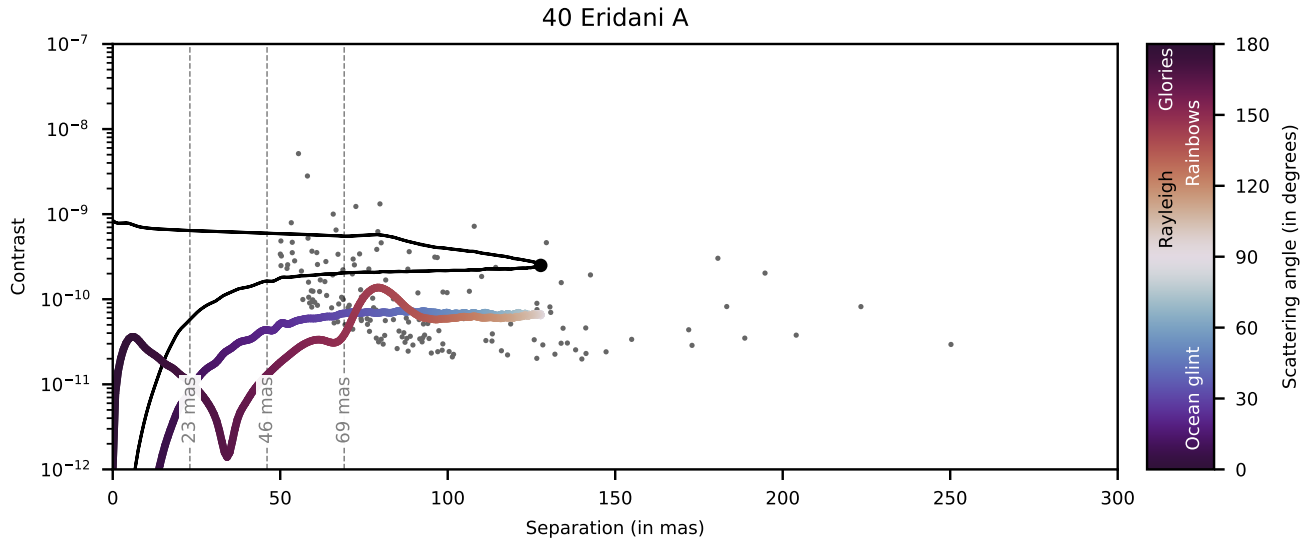

Figure 5.2: An example of the planet-to-star contrast ratio for an Earth-twin in a circular edge-on orbit around 40 Eridani A. The contrast in total flux at 670 nm is indicated by the solid black line, with the contrast at quadrature marked by a black dot. The small grey dots show the contrasts at quadrature of the other targets in the star list excluding Alpha Centauri A and B for visual clarity. The contrast for linearly polarised light at 670 nm is indicated by the coloured line where the colour represents the planetary phase. The vertical dashed lines mark 23 mas, 46 mas and 69 mas (corresponding to 1, 2, 3 λ/D at $\lambda = 670$ nm for a 6 m telescope). I chose this system in particular as it is the host star of the fictional inhabited planet 'Vulcan' in Star Trek (Ward 2016). Excitingly, the rainbow feature is accessible in this system!

$\lambda = 670$ nm. This is meant only as an example as many variables go into the modelling of the reflected flux of Earth-like exoplanets (Trees et al. 2019, 2022).

Figure 5.2 shows that overall contrast varies significantly for each system and throughout the orbit but generally, planets orbiting high-mass stars tend to offer larger angular separation but lower contrast ratios. The detectability of these scattering features will depend on whether low enough contrasts limits can be reached at the right separations. However, the ultimate limit is created by the coronagraph as the planet cannot be observed if it is behind it. Another important point to note is that the features from different scattering phenomena are more prominent in polarised light, however, the overall flux is an order of magnitude lower so careful consideration is required when deciding whether HWO will measure polarised light or total intensity.

5.5 The planetary phases accessible to HWO

The exact planetary phases at which the different scattering phenomena dominate depend on the atmospheric and surface properties of the planet as well as the wavelength. The phase angle ranges assumed for the different scattering phenomena are given in Table 5.1.

Table 5.1: The assumed ranges of the phase angle α for the scattering phenomena caused by water where the feature is present between $\alpha_{\min}$ and $\alpha_{\max}$. α_{peak} is the phase angle where the scattered flux peaks.

	$\alpha_{\min}$	α_{peak}	$\alpha_{\max}$
Glory	0°	5°	10°
Rainbow	22°	42°	63°
Rayleigh peak	50°	70°	110°
Ocean Glint	130°	150°	170°

5.5.1 Circular, edge-on orbits

For a circular edge-on orbit, the on-sky separation, r_{proj}, between the planet and star is related to the planetary phase by,

$$\sin(\varphi) = -\sin(\alpha) = \frac{r_{\text{proj}}}{a}\,, \tag{5.1}$$

where a is the semi-major axis, α is the phase angle and φ is the supplementary[2] scattering angle (shown schematically in Figure 5.1).

The maximum and minimum phase angles that are not blocked by the mask occur when r_{proj} reaches the inner working angle separation. For circular orbits, the minimum and maximum phase angles will be symmetric around quadrature. Therefore, $\Delta\alpha/2$, where $\Delta\alpha$ is the difference between the maximum and minimum phase angles, is equivalent to the angle between quadrature and either the maximum or minimum phase angle. So for a circular orbit, the range of accessible phase angles is given by,

$$\cos\left(\frac{\Delta\alpha}{2}\right) = \frac{\text{IWA}\cdot d_*}{a}\,, \tag{5.2}$$

where d_* is the distance to the star, as shown in Figure 5.1.

Figure 5.3 shows $\Delta\alpha/2$ for the systems in the HWO target list, assuming an IWA of $61.9\,\text{mas}$ which is equivalent to $3\lambda/D$ for $\lambda = 600\,\text{nm}$ and $D = 6\,\text{m}$, a reasonable assumption for the inner working angle of HWO. This shows that, for exoplanets in edge-on circular orbits, it will always be possible to observe the peak polarisation due to Rayleigh scattering, which occurs around quadrature whereas other scattering phenomena will only be accessible for a subset of exoplanets.

[2] A pair of angles are defined as supplementary when their sum is equal to 180°.

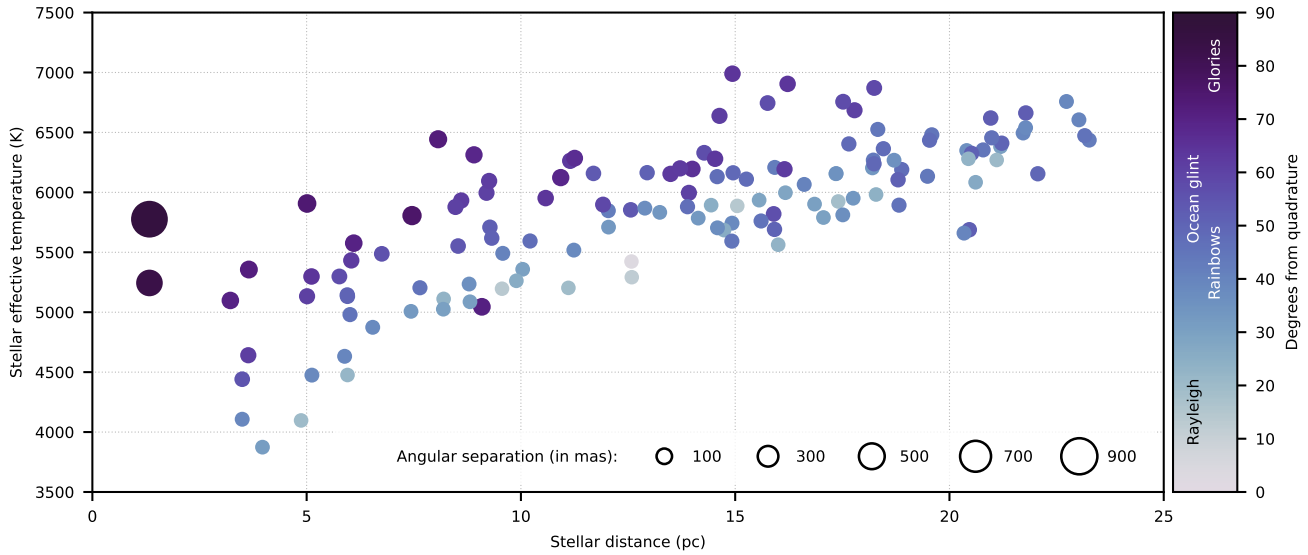

Figure 5.3: A scatter plot highlighting the range of accessible phase angles, $\Delta\alpha$, for hypothetical planets orbiting stars in the HWO target list. This figure assumes circular, edge-on orbits at a semi-major axis a corresponding to an Earth-like instellation and an IWA of $61.9\,\mathrm{mas}$. The axes show the temperature of the host star and the distance to the system. The size of the points indicates the angular separation and the colour represents $\Delta\alpha/2$. Since $\Delta\alpha$ is the difference between the maximum and minimum phase angles, and these are symmetric about quadrature, $\Delta\alpha/2$ is equivalent to degrees from quadrature. The colour bar has been labeled with the different scattering phenomena. All phenomena up to the colour of a given point will be accessible in that system so darker colours mean more phenomena are observable.

5.5.2 Circular, inclined orbits

Not all planetary systems are aligned edge on to Earth. For inclined orbits there are two regimes 1) the coronagraph does not cover any part of the sky-projected orbit, and 2) the coronagraph covers some part of the projected orbit. In regime 1, the maximum planetary phase observable is the maximum planetary phase shown by the system – which is dependent on the inclination. For regime 2, the maximum planetary phase is the same as for a circular edge-on orbit. If the inclination, i, is defined such that $i = 0°$ for a face-on orbit, the two regimes can be described by,

$$\Delta\alpha = \begin{cases} 2i & \text{for } \cos(i) > \frac{\mathrm{IWA}\cdot d_*}{a} \\ 2\cos^{-1}\left(\dfrac{\mathrm{IWA}\cdot d_*}{a}\right) & \text{for } \cos(i) < \frac{\mathrm{IWA}\cdot d_*}{a} \end{cases} . \tag{5.3}$$

For each of the stars in the HWO target list, assuming an orbital semi-major axis with Earth-equivalent-incident stellar flux, 1000[3] randomly inclined orbits were generate where the inclination was drawn from a distribution that is uniform in $\cos i$. The maximum observable phase was calculated using Equation 5.3 for each hypothetical planet assuming different values for the inner working angle. The

[3]This number is sufficiently large to provide a good estimation of the average accessibility for each star system.

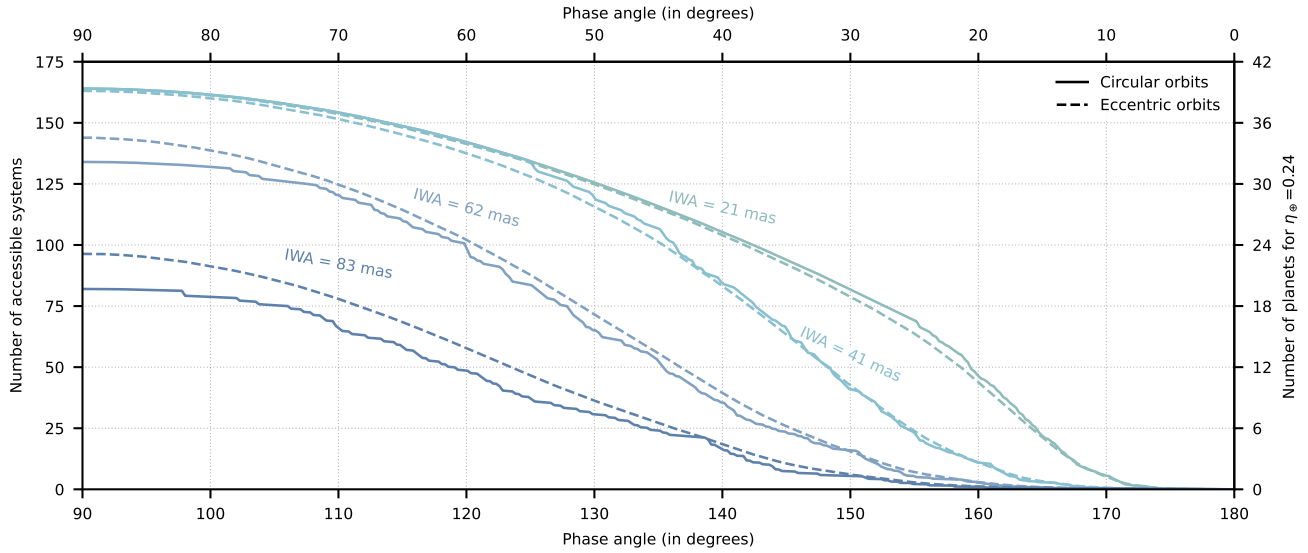

Figure 5.4: The expected number of star systems in the HWO target list for which different phase angles are accessible. These are symmetric about quadrature so the top x-axis indicates the minimum phase angle and the bottom the maximum. This is computed from the average of 1000 simulations for different IWAs where the orbit is randomly inclined and assumed to be circular (solid line) or eccentric (dashed line). The y-axis on the right assumes an occurrence rate of $\eta_\oplus = 24\,\%$ (as in Astro2020) to convert the number of systems to the number of habitable zone Earth-like planets that could be imaged at these phase angles.

cumulative distribution of the maximum and minimum accessible phase angles is shown as solid lines in Figure 5.4.

5.5.3 Eccentric, randomly inclined orbits

For eccentric orbits, the sky-projected orbits are computed following Murray et al. (2010) from which the maximum and minimum planetary phase are calculated. Another 1000 orbits are drawn for each star in the target list assuming the orbital eccentricity follows a beta-distribution with shape parameters $a = 0.867$ and $b = 3.03$ (Kipping 2013). The semi-major axis is kept the same as for circular orbits, meaning it has not been renormalised, so that the time-averaged flux is the same for all systems. The inclinations are again drawn from a distribution uniform in $\cos i$. The dashed lines in 5.4 show the cumulative distribution of the accessible phase angles for a range of inner working angles.

Eccentric planets reach orbital separations greater than their semi-major axis. This means they are more likely be viewable from behind the coronagraph albeit with worse contrast in reflected light due to the greater star-planet separation. This effect can be seen in the curves for larger inner working angles shown in Figure 5.4 as for these, the curves for eccentric orbits predict more systems where a given phase angle is accessible. For the smaller inner working angles, the eccentricity does not significantly affect the number of systems due to the selection that was used for the target list.

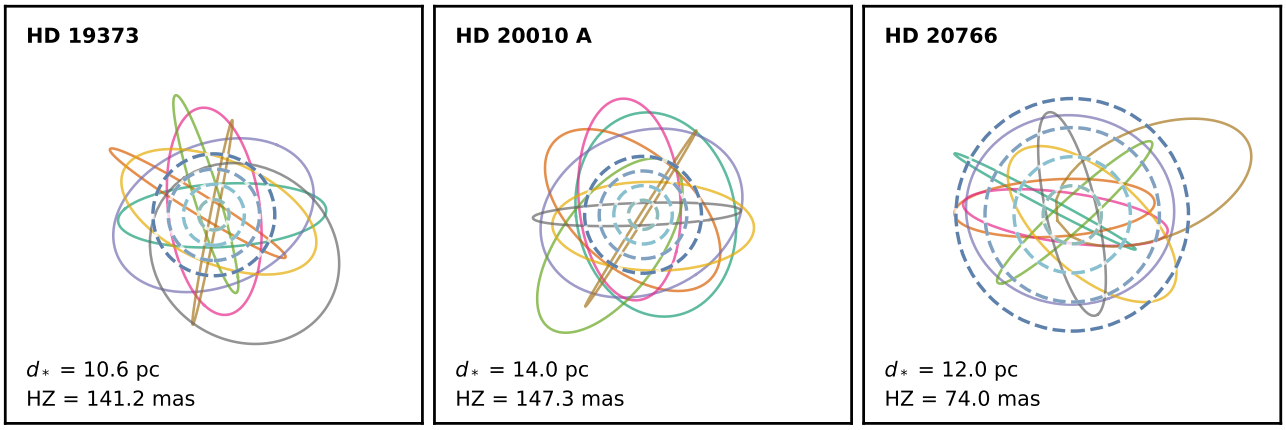

Figure 5.5: Some examples of the eccentric, randomly inclined orbits generated as part of the sample. The orbits have a semi-major axis with an Earth-like incident flux and have been scaled to the same physical size in the plots. This means the spatial scale is different in each image which can be seen with the four concentric circles indicating inner working angles of 20.6, 41.3, 61.9, and 82.5 mas. These have been coloured to match the lines in Figure 5.4.

5.6 Accessible scattering phenomena

To demonstrate how the inner working angle affects the accessibility of different scattering phenomena. Accessibility curves for eccentric orbits assuming a semi-major axis corresponding to an Earth-equivalent-incident stellar flux for a circular orbit, like those shown in Figure 5.4, are computed for a range of inner working angles. These are then used to compute the number of systems where a given phase angle is observable[4]. Figure 5.6 shows these numbers as a function of the inner working angle for phase angles of the key scattering phenomena listed in Table 5.1. These curves represent the number of systems where the phase angle of the corresponding scattering phenomenon could be observed as a function of inner working angle. This is also tabulated for a few values of the inner working angle in Table 5.2.

The Rayleigh scattering peak in polarization is observable in most of the systems in the HWO target list assuming the nominal inner working angle of 62 mas as it appears near quadrature. This feature is useful for determining if a planet has an atmosphere. The other scattering phenomena occur further from quadrature and so are accessible in fewer systems. Rainbows are still accessible in a significant fraction of systems and can be used to constrain the properties of cloud droplets although ideally the peak of the feature in polarisation would need to be reached for this. The start of the ocean glint feature is also accessible in a large number of systems although the peak is only reached in a handfull of them. However, this can still be used to identify a liquid ocean on the surface of a planet, a key indicator of habitability.

[4]This is done by taking the value of the curve at that angle.

	Inner Working Angle (IWA)			
Feature	21 mas	41 mas	62 mas	83 mas
	Number of Systems			
Glory	0	0	0	0
Ocean Glint	79	43	16	6
Rainbow	109	90	46	22
Rayleigh	154	152	125	78
	Number of Exo-Earths ($\eta_\oplus = 24\,\%$)			
Glory	0	0	0	0
Ocean Glint	20	11	4	1.5
Rainbow	27	22.5	11.5	5.5
Rayleigh	38.5	38	32	19.5

Table 5.2: The expected number of systems, out of the 164 in the list, for which the peak phase angle of each phenomenon would be accessible when assuming randomly inclined, eccentric orbits. These are converted to the approximate number of Exo-Earths that are accessible assuming $\eta_\oplus = 24\,\%$.

The results presented here assume a semi-major axis that has Earth-equivalent-incident stellar flux for a circular orbit. However, Earth is towards the inner edge of the habitable zone (Kopparapu et al. 2013) so these estimates for the accessibility of scattering features are conservative. Since the range of accessible features is determined only by the amount of the orbit covered by the mask, it is possible to scale the results presented here for different semi-major axis. This is because increasing the semi-major axis of an orbit (e.g. double) is equivalent to decreasing the apparent mask size by the same factor (e.g. half).

5.7 Summary

The Habitable Worlds Observatory is a coronagraphic space telescope, currently under development, that is envisioned to detect and characterize Earth-like exoplanets in the 2040s. If HWO measures the total flux or polarisation of an Earth-like exoplanet as a function of planetary phase, scattering phenomena linked to the presence of liquid water could be identified. However, these scattering phenomena are only observable at star-planet separations smaller than the maximum elongation which occurs at quadrature. This means that the coronagraph may obscure the planet at the phases at which these scattering phenomena occur.

An investigation was conducted on how the coronagraph size of the Habitable Worlds Observatory would affect the number of planetary systems from the HWO target list where the planetary phases of interest could be observed. Assuming a IWA of $62\,\mathrm{mas}$, $\sim 76\,\%$ of the planetary systems in the HWO target list would be accessible at phases corresponding to maximal polarisation from Rayleigh

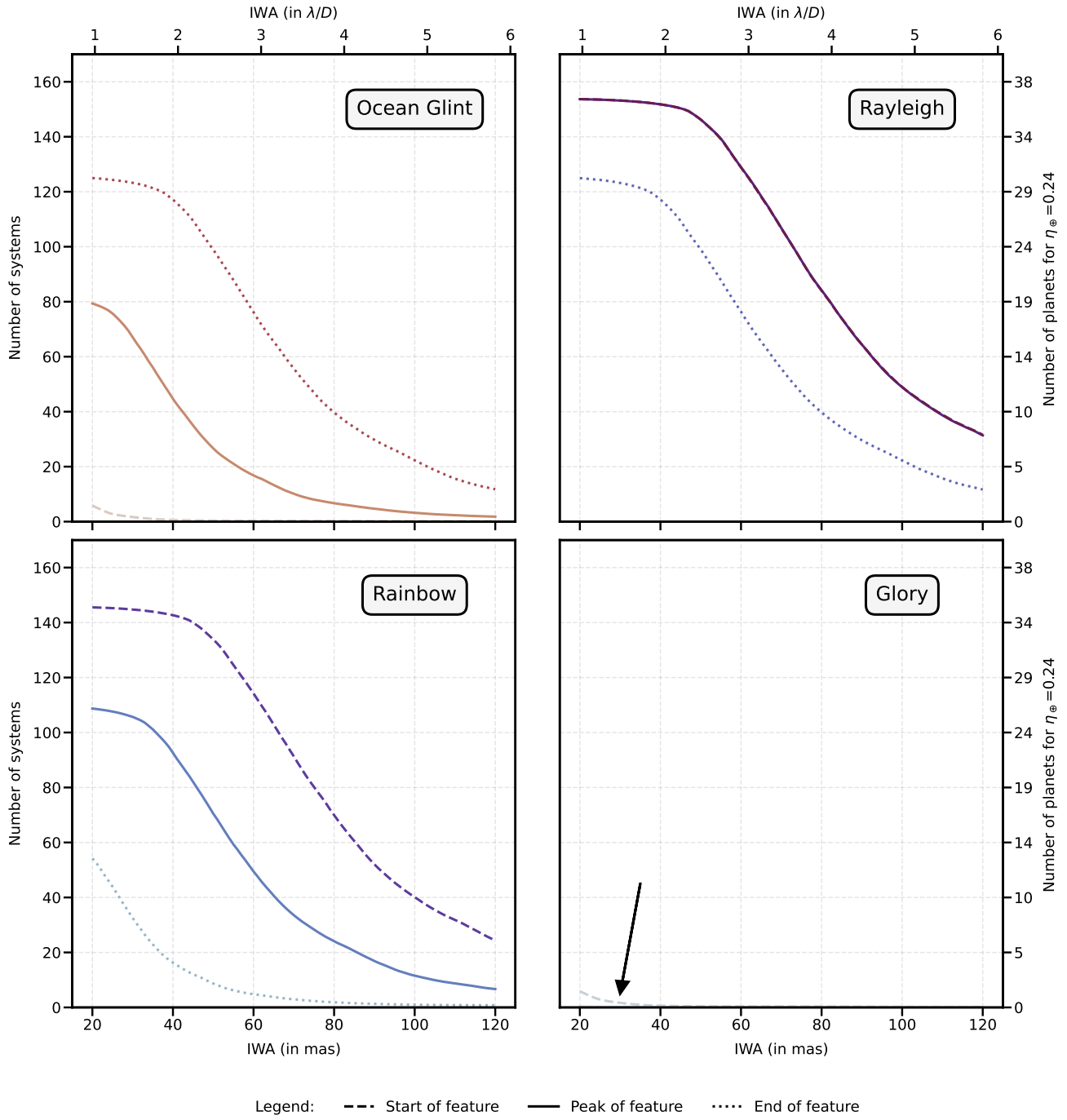

Figure 5.6: This plot shows the number of systems in the HWO target list, which contains 164 systems, where different scattering phenomena would be accessible as a function of IWA. The dashed lines indicate the number of systems where the start of the associated scattering feature could be observed, the solid lines show the peak and the dashed line, the end of the feature. The colour of the lines matches the colour bar in Figure 5.2. Note that for Rayleigh scattering the start of the feature and the peak occur on different sides but the same angle away from quadrature meaning their lines coincide. The x-axis at the top coverts the IWA to λ/D for $\lambda = 600\,\mathrm{nm}$ and $D = 6\,\mathrm{m}$. The y-axis on the right assumes an occurrence rate of $\eta_\oplus = 24\,\%$ (as in Astro2020) to convert the number of systems to the number of HZ Earth-like planets.

scattering. The peak of the feature created by water rainbows would be accessible in $\sim 28\,\%$ of systems and ocean glint in $\sim 10\,\%$. Assuming an $\eta_{\oplus} = 24\,\%$, this corresponds to approximately 22.5 and 11 Earth-like planets respectively. These latter two phenomena indicate the presence of a water cycle which provides additional context to the habitability of an exoplanet.

The size of the coronagraph will be a trade off between the angular separations that could be probed and the magnitude of the suppression of the diffracted star light. This work highlights some of the additional science that could be achieved if the coronagraph could be made smaller.

6 | Conclusions

Reflection spectroscopy is an important part of the future of exoplanet characterisation. The detection of key biomarkers, such as oxygen, on Earth-like worlds will rely on this part of the planet's spectrum due their low temperature and low transit probability. In addition to this, reflection can offer a more comprehensive understanding of the clouds, energy budget, and climate of an exoplanet. The upcoming Extremely Large Telescopes will offer us the first opportunities to characterised nearby potentially Earth-like worlds. Detections of biomarkers such as oxygen will use the reflected light of these worlds at high spectral resolution to ensure an unambiguous detection of such an important sign of life. However, the reflected light of an exoplanet has never been measured at high spectral resolution before. In this thesis, I have explored the atmospheric characterisation of exoplanets using reflected light, laying the groundwork for a roadmap towards the characterization of potentially Earth-like planets in the coming decades.

Today, exoplanet characterisation primarily focuses on the hot giant planets that have no analogue in our solar system as these are easier to detect and characterise. This means their atmospheric conditions are a mystery that can only be explored by studying exoplanets. In addition to this, these worlds offer a training ground for the characterisation techniques, such as High-Resolution Cross-Correlation Spectroscopy in reflected light, which we will be using on potentially Earth-like exoplanets in the near future with the ELTs. To be characterised in reflected light with current instrumentation, these giant exoplanets must have high albedos. Unfortunately, most of the known giant planets have low optical albedos due to the broad absorption features of sodium and potassium which has hindered past studies of these worlds.

However, some giant planets, like the Neptune-sized LTT-9779 b are known to have high albedos. This planet's high albedo may be the result of a high altitude cloud deck which makes characterisation at low spectral resolution difficult as the clouds will flatten the spectrum making measurements of spectral features tricky. However, it may be possible at high spectral resolution as the cores of the spectral lines form above the cloud deck. In Chapter 3, I show the initial analysis of my ESPRESSO@VLT PI program which used the combined power of all four VLT telescopes as the world's largest optical telescope. These data is analysed using High-Resolution Cross-Correlation Spectroscopy. I have begun the atmospheric characterisation with a search for gaseous iron which is one of the molecules most likely to be detectable. However, I have not obtained a robust detection, which requires detecting a signal with a signal-to-noise greater than five, of this molecule although there are some indications that it may be present with the current signal-to-noise of 3.75. Moving forward, I intend to investigate

different molecules and atmospheric conditions to see if I can increase the detection strength and verify its planetary origin. I will also investigate the efficiency of the cleaning process and identify potential improvements to this technique. However, in the event of a non-detection I will be able to constrain the altitude cloud deck using injection tests. This will be the first high spectral resolution study of a mini-Neptune in reflected light.

In the coming decade, the advent of the $30\,\mathrm{m}+$ class telescopes, the ELTs, will bring the characterisation of the first potentially Earth-like worlds. These large telescopes will have the spatial resolution to resolve the nearest, potentially Earth-like exoplanet, Proxima b. This system is amenable to characterisation via the molecule mapping technique in reflected light which would require an instrument such as the integral field spectrograph HARMONI@ELT. In Chapter 4, I investigated the possibility of using this instrument to characterise the atmosphere of an Earth-like Proxima b and search for the biomarkers CO_2 and CH_4. Unfortunately, HARMONI employs a focal plane mask to protect the detector from saturation but that will cover the entire orbit of Proxima b, making it impossible to observe in a standard configuration. Nonetheless, to determine if Proxima b could be characterised with HARMONI another way, I created a detailed instrumental simulation to create realistic observations. Then, by analysing these simulations as if they were real data, I explored whether Proxima b could be characterised with no modifications to HARMONI but in a non-standard observing configuration or with a change to the focal plane mask. In all cases, Proxima b could be detected in a reasonable 20–40 hours of integration time with around 50 hours being required for characterisation. This is promising but careful consideration is needed on what changes to HARMONI should be made. For example, while offsetting the current mask is feasible in these simulations, it requires knowledge of the planet's orbit which may not be available by the time the instrument is on-sky. I am working with the HARMONI team to investigate changing the focal plane mask to facilitate these observations.

Further in the future, new instruments and missions will allow us to characterise more and more potentially Earth-like exoplanets. Currently, exoplanet characterisation primarily focuses on the atmospheres of exoplanets so the identification of Earth-like worlds comes from measuring their atmospheric components. However, the presence of liquid water can be a far stronger indicator of habitability for these planets. Fortunately, liquid water creates a number of potentially detectable scattering phenomena, such as rainbows and ocean glints, in the polarised and un-polarised reflected light of Earth-like exoplanets. In Chapter 5, I show how the Habitable Worlds Observatory could have the potential to detect these phenomena in the directly imaged reflected light of Earth-like planets but that it would need to observe them close to their host stars. As HWO's coronagraph will block the star and a region around it, the coronagraph size will strongly affect the number of systems where such scattering phenomena

could be accessible. Since HWO is in the early design phase, this can be taken into consideration when designing and planning the mission as, for these types of observations, observing in polarised light with a smaller coronagraph is prefered.

In this thesis, I have been laying the groundwork of a roadmap towards the characterisation of Earth-like exoplanets in reflected light. This roadmap starts with the present day characterisation of highly reflective giant planets. Then it moves onto the near future with the Extremely Large Telescope offering some of the first opportunities in the 2030s to study Earth-like worlds in reflected light. And finally to the 2040s and beyond, with the possibility of detecting liquid water on a few tens of exoplanets using the Habitable Worlds Observatory. The future of exoplanet characterisation in reflected light is looking bright with Earth-like worlds soon within our reach however, there is still much work to be done.

6.1 Future Work

In the next few years, there are many avenues by which this roadmap can be advanced further. I recommend that the study of reflective giant planets continues, expanding to more worlds, and that the preparatory work for the ELTs continues with simulations of different instruments and combined analyses of these.

On the characterisation of reflective giants, I intend to continue my work on LTT-9779 b with the aim of refining my current analysis. Additionally, I am aiming to perform a joint analysis of the high-resolution reflection data with available low-resolution transit and emission data. This will be the most detailed study of a mini-Neptune to date and will highlight the complementarity of high- and low-resolution observations as well as different wavelength regimes and may reveal the mysteries of this unusual planet and its place in the photoevaporation desert. In addition to this, I intend to observe other reflective exoplanets such as HD 189733 b, KELT-20 b and WASP 189 b to learn more about the source of their reflectivity and to refine our reflected light characterisation techniques.

To further prepare for the arrival of the ELTs, I intend to expand my simulations to other ELT instruments such as METIS or ANDES to determine what complementary information these could provide. A joint analysis of observations from each of these instruments will reveal the spectrum of potentially Earth-like exoplanets from optical to the infrared. However, careful thought is needed to determine the best observing strategies for revealing the nature of a planet such as Proxima b with as little time as possible. By simulating these joint analyses, I intend to inform future observing strategies of potentially Earth-like planets and estimate what information could be obtained from them.

In the coming decade, the next generation of telescopes will begin observing and the observing strate-

gies we develop today can be put into practice. This will allow the nearest potentially Earth-like exoplanets to be characterised. At this time, it is unknown how likely these planets are to be Earth-like but if they are common then the first detections of biosignatures may be obtained. Any biosignature detections will need to be interpreted in the context of the planet's environment and it is likely there will be some uncertainty in their interpretation. Therefore, detections of biosignature molecules will need to be made with several instruments and over a range of wavelengths in order to gain confidence in their interpretation. In addition to Earth-like planets, the ELTs will also greatly aid in the characterisation of the reflective giants. Their larger collecting area will allow more planets to be characterised in greater detail and may reveal that these reflective planets form a new class of world.

Further in the future missions such as the Habitable Worlds Observatory will facilitate the characterisation of a larger number of potentially Earth-like exoplanets. This will allow populations studies of these worlds and could constrain their occurrence rates. Further to this, we may be able to detect liquid water on some of these worlds which is a key indicator of their habitability.

6.2 Final Remarks

When we think of the Earth, we do not picture it in terms of the light it thermally emits or the transparency of its atmosphere. Instead, we think of a gleaming blue marble illuminated gently by the light of our sun. We see our world in reflected light. This reflected light is the key towards a greater understanding of the atmospheres and climates of exoplanets of all types and to the search for life beyond our world. This thesis has focused on how the characterisation of exoplanets in reflected light in the coming decades could further our knowledge of all kinds of strange new worlds.

While interstellar space travel may be beyond us today, we can still explore the stars and their exoplanets. The coming decades may prove to be exciting times in the search for life beyond our home. Live long and prosper and do not forget to look up every now and then!

Bibliography

Agrawal, Shubh et al. (July 2023). “Detecting Exoplanets Closer to Stars with Moderate Spectral Resolution Integral-field Spectroscopy”. In: *The Astronomical Journal* 166.1, p. 15.

Airapetian, V. S. et al. (June 2016). “Prebiotic chemistry and atmospheric warming of early Earth by an active young Sun”. In: *Nature Geoscience* 9.6, pp. 452–455.

Akeson, R. L. et al. (Aug. 2013). “The NASA Exoplanet Archive: Data and Tools for Exoplanet Research”. In: *Publications of the Astronomical Society of the Pacific* 125.930, pp. 989–999.

Alei, Eleonora et al. (Sept. 2022). “Large Interferometer For Exoplanets (LIFE)”. In: *Astronomy & Astrophysics* 665, A106.

Allart, R. et al. (Dec. 2020). “WASP-127b: a misaligned planet with a partly cloudy atmosphere and tenuous sodium signature seen by ESPRESSO”. In: *Astronomy & Astrophysics* 644, A155.

Amara, Adam and Sascha P. Quanz (Dec. 2012). “pynpoint: an image processing package for finding exoplanets”. In: *Monthly Notices of the Royal Astronomical Society* 427.2, pp. 948–955.

Angerhausen, Daniel, Em DeLarme, and Jon A. Morse (Nov. 2015). “A Comprehensive Study of Kepler Phase Curves and Secondary Eclipses: Temperatures and Albedos of Confirmed Kepler Giant Planets”. In: *Publications of the Astronomical Society of the Pacific* 127.957, pp. 1113–1130.

Angerhausen, Daniel et al. (Feb. 2023). “Large Interferometer for Exoplanets: VIII. Where Is the Phosphine? Observing Exoplanetary PH3 with a Space-Based Mid-Infrared Nulling Interferometer”. In: *Astrobiology* 23.2, pp. 183–194.

Angerhausen, Daniel et al. (Jan. 2024). “Large Interferometer For Exoplanets (LIFE): XII. The Detectability of Capstone Biosignatures in the Mid-Infrared – Sniffing Exoplanetary Laughing Gas and Methylated Halogens”. In: *arxiv*.

Anglada-Escudé, Guillem et al. (Aug. 2016). “A terrestrial planet candidate in a temperate orbit around Proxima Centauri”. In: *Nature* 536.7617, pp. 437–440.

Azevedo Silva, T. et al. (Oct. 2022). “Detection of barium in the atmospheres of the ultra-hot gas giants WASP-76b and WASP-121b”. In: *Astronomy & Astrophysics* 666, p. L10.

Barman, Travis S. et al. (May 2011). “Clouds and chemistry in the atmosphere of extrasolar planet HR8799b”. In: *The Astrophysical Journal* 733.1, p. 65.

Barman, Travis S. et al. (May 2015). “Simultaneous detection of water, methane, and carbon monoxide in the atmosphere of exoplanet HR 8799 b”. In: *The Astrophysical Journal* 804.1, p. 61.

Batalha, Natasha E. et al. (Oct. 2018). “Color Classification of Extrasolar Giant Planets: Prospects and Cautions”. In: *The Astronomical Journal* 156.4, p. 158.

Batalha, Natasha E. et al. (June 2019). "Exoplanet Reflected-light Spectroscopy with PICASO". In: *The Astrophysical Journal* 878.1, p. 70.

Baxter, Claire et al. (July 2020). "A transition between the hot and the ultra-hot Jupiter atmospheres". In: *Astronomy & Astrophysics* 639, A36.

Bean, Jacob L., Eliza Miller-Ricci Kempton, and Derek Homeier (Dec. 2010). "A ground-based transmission spectrum of the super-Earth exoplanet GJ 1214b". In: *Nature* 468.7324, pp. 669–672.

Bell, Taylor J. et al. (Nov. 2023). "Methane throughout the atmosphere of the warm exoplanet WASP-80b". In: *Nature* 623.7988, pp. 709–712.

Benneke, Bjoern and Sara Seager (July 2012). "Atmospheric Retrieval for Super-Earths: Uniquely Constraining the Atmospheric Composition with Transmission Spectroscopy". In: *The Astrophysical Journal* 753.2, p. 100.

Berta, Zachory K. et al. (Mar. 2012). "The Flat Transmission Spectrum of the Super-Earth GJ 1214 b from Wide Field Camera 3 on the Hubble Space Telescope". In: *The Astrophysical Journal* 747.1, p. 35.

Bessell, M. S. (Feb. 1991). "The late-M dwarfs". In: *The Astronomical Journal* 101, p. 662.

Bidot, A., D. Mouillet, and A. Carlotti (Feb. 2024). "Exoplanet detection limits using spectral cross-correlation with spectro-imaging". In: *Astronomy & Astrophysics* 682, A10.

Birkby, J. L. et al. (Nov. 2013). "Detection of water absorption in the day side atmosphere of HD 189733 b using ground-based high-resolution spectroscopy at 3.2μm". In: *Monthly Notices of the Royal Astronomical Society: Letters* 436.1, pp. L35–L39.

Birkby, J. L. et al. (Mar. 2017). "Discovery of Water at High Spectral Resolution in the Atmosphere of 51 Peg b". In: *The Astronomical Journal* 153.3, p. 138.

Birkby, Jayne L. (2018). "Spectroscopic Direct Detection of Exoplanets". In: *Handbook of Exoplanets*. Cham: Springer International Publishing, pp. 1485–1508.

Bixel, A and D Apai (Nov. 2017). "Probabilistic Assessment of Planet Habitability and Biosignatures". In: *Habitable Worlds 2017: A System Science Workshop*. Ed. by LPI Editorial Board. Vol. 2042. LPI Contributions, p. 4066.

Blain, D., B. Charnay, and B. Bézard (Feb. 2021). "1D atmospheric study of the temperate sub-Neptune K2-18b". In: *Astronomy & Astrophysics* 646, A15.

Blain, Doriann, Alejandro Sánchez-López, and Paul Mollière (Apr. 2024). "A Formally Motivated Retrieval Framework Applied to the High-resolution Transmission Spectrum of HD 189733 b". In: *The Astronomical Journal* 167.4, p. 179.

Blažek, Martin et al. (May 2022). "Constraints on TESS albedos for five hot Jupiters". In: *Monthly Notices of the Royal Astronomical Society* 513.3, pp. 3444–3457.

Blind, Nicolas et al. (Aug. 2022). "RISTRETTO: coronagraph and AO designs enabling High Dispersion Coronagraphy at 2 λ/D". In: *Adaptive Optics Systems VIII*. Ed. by Dirk Schmidt, Laura Schreiber, and Elise Vernet. SPIE, p. 269.

Bonnefoy, M. et al. (Mar. 2016). "First light of the VLT planet finder SPHERE". In: *Astronomy & Astrophysics* 587, A58.

Borges, Schuyler R., Gabrielle G. Jones, and Tyler D. Robinson (Mar. 2024). "Detectability of Surface Biosignatures for Directly Imaged Rocky Exoplanets". In: *Astrobiology* 24.3, pp. 283–299.

Brandl, B et al. (Mar. 2021). "METIS: The Mid-infrared ELT Imager and Spectrograph". In: *The Messenger* 182, pp. 22–26.

Brogi, M. et al. (Feb. 2016). "Rotation and winds of exoplanet HD 189733 b measured with high-dispersion transmission spectroscopy". In: *The Astrophysical Journal* 817.2, p. 106.

Brogi, Matteo and Michael R. Line (Mar. 2019). "Retrieving Temperatures and Abundances of Exoplanet Atmospheres with High-resolution Cross-correlation Spectroscopy". In: *The Astronomical Journal* 157.3, p. 114.

Brogi, Matteo et al. (June 2012). "The signature of orbital motion from the dayside of the planet τ Boötis b". In: *Nature* 486.7404, pp. 502–504.

Bryan, Marta L. et al. (Dec. 2017). "Constraints on the spin evolution of young planetary-mass companions". In: *Nature Astronomy* 2.2, pp. 138–144.

Cabot, Samuel H C et al. (Feb. 2019). "On the robustness of analysis techniques for molecular detections using high-resolution exoplanet spectroscopy". In: *Monthly Notices of the Royal Astronomical Society* 482.4, pp. 4422–4436.

Cabot, Samuel H. C. et al. (May 2024). "High-resolution Spectroscopic Reconnaissance of a Temperate Sub-Neptune". In: *The Astrophysical Journal Letters* 966.1, p. L10.

Carlotti, Alexis et al. (July 2018). "System analysis and expected performance of a high-contrast module for HARMONI". In: *Ground-based and Airborne Instrumentation for Astronomy VII*. Ed. by Hideki Takami, Christopher J. Evans, and Luc Simard. SPIE, p. 352.

Carrión-González, O. et al. (Aug. 2020). "Directly imaged exoplanets in reflected starlight: the importance of knowing the planet radius". In: *Astronomy & Astrophysics* 640, A136.

Carrión-González, Oscar et al. (Sept. 2021). "Reflected-starlight phase curves: an observing strategy to constrain the radius and atmospheric properties of directly imaged exoplanets". In: *European Planetary Science Congress*, pp. 2021–694.

Carrión-González, Oscar et al. (Oct. 2023). "Large Interferometer For Exoplanets (LIFE)". In: *Astronomy & Astrophysics* 678, A96.

Catling, D.C. (2014). "The Great Oxidation Event Transition". In: *Treatise on Geochemistry*. Elsevier, pp. 177–195.

Catling, David C. et al. (June 2018). "Exoplanet Biosignatures: A Framework for Their Assessment". In: *Astrobiology* 18.6, pp. 709–738.

Charbonneau, David and Drake Deming (June 2007). "The Dynamics-Based Approach to Studying Terrestrial Exoplanets". In: *arxiv*.

Charbonneau, David et al. (Sept. 1999). "An Upper Limit on the Reflected Light from the Planet Orbiting the Star τ Bootis". In: *The Astrophysical Journal* 522.2, pp. L145–L148.

Charbonneau, David et al. (Mar. 2002). "Detection of an Extrasolar Planet Atmosphere". In: *The Astrophysical Journal* 568.1, pp. 377–384.

Charnay, B. et al. (Feb. 2021). "Formation and dynamics of water clouds on temperate sub-Neptunes: the example of K2-18b". In: *Astronomy & Astrophysics* 646, A171.

Chauvin, G. et al. (Sept. 2018). "Investigating the young solar system analog HD 95086". In: *Astronomy & Astrophysics* 617, A76.

Chaverot, Guillaume, Emeline Bolmont, and Martin Turbet (Dec. 2023). "First exploration of the runaway greenhouse transition with a 3D General Circulation Model". In: *Astronomy & Astrophysics* 680, A103.

Chazelas, Bruno et al. (Dec. 2020). "RISTRETTO: a pathfinder instrument for exoplanet atmosphere characterization". In: *Adaptive Optics Systems VII*. Ed. by Dirk Schmidt, Laura Schreiber, and Elise Vernet. SPIE, p. 329.

Chen, Guo et al. (May 2021). "Evidence for TiO in the Atmosphere of the Hot Jupiter HAT-P-65 b". In: *The Astrophysical Journal Letters* 913.1, p. L16.

Chen, Howard et al. (Dec. 2020). "Persistence of flare-driven atmospheric chemistry on rocky habitable zone worlds". In: *Nature Astronomy* 5.3, pp. 298–310.

Cheverall, Connor J., Nikku Madhusudhan, and Mans Holmberg (Mar. 2023). "Robustness Measures for Molecular Detections using High-Resolution Transmission Spectroscopy of Exoplanets". In: *Monthly Notices of the Royal Astronomical Society* 522.1, pp. 661–677.

Claudi, Riccardo et al. (Dec. 2020). "Super-Earths, M Dwarfs, and Photosynthetic Organisms: Habitability in the Lab". In: *Life* 11.1, p. 10.

Collier-Cameron, Andrew et al. (Dec. 1999). "Probable detection of starlight reflected from the giant planet orbiting τ Boötis". In: *Nature* 402.6763, pp. 751–755.

Collier-Cameron, Andrew et al. (Feb. 2002). "A search for starlight reflected from ν And's innermost planet". In: *Monthly Notices of the Royal Astronomical Society* 330.1, pp. 187–204.

Collier-Cameron, Andrew et al. (Jan. 2004). "τ Boo b: Not so bright, but just as heavy". In: *Planetary Systems in the Universe*. Ed. by A Penny. Vol. 202, p. 75.

Cowan, Nicolas B. and Eric Agol (Mar. 2011). "The statistics of albedo and heat recirculation on hot exoplanets". In: *The Astrophysical Journal* 729.1, p. 54.

Crossfield, Ian J. M. et al. (Nov. 2020). "Phase Curves of Hot Neptune LTT9779b Suggest a High-metallicity Atmosphere". In: *The Astrophysical Journal Letters* 903.1, p. L7.

Cugno, G. et al. (Sept. 2021). "Molecular mapping of the PDS70 system". In: *Astronomy & Astrophysics* 653, A12.

Currie, Miles H., Victoria S. Meadows, and Kaitlin C. Rasmussen (May 2023a). "There's More to Life than O2: Simulating the Detectability of a Range of Molecules for Ground-based, High-resolution Spectroscopy of Transiting Terrestrial Exoplanets". In: *The Planetary Science Journal* 4.5, p. 83.

Currie, T et al. (July 2023b). "Direct Imaging and Spectroscopy of Extrasolar Planets". In: *Protostars and Planets VII*. Ed. by S Inutsuka et al. Vol. 534. Astronomical Society of the Pacific Conference Series, p. 799.

Cutri, R. M. et al. (June 2003). *VizieR Online Data Catalog: 2MASS All-Sky Catalog of Point Sources (Cutri+ 2003)*. VizieR On-line Data Catalog: II/246. Originally published in: 2003yCat.2246....0C.

Damasso, Mario et al. (Jan. 2020). "A low-mass planet candidate orbiting Proxima Centauri at a distance of 1.5 AU". In: *Science Advances* 6.3.

Damiano, Mario and Renyu Hu (Nov. 2021). "Reflected Spectroscopy of Small Exoplanets I: Determining the Atmospheric Composition of Sub-Neptunes Planets". In: *The Astronomical Journal* 162.5, p. 200.

Damiano, Mario and Renyu Hu (June 2022). "Reflected Spectroscopy of Small Exoplanets II: Characterization of Terrestrial Exoplanets". In: *The Astronomical Journal* 163.6, p. 299.

Damiano, Mario, Renyu Hu, and Sergi R. Hildebrandt (Nov. 2020). "Multi-orbital-phase and Multi-band Characterization of Exoplanetary Atmospheres with Reflected Light Spectra". In: *The Astronomical Journal* 160.5, p. 206.

Damiano, Mario, Renyu Hu, and Bertrand Mennesson (Oct. 2023). "Reflected Spectroscopy of Small Exoplanets. III. Probing the UV Band to Measure Biosignature Gases". In: *The Astronomical Journal* 166.4, p. 157.

Davies, Richard and Markus Kasper (Sept. 2012). "Adaptive Optics for Astronomy". In: *Annual Review of Astronomy and Astrophysics* 50.1, pp. 305–351.

Davila, Alfonso F. and Christopher P. McKay (June 2014). "Chance and Necessity in Biochemistry: Implications for the Search for Extraterrestrial Biomarkers in Earth-like Environments". In: *Astrobiology* 14.6, pp. 534–540.

De Rosa, Robert J. et al. (June 2016). "Spectroscopic characterization of HD 95086 b with the Gemini Planet Imager". In: *The Astrophysical Journal* 824.2, p. 121.

Deline, A. et al. (Mar. 2022). "The atmosphere and architecture of WASP-189 b probed by its CHEOPS phase curve". In: *Astronomy & Astrophysics* 659, A74.

Domagal-Goldman, Shawn D. et al. (Aug. 2014). "Abiotic ozone and oxygen in atmospheres similar to prebiotic Earth". In: *The Astrophysical Journal* 792.2, p. 90.

Doshi, Dhvani, Nicolas B Cowan, and Yi Huang (July 2022). "Stratospheric clouds do not impede JWST transit spectroscopy for exoplanets with Earth-like atmospheres". In: *Monthly Notices of the Royal Astronomical Society* 515.2, pp. 1982–1992.

Dragomir, Diana et al. (Oct. 2020). "Spitzer Reveals Evidence of Molecular Absorption in the Atmosphere of the Hot Neptune LTT 9979b". In: *The Astrophysical Journal Letters* 903.1, p. L6.

Dyrek, Achrene et al. (Jan. 2024). "SO2, silicate clouds, but no CH4 detected in a warm Neptune". In: *Nature* 625.7993, pp. 51–54.

Edwards, Billy et al. (July 2020). "ARES I: WASP-76 b, A Tale of Two HST Spectra". In: *The Astronomical Journal* 160.1, p. 8.

Edwards, Billy et al. (Oct. 2023a). "Characterizing a World Within the Hot-Neptune Desert: Transit Observations of LTT 9779 b with the Hubble Space Telescope/WFC3". In: *The Astronomical Journal* 166.4, p. 158.

Edwards, Billy et al. (Nov. 2023b). "Exploring the Ability of Hubble Space Telescope WFC3 G141 to Uncover Trends in Populations of Exoplanet Atmospheres through a Homogeneous Transmission Survey of 70 Gaseous Planets". In: *The Astrophysical Journal Supplement Series* 269.1, p. 31.

Emde, Claudia et al. (Sept. 2017). "Influence of aerosols, clouds, and sunglint on polarization spectra of Earthshine". In: *Astronomy & Astrophysics* 605, A2.

Esteves, Lisa J., Ernst J. W. De Mooij, and Ray Jayawardhana (May 2015). "Changing phases of alien worlds: probing atmospheres of Kepler planets with high-precision photometry". In: *The Astrophysical Journal* 804.2, p. 150.

Evans, Thomas M. et al. (Aug. 2017). "An ultrahot gas-giant exoplanet with a stratosphere". In: *Nature* 548.7665, pp. 58–61.

Faria, J. P. et al. (Feb. 2022). "A candidate short-period sub-Earth orbiting Proxima Centauri". In: *Astronomy & Astrophysics* 658, A115.

Feng, Y. Katherina et al. (May 2018). "Characterizing Earth Analogs in Reflected Light: Atmospheric Retrieval Studies for Future Space Telescopes". In: *The Astronomical Journal* 155.5, p. 200.

Fernandez Fernandez, Jorge et al. (Oct. 2023). "Survival in the Neptune desert: LTT 9779 b kept its atmosphere thanks to an unusually X-ray faint host star". In: *Monthly Notices of the Royal Astronomical Society* 527.1, pp. 911–918.

Fétick, R. J. L. et al. (Aug. 2019). "Physics-based model of the adaptive-optics-corrected point spread function". In: *Astronomy & Astrophysics* 628, A99.

Fétick, Romain J L et al. (Dec. 2018). "Turbulent and adaptive optics corrected point-spread functions as convolutive orders of the phase power spectral density". In: *Monthly Notices of the Royal Astronomical Society* 481.4, pp. 5210–5215.

Finnerty, Luke et al. (July 2023). "Keck Planet Imager and Characterizer Emission Spectroscopy of WASP-33b". In: *The Astronomical Journal* 166.1, p. 31.

Finnerty, Luke et al. (Jan. 2024). "Atmospheric Metallicity and C/O of HD 189733 b from High-resolution Spectroscopy". In: *The Astronomical Journal* 167.1, p. 43.

Foreman-Mackey, Daniel et al. (June 2021). "exoplanet: Gradient-based probabilistic inference for exoplanet data other astronomical time series". In: *Journal of Open Source Software* 6.62, p. 3285.

Fujii, Yuka et al. (June 2018). "Exoplanet Biosignatures: Observational Prospects". In: *Astrobiology* 18.6, pp. 739–778.

Gaia Collaboration (Nov. 2020). *VizieR Online Data Catalog: Gaia EDR3 (Gaia Collaboration, 2020)*. VizieR On-line Data Catalog: I/350. Originally published in: 2021A&A...649A...1G; doi:10.5270/esa-1ug.

Gandhi, Siddharth et al. (June 2023). "Retrieval Survey of Metals in Six Ultrahot Jupiters: Trends in Chemistry, Rain-out, Ionization, and Atmospheric Dynamics". In: *The Astronomical Journal* 165.6, p. 242.

Gandhi, Siddharth et al. (Apr. 2024). "Revealing H2O dissociation in WASP-76 b through combined high- and low-resolution transmission spectroscopy". In: *Monthly Notices of the Royal Astronomical Society* 530.3, pp. 2885–2894.

Gao, Peter et al. (June 2015). "Stability of CO2 atmospheres on desiccated M dwarf exoplanets". In: *The Astrophysical Journal* 806.2, p. 249.

Gao, Peter et al. (Mar. 2017). "Sulfur Hazes in Giant Exoplanet Atmospheres: Impacts on Reflected Light Spectra". In: *The Astronomical Journal* 153.3, p. 139.

Gao, Peter et al. (May 2020). "Aerosol composition of hot giant exoplanets dominated by silicates and hydrocarbon hazes". In: *Nature Astronomy* 4.10, pp. 951–956.

Gaudi, B. Scott, Michael Meyer, and Jessie Christiansen (Oct. 2021). "The Demographics of Exoplanets". In: *ExoFrontiers*. IOP Publishing.

Giacobbe, Paolo et al. (Apr. 2021). "Five carbon- and nitrogen-bearing species in a hot giant planet's atmosphere". In: *Nature* 592.7853, pp. 205–208.

Gialluca, Megan T. et al. (May 2021). "Characterizing Atmospheres of Transiting Earth-like Exoplanets Orbiting M Dwarfs with James Webb Space Telescope". In: *Publications of the Astronomical Society of the Pacific* 133.1023, p. 054401.

Gibson, Neale P et al. (Jan. 2019). "Revisiting the potassium feature of WASP-31b at high resolution". In: *Monthly Notices of the Royal Astronomical Society* 482.1, pp. 606–615.

Gibson, Neale P et al. (Apr. 2020). "Detection of Fei in the atmosphere of the ultra-hot Jupiter WASP-121b, and a new likelihood-based approach for Doppler-resolved spectroscopy". In: *Monthly Notices of the Royal Astronomical Society* 493.2, pp. 2215–2228.

Gilbert, Emily A. et al. (Nov. 2021). "No Transits of Proxima Centauri Planets in High-Cadence TESS Data". In: *Frontiers in Astronomy and Space Sciences* 8.

Gilbert-Janizek, Samantha, Victoria S. Meadows, and Jacob Lustig-Yaeger (June 2024). "Retrieved Atmospheres and Inferred Surface Properties for Terrestrial Exoplanets Using Transmission and Reflected-light Spectroscopy". In: *The Planetary Science Journal* 5.6, p. 148.

Glidic, Kayli et al. (July 2022). "Atmospheric Characterization of Hot Jupiter CoRoT-1 b Using the Wide Field Camera 3 on the Hubble Space Telescope". In: *The Astronomical Journal* 164.1, p. 19.

Goode, P. R. et al. (Sept. 2021). "Earth's Albedo 1998â2017 as Measured From Earthshine". In: *Geophysical Research Letters* 48.17.

Grant, David et al. (Oct. 2023). "JWST-TST DREAMS: Quartz Clouds in the Atmosphere of WASP-17b". In: *The Astrophysical Journal Letters* 956.2, p. L32.

Greene, Thomas P. et al. (June 2023). "Thermal emission from the Earth-sized exoplanet TRAPPIST-1 b using JWST". In: *Nature* 618.7963, pp. 39–42.

Grenfell, John Lee (Nov. 2017). "A review of exoplanetary biosignatures". In: *Physics Reports* 713, pp. 1–17.

Gressier, A. et al. (Apr. 2023). "The Hubble PanCET program: The near-ultraviolet transmission spectrum of WASP-79b". In: *Astronomy & Astrophysics* 672, A34.

Guilluy, G. et al. (May 2019). "Exoplanet atmospheres with GIANO". In: *Astronomy & Astrophysics* 625, A107.

Gullikson, Kevin, Sarah Dodson-Robinson, and Adam Kraus (Aug. 2014). "Correcting for telluric absorption: Methods, case studies, and release of the TelFit code". In: *The Astronomical Journal* 148.3, p. 53.

Guo, B. et al. (July 2024). "Detection of Fe and Ti on the dayside of the ultrahot Jupiter MASCARA-1b with CARMENES". In: *Astronomy & Astrophysics* 687, A103.

Haffert, S. Y. et al. (June 2019). "Two accreting protoplanets around the young star PDS 70". In: *Nature Astronomy* 3.8, pp. 749–754.

Hall, Sawyer et al. (Dec. 2023). "Constraining Background N2 Inventories on Directly Imaged Terrestrial Exoplanets to Rule Out O2 False Positives". In: *The Astronomical Journal* 166.6, p. 254.

Hansen, James E. and J. W. Hovenier (May 1974). "Interpretation of the Polarization of Venus". In: *Journal of the Atmospheric Sciences* 31.4, pp. 1137–1160.

Hardegree-Ullman, Kevin K. et al. (June 2023). "Bioverse: A Comprehensive Assessment of the Capabilities of Extremely Large Telescopes to Probe Earth-like O2 Levels in Nearby Transiting Habitable-zone Exoplanets". In: *The Astronomical Journal* 165.6, p. 267.

Harman, C. E. et al. (Oct. 2015). "Abiotic O2 levels on planets around F, G, K, and M stars: Possible false positives for life?" In: *The Astrophysical Journal* 812.2, p. 137.

Hawker, George A and Ian R Parry (Apr. 2019). "High-resolution spectroscopy and high contrast imaging with the ELT: looking for O2 in Proxima b". In: *Monthly Notices of the Royal Astronomical Society* 484.4, pp. 4855–4864.

Heng, Kevin and Brice-Olivier Demory (Oct. 2013). "Understanding trends associated with clouds in irradiated exoplanets". In: *The Astrophysical Journal* 777.2, p. 100.

Henry, Todd J. et al. (July 1997). "The solar neighborhood IV: discovery of the twentieth nearest star". In: *The Astronomical Journal* 114, p. 388.

Henry, Todd J. et al. (June 2018). "The Solar Neighborhood XLIV: RECONS Discoveries within 10 parsecs". In: *The Astronomical Journal* 155.6, p. 265.

Hoeijmakers, H. J., I. A. G. Snellen, and S. E. van Terwisga (Feb. 2018a). "Searching for reflected light from τ Bootis b with high-resolution ground-based spectroscopy: Approaching the 10-5 contrast barrier". In: *Astronomy & Astrophysics* 610, A47.

Hoeijmakers, H. J. et al. (Mar. 2015). "A search for TiO in the optical high-resolution transmission spectrum of HD 209458b: Hindrance due to inaccuracies in the line database". In: *Astronomy & Astrophysics* 575, A20.

Hoeijmakers, H. J. et al. (Sept. 2018b). "Medium-resolution integral-field spectroscopy for high-contrast exoplanet imaging". In: *Astronomy & Astrophysics* 617, A144.

Holmberg, Mans and Nikku Madhusudhan (Mar. 2024). "Possible Hycean conditions in the sub-Neptune TOI-270 d". In: *Astronomy & Astrophysics* 683, p. L2.

Houllé, M. et al. (Aug. 2021). "Direct imaging and spectroscopy of exoplanets with the ELT/HARMONI high-contrast module". In: *Astronomy & Astrophysics* 652, A67.

Hoyer, S. et al. (July 2023). "The extremely high albedo of LTT 9779 b revealed by CHEOPS". In: *Astronomy & Astrophysics* 675, A81.

Hu, Renyu, Bethany L. Ehlmann, and Sara Seager (June 2012). "Theoretical spectra of terrestrial exoplanet surfaces". In: *The Astrophysical Journal* 752.1, p. 7.

Hu, Renyu et al. (Mar. 2015). "A semi-analytical model of visible-wavelength phase curves of exoplanets and applications to Kepler-7 b and Kepler-10 b". In: *The Astrophysical Journal* 802.1, p. 51.

Husser, T.-O. et al. (May 2013). "A new extensive library of PHOENIX stellar atmospheres and synthetic spectra". In: *Astronomy & Astrophysics* 553, A6.

Ih, Jegug et al. (July 2023). "Constraining the Thickness of TRAPPIST-1 bâs Atmosphere from Its JWST Secondary Eclipse Observation at 15 μm". In: *The Astrophysical Journal Letters* 952.1, p. L4.

Inglis, Julie et al. (May 2024). "Atmospheric Retrievals of the Young Giant Planet ROXs 42B b from Low- and High-resolution Spectroscopy". In: *The Astronomical Journal* 167.5, p. 218.

Irwin, P. G. J. et al. (June 2022). "Hazy Blue Worlds: A Holistic Aerosol Model for Uranus and Neptune, Including Dark Spots". In: *Journal of Geophysical Research: Planets* 127.6.

Irwin, Patrick G J et al. (Mar. 2020). "2.5D retrieval of atmospheric properties from exoplanet phase curves: application to WASP-43b observations". In: *Monthly Notices of the Royal Astronomical Society* 493.1, pp. 106–125.

Jacobs, Bob et al. (Oct. 2023). "Probing Reflection from Aerosols with the Near-infrared Dayside Spectrum of WASP-80b". In: *The Astrophysical Journal Letters* 956.2, p. L43.

Jaiswal, Bhavesh and Tyler D. Robinson (June 2023). "Scattering Transparency of Clouds in Exoplanet Transit Spectra". In: *arxiv*.

Jenkins, James S et al. (July 2019). "Proxima Centauri b is not a transiting exoplanet". In: *Monthly Notices of the Royal Astronomical Society* 487.1, pp. 268–274.

Jenkins, James S. et al. (Sept. 2020). "An ultrahot Neptune in the Neptune desert". In: *Nature Astronomy* 4.12, pp. 1148–1157.

Jiang, Zewen et al. (June 2023). "Detection of Rubidium and Samarium in the Atmosphere of the Ultrahot Jupiter MASCARA-4b". In: *The Astronomical Journal* 165.6, p. 230.

Jones, A. et al. (Dec. 2013). "An advanced scattered moonlight model for Cerro Paranal". In: *Astronomy & Astrophysics* 560, A91.

Kalman, Dan (Jan. 1996). "A Singularly Valuable Decomposition: The SVD of a Matrix". In: *The College Mathematics Journal* 27.1, p. 2.

Kaltenegger, L and F Selsis (Aug. 2007). "Biomarkers set in context". In: *Extrasolar Planets. Formation, Detection and Dynamics*. Ed. by Rudolf Dvorak, p. 79.

Kaltenegger, Lisa (Aug. 2017). "How to Characterize Habitable Worlds and Signs of Life". In: *Annual Review of Astronomy and Astrophysics* 55.1, pp. 433–485.

Karalidi, T., D. M. Stam, and J. W. Hovenier (June 2011). "Flux and polarisation spectra of water clouds on exoplanets". In: *Astronomy & Astrophysics* 530, A69.

Kasper, Markus et al. (Mar. 2021). "PCS – A Roadmap for Exoearth Imaging with the ELT". In: *The Messenger* 182, pp. 38–43.

Kempton, Eliza M.-R., Jacob L. Bean, and Vivien Parmentier (Aug. 2017). "An Observational Diagnostic for Distinguishing between Clouds and Haze in Hot Exoplanet Atmospheres". In: *The Astrophysical Journal Letters* 845.2, p. L20.

Kempton, Eliza M.-R. et al. (Aug. 2023). "A reflective, metal-rich atmosphere for GJ 1214b from its JWST phase curve". In: *Nature* 620.7972, pp. 67–71.

Kervella, P., F. Thévenin, and C. Lovis (Feb. 2017). "Proxima's orbit around α Centauri". In: *Astronomy & Astrophysics* 598, p. L7.

Khodachenko, Maxim L. et al. (Feb. 2007). "Coronal Mass Ejection (CME) Activity of Low Mass M Stars as An Important Factor for The Habitability of Terrestrial Exoplanets. I. CME Impact on Expected Magnetospheres of Earth-Like Exoplanets in Close-In Habitable Zones". In: *Astrobiology* 7.1, pp. 167–184.

Kiang, Nancy Y. et al. (Feb. 2007). "Spectral Signatures of Photosynthesis. II. Coevolution with Other Stars And The Atmosphere on Extrasolar Worlds". In: *Astrobiology* 7.1, pp. 252–274.

Kiefer, F. et al. (May 2024). "A new treatment of telluric and stellar features for medium-resolution spectroscopy and molecular mapping". In: *Astronomy & Astrophysics* 685, A120.

Kipping, David M. (Sept. 2013). "Parametrizing the exoplanet eccentricity distribution with the Beta distribution". In: *Monthly Notices of the Royal Astronomical Society: Letters* 434.1, pp. L51–L55.

Kirkpatrick, J. D. (Jan. 2001). "A New Census of the Solar Neighborhood". In: *Tetons 4: Galactic Structure, Stars and the Interstellar Medium*. Ed. by Charles E Woodward, Michael D Bicay, and J Michael Shull. Vol. 231. Astronomical Society of the Pacific Conference Series, p. 17.

Kok, R.J. de et al. (June 2013). "Detection of carbon monoxide in the high-resolution day-side spectrum of the exoplanet HD 189733b". In: *Astronomy & Astrophysics* 554, A82.

Kokori, A. et al. (Mar. 2023). "ExoClock Project. III. 450 New Exoplanet Ephemerides from Ground and Space Observations". In: *The Astrophysical Journal Supplement Series* 265.1, p. 4.

Kong, Hui, Hatice Cinar Akakin, and Sanjay E. Sarma (Dec. 2013). "A Generalized Laplacian of Gaussian Filter for Blob Detection and Its Applications". In: *IEEE Transactions on Cybernetics* 43.6, pp. 1719–1733.

Konopacky, Quinn M. et al. (Mar. 2013). "Detection of Carbon Monoxide and Water Absorption Lines in an Exoplanet Atmosphere". In: *Science* 339.6126, pp. 1398–1401.

Konrad, B. S. et al. (Aug. 2022). "Large Interferometer For Exoplanets (LIFE)". In: *Astronomy & Astrophysics* 664, A23.

Konrad, B. S. et al. (May 2023). "Large Interferometer For Exoplanets (LIFE)". In: *Astronomy & Astrophysics* 673, A94.

Kopparapu, Ravi Kumar et al. (Feb. 2013). "Habitable zones around main-sequence stars: New estimates". In: *The Astrophysical Journal* 765.2, p. 131.

Kreidberg, Laura and Abraham Loeb (Nov. 2016). "Prospects for characterizing the atmosphere of Proxima Centauri b". In: *The Astrophysical Journal* 832.1, p. L12.

Kreidberg, Laura et al. (Jan. 2014). "Clouds in the atmosphere of the super-Earth exoplanet GJ 1214b". In: *Nature* 505.7481, pp. 69–72.

Kreidberg, Laura et al. (Sept. 2019). "Absence of a thick atmosphere on the terrestrial exoplanet LHS 3844b". In: *Nature* 573.7772, pp. 87–90.

Krenn, A. F. et al. (Apr. 2023). "The geometric albedo of the hot Jupiter HD 189733b measured with CHEOPS". In: *Astronomy & Astrophysics* 672, A24.

Krissansen-Totton, Joshua, David S. Bergsman, and David C. Catling (Jan. 2016). "On Detecting Biospheres from Chemical Thermodynamic Disequilibrium in Planetary Atmospheres". In: *Astrobiology* 16.1, pp. 39–67.

Krissansen-Totton, Joshua, Stephanie Olson, and David C. Catling (Jan. 2018a). "Disequilibrium biosignatures over Earth history and implications for detecting exoplanet life". In: *Science Advances* 4.1.

Krissansen-Totton, Joshua et al. (Sept. 2018b). "Detectability of Biosignatures in Anoxic Atmospheres with the James Webb Space Telescope: A TRAPPIST-1e Case Study". In: *The Astronomical Journal* 156.3, p. 114.

Kurosaki, Kenji and Masahiro Ikoma (June 2017). "Acceleration of Cooling of Ice Giants by Condensation in Early Atmospheres". In: *The Astronomical Journal* 153.6, p. 260.

Lafreniere, David et al. (May 2007). "A New Algorithm for Point-Spread Function Subtraction in High-Contrast Imaging: A Demonstration with Angular Differential Imaging". In: *The Astrophysical Journal* 660.1, pp. 770–780.

Landman, R. et al. (Feb. 2024). "β Pictoris b through the eyes of the upgraded CRIRES+". In: *Astronomy & Astrophysics* 682, A48.

Latouf, Natasha et al. (Sept. 2023). "Bayesian Analysis for Remote Biosignature Identification on exoEarths (BARBIE). I. Using Grid-based Nested Sampling in Coronagraphy Observation Simulations for H2O". In: *The Astronomical Journal* 166.3, p. 129.

Latouf, Natasha et al. (Jan. 2024). "Bayesian Analysis for Remote Biosignature Identification on exoEarths (BARBIE). II. Using Grid-based Nested Sampling in Coronagraphy Observation Simulations for O2 and O3". In: *The Astronomical Journal* 167.1, p. 27.

Le Coroller, H. et al. (July 2020). "K-Stacker: an algorithm to hack the orbital parameters of planets hidden in high-contrast imaging". In: *Astronomy & Astrophysics* 639, A113.

Lécuyer, Christophe and Yanick Ricard (Jan. 1999). "Long-term fluxes and budget of ferric iron: implication for the redox states of the Earth's mantle and atmosphere". In: *Earth and Planetary Science Letters* 165.2, pp. 197–211.

Lee, Jae-Min, Kevin Heng, and Patrick G. J. Irwin (Nov. 2013). "Atmospheric retrieval analysis of the directly imaged exoplanet HR 8799b". In: *The Astrophysical Journal* 778.2, p. 97.

Leger, A, M Pirre, and F. J. Marceau (Sept. 1993). "Search for primitive life on a distant planet: relevance of 02 and 03 detections". In: *Astronomy and Astrophysics* 277, p. 309.

Leung, Michaela, Victoria S. Meadows, and Jacob Lustig-Yaeger (July 2020). "High-resolution Spectral Discriminants of Ocean Loss for M-dwarf Terrestrial Exoplanets". In: *The Astronomical Journal* 160.1, p. 11.

Li, Jiazheng et al. (Jan. 2022). "Rotation Period Detection for Earth-like Exoplanets". In: *The Astronomical Journal* 163.1, p. 27.

Li, Liming et al. (Sept. 2018). "Less absorbed solar energy and more internal heat for Jupiter". In: *Nature Communications* 9.1, p. 3709.

Liggins, Philippa et al. (July 2022). "Growth and Evolution of Secondary Volcanic Atmospheres: I. Identifying the Geological Character of Hot Rocky Planets". In: *Journal of Geophysical Research: Planets* 127.7.

Liggins, Philippa et al. (Mar. 2023). "Growth and Evolution of Secondary Volcanic Atmospheres: 2. The Importance of Kinetics". In: *Journal of Geophysical Research: Planets* 128.3.

Lightkurve Collaboration et al. (Dec. 2018). *Lightkurve: Kepler and TESS time series analysis in Python*. Astrophysics Source Code Library, record ascl:1812.013.

Lin, Z and L Kaltenegger (Nov. 2019). "High-resolution reflection spectra for Proxima b and Trappist-1e models for ELT observations". In: *Monthly Notices of the Royal Astronomical Society*.

Lin, Zifan et al. (June 2021). "Differentiating modern and prebiotic Earth scenarios for TRAPPIST-1e: high-resolution transmission spectra and predictions for JWST". In: *Monthly Notices of the Royal Astronomical Society* 505.3, pp. 3562–3578.

Lindegren, L. et al. (May 2021). "Gaia Early Data Release 3". In: *Astronomy & Astrophysics* 649, A2.

Line, Michael R. et al. (Dec. 2016). "No thermal inversion and a solar water abundance for the hot Jupiter HD 209458B from HST/WFC3 spectroscopy". In: *The Astronomical Journal* 152.6, p. 203.

Lopez, Eric D. (Nov. 2017). "Born dry in the photoevaporation desert: Kepler's ultra-short-period planets formed water-poor". In: *Monthly Notices of the Royal Astronomical Society* 472.1, pp. 245–253.

Lothringer, Joshua D. et al. (Apr. 2022). "UV absorption by silicate cloud precursors in ultra-hot Jupiter WASP-178b". In: *Nature* 604.7904, pp. 49–52.

Lovis, C. et al. (Mar. 2017). "Atmospheric characterization of Proxima b by coupling the SPHERE high-contrast imager to the ESPRESSO spectrograph". In: *Astronomy & Astrophysics* 599, A16.

Luger, R. and R. Barnes (Feb. 2015). "Extreme Water Loss and Abiotic O2 Buildup on Planets Throughout the Habitable Zones of M Dwarfs". In: *Astrobiology* 15.2, pp. 119–143.

Lupu, Roxana E. et al. (Dec. 2016). "Developing atmospheric retrieval methods for direct imaging spectroscopy of gas giants in reflected light. I. Methane abundances and basic cloud properties". In: *The Astronomical Journal* 152.6, p. 217.

Lustig-Yaeger, Jacob, Victoria S. Meadows, and Andrew P. Lincowski (July 2019). "The Detectability and Characterization of the TRAPPIST-1 Exoplanet Atmospheres with JWST". In: *The Astronomical Journal* 158.1, p. 27.

MacDonald, Ryan J. et al. (May 2018). "Exploring H2O Prominence in Reflection Spectra of Cool Giant Planets". In: *The Astrophysical Journal* 858.2, p. 69.

Macintosh, B. et al. (Oct. 2015). "Discovery and spectroscopy of the young jovian planet 51 Eri b with the Gemini Planet Imager". In: *Science* 350.6256, pp. 64–67.

Madhusudhan, N. and S. Seager (Dec. 2009). "A temperature and abundance retrieval method for exoplanet atmospheres". In: *The Astrophysical Journal* 707.1, pp. 24–39.

Madhusudhan, Nikku (Aug. 2019). "Exoplanetary Atmospheres: Key Insights, Challenges, and Prospects". In: *Annual Review of Astronomy and Astrophysics* 57.1, pp. 617–663.

Maguire, Cathal et al. (July 2024). "High resolution atmospheric retrievals of WASP-76b transmission spectroscopy with ESPRESSO: Monitoring limb asymmetries across multiple transits". In: *Astronomy & Astrophysics* 687, A49.

Mahapatra, G. et al. (Mar. 2023). "From exo-Earths to exo-Venuses: Flux and polarization signatures of reflected light". In: *Astronomy & Astrophysics* 671, A165.

Males, Jared R. et al. (Aug. 2022). "The conceptual design of GMagAO-X: visible wavelength high contrast imaging with GMT". In: *Adaptive Optics Systems VIII*. Ed. by Dirk Schmidt, Laura Schreiber, and Elise Vernet. SPIE, p. 170.

Malik, Matej et al. (Jan. 2017). "HELIOS: An open-source, gpu-accelerated radiative transfer code for self-consistent exoplanetary atmospheres". In: *The Astronomical Journal* 153.2, p. 56.

Mallama, Anthony, Bruce Krobusek, and Hristo Pavlov (Jan. 2017). "Comprehensive wide-band magnitudes and albedos for the planets, with applications to exo-planets and Planet Nine". In: *Icarus* 282, pp. 19–33.

Mallonn, M. et al. (Apr. 2019). "Low albedos of hot to ultra-hot Jupiters in the optical to near-infrared transition regime". In: *Astronomy & Astrophysics* 624, A62.

Mamajek, Eric and Karl Stapelfeldt (Feb. 2024). "NASA Exoplanet Exploration Program (ExEP) Mission Star List for the Habitable Worlds Observatory (2023)". In: *arxiv*.

Marconi, A et al. (Mar. 2021). "HIRES, the High-resolution Spectrograph for the ELT". In: *The Messenger* 182, pp. 27–32.

Marley, Mark et al. (Dec. 2014). "A Quick Study of the Characterization of Radial Velocity Giant Planets in Reflected Light by Forward and Inverse Modeling". In: *arxiv*.

Marois, Christian et al. (Apr. 2006). "Angular Differential Imaging: A Powerful High-Contrast Imaging Technique". In: *The Astrophysical Journal* 641.1, pp. 556–564.

Martins, J. H. C. et al. (Apr. 2015). "Evidence for a spectroscopic direct detection of reflected light from 51 Pegasi b". In: *Astronomy & Astrophysics* 576, A134.

Mayor, Michel and Didier Queloz (Nov. 1995). "A Jupiter-mass companion to a solar-type star". In: *Nature* 378.6555, pp. 355–359.

Mazeh, T., T. Holczer, and S. Faigler (May 2016). "Dearth of short-period Neptunian exoplanets: A desert in period-mass and period-radius planes". In: *Astronomy & Astrophysics* 589, A75.

Meadows, Victoria S. (Oct. 2017). "Reflections on O2 as a Biosignature in Exoplanetary Atmospheres". In: *Astrobiology* 17.10, pp. 1022–1052.

Meadows, Victoria S., Andrew P. Lincowski, and Jacob Lustig-Yaeger (Oct. 2023). "The Feasibility of Detecting Biosignatures in the TRAPPIST-1 Planetary System with JWST". In: *The Planetary Science Journal* 4.10, p. 192.

Meadows, Victoria S. et al. (June 2018). "Exoplanet Biosignatures: Understanding Oxygen as a Biosignature in the Context of Its Environment". In: *Astrobiology* 18.6, pp. 630–662.

Ment, Kristo and David Charbonneau (June 2023). "The Occurrence Rate of Terrestrial Planets Orbiting Nearby Mid-to-late M Dwarfs from TESS Sectors 1-42". In: *The Astronomical Journal* 165.6, p. 265.

Mettler, Jean-Noel et al. (Mar. 2024). "Earth as an Exoplanet. III. Using Empirical Thermal Emission Spectra as an Input for Atmospheric Retrieval of an Earth-twin Exoplanet". In: *The Astrophysical Journal* 963.1, p. 24.

Mikal-Evans, Thomas (Dec. 2021). "Detecting the proposed CH4-CO2 biosignature pair with the James Webb Space Telescope: TRAPPIST-1e and the effect of cloud/haze". In: *Monthly Notices of the Royal Astronomical Society* 510.1, pp. 980–991.

Morley, Caroline V. et al. (Dec. 2015). "Thermal emission and reflected light spectra of super Earths with flat transmission spectra". In: *The Astrophysical Journal* 815.2, p. 110.

Mukherjee, Sagnick, Natasha E. Batalha, and Mark S. Marley (Apr. 2021). "Cloud Parameterizations and their Effect on Retrievals of Exoplanet Reflection Spectroscopy". In: *The Astrophysical Journal* 910.2, p. 158.

Mulders, Gijs D., Ilaria Pascucci, and Daniel Apai (Nov. 2015). "An increase in the mass of planetary systems around lower-mass stars". In: *The Astrophysical Journal* 814.2, p. 130.

Murray, C. D. and A. C. M. Correia (2010). "Keplerian Orbits and Dynamics of Exoplanets". In: *Exoplanets*. Ed. by S Seager, pp. 15–23.

Nayak, Michael et al. (Mar. 2017). "Atmospheric Retrieval for Direct Imaging Spectroscopy of Gas Giants in Reflected Light. II. Orbital Phase and Planetary Radius". In: *Publications of the Astronomical Society of the Pacific* 129.973, p. 034401.

Nielsen, Eric L. et al. (July 2019). "The Gemini Planet Imager Exoplanet Survey: Giant Planet and Brown Dwarf Demographics from 10 to 100 au". In: *The Astronomical Journal* 158.1, p. 13.

Noll, S. et al. (July 2012). "An atmospheric radiation model for Cerro Paranal". In: *Astronomy & Astrophysics* 543, A92.

Nortmann, L. et al. (Apr. 2024). "CRIRES+ transmission spectroscopy of WASP-127b. Detection of the resolved signatures of a supersonic equatorial jet and cool poles in a hot planet". In: *arxiv*.

Nowak, M. et al. (July 2018). "K-Stacker: Keplerian image recombination for the direct detection of exoplanets". In: *Astronomy & Astrophysics* 615, A144.

Nugroho, Stevanus K. et al. (Dec. 2017). "High-resolution Spectroscopic Detection of TiO and a Stratosphere in the Day-side of WASP-33b". In: *The Astronomical Journal* 154.6, p. 221.

Owen, James E. and Yanqin Wu (Feb. 2016). "Atmospheres of low-mass planets: The "boil-off"". In: *The Astrophysical Journal* 817.2, p. 107.

Owen, Tobias (1980). "The Search for Early Forms of Life in Other Planetary Systems: Future Possibilities Afforded by Spectroscopic Techniques". In: pp. 177–185.

Packham, Christopher et al. (July 2018). "MICHI: a thermal-infrared instrument for the TMT". In: *Ground-based and Airborne Instrumentation for Astronomy VII*. Ed. by Hideki Takami, Christopher J. Evans, and Luc Simard. SPIE, p. 366.

Pagano, I. et al. (Nov. 2023). "Constraining the reflective properties of using CHEOPS photometry". In: *Astronomy & Astrophysics*.

Pallé, E. et al. (Nov. 2003). "Earthshine and the Earth's albedo: 2. Observations and simulations over 3 years". In: *Journal of Geophysical Research: Atmospheres* 108.D22.

Parker, Luke T et al. (May 2024). "Into the red: an M-band study of the chemistry and rotation of β Pictoris b at high spectral resolution". In: *Monthly Notices of the Royal Astronomical Society* 531.2, pp. 2356–2378.

Parmentier, Vivien et al. (Sept. 2016). "Transitions in the cloud composition of hot Jupiters". In: *The Astrophysical Journal* 828.1, p. 22.

Patapis, P. et al. (Oct. 2021). "Direct emission spectroscopy of exoplanets with the medium resolution imaging spectrometer on board JWST MIRI: I. Molecular mapping and sensitivity to instrumental effects". In: *Astronomy & Astrophysics* 658, A72.

Pepe, F. et al. (Jan. 2021). "ESPRESSO at VLT". In: *Astronomy & Astrophysics* 645, A96.

Perrin, Marshall D. et al. (Aug. 2014). "Updated point spread function simulations for JWST with WebbPSF". In: ed. by Jacobus M. Oschmann et al., p. 91433X.

Petit dit de la Roche, D. J. M., H. J. Hoeijmakers, and I. A. G. Snellen (Aug. 2018). "Molecule mapping of HR8799b using OSIRIS on Keck". In: *Astronomy & Astrophysics* 616, A146.

Petrus, S. et al. (Apr. 2021). "Medium-resolution spectrum of the exoplanet HIP 65426 b". In: *Astronomy & Astrophysics* 648, A59.

Phillips, M. W. et al. (May 2020). "A new set of atmosphere and evolution models for cool T-Y brown dwarfs and giant exoplanets". In: *Astronomy & Astrophysics* 637, A38.

Pidhorodetska, Daria et al. (Aug. 2020). "Detectability of Molecular Signatures on TRAPPIST-1e through Transmission Spectroscopy Simulated for Future Space-based Observatories". In: *The Astrophysical Journal Letters* 898.2, p. L33.

Pont, F. et al. (Feb. 2008). "Detection of atmospheric haze on an extrasolar planet: the 0.55-1.05 μm transmission spectrum of HD 189733b with the Hubble Space Telescope". In: *Monthly Notices of the Royal Astronomical Society* 385.1, pp. 109–118.

Pont, F. et al. (July 2013). "The prevalence of dust on the exoplanet HD 189733b from Hubble and Spitzer observations". In: *Monthly Notices of the Royal Astronomical Society* 432.4, pp. 2917–2944.

Poser, A J and R Redmer (Mar. 2024). "The effect of cloudy atmospheres on the thermal evolution of warm giant planets from an interior modelling perspective". In: *Monthly Notices of the Royal Astronomical Society* 529.3, pp. 2242–2257.

Prinoth, B. et al. (Oct. 2023). "Time-resolved transmission spectroscopy of the ultra-hot Jupiter WASP-189 b". In: *Astronomy & Astrophysics* 678, A182.

Qiu, J. et al. (Nov. 2003). "Earthshine and the Earth's albedo: 1. Earthshine observations and measurements of the lunar phase function for accurate measurements of the Earth's Bond albedo". In: *Journal of Geophysical Research: Atmospheres* 108.D22.

Racine, Rene et al. (May 1999). "Speckle Noise and the Detection of Faint Companions". In: *Publications of the Astronomical Society of the Pacific* 111.759, pp. 587–594.

Radica, Michael et al. (July 2023). "Awesome SOSS: transmission spectroscopy of WASP-96b with NIRISS/SOSS". In: *Monthly Notices of the Royal Astronomical Society* 524.1, pp. 835–856.

Radica, Michael et al. (Feb. 2024). "Muted Features in the JWST NIRISS Transmission Spectrum of Hot Neptune LTT 9779b". In: *The Astrophysical Journal Letters* 962.1, p. L20.

Rajan, Abhijith et al. (Aug. 2015). "Characterizing the atmospheres of the HR8799 planets with HST/WFC3". In: *The Astrophysical Journal* 809.2, p. L33.

Rajan, Abhijith et al. (July 2017). "Characterizing 51 Eri b from 1 to 5 μm: A Partly Cloudy Exoplanet". In: *The Astronomical Journal* 154.1, p. 10.

Rameau, J. et al. (May 2021). "Spectral unmixing for exoplanet direct detection in hyperspectral data". In: *Astronomy & Astrophysics* 649, A143.

Ramkumar, Swaetha et al. (Aug. 2023). "High-resolution emission spectroscopy retrievals of MASCARA-1b with CRIRES+: strong detections of CO, H2O, and Fe emission lines and a C/O consistent with solar". In: *Monthly Notices of the Royal Astronomical Society* 525.2, pp. 2985–3005.

Rasmussen, Kaitlin C. et al. (Oct. 2023). "A Nondetection of Iron in the First High-resolution Emission Study of the Lava Planet 55 Cnc e". In: *The Astronomical Journal* 166.4, p. 155.

Rauer, H. et al. (May 2011). "Potential biosignatures in super-Earth atmospheres". In: *Astronomy & Astrophysics* 529, A8.

Read, P. L. et al. (Jan. 2016). "Global energy budgets and 'Trenberth diagrams' for the climates of terrestrial and gas giant planets". In: *Quarterly Journal of the Royal Meteorological Society* 142.695, pp. 703–720.

Reiners, A. and G. Basri (Feb. 2010). "A volume-limited sample of 63 M7-M9.5 dwarfs. II. Activity, magnetism, and the fade of the rotation-dominated dynamo". In: *The Astrophysical Journal* 710.2, pp. 924–935.

Reyle, C. et al. (Feb. 2023). "The 10 parsec sample in the Gaia era: first update". In: *The 21st Cambridge Workshop on Cool Stars, Stellar Systems, and the Sun*. Cambridge Workshop on Cool Stars, Stellar Systems, and the Sun, p. 218.

Reylé, C. et al. (June 2021). "The 10 parsec sample in the Gaia era". In: *Astronomy & Astrophysics* 650, A201.

Ridden-Harper, Andrew et al. (May 2023). "High-resolution Emission Spectroscopy of the Ultrahot Jupiter KELT-9b: Little Variation in Day- and Nightside Emission Line Contrasts". In: *The Astronomical Journal* 165.5, p. 211.

Robinson, Tyler D., Victoria S. Meadows, and David Crisp (Sept. 2010). "Detecting oceans on extrasolar planets using the glint effect". In: *The Astrophysical Journal* 721.1, pp. L67–L71.

Robinson, Tyler D. et al. (June 2011). "Earth as an Extrasolar Planet: Earth Model Validation Using EPOXI Earth Observations". In: *Astrobiology* 11.5, pp. 393–408.

Rodler, F., M. Kürster, and T. Henning (May 2010). "τ Boötis b: Hunting for reflected starlight". In: *Astronomy and Astrophysics* 514, A23.

Rodler, F., M. Lopez-Morales, and I. Ribas (July 2012). "Weighing the non-transiting hot Jupiter τ Boo b". In: *The Astrophysical Journal* 753.1, p. L25.

Rodler, F. et al. (Feb. 2013). "The return of the mummy: Evidence for starlight reflected from the massive hot Jupiter τ Boo b?" In: *Astronomische Nachrichten* 334.1-2, pp. 188–191.

Rotman, Yoav et al. (Jan. 2023). "General Circulation Model Constraints on the Detectability of the CO2-CH4 Biosignature Pair on TRAPPIST-1e with JWST". In: *The Astrophysical Journal Letters* 942.1, p. L4.

Ruffio, Jean-Baptiste et al. (Nov. 2019). "Radial Velocity Measurements of HR 8799 b and c with Medium Resolution Spectroscopy". In: *The Astronomical Journal* 158.5, p. 200.

Ruffio, Jean-Baptiste et al. (Dec. 2021). "Deep Exploration of the Planets HR 8799 b, c, and d with Moderate-resolution Spectroscopy". In: *The Astronomical Journal* 162.6, p. 290.

Russell, Henry Norris (Apr. 1916). "On the Albedo of the Planets and Their Satellites". In: *The Astrophysical Journal* 43, p. 173.

Sabotta, S. et al. (Sept. 2021). "The CARMENES search for exoplanets around M dwarfs". In: *Astronomy & Astrophysics* 653, A114.

Sagan, Carl et al. (Oct. 1993). "A search for life on Earth from the Galileo spacecraft". In: *Nature* 365.6448, pp. 715–721.

Salvatier, John, Thomas V. Wiecki, and Christopher Fonnesbeck (Apr. 2016). "Probabilistic programming in Python using PyMC3". In: *PeerJ Computer Science* 2, e55.

Samland, M. et al. (July 2017). "Spectral and atmospheric characterization of 51 Eridani b using VLT/SPHERE". In: *Astronomy & Astrophysics* 603, A57.

Scandariato, G. et al. (Feb. 2021). "The GAPS Programme at TNG". In: *Astronomy & Astrophysics* 646, A159.

Schubert, Gerald and Richard L Walterscheid (2000). "Earth". In: *Allen's Astrophysical Quantities*. Ed. by Arthur N Cox, p. 239.

Schwarz, Henriette et al. (Apr. 2015). "Evidence against a strong thermal inversion in HD 209458b from high-dispersion spectroscopy". In: *Astronomy & Astrophysics* 576, A111.

Schwarz, Henriette et al. (Sept. 2016). "The slow spin of the young substellar companion GQ Lupi b and its orbital configuration". In: *Astronomy & Astrophysics* 593, A74.

Schwieterman, Edward W. and Michaela Leung (July 2024). "An Overview of Exoplanet Biosignatures". In: *Reviews in Mineralogy and Geochemistry* 90.1, pp. 465–514.

Schwieterman, Edward W. et al. (June 2018). "Exoplanet Biosignatures: A Review of Remotely Detectable Signs of Life". In: *Astrobiology* 18.6, pp. 663–708.

Seager, Sara and William Bains (Mar. 2015). "The search for signs of life on exoplanets at the interface of chemistry and planetary science". In: *Science Advances* 1.2.

Seager, Sara and Drake Deming (Aug. 2010). "Exoplanet Atmospheres". In: *Annual Review of Astronomy and Astrophysics* 48.1, pp. 631–672.

Seager, Sara, Matthew Schrenk, and William Bains (Jan. 2012). "An Astrophysical View of Earth-Based Metabolic Biosignature Gases". In: *Astrobiology* 12.1, pp. 61–82.

Segura, Antigona et al. (Dec. 2005). "Biosignatures from Earth-Like Planets Around M Dwarfs". In: *Astrobiology* 5.6, pp. 706–725.

Seidel, J. V. et al. (Oct. 2023). "Detection of atmospheric species and dynamics in the bloated hot Jupiter WASP-172 b with ESPRESSO". In: *Astronomy & Astrophysics* 678, A150.

Serindag, Dilovan B. and Ignas A. G. Snellen (Jan. 2019). "Testing the Detectability of Extraterrestrial O2 with the Extremely Large Telescopes Using Real Data with Real Noise". In: *The Astrophysical Journal Letters* 871.1, p. L7.

Sharp, Rob et al. (Aug. 2016). "GMTIFS: The Giant Magellan Telescope integral fields spectrograph and imager". In: ed. by Christopher J. Evans, Luc Simard, and Hideki Takami, 99081Y.

Shields, Aomawa L., Cecilia M. Bitz, and Igor Palubski (Oct. 2019). "Energy Budgets for Terrestrial Extrasolar Planets". In: *The Astrophysical Journal Letters* 884.1, p. L2.

Showman, A. P. et al. (2013). "Atmospheric Circulation of Terrestrial Exoplanets". In: *Comparative Climatology of Terrestrial Planets*. University of Arizona Press.

Shporer, Avi and Renyu Hu (Sept. 2015). "Studying atmosphere-dominated hot Jupiter Kepler phase curves: evidence that inhomogeneous atmospheric reflection is common". In: *The Astronomical Journal* 150.4, p. 112.

Sing, David K. et al. (Jan. 2016). "A continuum from clear to cloudy hot-Jupiter exoplanets without primordial water depletion". In: *Nature* 529.7584, pp. 59–62.

Singla, Manika and Sujan Sengupta (Aug. 2023). "New models of reflection spectra for terrestrial exoplanets: Present and prebiotic Earth orbiting around stars of different spectral types". In: *New Astronomy* 102, p. 102024.

Sluijs, Lennart van et al. (Apr. 2023). "Carbon monoxide emission lines reveal an inverted atmosphere in the ultra hot Jupiter WASP-33 b consistent with an eastward hot spot". In: *Monthly Notices of the Royal Astronomical Society* 522.2, pp. 2145–2170.

Smette, A. et al. (Apr. 2015). "Molecfit: A general tool for telluric absorption correction". In: *Astronomy & Astrophysics* 576, A77.

Smith, Adam J. R. W. et al. (Feb. 2020). "Detecting and Characterizing Water Vapor in the Atmospheres of Earth Analogs through Observation of the 0.94 μm Feature in Reflected Light". In: *The Astronomical Journal* 159.2, p. 36.

Smith, Peter C. B. et al. (Mar. 2024). "A Combined Ground-based and JWST Atmospheric Retrieval Analysis: Both IGRINS and NIRSpec Agree that the Atmosphere of WASP-77A b Is Metal-poor". In: *The Astronomical Journal* 167.3, p. 110.

Snellen, I. et al. (Apr. 2015). "Combining high-dispersion spectroscopy with high contrast imaging: Probing rocky planets around our nearest neighbors". In: *Astronomy & Astrophysics* 576, A59.

Snellen, I. A. G. et al. (Feb. 2013). "Finding extraterrestrial life using ground-based high-dispersion spectroscopy". In: *The Astrophysical Journal* 764.2, p. 182.

Snellen, Ignas A. G. et al. (June 2010). "The orbital motion, absolute mass and high-altitude winds of exoplanet HD 209458b". In: *Nature* 465.7301, pp. 1049–1051.

Snellen, Ignas A. G. et al. (May 2014). "Fast spin of the young extrasolar planet β Pictoris b". In: *Nature* 509.7498, pp. 63–65.

Soummer, Remi, Laurent Pueyo, and James Larkin (Aug. 2012). "Detection and characterization of exoplanets and disks using projections on Karhunen-Loève eigenimages". In: *The Astrophysical Journal* 755.2, p. L28.

Sparks, William B. and Holland C. Ford (Oct. 2002). "Imaging Spectroscopy for Extrasolar Planet Detection". In: *The Astrophysical Journal* 578.1, pp. 543–564.

Spring, E. F. et al. (Mar. 2022). "Black Mirror: The impact of rotational broadening on the search for reflected light from 51 Pegasi b with high resolution spectroscopy". In: *Astronomy & Astrophysics* 659, A121.

Stam, D. M. (May 2008). "Spectropolarimetric signatures of Earth-like extrasolar planets". In: *Astronomy & Astrophysics* 482.3, pp. 989–1007.

Stephan, Katrin et al. (Apr. 2010). "Specular reflection on Titan: Liquids in Kraken Mare". In: *Geophysical Research Letters* 37.7.

Sterzik, Michael F. et al. (Feb. 2019). "Spectral and temporal variability of Earth observed in polarization". In: *Astronomy & Astrophysics* 622, A41.

Stevenson, Kevin B. et al. (Apr. 2010). "Possible thermochemical disequilibrium in the atmosphere of the exoplanet GJ 436b". In: *Nature* 464.7292, pp. 1161–1164.

Stone, Jordan M. et al. (Dec. 2020). "High-contrast Thermal Infrared Spectroscopy with ALES: The 3â4 μm Spectrum of κ Andromedae b". In: *The Astronomical Journal* 160.6, p. 262.

Stüeken, Eva E. et al. (July 2024). "The Early Earth as an Analogue for Exoplanetary Biogeochemistry". In: *Reviews in Mineralogy and Geochemistry* 90.1, pp. 515–558.

Swain, Mark et al. (July 2013). "Probing the extreme planetary atmosphere of WASP-12b". In: *Icarus* 225.1, pp. 432–445.

Takahashi, J. et al. (Sept. 2021). "Polarimetric signature of the oceans as detected by near-infrared Earthshine observations". In: *Astronomy & Astrophysics* 653, A99.

Tamuz, O., T. Mazeh, and S. Zucker (Feb. 2005). "Correcting systematic effects in a large set of photometric light curves". In: *Monthly Notices of the Royal Astronomical Society* 356.4, pp. 1466–1470.

Taylor, Jake and Vivien Parmentier (Sept. 2023a). "Another look at the dayside spectra of WASP-43b and HD 209458b: Are there scattering clouds?" In: *Monthly Notices of the Royal Astronomical Society* 526.2, pp. 2133–2140.

Taylor, Jake et al. (July 2023b). "Awesome SOSS: atmospheric characterization of WASP-96b using the JWST early release observations". In: *Monthly Notices of the Royal Astronomical Society* 524.1, pp. 817–834.

Tecza, Matthias et al. (2009). "HARMONI: A Narrow Field Near-infrared Integral Field Spectrograph for the E-ELT". In: *Science with the VLT in the ELT Era*. Dordrecht: Springer Netherlands, pp. 267–271.

Teinturier, L. et al. (Mar. 2024). "The radiative and dynamical impact of clouds in the atmosphere of the hot Jupiter WASP-43 b". In: *Astronomy & Astrophysics* 683, A231.

Thatte, N (June 2010). "HARMONI: A Single Field, Visible and Near-infrared Integral Field Spectrograph for the E-ELT". In: *The Messenger* 140, pp. 26–27.

Thatte, Niranjan et al. (Dec. 2020). "HARMONI: first light spectroscopy for the ELT: instrument final design and quantitative performance predictions". In: *Ground-based and Airborne Instrumentation for Astronomy VIII*. Ed. by Christopher J. Evans, Julia J. Bryant, and Kentaro Motohara. SPIE, p. 337.

Thatte, Niranjan et al. (Mar. 2021). "HARMONI: the ELT's First-Light Near-infrared and Visible Integral Field Spectrograph". In: *The Messenger* 182, pp. 7–12.

Thatte, Niranjan . et al. (Aug. 2022). "HARMONI at ELT: overview of the capabilities and expected performance of the ELT's first light, adaptive optics assisted integral field spectrograph." In: *Ground-based and Airborne Instrumentation for Astronomy IX*. Ed. by Christopher J. Evans, Julia J. Bryant, and Kentaro Motohara. SPIE, p. 71.

Thatte, Niranjan A. et al. (July 2014). "HARMONI: the first light integral field spectrograph for the E-ELT". In: ed. by Suzanne K. Ramsay, Ian S. McLean, and Hideki Takami, p. 914725.

Thatte, Niranjan A. et al. (Aug. 2016). "The E-ELT first light spectrograph HARMONI: capabilities and modes". In: ed. by Christopher J. Evans, Luc Simard, and Hideki Takami, p. 99081X.

Tian, Feng (Dec. 2015). "History of water loss and atmospheric O2 buildup on rocky exoplanets near M dwarfs". In: *Earth and Planetary Science Letters* 432, pp. 126–132.

Tian, Feng et al. (Jan. 2014). "High stellar FUV/NUV ratio and oxygen contents in the atmospheres of potentially habitable planets". In: *Earth and Planetary Science Letters* 385, pp. 22–27.

Trees, V. J. H. and D. M. Stam (June 2019). "Blue, white, and red ocean planets". In: *Astronomy & Astrophysics* 626, A129.

Trees, V. J. H. and D. M. Stam (Aug. 2022). "Ocean signatures in the total flux and polarization spectra of Earth-like exoplanets". In: *Astronomy & Astrophysics* 664, A172.

Turbet, Martin et al. (June 2020). "Revised mass-radius relationships for water-rich rocky planets more irradiated than the runaway greenhouse limit". In: *Astronomy & Astrophysics* 638, A41.

Turbet, Martin et al. (Oct. 2021). "Day-night cloud asymmetry prevents early oceans on Venus but not on Earth". In: *Nature* 598.7880, pp. 276–280.

Vaughan, Sophia R et al. (July 2023). "Chasing rainbows and ocean glints: Inner working angle constraints for the Habitable Worlds Observatory". In: *Monthly Notices of the Royal Astronomical Society* 524.4, pp. 5477–5485.

Vaughan, Sophia R et al. (Jan. 2024). "Behind the mask: can HARMONI@ELT detect biosignatures in the reflected light of Proxima b?" In: *Monthly Notices of the Royal Astronomical Society* 528.2, pp. 3509–3522.

Vigan, A. et al. (July 2021). "The SPHERE infrared survey for exoplanets (SHINE)". In: *Astronomy & Astrophysics* 651, A72.

Villanueva, G.L. et al. (Sept. 2018). "Planetary Spectrum Generator: An accurate online radiative transfer suite for atmospheres, comets, small bodies and exoplanets". In: *Journal of Quantitative Spectroscopy and Radiative Transfer* 217, pp. 86–104.

Vissapragada, Shreyas et al. (Feb. 2024). "A High-resolution Non-detection of Escaping Helium in the Ultrahot Neptune LTT 9779b: Evidence for Weakened Evaporation". In: *The Astrophysical Journal Letters* 962.1, p. L19.

Walker, Sara I. et al. (June 2018). "Exoplanet Biosignatures: Future Directions". In: *Astrobiology* 18.6, pp. 779–824.

Wang, Ji et al. (Apr. 2017). "Observing Exoplanets with High Dispersion Coronagraphy. I. The Scientific Potential of Current and Next-generation Large Ground and Space Telescopes". In: *The Astronomical Journal* 153.4, p. 183.

Wang, Ji et al. (July 2018a). "Baseline requirements for detecting biosignatures with the HabEx and LUVOIR mission concepts". In: *Journal of Astronomical Telescopes, Instruments, and Systems* 4.03, p. 1.

Wang, Ji et al. (Dec. 2018b). "Detecting Water in the Atmosphere of HR 8799 c with L-band High-dispersion Spectroscopy Aided by Adaptive Optics". In: *The Astronomical Journal* 156.6, p. 272.

Ward, Dayton (2016). *Star Trek Vulcan*. London: Titan Books.

Ward-Duong, K. et al. (Jan. 2021). "Gemini Planet Imager Spectroscopy of the Dusty Substellar Companion HD 206893 B". In: *The Astronomical Journal* 161.1, p. 5.

West, Robert A. et al. (Dec. 2022). "Spectropolarimetry as a Means to Address Cloud Composition and Habitability for a Cloudy Exoplanetary Atmosphere in the Habitable Zone". In: *The Astrophysical Journal* 940.2, p. 183.

Whiteford, Niall et al. (Aug. 2023). "Retrieval study of cool, directly imaged exoplanet 51 Eri b". In: *Monthly Notices of the Royal Astronomical Society* 525.1, pp. 1375–1400.

Wilcomb, Kielan K. et al. (Nov. 2020). "Moderate-resolution K-band Spectroscopy of Substellar Companion κ Andromedae b". In: *The Astronomical Journal* 160.5, p. 207.

Williams, Darren M. and Eric Gaidos (June 2008). "Detecting the glint of starlight on the oceans of distant planets". In: *Icarus* 195.2, pp. 927–937.

Windsor, James D. et al. (Jan. 2024). "Inner Edge Habitable Zone Limits Around Main Sequence Stars: Cloudy Estimates". In: *arxiv*.

Wordsworth, Robin and Raymond Pierrehumbert (Apr. 2014). "Abiotic oxygen-dominated atmospheres on terrestrial habitable zone planets". In: *The Astrophysical Journal* 785.2, p. L20.

Wright, Shelley A. et al. (July 2016). "The infrared imaging spectrograph (IRIS) for TMT: latest science cases and simulations". In: ed. by Enrico Marchetti, Laird M. Close, and Jean-Pierre Véran, p. 990905.

Wunderlich, Fabian et al. (Apr. 2019). "Detectability of atmospheric features of Earth-like planets in the habitable zone around M dwarfs". In: *Astronomy & Astrophysics* 624, A49.

Xie, Chen et al. (Oct. 2022). "Reference-star differential imaging on SPHERE/IRDIS". In: *Astronomy & Astrophysics* 666, A32.

Yan, F. et al. (Apr. 2023). "CRIRES+ detection of CO emissions lines and temperature inversions on the dayside of WASP-18b and WASP-76b". In: *Astronomy & Astrophysics* 672, A107.

Yang, Jun, Nicolas B. Cowan, and Dorian S. Abbot (June 2013). "Stabilizing cloud feedback dramatically expands the habitable zone of tidally locked planets". In: *The Astrophysical Journal* 771.2, p. L45.

Yang, Yuanheng et al. (Jan. 2024). "High-resolution Transmission Spectroscopy of Ultrahot Jupiter WASP-33b with NEID". In: *The Astronomical Journal* 167.1, p. 36.

Young, M E, E F Spring, and J L Birkby (May 2024). "Searching for NLTE effects in the high-resolution transmission spectrum of WASP-121 b with cloudyâforâexoplanets". In: *Monthly Notices of the Royal Astronomical Society* 530.4, pp. 4356–4377.

Zellner, Ben (Apr. 1973). "The polarization of Titan". In: *Icarus* 18.4, pp. 661–664.

Zhang, Huihao, Ji Wang, and Michael K. Plummer (Jan. 2024). "Detecting Biosignatures in Nearby Rocky Exoplanets Using High-contrast Imaging and Medium-resolution Spectroscopy with the Extremely Large Telescope". In: *The Astronomical Journal* 167.1, p. 37.

Zieba, Sebastian et al. (Aug. 2023). "No thick carbon dioxide atmosphere on the rocky exoplanet TRAPPIST-1 c". In: *Nature* 620.7975, pp. 746–749.

Zieleniewski, S. et al. (Nov. 2015). "hsim: a simulation pipeline for the HARMONI integral field spectrograph on the European ELT". In: *Monthly Notices of the Royal Astronomical Society* 453.4, pp. 3755–3766.

Zsom, Andras, Lisa Kaltenegger, and Colin Goldblatt (Nov. 2012). "A 1D microphysical cloud model for Earth, and Earth-like exoplanets: Liquid water and water ice clouds in the convective troposphere". In: *Icarus* 221.2, pp. 603–616.

Zugger, M. E. et al. (Sept. 2011). "Searching for water Earths in the near-infrared". In: *The Astrophysical Journal* 739.1, p. 12.

Zurlo, Alice (Apr. 2024). "Direct imaging of exoplanets". In: *arxiv*.